Fully-passive Wireless Acquisition of Biosignals

by

Shiyi Liu

A Dissertation Presented in Partial Fulfillment
of the Requirements for the Degree
Doctor of Philosophy

Approved October 2020 by the
Graduate Supervisory Committee:

Jennifer Blain Christen, Chair
Mehdi Nikkhah
Michael Goryll
Stephen Phillips
Yu Cao

ARIZONA STATE UNIVERSITY

December 2020

ABSTRACT

The recording of biosignals enables physicians to correctly diagnose diseases and prescribe treatment. Existing wireless systems failed to effectively replace the conventional wired methods due to their large sizes, high power consumption, and the need to replace batteries. This thesis aims to alleviate these issues by presenting a series of wireless fully-passive sensors for the acquisition of biosignals: including neuropotential, biopotential, intracranial pressure (ICP), in addition to a stimulator for the pacing of engineered cardiac cells. In contrast to existing wireless biosignal recording systems, the proposed wireless sensors do not contain batteries or high-power electronics such as amplifiers or digital circuitries. Instead, the RFID tag-like sensors utilize a unique radiofrequency (RF) backscattering mechanism to enable wireless and battery-free telemetry of biosignals with extremely low power consumption. This characteristic minimizes the risk of heat-induced tissue damage and avoids the need to use any transcranial/transcutaneous wires, and thus significantly enhances long-term safety and reliability. For neuropotential recording, a small (9mm x 8mm), biocompatible, and flexible wireless recorder is developed and verified by *in vivo* acquisition of two types of neural signals, the somatosensory evoked potential (SSEP) and interictal epileptic discharges (IEDs). For wireless multichannel neural recording, a novel time-multiplexed multichannel recording method based on an inductor-capacitor delay circuit is presented and tested, realizing simultaneous wireless recording from 11 channels in a completely passive manner. For biopotential recording, a wearable and flexible wireless sensor is developed, achieving real-time wireless acquisition of ECG, EMG, and EOG signals. For

ICP monitoring, a very small (5mm x 4mm) wireless ICP sensor is designed and verified both *in vitro* through a benchtop setup and *in vivo* through real-time ICP recording in rats. Finally, for cardiac cell stimulation, a flexible wireless passive stimulator, capable of delivering stimulation current as high as 60 mA, is developed, demonstrating successful control over the contraction of engineered cardiac cells. The studies conducted in this thesis provide information and guidance for future translation of wireless fully-passive telemetry methods into actual clinical application, especially in the field of implantable and wearable electronics.

DEDICATION

To my family and my former advisor Junseok Chae

ACKNOWLEDGMENTS

I am especially grateful to my family. My mother Yan Xu and my father Weinong Liu have been continuously giving me encouragement and strength throughout my Ph.D. study. My brother, Shihong Liu, shared with me stories of his Ph.D. experience, which brought me peace and lifted my spirit when I encountered failure or difficulties. Without their support, it would be impossible for me to finish this long and difficult pursuit of a doctoral degree.

I wish to express my sincere gratitude to my former advisor, Dr. Junseok Chae. It was Dr. Chae who offered me the chance to join the Ph.D. program at ASU. His support, resources, and guidance helped me overcome difficulties in my research and enabled me to complete this thesis. I have learned a lot about how to become an excellent researcher from working with him. I sincerely thank Dr. Chae for everything he did and will always miss him as a great mentor and a good friend.

I am very grateful to my supervisor Dr. Jennifer Blain Christen. Dr. Christen kindly offered me support during my difficult time. She is always willing to help me as much as possible. She provided me with all the resources I needed to finish my thesis, and kindly offered me numerous opportunities to establish my networks for my future career development. Dr. Christen has been a truly wonderful advisor and I enjoyed working with her very much.

I am thankful to my committee members, including Dr. Mehdi Nikkhah, Dr. Michael Goryll, Dr. Stephen Phillips, and Dr. Yu Cao for contributing their valuable time

to my research studies. I thank Dr. Nikkhah for his kind guidance and advice on our collaborated project, and his efforts on our co-authored journal paper.

I am also thankful to my collaborators at Florida International University. I thank Dr. John Volakis, and Dr. Jorge Riera Diaz for offering me the opportunity to test our sensors in their laboratory, and for giving me valuable suggestions on how to revise my paper. I also thank Carolina Moncion and Lakshmini Balachandar for their great help and efforts in conducting the animal surgery at FIU and processing the data.

I am also grateful to my colleagues at ASU. I thank my former groupmates, Ang Chen, Jianwei Zhang, Seunghyun Lee, Hao Ren, Jennie Appel, and Ran Wang for their friendships and help in everyday life. I thank Jianwei Zhang for his valuable aid in machine learning data analysis. I thank my current group mates, Daniel Gulick, Johnathan Garich, and Ian Akamine for their time and support on animal surgery and the use of lab equipment. I also thank my colleague and coauthor Ali Navaei for his efforts in culturing the cardiac tissue and his editing on my first journal paper.

Finally, I would like to thank all the staff at ASU CSSER (Center for Solid State Electronics Research) for their help with microfabrication, and the staff at ASU Biodesign Institutes for their training on animal handling.

TABLE OF CONTENTS

Page

LIST OF TABLES ix

LIST OF FIGURES x

CHAPTER

1 INTRODUCTION 1

1.1 Background 1

1.2 Original Contributions 26

2 LITERATURE REVIEW 31

2.1 Wireless Neuropotential Recording 31

2.2 Wireless Biopotential Recording 41

2.3 Wireless Intracranial Pressure (ICP) Monitoring 45

2.4 Wireless Stimulation 52

2.5 Prior Works Related to This Thesis 56

3 BASIC PRINCIPLE OF RF BACKSCATTERING METHOD 60

3.1 The Mixing Characteristic of Varactor Diode 61

3.2 Basic of Antenna 67

3.3 Estimation of Backscattered Power 75

3.4 Simulation of Backscattered Power 79

4 WIRELESS FULLY-PASSIVE NEURAL RECORDER 85

4.1 Design and Fabrication 86

4.2 The External Interrogator 96

CHAPTER Page

4.3 Material and Method 97

4.4. Experiment Results....103

4.5 Discussion....117

5 WIRELESS MULTICHANNEL NEURAL RECORDER 121

5.1 Design of the Multichannel Recorder....122

5.2 The External Interrogator 151

5.3 Device Fabrication and Verification....155

6 WIRELESS FULLY-PASSIVE ACQUISITION OF BIOPOTENTIAL....162

6.1 Wireless Fully-passive Biopotential Sensor 163

6.2 The External Interrogator 168

6.3 Material and Method 170

6.4 Experiment Results....177

6.5 Discussion....195

7 WIRELESS FULLY-PASSIVE ICP MONITORING 197

7.1 Design of the Wireless Fully-passive ICP Sensor....198

7.2 Fabrication of the Wireless Fully-passive ICP Sensor....208

7.3 The External System 214

7.4 Experiment Results....217

8 WIRELESS PASSIVE STIMULATION OF CARDIAC CELL....224

8.1 Design of the Passive Wireless Stimulator....225

8.2 The External Transmitter 233

CHAPTER Page

8.3 Material and Method 235

8.4. Experiment Results and Discussion.....240

9 CONCLUSION 258

REFERENCES 260

APPENDIX

A COPYRIGHT 284

LIST OF TABLES

Table		Page
4.1	List of Discrete Electronic Components on the Neural Recorder	89
4.2	Characteristics of the Target Neuropotentials	91
4.3	Recipes for the Five-layers Tissue-emulating Phantom	104
4.4	Wired and Wireless In Vivo SSEP Recording Summary	111
4.5	Comparison of the Labeled IED and Machine Learning Recognized IED	114
4.6	Specification of the Proposed Wireless Neural Recorder in Comparison with Other State-of-the-art Systems	120
6.1	Amplitude and Frequency Range of the Target Biopotentials	169
6.2	SNR and Feature Extraction of the Wireless EMG	190
8.1	Design Requirement of the Wireless Stimulator	226
8.2	Impedance of the Bioreactor Chamber	247
8.3	Comparison of the Prior Wireless Stimulators with This Work	256

LIST OF FIGURES

Figure		Page
1.1	The Brain-Computer Interfaces (BCI)	4
1.2	Standard ECG Recording Method	11
1.3	Electrodes Placement in EOG Recording	12
1.4	External Ventricular Drainage (EVD) System	19
1.5	Electrical Stimulation Promotes the Growth of Engineered Cardiac Tissue	24
1.6	Comparison Between Wireless Fully-passive System and Conventional IC-based Passive Systems	27
2.1	Wireless Neural Recording Systems in the Form of Wireless Head Stages or Subcutaneous Microsystem	33
2.2	Fully-implantable Wireless Neural Recording System	40
2.3	Battery-free Wireless Biopotential Acquisition System	42
2.4	Epidermal Electronic System for Wireless Biopotential Acquisition	45
2.5	Wireless ICP Monitoring Systems Incorporating MEMS Pressure Sensors	48
2.6	Wireless Passive Pressure Sensors Based on LC Resonance Circuit	50
2.7	Miniaturized Injectable Wireless Stimulator	56
2.8	Prior Wireless Fully-passive Neural Recorder	58
2.9	Wireless Fully-passive Neural Recorder Based on PCB	59
3.1	Block Diagram of an RF Backscattering System	60
3.2	C-V Plot of the Varactor Diode MA46H120	64
3.3	Frequency Spectrum of the Current Generated by the Varactor MA46H120	65

Figure Page

3.4 Basic Model of Antenna Transmission 67

3.5 Radiation Pattern of a Dipole Antenna 72

3.6 Simulation of the Wireless Link Between Antennas 80

3.7 ADS Circuit Simulation 82

4.1 Full-passive Wireless Neural Recorder 87

4.2 Design and Fabrication of the Fully-passive Wireless Neural Recorder.....90

4.3 Simulation of the Fully-passive Wireless Neural Recorder.....92

4.4 Simulation Result of the Fully-passive Wireless Neural Recorder 93

4.5 Design and Optimization of the Circuitry 94

4.6 Circuit Model for Simulation of the External Interrogator 95

4.7 Schematic of the Experimental Setup for In Vivo SSEP Recording 99

4.8 Schematic of the Experimental Setup for In Vivo IED Recording.....100

4.9 Testing Setup of the Fully-passive Wireless Neural Recorder Inside the Tissue-Emulating Phantom 105

4.10 Characterization of the Fully-passive Wireless Neural Recorder Inside the Tissue-Emulating Phantom 106

4.11 Calibration of the Fully-passive Wireless Neural Reorder Using ECG 108

4.12 Fully-passive Wireless SSEP Recording.....110

4.13 Fully-passive Wireless IED Recording 113

4.14 Mean and Standard Deviation of the Recorded IED.....115

5.1 Schematic of Passive Multichannel Wireless Neural Recording.....123

Figure Page

5.2 The LC Delay Line Circuit 125
5.3 Effect of the DC Resistance of Inductors 126
5.4 Antenna Follow-up Circuits for Accumulating Voltage 129
5.5 Geometry of the Antenna for Pulse Generation 130
5.6 Basic Pulse Generation Circuit 132
5.7 External System for Generating Pulse Signal on the Wireless Sensor 133
5.8 Effect of the Diode Parasitic Capacitance 134
5.9 Effect of the Input Parasitic Capacitance of the PMOS Transistor 135
5.10 Revised Circuit Structure for Pulse Generation 139
5.11 Adding transistors to Improve the Fall Speed of V_g 139
5.12 Isolation Effect of the PMOS Transistor 140
5.13 Basic Diode Switching Circuit 141
5.14 Diode Switching Circuit and Its Connection with LC Delay Line 142
5.15 Output Signals of the Diode Switching Circuit 144
5.16 Relationship Between the Output Signal and the Propagating Pulse in the LC Delay Line Circuit 146
5.17 An Example Design of the Antenna for RF Backscattering. 148
5.18 Schematic of the Circuitry for Wireless Telemetry 150
5.19 Layout of the Antenna for RF Backscattering 151
5.20 Block Diagram of the External Interrogator for Wireless Multichannel Neural Recording 153

Figure Page

5.21 Images of a Fabricated 16 Channels Passive Wireless ECoG Array.....154

5.22 Test 1 of the Fabricated 16 Channels Wireless ECoG Array Prototype 157

5.23 Test 2 of the Fabricated 16 Channels Wireless ECoG Array Prototype 158

5.24 Test 3 of the Fabricated 16 Channels Wireless ECoG Array Prototype 159

5.25 Test 4 of the Fabricated 16 Channels Wireless ECoG Array Prototype 160

5.26 Summary of the Measured SNR and Channel-channel Isolation 161

6.1 Wireless Fully-passive Biopotential Sensor 164

6.2 Simulation of the Wireless Fully-passive Biopotential Sensor.....166

6.3 Structure of the External Interrogator for Wireless Fully-passive Biopotential Acquisition 169

6.4 Electrodes Placement for Wireless Fully-passive ECG Acquisition 171

6.5 Electrodes Placement for Wireless Fully-passive EMG Acquisition 172

6.6 Electrodes Placement for Wireless Fully-passive EOG Acquisition.....173

6.7 Measured Minimum Detectable Voltage as a Function of Input Resistance 174

6.8 Structure Diagram of the Deep Learning Model for Biopotential Analysis.....175

6.9 Experiment setup for Benchtop Characterization 178

6.10 Results of Benchtop Characterization 179

6.11 Wireless Fully-passive Acquisition of Electrocardiogram (ECG) 181

6.12 Polynomial Fitting to Remove Baseline Drifting and Reduce Artifacts 182

6.13 Distance and Angle Dependence of the Wireless Biopotential Sensor 184

6.14 Artifact and Noise of the Wireless ECG at Different Distances.....185

Figure Page

6.15 Wireless Fully-passive Acquisition of Electromyography (EMG).....188
6.16 EMG Signal Quality Analysis by Deep Learning Algorithm.....189
6.17 Wireless Fully-passive Acquisition of Electrooculography (EOG) 193
6.18 Wireless Recorded EOG Signals for Eye Tracking 195
7.1 Three Dimensional Schematics of the Wireless Fully-passive ICP Sensor 199
7.2 Working Principle of the Wireless Fully-passive ICP Sensor 201
7.3 The Backscattering Antenna of the Wireless Fully-passive ICP Sensor.....202
7.4 The Varactor Mixing Circuit of the Wireless Fully-passive ICP Sensor 204
7.5 ADS Circuit Model for Simulating of the RF Backscattering Operation.....205
7.6 Modified Wheatstone Bridge Circuit for Absolute Pressure Measurement.....206
7.7 Schematic of the Pressure Sensing Resistor (PSR).....209
7.8 Cross-section View of the Fabrication Process of the PSR 210
7.9 Fabricated Wireless Fully-passive ICP sensor 213
7.10 Block Diagram of the External Interrogator for Wireless ICP Monitoring.....215
7.11 Structure of External IR Generator.....217
7.12 Experiment Setup for Testing the PSR.....218
7.13 PSR Testing Results.....219
7.14 In Vitro Verification of the Wireless Fully-passive ICP sensor 220
7.15 In Vivo Verification of the Wireless Fully-passive ICP sensor.....222
8.1 The Passive Wireless Stimulator 227
8.2 HFSS Simulation of the Electromagnetic Coupling Efficiency 230

Figure Page

8.3 Design of the Antenna of the Wireless Passive Stimulator....232
8.4 Fabrication Procedures of the Onboard Antenna....233
8.5 External Transmitter for Generating Modulated RF Pulses....234
8.6 The Experiment Setup of Cardiac Tissue Stimulation....242
8.7 Characterization of the Passive Wireless Stimulator....243
8.8 Impact of Wireless Transmission Distance and Stimulation Frequency....243
8.9 Characterization of the Wireless Stimulator on Resistive/Capacitive Load....245
8.10 Effect of the Load on the Stimulation Waveforms....246
8.11 Wireless Passive Stimulation of Cardiomyocytes....248
8.12 Cells Viability Assays....249
8.13 Analysis of Cardiac Tissue Construct....250
8.14 Comparison of the Electrical Output of the Wired/Wireless Stimulator....252
8.15 Comparison of the Excitation Threshold....253
8.16 Analysis of Intracellular Calcium Transient under Wireless Stimulation....255

CHAPTER 1

INTRODUCTION

1.1 Background

The human body is the source of various biological signals, such as biopotential, pressure, temperature, flow, etc. These signals are generated from relevant organs or physiological systems representing their general functions. Based on the type of energy, human biosignals can be classified into different types: bioelectrical signals such as the electrocardiogram (ECG) and electroencephalogram (EEG); biomechanical signals like pressure and respiration; and biochemical signals such as blood oxygen or glucose levels. Regardless of the classification, biosignals all contain vital information to help us examine the state of organs and diagnose disease.

1.1.1 Neuropotentials

Neuropotentials are one of the most important biosignals. Neuropotentials are generated in the central and peripheral nervous systems. Herein, we focus on the brain - the central organ of the human body which serves to processes information, make decisions, and give instructions to all the other organs inside our body. The brain contains billions of excitable cells called neurons, which are the basic information processing units in our nervous system (Maguire et al. 2013). Each neuron can receive/transfer information from/to other neurons via electrical currents (Buzsáki, Anastassiou, and Koch 2012). The electrical currents generated from all the neurons within a given area of the brain tissue superimpose to generate an extracellular electrical field, namely, the neuropotentials.

Recording of neuropotentials can date back to the 1950s when intracellular recording in the central nervous system (CNS) was first accomplished by John Eccles (Stuart and Brownstone 2011). Since then, neuropotential recording has become a basic method to study the relationship between neurons and behaviors. Numerous recording practices have been attempted by scientists, revealing findings that greatly facilitate the advancement of neuroscience. Studies have shown that neuropotentials are correlated with our language, perception, motor function, and thought (Khodagholy et al. 2015; Christoff, Ream, and Gabrieli 2004). Understanding and exploiting this relationship will have a profound impact on our way of living, and thus it is one of the fundamental tasks for all neuroscientists.

One of the most remarkable applications of neuropotential recording is in the field of clinical neurosurgery. Many neurological disorders, such as Alzheimer's disease, Parkinson's disease, brain tumor, and epilepsy, have been affecting an ever-growing percentage of the people worldwide each year, imposing billions of dollars of economic burden on public health systems (R. Chen, Canales, and Anikeeva 2017). The emergence of neurorecording devices has resulted in improved surgical procedures and outcomes in diagnosing and treating these diseases (Sahakian et al. 2015). For example, intraoperative recordings are widely used during neurosurgery for brain functional mapping, localizing the epileptogenic zone, and guiding the surgical resection (Berger and Ojemann 1992; S.-M. Kim et al. 2013; Quiñones-Hinojosa et al. 2005; Jung et al. 2013); closed-loop deep brain stimulation (DBS) has been used as a treatment for Parkinson's disease (A. Singh et al. 2016; Parastarfeizabadi and Kouzani 2017; Tekriwal et al. 2019); Electroencephalogram (EEG) recordings can diagnose early-stage Alzheimer's disease

(Babiloni et al. 2016; Petrosian et al. 2001). In addition, the fast-paced technological advancement in the past decades has brought new possibilities to what neural recording can achieve. The development of neurosurgery methodology, together with the evolution of computer and software engineering, has enabled brain-computer interface (BCI) systems. A BCI system is a device that measures the activities from the brain or central nervous system and converts these signals to artificial output to control external devices without the involvement of muscles (Nicolas-Alonso and Gomez-Gil 2012). In recent years, many BCI systems have achieved notable success in clinical trials. Vanstenensel et al. reported an implanted BCI system that partially restored the communication ability of a severely paralyzed ALS (Amyotrophic lateral sclerosis) patient (Vansteensel et al. 2016) (**Figure 1.1**). Hochberg et al. reported that the BrainGate, a silicon-based neuro recording device, enabled a tetraplegic patient with spinal cord injury to control a computer and operate a prosthetic hand (Hochberg et al. 2006). As research on BCI systems is attracting more and more attention, the boundary between human and machine is blurring. It is reasonable to assume that neural recording and BCI devices will one day greatly reform our way of living.

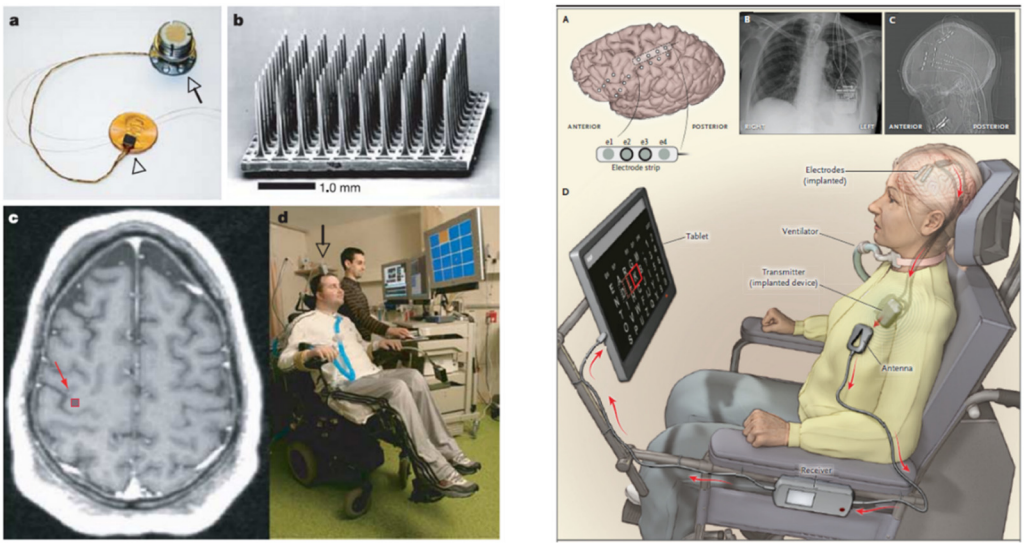

Figure 1.1. Brain-computer interfaces (BCI). Left: the BrainGate neuromotor prosthesis system consisting of an implanted microelectrode array and an external signal decoder. The system allowed a tetraplegic patient to control a computer and operate a robotic hand (Hochberg et al. 2006). Image reprinted by permission from Springer: Nature, Neuronal ensemble control of prosthetic devices by a human with tetraplegia, Hochberg, L. R. et al. 2006. Right: a brain-computer interface implanted in a patient with late-stage amyotrophic lateral sclerosis (ALS), consisting of a subdural electrode array placed on the motor cortex and a transmitter placed subcutaneously at the thorax. The system enables the patient to control a computer and communicate with others. Reproduced with permission from Vansteensel et al. Fully implanted brain-computer interface in a locked-in patient with ALS. New England Journal of Medicine 375 (21): 2060–66, Copyright Massachusetts Medical Society.

Despite the exciting accomplishments achieved through neural recording practices, the technique itself still has many challenges that may limit its future development and

applications. These challenges include 1) the difficulty in developing effective recording systems that can measure electrical activities of large populations of neurons at high spatial and temporal resolutions (Schwarz et al. 2014) and 2) the high safety and reliability of this technology (Welle and Krauthamer 2012), as required by real clinical applications, are difficult to achieve with current neural recording instrumentation.

Current existing neural recording practices generally include electroencephalogram (EEG), electrocorticogram (ECoG) or stereo-electroencephalography (sEEG), and local field potentials (LFP). They refer to the measurement of neural signals on the scalp, on the cortical surface, and within cortical tissue, respectively (Buzsáki, Anastassiou, and Koch 2012; Thakor 2013). While EEG is a non-invasive method, the recorded EEG signal is a summation of neural activities over a relatively large area — a few square centimeters of the cortex (Buzsáki, Anastassiou, and Koch 2012; Smith 2005). This results in poor spatial resolution of the collected signal. Consequently, clinical EEG studies often fail to recognize interictal epileptiform discharge (IED) in patients with seizure disorders (Smith 2005). On the other hand, ECoG or sEEG offers much improved temporal and spatial resolution (Ramantani, Maillard, and Koessler 2016). ECoG is well-suited for seizures on the outside cortical surface, while sEEG can localize seizures deep in the brain. In both techniques, the neural activities are precisely detected through direct coupling between neural tissue and sensing electrodes (Khodagholy et al. 2015). The surgical procedure of ECoG/sEEG is invasive because the recording electrodes need to be directly implanted on the surface of the cortex for ECoG, or deep into the brain for sEEG (Buzsáki, Anastassiou, and Koch 2012; Ramantani, Maillard, and Koessler 2016). Additionally, long wire bundles

are needed to connect implanted electrodes to external instruments. Due to the safety issue and the cumbersome recording settings, ECoG/sEEG are generally conducted during brain surgery for only a short period of time (intraoperative) (Khodagholy et al. 2015; W. Wang et al. 2009) or during a few weeks in between two consecutive surgical procedures (extraoperative). In either case, the invasive and cabled ECoG/sEEG electrodes have become the major cause of numerous complications, including bleeding (Rolston et al. 2016; 2015; Van Gompel et al. 2008), CSF (cerebrospinal fluid) leakage (Rolston et al. 2015), urinary tract infection (Rolston et al. 2016), and osteomyelitis (Van Gompel et al. 2008). Finally, local field potentials (LFP) and action potentials can be measured by inserting microelectrodes into the brain at a depth of several millimeters. These microelectrodes are often silicon-based and contain a large number of recording channels. Since the microelectrodes can reach the proximity of neurons, the recorded LFP (many neurons) or action potentials (single neuron) have the highest signal quality as compared to that of EEG or ECoG/sEEG. However, this is also the most invasive method as the brain penetrating electrodes will damage the brain tissue. In addition, the microelectrodes are generally based on rigid material while the brain is soft and always in micromotion, resulting in unstable electrical contact and inducing further tissue damage (Thakor 2013). Consequently, LFP recordings are primarily used in animals rather than humans. For all these methods mentioned above, long-term recordings will likely not be feasible outside of the research environment due to their safety and reliability issues. This has become the major barrier impeding their future application in the field of medicine and neuroscience. Notably, this barrier mostly comes from the need to use wires/cables to transmit neural

signals from the implanted electrodes to external equipment. These wires inevitably increase the risk of infection and impose great constrain on patient free movement, causing discomfort and disfiguration (Vansteensel et al. 2016). Thus, a wirelessly neural recording system, if successfully developed, may have huge potential in overcoming all the challenges described above.

1.1.2 Biopotenials

Biopotentials are defined as electrical signals generated from the body. Strictly speaking, the neuropotential can also be defined as biopotential. However, in this thesis, the neuropotential is separated from all the other biopotentials signals because the techniques involved in neural recordings are very different from other biopotentials. The term biopotentials is used to specifically refer to the electrocardiogram (ECG), electromyogram (EMG), and electrooculogram (EOG) signals, as all these signals can be measured noninvasively using electrodes placed on the skin. On the other hand, neuropotentials are often measured with invasive electrodes inside the brain. This discrepancy results in very different design considerations and requirements for the recording systems.

Biopotentials originate from electrical activities of cells (Thakor 2015). For example, cardiac pacemaker cells can generate and propagate an electrical impulse signal throughout the heart. This signal causes the cardiomyocytes to contract, causing the beating of the heart. The electrical activity of large groups of cardiac cells results in an electrical field propagating in the conductive tissue of the body, forming the ECG signal (Severs

2000). EMG signals are associated with the electrical activity of muscle fibers. Each muscle fiber is connected to a motor neuron through the neuromuscular junction, which allows the neuron to transmit an electrical signal, i.e., motor unit potential, to the muscle fiber, inducing the muscle contraction. The motor unit potentials from groups of muscle fibers on the surface of the body exhibit an EMG signal (Roeleveld et al. 1997; Wu, Martínez, and Balaguer 2013). The EOG signal originates from the transepithelial potential of the retinal pigment epithelium of the eye (Creel 2019; Zrenner 2008). The potential difference between the cornea and the Bruch's membrane of the retina forms an electrical dipole, with the cornea being the positive end. As the eyes move, the direction of the dipole electrical field change accordingly, resulting in the EOG signals generated in the conductive tissue around the eyes. Different from the ECG and EMG, the EOG does not measure the electrical activity of muscles.

Biopotential recordings have been intensively used in the medical field for various purposes. The first clinical use of the ECG signal was in 1901 when it was invented by Einthoven to detect arrhythmias (Yang et al. 2015; AlGhatrif and Lindsay 2012). Later, he invented the standard three leads ECG recording method, which led him to win the Nobel Prize in 1924. The invention of ECG has been viewed as a revolution in the development of cardiology. Before ECG, cardiologists primarily relied on their senses or sphygmograph for disease diagnosis, and as a result, many heart diseases were poorly understood (Fye 1994). The recording of electrical activities directly from the heart, on the other hand, gave the doctors a powerful tool to thoroughly characterize and differentiate each type of abnormality. Since the invention of ECG, numerous cardiovascular diseases have been

discovered, such as atrial fibrillation (AF), long QT syndrome (LQTS), angina, myocardial infarction (MI), and *torsades de pointes* (TdP)(Yang et al. 2015). With technological advancements, ECG recording devices are becoming lighter and smarter. There is no denying that the ECG still plays a critical role in modern clinical diagnosis. Different from ECG, the EMG does not have a well-defined signal pattern, and thus clinical practices using EMG for diagnosis are less common. EMG signals can be used to identify and study neuropathies, myopathies, chronic fatigue syndrome (CSF), and motor neuron diseases (MND) (Miller 1958; Rodríguez-Tapia et al. 2020; Drost et al. 2006). Furthermore, since the EMG signals collected at muscles reflect a person's intention to perform certain muscle actions, they can be used in the field of human-computer interface (HCI) to enable control of devices such as robotic arms. These devices can be used as prosthetics to assist patients with motor impairment, or as training tools to facilitate rehabilitation. Studies have reported successful designs and implementations of such devices which improved the outcome of post-stroke rehabilitation (Klein et al. 2018; Lu et al. 2017; Pasquina et al. 2015). Finally, EOG recordings measure the electrical potential difference between the cornea and retina to track the movement of eyes. Clinical applications of EOG signal recordings are primarily in the diagnosis of retinal disorders such as Best vitelliform macular dystrophy, Stargardt macular dystrophy, cone-rod dystrophy, and retinitis pigmentosa (Bi 2018). EOG signals also help diagnose some neurological or vestibular diseases such as Huntington's disease, spinocerebellar ataxia, schizophrenia, Parkinson's disease, or frontal lobe lesions (Heide et al. 1999). Like EMG, EOG recordings also find their applications in the field of human-computer interface (HCI) systems, leading to the

development of devices that can be controlled by eye movements. These devices may become very useful for patients who have difficulty using other communication methods, for example, patients with advanced amyotrophic lateral sclerosis (ALS). Researchers have reported EOG-based devices in the form of goggles or helmets, enabling people to drive wheelchairs, operate keyboards or control robotic arms (H. Singh and Singh 2012).

All the biopotentials mentioned above can be measured with commercially available surface electrodes. The silver/silver chloride (Ag/AgCl) electrodes are commonly used because of their low impedance, low noise, and low artifacts (Albulbul 2016). The method for ECG signal recording was standardized by the American Heart Association in 1954, which is called the 12 leads ECG recording (AlGhatrif and Lindsay 2012). The 12 leads ECG recording method is widely accepted in clinical diagnosis today as it provides the most comprehensive measurement of the heart. The 12 leads include 6 leads that measure the vertical plane of the heart (also called frontal plane): lead I, II, III, Augmented Vector Right (aVR), Augmented Vector Left (aVL), and Augmented Vector Foot (aVF); the other 6 leads that measure the horizontal plane of the heart: Lead V1 – V6. **Figure 1.2 (a)** shows the direction of the 12 leads (Thakor 2015). It should be noted that the 12 leads method is developed from the basic 3 leads electrocardiogram proposed by the Dutch physiologist Willem Einthoven. These three leads are the bipolar lead I, II, and III, measured by electrodes placed at the limbs. **Figure 1.2(b)** shows a typical waveform of the ECG signal. The waveform has several very clear deflections, which are named as PQRST, respectively. ECG features such as R-R interval, PR-interval, QRS duration, and QT interval are all frequently used parameters for detecting heart abnormality.

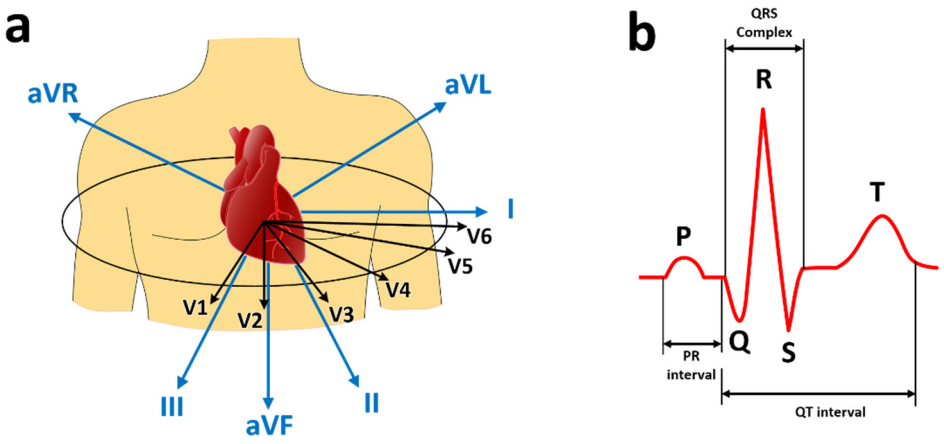

Figure 1.2. Standard ECG recording method. (a) The 12 Leads ECG recording method. The 12 leads are leads I, II, III, aVR, aVL, aVF, and V1 – V6. For the 12 leads, a total of 10 electrodes are required. (b) A typical ECG waveform contains a P wave, a QRS complex, and a T wave.

Unlike ECG, the EMG recording has not been standardized as a clinical diagnostic tool (Tankisi et al. 2020). Applications of EMG recordings have been mainly centered on research on diseases, rehabilitation, and human-computer-interface (HCI) systems. Surface electrodes are generally placed close to the muscle of interest to capture target muscle activities. Usually, multiple electrodes are required to capture EMG signals from different locations along the target muscle to provide comprehensive information about the motor units. For example, Lu et al. placed 7 electrodes on a subject's forearm to measure EMG signals at the first dorsal interossei, flexor digitorum superficialis, flexor digitorum profundus, extensor digitorum, abductor pollicis longus, extensor digiti minimi, and

extensor pollicis longus muscles to enable control of an exoskeleton hand (Lu et al. 2017). The frequency range of EMG signals is generally higher than that of ECG and EOG. As a result, high pass filters can be applied in EMG signal processing to suppress motion artifacts (Thakor 2015).

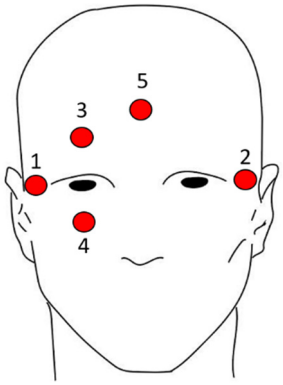

Figure 1.3. Electrodes placement for EOG recording. Electrode 1 and electrode 2 measure the horizontal channel while electrode 3 and electrode 4 measure the vertical channel. Electrode 5 is the reference.

EOG signals can be measured with surface electrodes placed near the eyes. **Figure 1.3** shows a typical electrode arrangement for EOG signal recordings. Electrode 1 and electrode 2 are placed beside the external canthus of each eye for measuring the horizontal movement of eyes. Electrode 3 and electrode 4 are placed above and below one eye to measure its vertical movement. Electrode 5 is the reference electrode, which is often placed either on the forehead, in the middle of the eyes, or on the mastoids. This electrode arrangement produces two channels of EOG signals, representing the motion of eyes in the

horizontal and vertical direction respectively (Chang 2019). The amplitude of EOG signals is very small, typically less than 500 μV, and it is proportional to the movement of the eyes. Due to the small voltage and low-frequency characteristics, recording of EOG signals is more difficult than the recording of EMG or ECG. The measurement systems generally require a signal amplifier with very low noise, good low-frequency response, and low DC offsets. Nonetheless, practically recorded EOG signals are often contaminated by DC drift and motion artifacts. As a result, most EOG recordings are done within a short time period and require the subject to produce rather large eye movements (Thakor 2015; Heide et al. 1999; Chang 2019).

The majority of current existing biopotentials recording systems use cables or wires to connect the surface electrodes on individuals' skin to the measuring instrument or equipment for signal monitoring and storage. The cables and wires, again, cause severe movement restriction and inconvenience to individuals, prohibiting long-term ambulatory monitoring of their physiological data. As technology advances, the topics of e-healthcare, wearable medical devices, and at-home diagnosis have become research hotspots. Many researchers are spending an increasing amount of effort on developing wireless and/or portable biopotential monitoring systems. Some of these devices, such as the Holter ECG monitor, have been accepted by clinicians as an effective diagnostic tool (J. P. DiMarco and Philbrick 1990). However, most of the developed wireless biopotential recording systems still rely on batteries to power the measurement electronics, resulting in their limited continuous collection of biopotentials. The state-of-art wireless sensors offer an average of merely one to two days operating time. This limited operation time mainly

comes from the high power consumption demanded by wireless communication protocols for data transmission (Dementyev and Smith 2013). Some diseases or abnormalities, such as syncope and atrial fibrillation (AF), often require an extended long period of recording for months or even years to produce a high diagnosis yield (Thomsen et al. 2010; Israel et al. 2004). The lack of long-term continuous wireless biopotentials monitoring greatly limits the diagnosis and study of those diseases or abnormalities. Also, the trend of future wearable electronics is moving toward flexible, light-weight, small-sized epidermal electronics equipped with wireless communication capability (J. Kim et al. 2018). The bulky and rigid batteries pose great difficulties being integrated into such skin-liked devices.

1.1.3 Intracranial Pressure (ICP)

The intracranial pressure (ICP) is another very common and critical biosignal. ICP refers to the pressure inside the skull. Under normal circumstances, the brain can automatically regulate the ICP value within a healthy range. The physical principle behind this regulation is known as the Monro-Kellie hypothesis, which was first proposed by Alexander Monro and Geoge Kellie back in the 18th century and later refined by Harvey Cushing (Harary, Dolmans, and Gormley 2018). The Monro-Kellie hypothesis states that the total volume of the intracranial space is constant and the skull can be considered as an enclosed and inelastic container. To keep the ICP value steady, the volume of the three major components occupying the intracranial space needs to be balanced. These three major components are (1) the brain tissue, (2) the cerebrospinal tissue (CSF), and (3) the

blood (Canac et al. 2020). An increase of volume in any of these three contents must be compensated by the decrease of volume in the others, otherwise, it will result in an elevated ICP. Since the volume of the brain is fixed, the main factors contributing to the ICP are the blood and CSF. Thus, regulating of the ICP is mainly accomplished by balancing the in/out flow of the blood and the production/drainage of CSF (Harary, Dolmans, and Gormley 2018; Dunn 2002). Normally, the ICP is not a constant value but a pulsatile signal because of the pressure force generated from the heart beating. For most clinical applications, the pulsatile ICP wave is usually ignored. Instead, the mean ICP value is the variable of interest (Canac et al. 2020). The mean ICP in a healthy person may still change due to some normal physiologic activity such as posture change or physical exercise (Harary, Dolmans, and Gormley 2018; Brimioulle et al. 1997). Therefore, the mean ICP value is expected to have a fluctuating characteristic, and any change of ICP is meaningful only when it is sustained for over 5 minutes.

The normal ICP range of a person can vary with age. Generally, the safe threshold of ICP for an adult is 15 mmHg, and it is 7 mmHg for a child and 6 mmHg for an infant (Harary, Dolmans, and Gormley 2018; Canac et al. 2020; Dunn 2002). Since ICP regulation is accomplished by balancing the volume of blood and CSF, when this balancing is disturbed due to abnormalities such as intracranial hemorrhage or traumatic brain injury (TBI), the total volume of the fluid inside the intracranial space will increase. Within a certain range, this volume change in the fluid will not cause the ICP to rise because some intrinsic compensating mechanisms exist to keep the ICP stable. These mechanisms include modifying the cerebral venous blood pool and dispensing of the CSF into the spinal

canal (Harary, Dolmans, and Gormley 2018). However, the buffering capacity of the ICP compensation is finite. As the volume increases, the compensatory reserve quickly depletes, and the ICP will rise sharply to a very dangerous level, leading to the collapse of cerebral microvasculature (Canac et al. 2020). The ICP also affects cerebral perfusion pressure (CPP), which in turn determines the cerebral blood flow (CBF). The CPP is controlled by the mean arterial pressure (MAP) and the ICP with the following relationship: CPP = MAP – ICP. To remain at a steady cerebral blood flow, when the ICP increases, the MAP will also increase accordingly. However, there is also a limit of how much the MAP can increase to compensate the elevation of ICP. When the ICP goes beyond this limit, the CBF will decrease and eventually stop, causing cerebral ischemia.

Many neurological conditions or injuries can lead to elevated ICP. Some common causes include the Traumatic Brain Injury (TBI), hydrocephalus, stroke, and brain tumors (Ordookhanian et al. 2018; Helbok et al. 2014; Chari et al. 2017; Jeon et al. 2014; A. L. Lin and Avila 2017). TBI refers to the damage to the brain caused by external mechanical forces, which can be the result of a severe accident (Ordookhanian et al. 2018). A TBI can change the volume of intracranial spaces, damage brain tissues, induce hemorrhage, and destroy the pressure-regulating function of the brain, leading to the rise of ICP. Hydrocephalus is a condition in which an increased amount of CSF is built up inside the cranium. The CSF is produced by the choroid plexus for protecting and cushioning the brain (Neumiller 2013). Normally, the CSF runs from the brain to the spinal cord and can be removed from the circulation through the arachnoid granulations and vertebra venous plexus. When this process is blocked, either due to congenital or acquired causes,

hydrocephalus occurs. The accumulation of CSF inside the cranium will inevitably lead to the rise of ICP. Stoke refers to the disturbance of cerebral function due to the supply of blood (Party 2012). A stroke can be classified into three mains types, ischemic, hemorrhagic, and transient ischemic (Parmar, Sumaria, and Hashi 2011). The most common type is ischemic stroke, which happens when arteries supplying blood to the brain are blocked. The second type is hemorrhagic stroke, this type of stroke happens when a blood vessel ruptures, leaking blood into surround brain tissue and causing damage. The third type is called a transient ischemic attack (TIA), also called "mini-stroke" because it refers to the blockage of blood flow for only a short time. Finally, brain tumor is the growth of abnormal cells inside the brain. As the tumor grows, it will increase pressure in the surrounding tissue, causing an elevated ICP and inflicting damage to the brain (A. L. Lin and Avila 2017). Despite different causes, patient with an increased ICP will show similar symptoms such as headache, blurred vision, vomiting, confusion, and coma. Without proper management, an increase in ICP can be a life-threatening condition. Therefore, early identification of elevated ICP is of crucial importance to improve the outcome of associated treatments.

Clinical methods for ICP monitoring can be classified into non-invasive and invasive methods (Harary, Dolmans, and Gormley 2018; Canac et al. 2020; Changa, Czeisler, and Lord 2019; Khan et al. 2017; Raboel et al. 2012). The noninvasive methods include Transcranial Doppler Ultrasonography (TCD), Tympanic Membrane Displacement (TMD), Optic Nerve Sheath Diameter (ONSD), and imaging methods such as Magnetic Resonance Imaging (MRI) and Computer Tomography (CT). Among those

noninvasive methods, TCD, TMD, and ONSD are indirect measurements that estimate the ICP value by measuring related physiological parameters (Canac et al. 2020; Khan et al. 2017; Raboel et al. 2012). For example, TCD utilizes ultrasound to measure the pulsatility index (PI) in the middle cerebral artery. The PI is known to correlate with the ICP and thus can be used to estimate the actual ICP value (Bellner et al. 2004). TMD is based on the response of stapedius muscle to acoustic stimulation. Under stimulation, the positions of the stapes and the tympanic membrane are correlated to the pressure of the fluid in the cochlea (Lang et al. 2003). Therefore, measurements of the membrane movement can be used to quantify the ICP. The ONSD measures the ICP using the expansion of the optic nerve sheath. The optic nerve sheath is surrounded by the CSF in the subarachnoid space. In cases of increased ICP, the optic nerve sheath expands (Geeraerts, Duranteau, and Benhamou 2008). Changes of the diameter of the optic nerve sheath can be detected using transocular ultrasound. These noninvasive methods are attractive because they can effectively avoid potential safety risk of numerous complications associated with the invasive methods, such as hemorrhage and infection. In addition, they do not require a professionally trained neurologist to perform the measurement procedures, making them suitable to be used in the situations where a neurosurgeon is not available (Harary, Dolmans, and Gormley 2018). However, the biggest challenge of these methods is their low measurement accuracy. As the ICP values are derived from other physiological parameters, the accuracy of measurement largely depends on the established correlation models between the ICP and the measurand. Yet in many methods, such models can vary from person to person, and their effectiveness and reliability are still controversial (Khan et al.

2017; Raboel et al. 2012). Currently, due to the lack of accuracy, none of the noninvasive methods introduced above are allowed to be used in an intensive care unit (ICU) (Canac et al. 2020). On the other hand, image scanning methods such as CT and MRI can provide a qualitive estimation of the ICP, i.e., labeling ICP as high or normal, using features such as effacement of ventricles, basal cisterns and significant midline shifts (Canac et al. 2020). Study have shown that MRI or CT images are sensitive enough to differentiate between normal and elevated ICP without surgical intervention (Glick et al. 2006). However, these imaging methods also suffer from accuracy and reliability issues and cannot provide continuous ICP monitoring. As a result, they are not suited to be used as clinical standard ICP evaluation tools for guiding treatment (Le Roux 2016). So far, the MRI or CT techniques are routinely used only to provide initial diagnose of ICP, or as an indicator for identifying whether further invasive ICP monitoring is required. For accurate and reliable ICP measurement, invasive ICP monitoring is the only option.

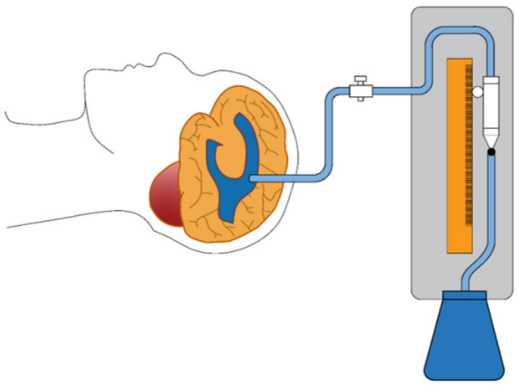

Figure 1.4. Schematic showing an external ventricular drainage system. A catheter is inserted from a burr hole drilled at the skull into the brain ventricles. The catheter allows

the CSF to flow out into the external pressure gauge and the collecting bags. Despite the invasive approaches, the EVD is commonly considered to be a relatively safe, effective, and lifesaving neurosurgical technique (Garcia-Conde et al. 2017).

For invasive ICP monitoring, the current gold standard is the external ventricular drainage (EVD) system (**Figure 1.4**). In EVD, a catheter is inserted directly into one of the ventricles through a burr hole. The catheter is connected to an external strain-gauge pressure transducer to accurately monitor the ICP. An additional collecting bag is attached at the end of the catheter to collect the CSF drained from the ventricles (Garcia-Conde et al. 2017). Thus, an EVD system can provide both ICP monitoring and treatment if needed. However, as mentioned above, the EVD system is often accompanied by complications such as hemorrhage, infection, and technical failure (Le Roux 2016). The risk of hemorrhage in EVD is around 5% - 7% while the risk of infection is between 5% - 20%. The infection may include a variety of conditions, from benign skin infection to ventriculitis, meningitis, and fatal septicemia (Raboel et al. 2012). The infection risk also increases with the presence of other systemic infections, hemorrhage, CSF leakage, cranial fracture, CSF sampling rate, or long duration of monitoring (Le Roux 2016). Technique failure in EVD includes catheter displacement, accidental removal, or blockage. They occur mostly when a patient is moved but will not greatly affect the patient outcome because they are easy to recognize. Due to the existence of the complications mentioned above, the guideline on whether or when to use the EVD system for ICP monitoring is still in debate (Canac et al. 2020; Raboel et al. 2012). Clinicians may be reluctant to use this

invasive technique fearing it could worsen the clinical outcome, although such situations do not happen very often. Some studies reported that invasive ICP monitoring demonstrated better survival and outcomes (Fakhry et al. 2004), while other studies came to the opposite conclusion, indicating invasive ICP monitoring achieved worse outcomes (Shafi et al. 2008). To this date, there is still not sufficient evidence proving the benefits of invasive ICP monitoring.

1.1.4 Electrical Stimulation

As mentioned above, both the neuron and muscle cells can be excited to generate action potentials. In neural or biopotential recordings, the origin of action potentials comes from the nervous system, especially from the brain. External electrodes are used to sense and collect these biosignals for various diagnostic or analytical purposes. On the other hand, the electrodes can also be used to excite cells and induce action potentials. This practice is called electrical stimulation. In other words, the goal of the electrical stimulation is the artificial generation or suppression of action potentials in target excitable cells. Action potentials (APs) are the basic units for information transformation between neurons, and their generation is related to the membrane activity of cells (Bhadra 2015). For an excitable cell such as a neuron or muscle cell, the potential of the cell membrane is polarized. The transmembrane potential, defined as the difference between intracellular and extracellular potential, is around -70mV when the cell is at rest (Brocker and Grill 2013). When an external electrode creates an electric field, the transmembrane potential will be less negative, i.e., depolarized. When this depolarization achieves a certain threshold, the

voltage-gated sodium channels are opened, resulting in a large influx of sodium ion (Na+) into the cell, and initiating the APs (Bhadra 2015). The APs will propagate through the peripheral nerve axons that can innervate muscles and eventually be transmitted to target muscle cells.

Electrical stimulation has been widely used in many clinical applications. Commercially available implantable medical devices such as the artificial pacemakers and the cochlear implant have gone through successful clinical trials and are already being used as standardized therapies (Takeda, Tanino, and Miyasaka 2017). An artificial pacemaker is an electronic device containing batteries, electronics, and leads. It is usually implanted under the skin or inside the chest with the leads surgically inserted to the right heart through the subclavian vein for detecting abnormal cardiac rhythms and delivering electrical pulses to regulate heartbeat (Mulpuru et al. 2017). The cochlear implant is an electronic device for restoring hearing function by applying electrical stimulation to the auditory nerve. The device consists of a transmitter near the patient's ear and a receiver/stimulator unit implanted under the skin. The transmitter receives external sound signals and processes and transmits them to the internal implant. The internal stimulator receives the signals and generates electrical pulses to stimulate the auditory nerve, and thus partially substituting the function of the cochlea (Martins et al. 2012). Electrical stimulation is also used for the treatment of numerous neurological disorders, including Alzheimer's disease, Parkinson's disease, essential tremor, and dystonia (Ponce 2014). This method is called deep brain stimulation (DBS). In DBS, electrodes are inserted into a specific area of the brain through small holes drilled atop the skull. A stimulator connects the electrodes and sends electrical

pulses to the brain tissue. The electrical pulses generate an information lesion in the stimulated neurons, suppressing the low-frequency signals in the brain and relieving the tremor and rigidity associated with the diseases (Lozano et al. 2019). In modern medicine, electrical stimulation has also been prescribed for pain management. This clinical practice is called transcutaneous electrical stimulation (TENS) (Takeda, Tanino, and Miyasaka 2017; Recio and Schneider 2011). As suggested by its name, TENS uses surface electrodes placed on the skin to deliver low voltage electrical pulses to target nerves. The electrodes may be placed over the peripheral nerve, nerve roots, or acupuncture points, depending on where the pain is felt. The principle of pain control is based on the Gate theory, which asserts that electrical stimulation at large myelinated fibers blocks the transmission of pain signals at the spinal cord, preventing them from being transmitted to the thalamus and perceived by the individual (Recio and Schneider 2011). TENS has demonstrated efficiency in the management of chronic back pain, dysmenorrhea, hemiplegic shoulder pain, and arthritic pain. Lastly, functional electrical stimulation (FES) is another widely used clinical procedure in neurorehabilitation (Sheffler and Chae 2007; Luo et al. 2020). An FES system can deliver electrical pulses to activate paralyzed muscles or nerves, restoring lost motor functions of tetraplegia patients. Most FES systems are percutaneous systems in which electrodes are implanted under the skin to make direct contact with the muscles (Peckham and Knutson 2005). This arrangement can achieve higher stimulation efficiency as well as reduce the pain from stimulation since the sensory afferents in the skin are bypassed. Many researchers have demonstrated the effect of FES on various upper/lower limb functions such as grasping (Kilgore et al. 2008), cycling (Bellman et al.

2014), standing (Lissy and Kukke 2001), walking (Kobetic et al. 2003), and stair-climbing (Kobetic et al. 2009). FES is also being used in assisting the bladder and bowel function for those who lose control of these organs (Rijkhoff 2004), and in restoring respiratory function for individuals with cervical spinal cord injury (SCI) or central alveolar hypoventilation (CAH) (A. DiMarco 1999).

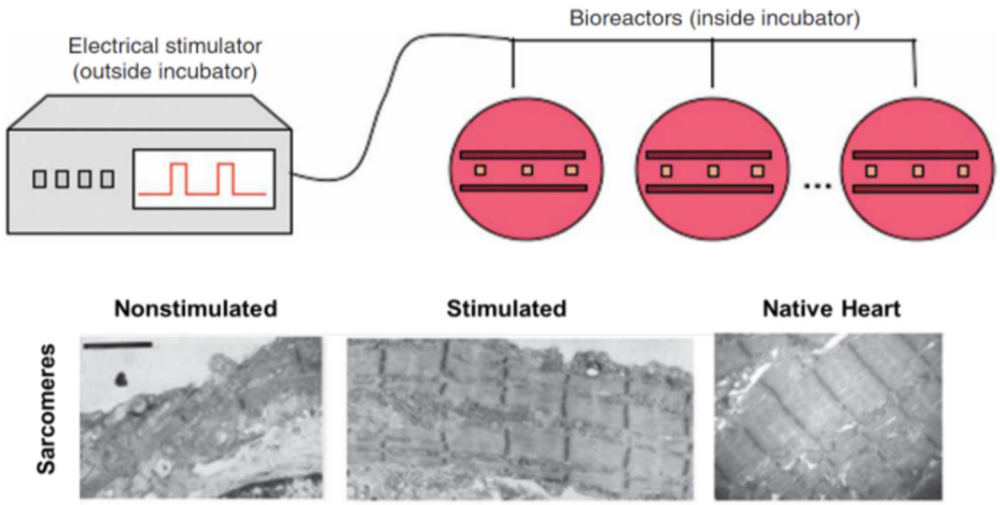

Figure 1.5. Electrical stimulation promotes the growth of engineered cardiac tissue. Top: an electrical stimulator delivers pulsatile stimulation to engineered cardiac tissues (orange rectangular) in the bioreactors. Bottom: after 8 days of culturing, stimulated cardiac tissues demonstrated substantially improved cell alignment and organization as compared to unstimulated tissues. Image reprinted by permission from springer: Nature Protocols, Electrical stimulation systems for cardiac tissue engineering. Tandon, N. et al., 2009.

Beyond clinical applications, electrical stimulation is also widely applied in cell and tissue engineering. The overall goal of tissue engineering is to cultivate functional

biological tissues *in vitro*, which can be subsequentially used for diseases study and eventually implanted to repair or replace damaged tissues (C. Chen et al. 2019). Many studies have shown that electrical stimulation can enhance cell proliferation, differentiation, adhesion, and matrix formation (C. Chen et al. 2019; Mobini, Leppik, and Barker 2016; Hirt et al. 2014; Serena et al. 2009). One typical example is the engineered cardiac tissues. In recent years, the emerging of pluripotent stem cell (hPSCs) technology has greatly advanced cardiac tissue engineering (Hirt et al. 2014). However, the cardiomyocytes cultured with conventional methods do not align and remain poorly differentiated (Radisic et al. 2004). One possible reason is the spontaneous, unsynchronized contraction of the engineered cardiac tissues. In contrast, adult cardiomyocytes are quiescent without stimuli, allowing them to beat in synchrony with the native heart (Hirt et al. 2014). To solve this problem, Tandon et al. designed a biomimetic system that can deliver pulsatile electrical stimulation to engineered cardiac tissues, mimicking the electrical field presented in the native heart (Tandon et al. 2009) (**Figure 1.5**). Through the stimulation, the engineered cardiac tissues demonstrated largely enhanced key biological properties, such as alignment, protein expression, and contractility. This result shows that the electrical stimulation may have great potential for promoting cell growth *in vitro* or *in vivo*. Once the engineered cardiac cells are transplanted for cardiac regeneration or repair, applying electrical stimulation may greatly improve the survival rate of the cells.

Similar to previously mentioned biosignal measurement systems, most current existing electrical stimulation systems use wires to connect the surface/subcutaneous electrodes to an external electrical pulse generator (Pfurtscheller et al. 2003; Shimada et al.

1996). Such configuration encumbers patients and clinicians maneuver capability, increases the likelihood of infection, and ultimately fails to provide efficient treatment due to losing the contacts of the electrodes (Shimada et al. 1996; Loeb et al. 2001; Wise et al. 2004; Ziaie et al. 1997). For continuous and long term stimulation, wireless implantable systems are preferred as they can be used in patients' home without restricting movement (Peckham and Knutson 2005). In the past years, many wearable/implantable wireless stimulators targeting long-term use have been reported. The detail of those systems will be discussed in the next chapter.

1.2 Original Contributions

All the previously discussed biosignal acquisition systems, namely, the neuropotential, biopotential, intracranial pressure recorders/monitors, and the electrical stimulators, have been sharing one common challenge: the need to use cables or wires. Therefore, the goal of this thesis is to alleviate this challenge by presenting a novel method to achieve the wireless telemetry of different types of biosignal in a fully-passive manner. Several wireless sensors are designed, fabricated, and verified *in vitro* or *in vivo*. Each of the wireless sensors is targeting at a specific biosignal, such as the neuropotentials, ICP, and biopotentials. Despite different applications, these sensors are based on one basic operating principle, radiofrequency (RF) backscattering. In this method, RF energy is used not to power the electronics on the sensor, but rather to allow bi-directional communication by reflecting the incident electromagnetic (EM) wave. Wireless sensors presented in this thesis contain a minimum amount of active circuitry, which results in their extremely low

power consumption. Additionally, these sensors have small sizes, high flexibility, and good biocompatibility. Because of these attractive features, these fully-passive wireless sensors could potentially be implanted inside the skull. A comparison between the conventional wireless biosignal sensors and the fully-passive wireless biosignal sensor is shown in **Figure 1.6**. Conventional wireless sensors only have the sensing electrode array implanted under the skull while other parts of the systems including the recording electronics, batteries, and antennas have to sit outside the skull due to their high power consumption, rigid structure, large footprint, and hazardous content. The two parts are connected through transcranial wiring. This arrangement has many long-term safety and reliability issues such as high failure rate, risk of infection, and heat trauma. In contrast, the fully-passive wireless system can safely be implanted under the skull due to its size, flexibility, and near-zero power consumption, and thus avoiding all the safety and reliability issues.

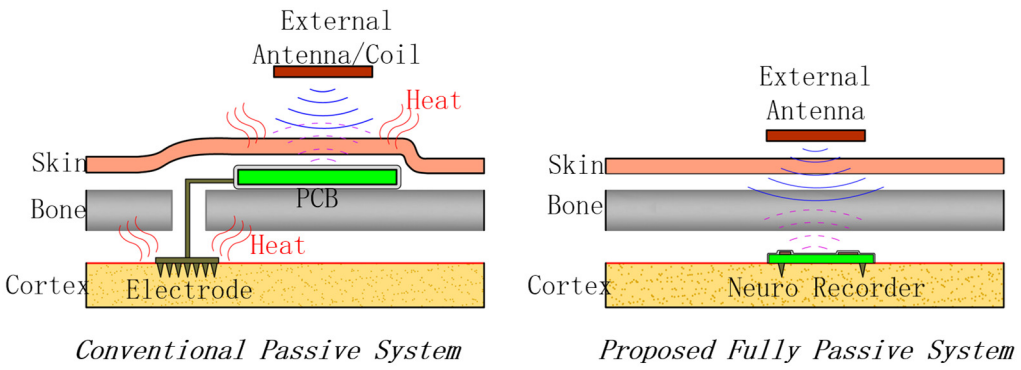

Figure 1.6. Comparison between the wireless fully-passive system and conventional IC-based passive system. With a near-zero power consumption, the fully passive system can be completely implanted inside the skull without any intracranial wiring. This configuration avoids the potential physical/heat damage associated with the wiring.

The structure of this thesis is arranged as follows. Chapter 2 will review previous reported wireless biosignal sensors and discuss their advantage and limitation. Some fundamental works related to this thesis will also be reviewed. Chapter 3 will introduce the basic theory and methodology of wireless fully-passive biosignal acquisition using the RF backscattering method. Design considerations and optimization of wireless transmission will be discussed using both theoretical calculations and Computer-Aided Design (CAD) models. Chapter 4 will present a small, biocompatible, flexible, implantable, wireless, and fully-passive neural recorder. This neural recorder is composed entirely of passive electronic components, namely, a planer antenna, inductors, and capacitors. The sensor was fabricated on polyimide and occupies a total footprint of 9 mm x 8 mm. The sensor was first verified *in vitro* using a multilayer tissue-emulating phantom, then *in vivo* using an epileptic rat model. The fabricated sensor demonstrates successful detection of two types of neuro potentials, the somatosensory evoked potential (SSEP) and interictal epileptic discharge (IED). Machine learning-based signal processing methods further verified the measurement result. Although those results are promising, a major disadvantage of this sensor is that it has only a single recording channel. To overcome this problem, Chapter 5 presents the design and verification of a wireless passive multichannel neural recorder. The multichannel recording is achieved with a novel time-multiplexed method, in which capacitors and inductors are exploited to construct a time delay circuit. Upon receiving the incident EM waves, the recorder creates an electrical pulse signal at the input of the time delay circuit, initiating the propagation of the pulse signal along the inductor-capacitor delay line. As a result, each channel of the recorder is alternately turned

on as the pulse signal pass through it, creating a time-multiplexed multichannel signal at the output, which is then wireless recorded using the RF backscattering method. Based on this method, a 16-channel wireless ECoG array prototype was fabricated on a polyimide substrate and verified with emulated input signals. Chapter 6 introduces a small-size, flexible, and wearable wireless fully-passive biopotential sensor. Compared to the neural recorder presented in Chapter 4, the biopotential sensor adapts a new antenna and circuit structure specifically optimized for the acquisition of ECG, EMG, and EOG signals from the skin. This change leads to a substantially improved wireless working distance of up to 240 mm. The wireless biopotential sensor was verified with the real-time acquisition of ECG, EMG, and EOG signals from a volunteer subject, respectively. Besides electrical signals, the wireless fully-passive technique can also be used for measuring other physical parameters, such as pressure. In Chapter 7, a wireless fully-passive sensor for intracranial pressure (ICP) monitoring is presented. With a further minimized antenna and circuit structure, the ICP sensor occupies a total footprint as small as 5 mm x 4 mm. A piezoresistive pressure sensor was fabricated on a parylene substrate. Wireless telemetry is realized by using both infrared (IR) and RF energy. The sensor was first verified *in vitro* using a benchtop setup, and then *in vivo* by implanting the device on the skull of a rat. The result shows the wireless ICP sensor accurately tracked the ICP of the rat when external pressure was applied onto the rat by thoracic compressions using a blood pressure cuff. Chapter 8 presents a flexible and passive wireless stimulator. With a total footprint of 25 mm x 42 mm x 1.6 mm, the wireless passive stimulator contains a PDMS-based antenna to receive incoming RF signals, multistage diode multipliers to accumulate charge, and a

transistor to control the timing. Comprising only one active component, the stimulator exhibits low power consumption yet generates output current as high as 60 mA. To verify the function, neonatal ventricular rat cardiomyocytes were seeded on electrically conductive gelatin-based hybrid hydrogels to form cardiac tissues. The wireless passive stimulator successfully induced synchronous contraction of the engineered cardiac tissue, demonstrating its precise control of the beating frequency over 0.5 - 2 Hz. Finally, Chapter 9 will conclude the thesis.

CHAPTER 2

LITERATURE REVIEW

Conventional methods of biosignal recording severely constrain the movement of individuals due to the use of wires or cables. To overcome the problems of wires, there have been extensive studies in developing wireless biosignal recording systems. Generally, a wireless telemetry system can be classified into an active or passive system. Active wireless systems need an internal energy source for operation, which is usually a battery. Passive systems, on the other hand, do not contain any internal power source. Both passive and active telemetry schemes have been adopted in existing wireless biosignal acquisition systems. This chapter reviews some literature published in this field, which covers wireless neuropotential recording, wireless biopotential recording, wireless ICP monitoring, and wireless stimulation.

2.1 Wireless Neuropotential Recording

As mentioned in the previous chapter, neuropotentials can be classified into EEG, ECoG, and LFP based on where they are measured. Although EEG is a noninvasive method, the poor signal integrity of EEG results in their limited value for application in clinical diagnoses or BCI systems. Therefore, most researches on wireless neuro recording systems target ECoG or LFP signal measurement rather than EEG, which requires the systems being implanted inside the head for a long period. Designing such a system involve solving a series of technical challenges including the strict constrain on size, material, and power

consumption. In addition, the system should have long term safety and reliability, as these are the basic and most important requirements for any medical device.

When designing a wireless neural recording system, one common approach used by many researchers is placing a head mount on top of the skull. Chestek et al. developed a wireless neural recording system for freely moving primates (Chestek et al. 2009) (**Figure 2.1a**). A 51 x 38 x 38 mm^3 aluminum metal case is used to house the electronic measurement system, containing a battery, a PCB, and an antenna. The neural recording is realized by implanting a 96-channels cortical array into the motor and premotor cortex of a macaque. The array is connected to a PCB using a flexible cable. The total power consumption of the system is 63.2 mW, where 28mW is used by the RF transmitter and 21 mW is used by the controlling digital circuitry. Using a battery as the power supply, the system is able to continuously operate for 5.8 days. The testing results showed that the system recorded neural signals with high fidelity from a free moving animal, differentiating the activities of the animal by decoding the recorded neural data.

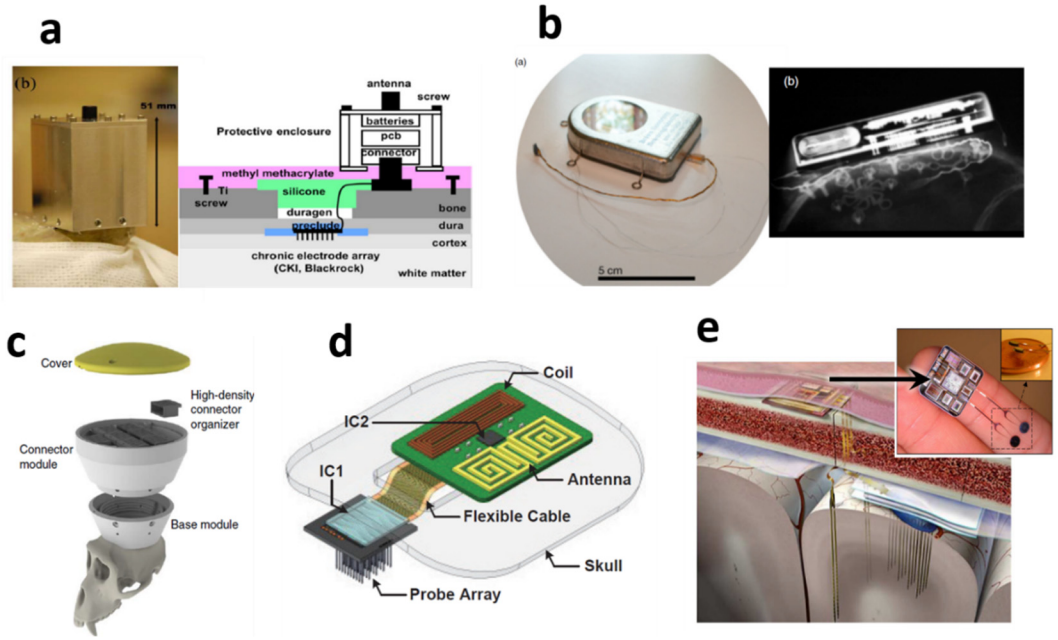

Figure 2.1. Existing wireless neural recording systems in the form of wireless head stages or subcutaneous microsystems. (a) A 100 channels implantable wireless microsystem (Chestek et al. 2009). Image copyright: © [2009] IEEE. The electrode array was implanted inside the cortex. An aluminum case containing all the electronic components was fixed on the skull. The two parts were connected through transcranial wires. (b) A wireless head stage for neural recording of primates (Borton et al. 2013). Left: the hermetic head stage contained a battery, an electronic circuit board, and inductive coils for wireless transmission. A commercial MEA array was wired to the circuit board of the head stage. Right: X-ray image of the implanted wireless system on a primate. Images reprinted with permission from IOP Publishing, Borton et al. 2013, An implantable wireless neural interface for recording cortical circuit dynamics in moving primates, Journal of Neural Engineering 10 (2). (c) A wireless head stage for large-scale neural activity recording in freely moving rhesus monkeys (Schwarz et al. 2014). The system achieved a total of 1792

recording channels. Image reprinted by permission from Springer: Nat. Methods. Chronic, wireless recordings of large-scale brain activity in freely moving rhesus monkeys. Schwarz, D. A. et al, 2014. (d) Schematic of a 100 channels wireless neural recording system consisting of a neural recording IC and an external subcutaneous chip (Cheng et al. 2012). The two parts were connected through flexible cables. Image copyright: © [2012] IEEE. (e) An implantable 64 channels wireless microsystem for single unit neural recording (Sodagar et al. 2009). The microsystem mounted above the skull. Intracranial wiring was required to transmit signals from implanted electrodes to external circuitry. Image copyright: © [2009] IEEE.

Another similar wireless neurorecording system was reported by Borton et al. (Borton et al. 2013) (**Figure 2.1b**). This device consists of a 100 channels intracortical silicon-based microelectrode array (MEA) and a head-stage, which contains a rechargeable battery, an inductive coil, and electronic circuitries for wireless transmission. The head stage is enclosed by a 56 x 42 x 9 mm^3 titanium hermetic case. The implantable MEA is connected to the head stage using a bundle of wires. The system consumed 90.6 mW under normal operation and is able to continuously record from 100 channels for up to 7 hours. When the battery runs out, it can be recharged by an external inductive coil, placed around 5 mm above the titanium case, via inductive coupling. The total weight of the system is 44.5 grams. For *in vivo* verification, the MEA was implanted into the cortex of a rhesus macaque and the titanium case of the device was secured to the cranium of the animal with five bone screws. The system was able to continuously record from a freely moving primate.

The recorded signals showed clear detection of neural spike activities with a peak to peak amplitude ranging from 40 to 250 μV in all the 100 channels.

Schwarz et al. reported a wireless neural recording system that has the largest number of recording channels to date (Schwarz et al. 2014) (**Figure 2.1c**). This system is composed of 4 recording cubes, each recording cube contained 448 microwire electrodes, achieving a total of 1792 recording channels. All the recording cubes are housed in a 3D printed head cup, together with the wireless module and a lithium-ion battery. The dimension of the system was not reported, but it is clear that its total volume is comparable or even larger than the entire head of the animal. The power consumption of the system is 264 mW per 128 channels, enabling a continuous operation time of 30 hours. The maximum number of channels allowed for simultaneous recording was 512 channels. This wireless head stage was also verified in a freely moving monkey. The use of large-scale neural recordings over multiple cortex areas results in largely improved performance of the neural decoding model and better accuracy in the classification of behaviors.

The wireless systems described above all shared one common characteristic: only the microelectrode array (MEA), such as Utah, Michigan (Kipke et al. 2003), or μECoG (Tolstosheeva et al. 2013; Muller et al. 2014) array, was implanted onto the cortex surface, while the remaining system was placed outside the skull in the form of a head-stage (Schwarz et al. 2014; Borton et al. 2013; Chestek et al. 2009; B. Lee et al. 2018; 2019). The connection between the implanted electrodes and the external system was accomplished using a bundle of cables penetrating through the skull. This separation of MEA and the external system is a compromise to avoid the stringent requirement on the

size and power consumption of the wireless system. Obviously, electronic systems placed on the skull would have much more design flexibility as compared to those inside the skull. As a result, the wireless head-stage systems described above all have rather large sizes and high power consumption, which is technically much easier to achieve as compared to a low-power, small-sized system. However, the intracranial wiring configuration also gives rise to numerous challenges and issues. A major concern is the high failure rate. Barrese et al. (Barrese et al. 2013) examined the long-term functionality of 78 MEA head stages mounted on primates. It was discovered that 48% of the arrays completely lose functionality within one year due to mechanical failures associated with transcranial cables. Notably, the protrusion of the head-stage from the skin made them particularly susceptible to external damage, causing the breakage of intracranial wire bundles, removal of implanted MEA, or even cortical injury. Besides this high failure rate, other potential issues include the risk of infection at the surgical wound (Bjerknes et al. 2014) and the negative impact of the head-stage on the patient's cosmetic appearance. Overall, the wireless head stage method is not safe and robust enough to be used in standard medical treatment. In fact, currently this method is only suited to be used on animals, such as lab rats or primates, for studies on animal behavior or pathology of neurological disorders.

Besides the wireless head-stages, some researchers have developed wireless neural recording systems in the form of subcutaneous microsystems. Cheng et al. reported a 100 channels wireless neural recording system, composed of an implanted 100 channels recording integrated circuit (IC) and an external wireless module (Cheng et al. 2012) (**Figure 2.1d**). The implanted IC is integrated with a probe electrode array, and the external

system, containing an antenna and an inductive coil, mounted subcutaneously on the skull. The total power consumption of the system is less than 30 mW and the wireless telemetry operation of the system was verified in a rat model by separate neural recordings using a glass electrode. Sodagar et al. presented another implantable 64 channels wireless microsystem for recordings of single-unit neural activities (Sodagar et al. 2009) (**Figure 2.1e**). This system contains two 32 channels Michigan arrays and an external microsystem with a dimension of 14 mm x 15.5 mm. The external microsystem is implanted between the skin and the skull; it is inductively powered by an external transmitter. A bundle of intracranial wires connects the system to the electrodes through the skull. This system was not verified *in vivo*. Subcutaneous microsystems can reduce the height of the protrusion, making the system less susceptible to external physical damage and effectively minimizing the negative effect of the system on the patient's cosmetic appearance. However, the issues associated with the intracranial wiring, including infection and high failure rate, still exist. Also, since the *in vivo* testing for those systems were either not conducted or not well reported, it is still unclear if those subcutaneous systems can function properly when they are implanted.

The problems with the intracranial wiring can be effectively solved if the entire wireless system, rather than only a part of it, is implanted onto the cortical surface to enable complete closure of the surgical wound. However, developing such a fully-implanted wireless system faces tremendous technical challenges due to the restriction in size, power consumption, biocompatibility, and long-term reliability (Muller et al. 2014; C. W. Lee et al. 2015; Schulman 2008). Batteries should also be avoided because of their limited lifetime

and hazardous content (Marom et al. 2010). In the past years, researchers have been resorting to ultra-low power consumption integrated circuit (IC) technology to overcome these challenges (Chestek et al. 2009; Chae et al. 2008; Neihart and Harrison 2005). Mestais et al. developed a wireless ECoG system for long-term clinical applications (Mestais et al. 2015) (**Figure 2.2a**). This wireless system uses two custom-designed 32 channels low power ICs for neural recording. A commercial low power microcontroller is implemented as the logic controller. The electronic components are soldered on rigid PCB boards and packaged by a titanium case. The system is powered by an external antenna. Although this system is intended for complete implantation, it exhibits several potential safety issues. First, the system has a large footprint of 50 mm in diameter and 12.54 mm in height. As a result, implantation of the system required the complete removal of a piece of skull, introducing potential safety issues such as infection. Additionally, the power consumption of the system achieves as high as 350 mW, which may bring heat damage to the brain tissues. Finally, the system is based on rigid PCB, which may cause physical damage to the brain and may eventually result in loss of contact between electrodes and tissues. Besides the potential safety issues, validation of the system was only conducted in the air with intracranial cables connected to a commercial cortical array. This experiment setting largely deviated from the intended application of the system, thus it greatly diminished the efficacy of the study.

Muller et al. developed a 64 channels fully implantable wireless micro-ECoG array which incorporates a specially designed low power IC with micro-fabricated parylene electrodes (Muller et al. 2014) (**Figure 2.2b**). The IC, powered by an external inductive

coil, exhibits low power consumption of 225 μW and a small footprint of 2.4 mm x 2.4 mm. The parylene-based electrode array is also integrated with a rectangular loop antenna, resulting in a total footprint of 6.5 mm x 6.5 mm. The small size, flexible substrate, and very low power consumption made the system very promising to be used as a chronic implant for long-term neural recording applications. However, verification of the system was not performed through complete implantation in the animal. Instead, the IC was soldered on a printed circuit board (PCB), which was connected to the parylene electrodes through flexible cables. The cranium of the animal was opened for electrode placement, but it was not closed during the measurement. In addition, the recorded wireless signal did not show a very clear neural signal pattern.

Another wireless neural recording system worth mentioning is the Neuron Dust device presented by Seo et al. (Seo et al. 2016) (**Figure 2.2c**). The neuron dust is an mm-scale, passive, single-channel wireless neuro recording device using ultrasonic energy as wireless telemetry media. The device contains a piezoelectrical crystal to transmit and receive ultrasonic energy, and a transistor as a modulator. An external transducer is used to establish communication with the Neural Dust sensor. Wireless telemetry of the neuropotential is achieved through the backscattering of ultrasound. Unlike RF energy, ultrasonic energy does not attenuate dramatically inside the tissue. In addition, the system achieved a very small dimension of 0.8 mm x 3 mm x 1 mm with the miniature ultrasound transducer. However, a major disadvantage of the system is that ultrasound cannot penetrate the skull. Due to this reason, the Neuron Dust was only verified by *in vivo* recording from a frog sciatic nerve at where there was no bone impeding the propagation

of ultrasound. The actual implementation of Neural Dust will require either the patient to remove a portion of the skull, or converting of the ultrasound to other forms of energy by implanting additional electronic devices, both of which will introduce unwanted safety issues. Thus, the efficacy of the Neural Dust being used as a brain implant remains unclear.

In summary, existing wireless implantable systems based on active integrated IC technology have not been effective in addressing the aforementioned challenges, partly due to their rigidity, high power consumption, and lack of potential long-term reliability.

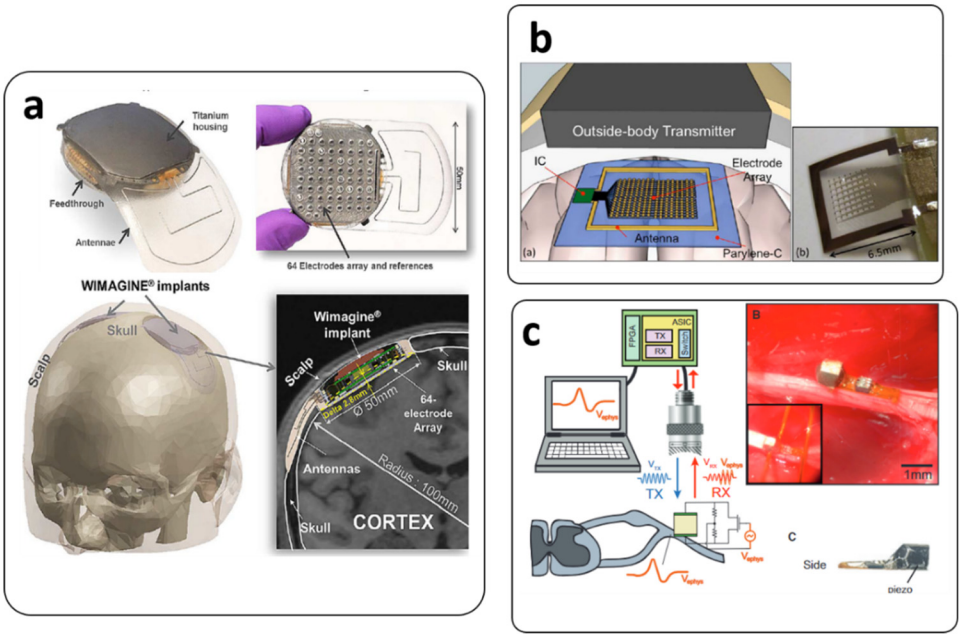

Figure 2.2. Wireless neural recording systems targeted for fully-implantable applications. (a) The WIMAGINE system is a 64-Channel ECoG recording system developed for long-term implantation (Mestais et al. 2015). A titanium case was used to house all electronics and an ECoG electrode array on the backside formed the neural interface. The implantation surgery required removing a portion of the skull and inserting the titanium case of the

device. The system was powered by an external antenna. Image copyright: © [2015] IEEE. (b) A 64 channels wireless μECoG array based on a microfabricated parylene electrode array and an IC chip (Muller et al. 2014). The system was intended to be implanted on the surface of the cortex. An external transmitter was used to power the system and read wireless telemetry data. Image copyright: © [2014] IEEE. (c) The neural dust is a passive, battery-free single channel wireless neural recorder utilizing ultrasonic energy as the media (Seo et al. 2016). The neural dust uses a piezoelectric crystal to convert electrical signals to ultrasound and vice versa. The device was used to measure stimulation response from a frog sciatic nerve. Reprinted from Neuron, 91, Seo, D. et al. Wireless recording in the peripheral nervous system with ultrasonic neural dust, 529–539, 2016, with permission from Elsevier.

2.2 Wireless Biopotential Recording

Unlike neuro signals, biopotential signals can be collected from the skin. Thus, the technical challenges of wireless biopotential recordings are significantly less than that of neural recordings. As a matter of fact, wireless portable biopotential monitors like the Holter ECG monitors have already been commercialized and accepted as clinical diagnostic tools (Kennedy 1992). Wireless wearable biopotential sensors also exist in the market, such as the Trigno EMG sensor and the Qardio ECG monitor. However, those commercialized wireless sensors all rely on batteries to power electronics, which results in their limited continuous operation time. Therefore, one of the trends in the field of wireless biopotential sensing is to develop completely wireless, wearable, and battery-free systems.

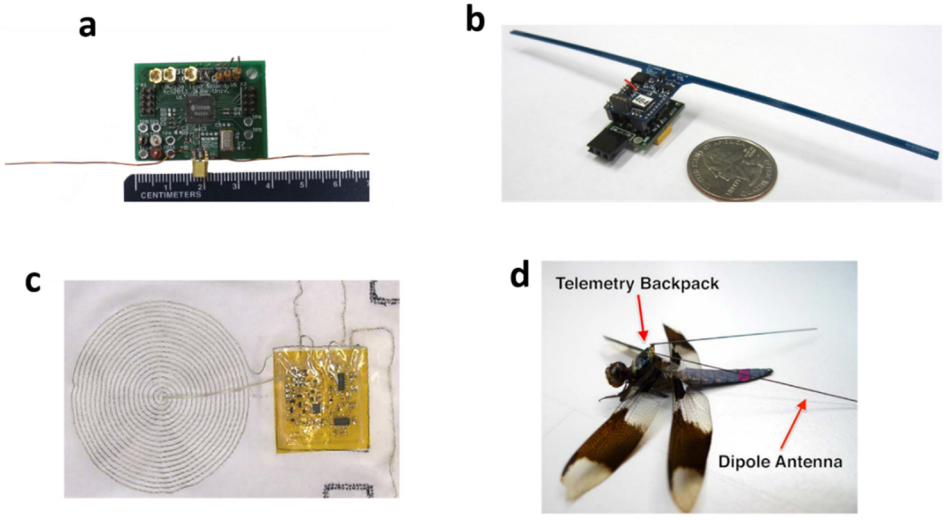

Figure 2.3. Battery-free wireless biopotential recording systems. (a) A battery-free multichannel digital ECG recorder based on ultra-high frequency (UHF) radio frequency identification (RFID) technology (Besnoff et al. 2013). Image copyright: © [2013] IEEE. (b) A wearable UHF RFID-based electroencephalogram (EEG) monitoring system (Dementyev and Smith 2013). Image copyright: © [2013] IEEE. (c) A wireless, battery-free ECG monitoring system fabricated on Kapton film and embroidered on a baby suit (Coosemans, Hermans, and Puers 2006). Reprinted from Sensor and Actuators A: Physical, 130, Coosemans, J., Hermans, B. & Puers, R, Integrating wireless ECG monitoring in textiles, 48–53, 2006, with permission from Elsevier. (d) A wireless battery-free multichannel wireless telemetry package mounted on a dragonfly (Thomas et al. 2012). The system can record both neural signals and EMG signals from the insect. Image copyright: © [2012] IEEE.

Several research groups have reported wireless, battery-free biopotential sensors based on RFID (Radio Frequency Identification) technology (Besnoff et al. 2013; Dementyev and Smith 2013) (**Figure 2.3 a, b**). These sensors contain sophisticated electronic circuitries that harvest power for operation from such as inductive or RF coupling, thereby eliminating the demand for battery replacement. However, the rigid substrate and the large size prevent these RFID systems from being used as wearable wireless electronic devices. Some researchers integrated wireless and battery-free ECG monitor on clothing by embroidering the antenna and flexible electronics (Coosemans, Hermans, and Puers 2006) (**Figure 2.3c**). This setting avoids the use of any surface electrodes, enabling long term ECG monitoring without causing much discomfort, thus it is especially suited for ECG monitor on a baby. However, since all the electrodes and electronic systems are exposed, this system harms the individual's appearance and may draw unwanted attention from others. Also, the embroidered electrodes may not maintain reliable contact with the skin all the time during the individual's routine activities. Another work worth mentioning is the wireless battery-free digital neural/EMG telemetry system presented by Thomas et al. (Thomas et al. 2012) (**Figure 2.3d**). This system has a very small size of 4.6 mm x 6.8 mm, and it can be mounted on the back of a dragonfly. Wireless telemetry is achieved through backscattering the EM wave radiated from an external transmitter. The transmitter radiated a maximum of 4 W RF energy, enabling wireless telemetry within 0.5 – 1 m distance. Although this system was not verified *in vivo* with actual biopotential signals, the concept of presented by this work has great potential to be used in the future wearable electronic applications.

The recent highlights of wireless battery-free sensors focus on flexible and light-weight, small-size epidermal electronics, having wireless communication capability, being the ideal form of wearable electronics (J. Kim et al. 2016). Several recent studies have demonstrated epidermal electronics for measuring temperature (J. Kim et al. 2018) and pulse (J. Kim et al. 2016). For biopotential measurement, Xu et al. reported completely wireless, battery-free epidermal electronics that can be laminated onto the surface of the skin to measure physiological signals including ECG, EEG, and EMG (Xu et al. 2014) (**Figure 2.4a**). Based on a filamentary, serpentine mesh structure, this sensor is stretchable and bendable, and can be robustly adhered to the skin through van der Waals forces. The sensor is powered by an inductive coil placed in proximity (within millimeters). Another similar work was presented by Chung et al. (Chung et al. 2019) (**Figure 2.4b**), which introduced the epidermal electronic systems (EES) for measuring both ECGs and PPGs (photoplethysmograms). The electronic circuits in these wireless EES are formed by narrow serpentine metal traces. A microfluidic chamber filled with ionic liquid is used as an isolation layer between the electronics and the skin, which effectively reduces the mechanical stress on the sensor and results in better adhesion between the device and the skin through van der Waals forces. Wireless telemetry is accomplished through near-field communication (NFC) protocol. These epidermal electronic systems represent the future research direction of wireless biopotential acquisition. Unfortunately, the wireless telemetry presented in these works suffers from the limited communication protocol, i.e., near field communication (NFC), or the stringent requirement of precise alignment of primary/secondary coils.

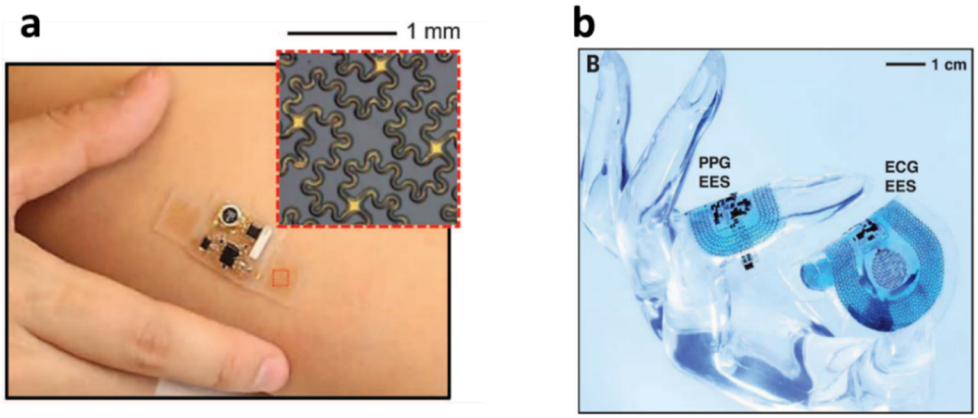

Figure 2.4 Epidermal electronic systems for wireless and battery-free biopotential acquisition. (a) An epidermal wireless sensor based on serpentine mesh layout attached to the skin for measurement of ECG, EMG, and EEG (Xu et al. 2014). The sensor is powered by an external inductive coil. Image from Science, 344, Xu et al. Soft microfluidic assemblies of sensors, circuits, and radios for the skin. 70–74, 2014. Reprinted with permission from AAAS. (b) Binodal epidermal electronic systems (EES) developed for ECG and PPG monitoring in the neonatal intensive care unit (Chung et al. 2019). The flexible sensors use serpentine metal traces to construct electrodes and electronics. Wireless communication is achieved through near field communication protocol (NFC).

2.3 Wireless Intracranial Pressure (ICP) Monitoring

Continuous, long-term, and safe intracranial pressure (ICP) monitoring enables early diagnose of any intracranial hypertension disorders, and thereby improves the outcome of associated clinical treatment. For patient implanted with ventricular-peritoneal (VP) shunts, regular ICP monitoring is also necessary to detect any malfunction of the

implanted shunts (Harary, Dolmans, and Gormley 2018). The current gold standard of ICP monitoring, i.e., the external ventricular drainage system (EVD), is not suited for routine ICP monitoring due to its invasive nature, cumbersome setting, and the potential safety risks including hemorrhage and infection. On the other hand, wireless implantable ICP sensors offer a possible solution to this challenge, and thus they have been explored by many researchers during the past years. Some wireless ICP sensors incorporate commercially available pressure sensors as the ICP sensing elements. These sensing elements can be either resistive or capacitive, and they are usually fabricated through micro-electro-mechanical system (MEMS) technology. The wireless ICP sensors utilize those microfabricated piezoresistive strain-gauges or capacitive micro-transducers to convert pressure change into resistance/capacitance change. This change is then measured with analog circuitries, digitalized, and processed by sophisticated ICs, and then wirelessly sent out to external reader systems by antennas.

A commercially available wireless ICP sensor, the Neurovent P-tel (Kiefer et al. 2011; Antes et al. 2016), is shown in **Figure 2.5a**. The piezoresistive pressure sensor is located at the tip of a polyurethane catheter. The resistive change is acquired by a microchip inside a round ceramic housing located at the other end of the catheter. The catheter has a length of 30 mm and the ceramic housing has a total footprint of 31.5 mm in diameter and 4.3 mm in height. Implantation of the sensor requires drilling a burr hole on the skull of the patient and then inserting the catheter carefully into the frontal brain parenchyma until the ceramic housing lies on the surface of the skull. The sensor is a passive device and its operation requires power supplied from an external reader, which must be positioned and

fixed over the implant on the skin. This system has gone through clinical trials and the testing results on patients have proven its efficacy. However, it also exhibits significant limitation. The external reader must be fixed over the implant on skin, and thus this telemetric system still restricts patient activities. Also, due to its rather large size, the device cannot be fully implanted inside the skull. As a result, complications such as infection, brain abscess, and technical failure still exists.

Some other examples of wireless ICP monitoring system based on commercialized MEMS sensors are shown in **Figure 2.5 b and c**. Jiang et al. developed an implantable wireless intracranial pressure sensor based on air pressure sensing (Jiang et al. 2018) (**Figure 2.5b**). This system converted the ICP pressure to air pressure by utilizing an implanted air pouch. The air pressure was then detected by a commercialized MEMS capacitive sensor. A very sophisticated custom-designed system on a chip (SoC) is used to realize data acquisition and wireless telemetry function. This wireless ICP sensor has rather large dimensions, and it needs a battery to power all the electronics, which results in its short operation time for only one week. In addition, this system was only tested by *in vitro* experiments. Meng et al. reported a wireless ICP sensor incorporating a capacitive MEMS sensor, a battery, and a titanium casing containing all the required electronic components (Meng et al. 2012) (**Figure 2.5c**). Again, the use of battery and titanium casing results in large size and limited operation time, making the device unsuitable for clinical applications. Since the commercially available MEMS pressure sensors do not possess wireless communication capability themselves, they always require additional circuitries, such as digital logic controllers and wireless modulation modules, to achieve the telemetry function.

Eventually, this factor unavoidably leads to the large size and high power consumption of the developed wireless ICP monitoring systems, making them difficult for actual implantation.

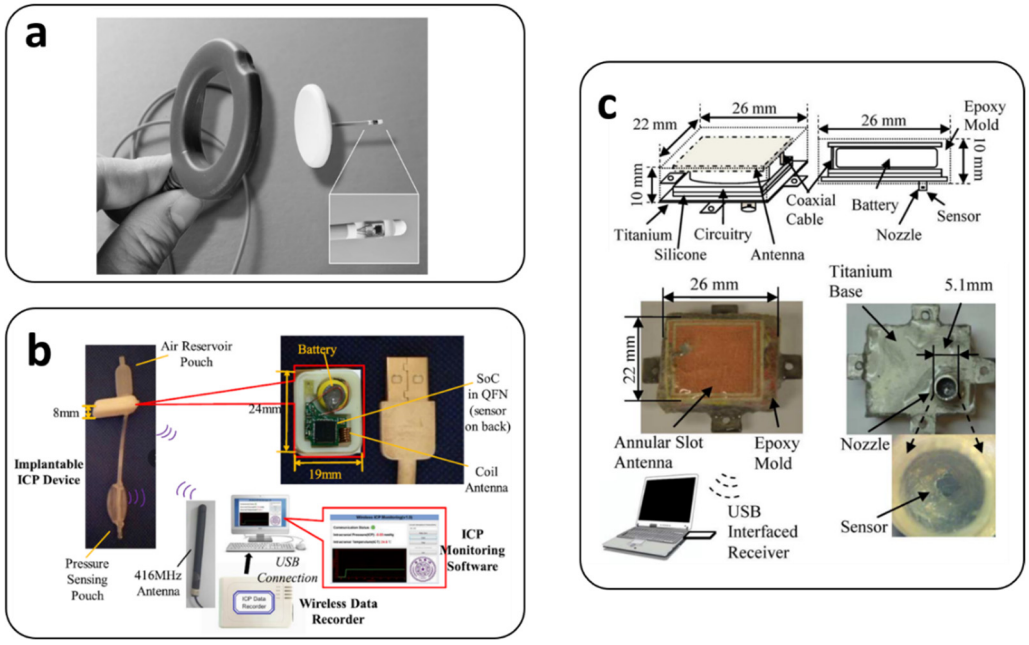

Figure 2.5. Wireless ICP monitoring systems incorporating MEMS pressure sensors. (a) The commercially available Neurovent P-tel (Raumedic) telemetric ICP monitoring system (Antes et al. 2016). A piezoresistive MEMS sensor is located at the tip of the catheter. Reprinted from World Neurosurgery, 91, Antes, S., Tschan, C. A., Heckelmann, M., Breuskin, D. & Oertel, J., Telemetric intracranial pressure monitoring with the Raumedic Neurovent P-tel, 133–148, 2006, with permission from Elsevier. (b) A wireless ICP monitoring system based on air pressure sensing (Jiang et al. 2018). The air pouch converts the ICP to air pressure which is detected by a MEMS capacitive pressure sensor. Image copyright: © [2018] IEEE. (c) Another wireless ICP monitoring system using a capacitor

MEMS sensor as the pressure sensing element (Meng et al. 2012). A large titanium case is used to house all the required electronic components including digital circuitries, an antenna, and a battery. Image copyright: © [2012] IEEE.

In order to reduce the size and avoid the use of batteries, Fonseca et al. proposed a flexible passive wireless pressure sensor based on the principle of LC resonant circuits (Fonseca et al. 2006). The sensor is composed of two spiral inductors and a parallel plate capacitor. Each of the spiral inductors is printed on a liquid crystal polymer (LCP), together with the top/bottom copper plate. By laminating the two LCP sheets on a polytetrafluoroethylene (PTFE) bonding layer, the top and bottom copper plates form a parallel plate capacitor at the center of the sensor, interconnected with both spiral inductors. In essence, the senor is equivalent to a series LC resonance circuit. The parallel plate capacitor has a cavity in the center. Under external pressure, the cavity deforms, resulting in capacitance change, which in turn leads to shifting of the resonance frequency. Thus, the pressure value can be determined by measuring the resonance frequency of the sensor, which can be accomplished wirelessly using an external inductive coil. This sensor has many advantages, including small size, high flexibility, no battery, and near-zero power consumption. The sensor accurately recorded the pulse pressure *in vivo* in a canine model. Furthermore, a revision of the sensor, the cardioMEMS HF system has already been commercialized and is now being used by many patients for pulmonary artery (PA) pressure monitoring.

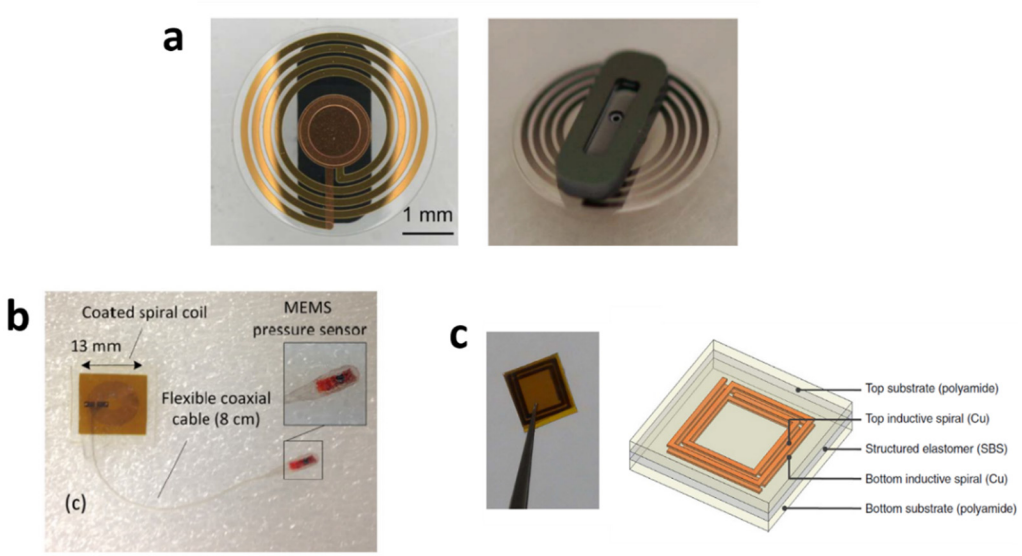

Figure 2.6. Wireless passive pressure sensors based on the LC resonance circuit. (a) A wireless LC resonance sensor developed for intraocular pressure sensing (P.-J. Chen et al. 2010). The inductor of the sensor is printed on parylene, while the capacitor of the sensor is microfabricated on silicon. Image copyright: © [2010] IEEE. (b) Wireless LC resonance sensor developed for ICP monitoring (Behfar et al. 2016). The pressure sensing element is the MEMS capacitive sensor located at the tip of the coaxial cable. The inductor is fabricated on a polyimide substrate. Image copyright: © [2016] IEEE. (c) A miniaturized wireless ICP sensor (L. Y. Chen et al. 2014). The capacitor is formed on a pyramid structured SBS dielectric, sandwiched by two spiral inductors. The sensor has a very small dimension of 1 x 1 x 0.1 mm^3. Image reprinted by permission from Springer: Nature Communications, Continuous wireless pressure monitoring and mapping with ultra-small passive sensors for health monitoring and critical care, Chen, L. Y. et al., 2014.

Because of the attractive features demonstrated by the LC resonance telemetry, many researchers adopted this method to design wireless passive pressure sensors for different applications. Chen et al. developed an LC-based pressure sensor for intraocular pressure (IOP) sensing (P.-J. Chen et al. 2010) (**Figure 2.6a**). This device has a total diameter of 4 mm and is composed of a microfabricated MEMS capacitive sensor and a spiral inductor printed on a parylene substrate. The sensor was tested *in vivo* inside a rabbit eye, demonstrating a wireless pressure measurement accuracy of 2.5 mmHg. Behfar et al. developed an LC resonance based wireless ICP sensor composed of a spiral inductor and a MEMS capacitive sensor (Behfar et al. 2016) (**Figure 2.6b**). The inductor is fabricated on polyimide substrate and connected to the capacitive MEMS sensor through a flexible coaxial cable. For ICP measurement, the capacitive sensor is intended to be inserted into the ventricle, while the spiral inductor is placed under skin. *In vitro* verification showed the sensor has a pressure measuring accuracy of 5 mmHg. Another similar wireless ICP device was presented by Chen et al. (L. Y. Chen et al. 2014) (**Figure 2.6c**). In this work, the capacitive sensing element is formed directly using the two metal traces of the spiral inductors sandwiching a pyramidal structured styrene-butadiene-styrene (SBS) elastomer. This method results in the sensor scaled down to an unprecedented dimension of 1 x 1 x 0.1 mm^3. Overall, wireless pressure sensing based on the LC resonance principle is becoming increasingly popular in the past few years owing to their passive characteristic, simple structure, and small dimensions. However, this solution also has its inherent limitations. First, the resonant frequency of the LC circuitry is largely affected by external environment. In fact, all the works mentioned above reported dramatic changes in LC

resonance frequency and quality factor when the wireless sensor was moved from air into saline (Fonseca et al. 2006; P.-J. Chen et al. 2010; Behfar et al. 2016; L. Y. Chen et al. 2014). This is because capacitance is always a function of the permittivity in the surrounding environment. Many factors can change the capacitance of the sensor, such as the moisture absorption of polymers and the growth of tissue. This uncertainty will result in significant baseline drifts. Fonseca et al. reported a baseline drift as large as 28.52 mmHg after 6 days implantation (Fonseca et al. 2006). This indicates that LC resonance-based wireless pressure sensor may not be suitable for application where an accurate mean pressure reading is important, such as the case in ICP monitoring. Secondly, LC-based wireless pressure sensors generally need the external reader placed at a very close range, often within millimeters, to function properly. This raises question whether the sensor can still function when placed within the skull, as the total thickness of the skull and the skin can be as large as several centimeters. In addition, wireless transmission distance, quality factor, and alignment between the external reader and the sensor can all affect the wireless readout (Nopper, Niekrawietz, and Reindl 2009). Any movement or misalignment of the external reader may lead to inaccurate measurement results, reducing the reliability of the system. In summary, wireless passive pressure telemetry schemes based on the LC resonance circuitry may not work well for continuous ICP monitoring.

2.4 Wireless Stimulation

One of the major motivations for developing wireless stimulation systems is to give continuous functional electrical stimulation (FES) to neurologically impaired individuals,

exciting their paralyzed muscle in order to restore the lost motor functions (Peckham and Knutson 2005). The FES systems are designed to be worn by the user, therefore, wireless implantable stimulation systems are attractive, particularly for long-term implementation, as they can be portably used at home without restricting movement. To date, numerous wireless stimulators have been proposed. The first and probably the most well-known wireless implantable simulator is the Freehand system developed by Peckham et al. (Peckham and Knutson 2005; Keith et al. 1989). The purpose of the Freehand system is to provide lateral and palmar grasp to patients with C5 or C6 tetraplegia. The system is consisted of a stimulator/receiver unit implanted at the chest, and eight intramuscular electrodes implanted at the motor points of hand and forearm muscles. All of the electrodes are connected to the stimulator through long electrical leads (Peckham and Knutson 2005). The system does not contain any battery, it is powered by an external coil placed over the chest. A separate controller unit is connected to the coil to give stimulation commends. The system has FDA approval and has been implanted in more than 250 patients. Clinical trials demonstrated an effective reduction of impairment in tetraplegia patients, and more than 90% of participants were satisfied with the device (Sheffler and Chae 2007). However, the system requires a very complex and extensive surgical implantation procedure, mainly due to its multiple long, unconcealed electrical leads. In addition, the large surface area of the implanted stimulator and wires also increases the risk of infection. Due to these problems, the Freehand system is no longer being used in clinical practice (Sheffler and Chae 2007).

To address the challenge associated with large size and long wires, several research groups developed miniaturized implantable and injectable wireless stimulators. Loeb et al.

developed the BION system, a RF powered, single channel stimulator, featuring a total dimension of 2 mm in diameter and 16 mm in length (Loeb et al. 2001; Loeb, Richmond, and Baker 2006; Schulman 2008) (**Figure 2.7a**). The small size and cylindrical shape of the device enable it to be implanted by injection through a needle, thereby greatly reducing the surgery effort and minimizing the risk of infection. The BION system is powered by an external inductive coil and can output pulsatile stimulation current from 0.2 to 30 mA. Several similar devices were also developed by other research groups. Ziaie et al. (Ziaie et al. 1997) developed a wireless neuromuscular stimulator measuring 2 x 2 x 10 mm^3 (**Figure 2.7b**). Like BION, the stimulator can be injected into the body through a needle. Powered by an inductive coil, the stimulator delivers stimulation current up to 10 mA. Cho et al. reported a wireless battery-free neurostimulator based on MEMS technology (Cho et al. 2010) (**Figure 2.7c**). The stimulator is fabricated on a SU-8 substrate and has a total dimension of 3.1 x 1.5 x 0.3 mm^3. This system is also powered by an external inductive coil. For all these passive, injectable wireless stimulators, the user needs to wear a large and heavy external inductive coil to power the implanted stimulators (Loeb et al. 2001; Ziaie et al. 1997), which is cumbersome and may cause discomforts. The voltage applied on the external coil can be as high as 500 V (Loeb, Richmond, and Baker 2006). Such large voltage is potentially dangerous to the user. Moreover, the high power RF field produced by the coil can interfere with other implanted electronics, and induce unwanted temperature rise within the tissue due to ohmic loss (Ziaie et al. 1997; Larson and Towe 2011). Some researchers wish to solve this challenge by using implantable and rechargeable batteries to power all the required electronics. Lee et al. proposed a rechargeable battery-powered

implantable FES microstimulator (E. Lee et al. 2009) (**Figure 2.7d**), which avoids using bulky inductive coils. However, although the stimulator can operate independently, the user still needs to recharge the battery for a few hours every three or four days by placing a large inductive coil above the implant. In addition, since all batteries has hazardous content in them, they are not suitable for long-term implantation. Aside from these challenges, all of the reported wireless injectable stimulators have relatively low current output, ranging from 2.5 μA to 30 mA (Ziaie et al. 1997; E. Lee et al. 2009; Schulman 2008; Arfin et al. 2009), which is insufficient for many applications demanding high-current. One of these applications is the electrical stimulation for engineered cardiac tissue. Many studies have shown that relatively large stimulating current, at least 60 mA (Hirt et al. 2014; Tandon et al. 2011), is required for effective pacing of engineered cardiac tissue. While a wire connected electrical stimulating system can easily achieve such high current, it is still a challenging specification for a wireless system, and existing wireless stimulating systems have yet to meet this requirement.

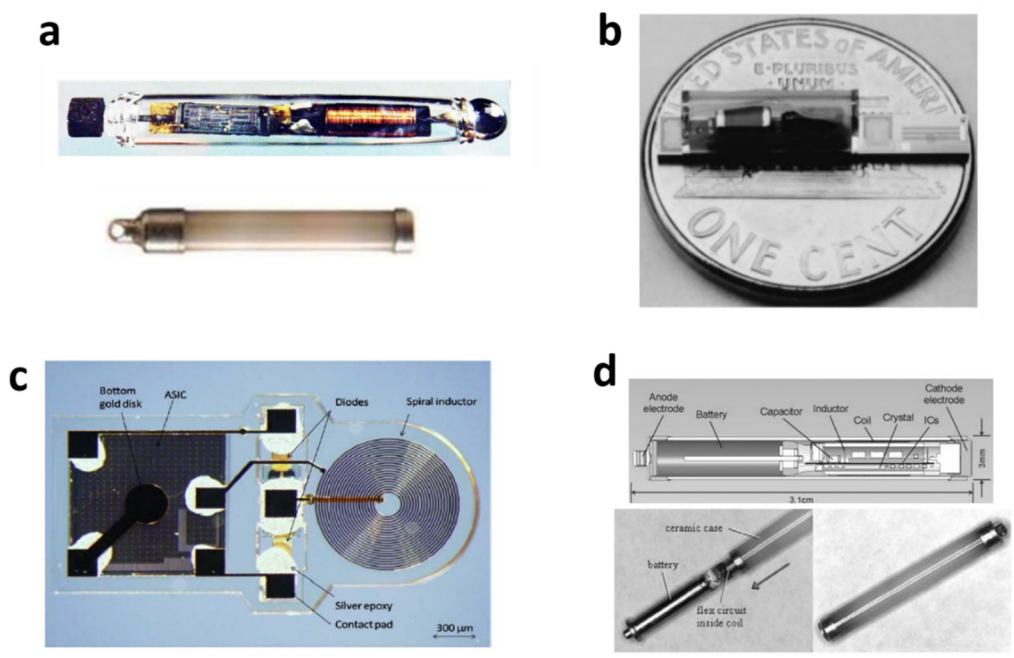

Figure 2.7. Miniaturized injectable wireless stimulators. (a) Photographs of the BION injectable microstimulator (Schulman 2008). Image copyright: © [2008] IEEE. (b) A single channel implantable stimulator for functional neuromuscular stimulation (Ziaie et al. 1997). Image copyright: © [1997] IEEE. (c) A MEMS-based wireless neurostimulator fabricated on a SU-8 substrate (Cho et al. 2010). Image copyright: © [2010] IEEE. (d) An injectable FES microstimulator powered by a rechargeable battery (E. Lee et al. 2009). Image copyright: © [2009] IEEE.

2.5 Prior Works Related to This Thesis

This thesis aims to address the challenges of the aforementioned wireless biosignal acquisition systems by using a wireless and fully-passive telemetry scheme. Some prior works are described to provide the context for this work within the same application space. The concept of wireless fully-passive acquisition of neuropotentials using RF

backscattering was proposed by Schwerdt et al. (Helen N. Schwerdt et al. 2011; H. N. Schwerdt, Miranda, and Chae 2012; 2013) (**Figure 2.8**). In this method, the wireless recorder receives an incident RF signal from an external interrogator and then reflects a modulated RF signal back, which carries the information of the targeted biological signal. This working principle is similar to RFID technology. The microfabricated wireless neural recorder has a very small dimension of 12 mm x 4 mm. Due to the absence of any active component, the recorder features a near zero power consumption. Unfortunately, the device suffers from low sensitivity and very short communication distance. *In vitro* validation was conducted using a multi-layer tissue-emulating phantom, and the minimum detectable signal of the sensor inside the phantom was 6 mV_{pp}. *In vivo* validation of the sensor was conducted in the air by wiring the sensor to needle electrodes inserted at frog sciatic nerve to record stimulation evoked response. This test showed an improved minimum detectable signal of 500 μV, however, the testing setup was far from realistic. Thus, the actual feasibility of fully-passive wireless neural recording in real implant environment was unproven. Additionally, the device was fabricated on a rigid and brittle silicon substrate, which could potentially cause damage to the brain tissue.

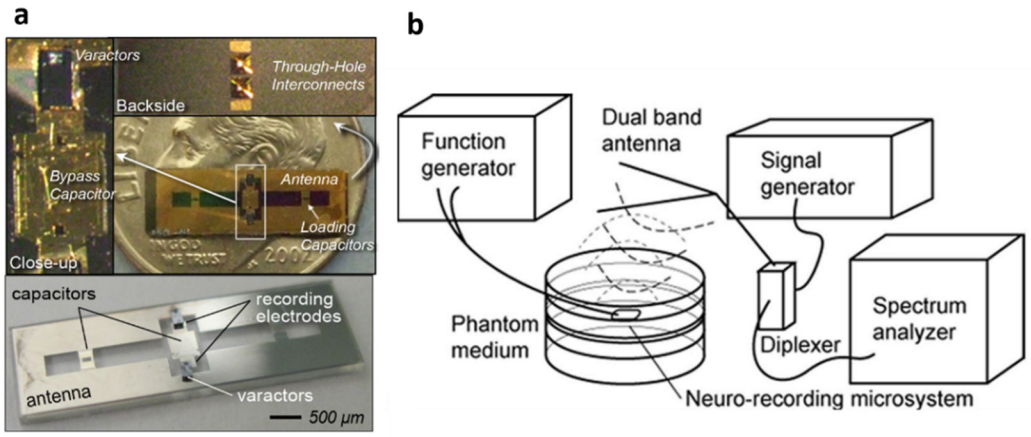

Figure 2.8. The prior wireless fully-passive neural recorder (Helen N. Schwerdt et al. 2011; H. N. Schwerdt, Miranda, and Chae 2012; 2013). (a) Top: photographs of a device fabricated on a silicon substrate. Bottom: another device fabricated on a glass substrate. Image copyright: © [2011] IEEE, © [2012] IEEE. (b) The experiment setup used for *in vitro* verification of the neural recorder. The device was buried inside a multi-layer phantom model. An external dual-band antenna was placed above the phantom for the wireless telemetry of emulated neuropotential signals. Image copyright: © [2013] IEEE.

Another fully-passive wireless neural recorder was reported by Kiourti et al. (Kiourti et al. 2016) (**Figure 2.9**). This work utilized the same working principle as Schwerdt's work, but the antenna was optimized, which resulted in a much-improved sensitivity of 50 μV_{pp}. The device was fabricated on a printed circuit board (PCB) with a total dimension of 15 mm x 16 mm x 1.5 mm. *In vivo* testing was performed by measuring somatosensory evoked potential (SSEP) from a rat scalp. However, this was done by wiring the electrodes inside the scalp of the animal to the wireless sensor, which was placed

outside the body. This setting, again, was not realistic. Also, similar to Schwerdt's work, the rigid substrate of the device makes it unsuitable for long-term implantation.

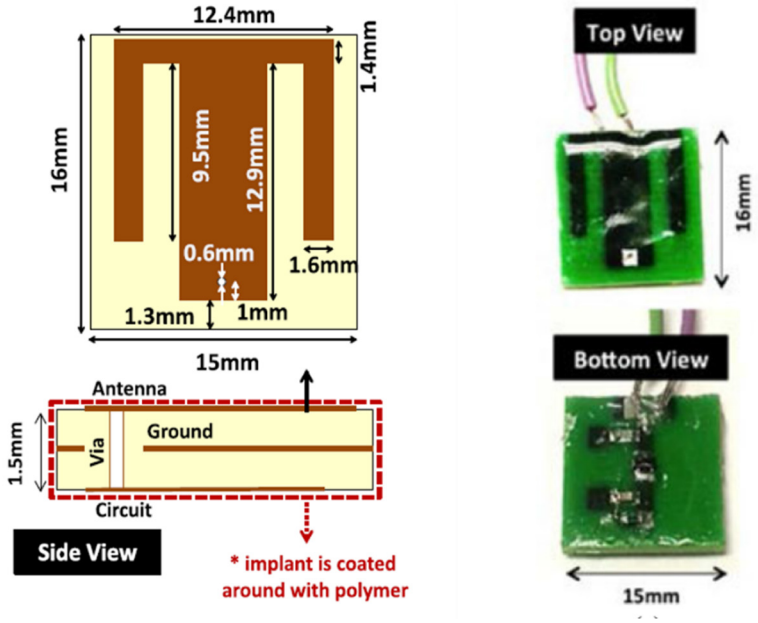

Figure 2.9. Wireless fully-passive neural recorder on a PCB (Kiourti et al. 2016). The sensor achieves a sensitivity of 50 μV, tested by wiring the sensor to the electrodes inside the scalp of a rat, which was not truly an implanted setting. Image copyright: © [2016] IEEE.

CHAPTER 3

BASIC PRINCIPLE OF RF BACKSCATTERING METHOD

In the following chapters, this thesis will present several wireless fully-passive sensors for different biosignal acquisition. Most of these sensors are based on the same operation principle – RF backscattering. Therefore, before presenting each of those wireless sensors, this chapter will first introduce the method of RF backscattering and shows how it can be used for the wireless telemetry of biosignals.

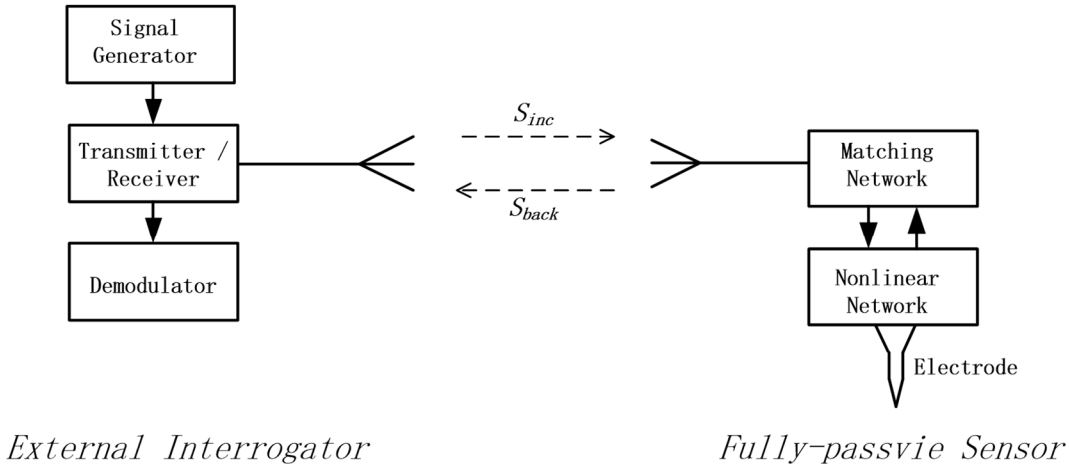

Figure 3.1. Block diagram of an RF backscattering system

The idea of applying the wireless fully-passive RF backscattering method for biosignal telemetry was first presented by Abbaspour-Tamijani et al (Abbaspour-Tamijani et al. 2008). **Figure 3.1** shows the block diagrams of an RF backscattering system, which includes two parts: the external interrogator and the fully-passive sensor. The two parts communicate through an RF electromagnetic (EM) wave. The incident RF signal (S_{inc}) is generated from the signal generator and transmitted by an external antenna. The fully-

passive sensor receives the incident signal, and through the matching network, the S_{inc} is transferred to the nonlinear network and mixed with the biosignal recorded from the electrode. The mixed signal is then radiated back, backscattered by the antenna on the sensor. The external interrogator detects the backscattered signal S_{back} and extracts the target biosignal through demodulation. The concept of an RF backscattering system is very similar to an RFID tag, except for the "fully-passive" characteristic of the sensor. Here, "fully-passive" denotes that the sensor is composed entirely of passive electronics, i.e., inductors, capacitors, diodes, etc. No active circuitry exists to amplify or digitalize the input biosignal. The wireless telemetry is accomplished by amplitude modulating (AM) the biosignal on an RF carrier (S_{inc}). Thus, the performance of the sensor is primarily determined by how the antenna, the matching network, and the nonlinear network are designed. In other words, the design and optimization of these elements can determine the sensitivity of the sensor and the maximum achievable wireless communication distance. In the following sections, both theoretical analysis and simulation models will be discussed to provide a general design methodology on how to achieve the best sensor performance.

3.1 The Mixing Characteristic of Varactor Diodes

The nonlinear network in **Figure 3.1** functions as a frequency mixer. Theoretically, any nonlinear electronic component can be used as a mixer, such as transistors, diodes, or varactors. This work chooses to use varactors because of their high impedance at low frequency. High input impedance is generally desired in biosignal measurement to

compensate for the impedance at the tissue-electrodes interface. The detail of this will be discussed in the later section of this chapter.

Varactors, or varactor diodes, are variable capacitors whose capacitance can be controlled by the voltage applied at their terminals (Helen N. Schwerdt et al. 2011):

$$C(V_r) = \frac{C_0}{\left(1 + \frac{V_r}{V_j}\right)^{\gamma}} \tag{3.1}$$

Where V_r is the voltage applied at the terminal of the varactor diode; C_0 is the zero-bias capacitance of the varactor diode; V_j is junction potential determined by the material; γ is gamma coefficient associated with doping parameters. The variance of capacitance as a function of voltage results in a non-linear relationship between the voltage and current of the varactor diode. Considering two single-tone sinusoidal signals of different frequencies are both applied on a varactor. The first signal has a higher frequency in the RF range, denoted as f_0. The second signal, which is our measurement target, has a lower frequency denoted as f_m. For simplicity, these two signals can be written as $V_0 \cos(\omega_0 t)$ and $V_m \cos(\omega_m t)$, respectively. Because of the nonlinear characteristic of the varactor, these two signals will be mixed. To explain this outcome, apply the Taylor expansion on equation (3.1) to yield:

$$C(V_r) = C_0 - \frac{C_0 \gamma V_r}{V_j} + \frac{C_0 \gamma (1+\gamma) V_r^2}{2V_j^2} - \frac{(C_0 \gamma (1+\gamma)(2+\gamma)) V_r^3}{6V_j^2} + \cdots \tag{3.2}$$

Equation (3.2) is the power series approximation of equation (1). Since V_r is the total voltage on the varactor, it can be written as:

$$V_r = V_0 \cos(\omega_0 t) + V_m \cos(\omega_m t) \tag{3.3}$$

Substituting equations (3.2) and (3.3) into the varactor diode's current-voltage relationship equation $I=d/dt[C(V_r)V_r]$:

$$\mathrm{I} = \frac{d}{dt}\left\{\left[C_0 - \frac{C_0\gamma V_r}{V_j} + \frac{C_0\gamma(1+\gamma)V_r^2}{2V_j^2} + \cdots\right] * [V_0\cos(\omega_0 t) + V_m\cos(\omega_m t)]\right\}$$

$$\begin{aligned}\mathrm{I} &= (c_{1a} + c_{3a})\cos(\omega_0 t) + (c_{1b} + c_{3b})\cos(\omega_0 t) \\ &+ c_{2a}\cos(2\omega_0 t) + c_{2b}\cos(2\omega_m t) + c_{2c}\cos(\omega_0 t \pm \omega_m t) \\ &+ c_{3a}\cos(2\omega_0 t \pm \omega_m t) + c_{3b}\cos(\omega_0 t \pm 2\omega_m t) + \cdots \end{aligned} \quad (3.4)$$

where c_{na}, c_{nb}, c_{nc}, etc, represent the magnitude of the nth-order harmonic mixing products of all possible combinations of ω_0 and ω_m ($k\omega_0 \pm j\omega_m$, where k and j are arbitrary integers and $k+j=n$). Equation (3.4) indicates when two signals of different frequencies are inputted to a varactor, harmonic mixing products of multiple frequencies will be generated, thus, the non-linear varactor diode functions as a frequency mixer. Each of the generated harmonic mixing components has a different amplitude. To better visualize this, we will use a commercially available varactor diode as an example.

The varactors used in this thesis are the hyperabrupt varactor diodes MA46H120 (M/A-COM). The zero-bias capacitance C_0 of this varactor is 1.1 pF, the built-in potential V_j is 1.3 V, and the γ value is 1. Take these parameters into equation (3.1):

$$\mathrm{C} = \frac{1.1}{\frac{V}{1.3} + 1} \quad (3.5)$$

Figure 3.2 illustrates the plotted C-V curve from (3.5). Comparing it with the C-V curve obtained from the manufacturer datasheet, the two curves are very similar.

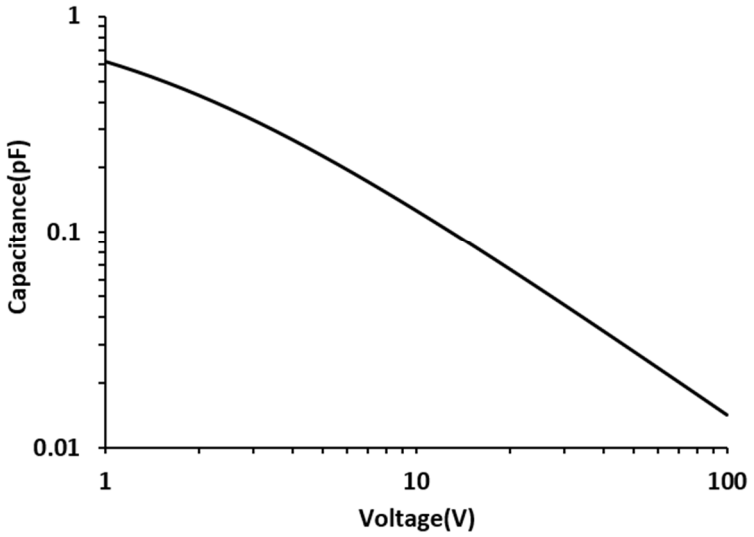

Figure 3.2. C-V Plot of the varactor diode MA46H120.

To calculate the harmonic products, equation (3.5) should be expanded into the Taylor series first. The sixth order Taylor expansion of (3.5) is as follow:

$$\mathrm{C} = 1.1 - 0.846154\mathrm{V} + 0.650888\mathrm{V}^2 - 0.500683\mathrm{V}^3 + 0.385141\mathrm{V}^4 - 0.296262\mathrm{V}^5 + 0.227894\mathrm{V}^6 + \mathrm{o}(\mathrm{V}^7) \quad (3.6)$$

For convenience, we can assume V_m = 1 mV, V_0 = 7 mV, f_0 = 2.4 GHz, and f_m = 0.05 GHz. Note that these values are chosen only as an example to better show the harmonic mixing operation of the varactor. In real measurement, these values will be largely different (For instance, f_m is the frequency of biosignal, which is typically less than 1000 Hz. But for better visualization, here we use 0.05 GHz). Using these values, equation (3.3) turns into $V_r = 0.007\cos(2.4t) + 0.001\cos(0.05t)$. Replace the V_r and C, equation (3.4) will change into a superposition of different harmonics. **Figure 3.3** shows the current amplitude at each harmonic mixing product. For example, the signal at 4.8GHz is the 2nd

order harmonic $2f_0$; the signals at 4.85 GHz and 4.75 GHz, are the 3rd order mixing product $2f_0 + f_m$ and $2f_0 - f_m$, respectively.

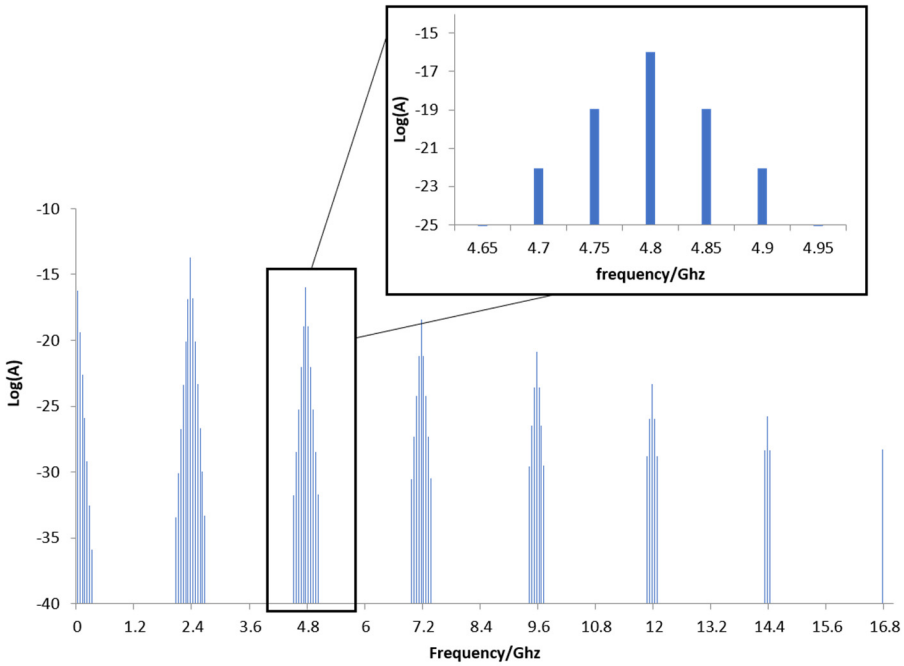

Figure 3.3 Frequency spectrum of the current generated by the varactor MA46H120. The inlet shows a zoom-up view on the 3rd other mixing products ($2f_0 \pm f_m$).

From **Figure 3.3**, we can see that the amplitude of mixing products decreases with the increase of mixing order. Theoretically, all these mixing products can be used in demodulation to extract our target measurand. In practice, we want to choose that harmonic component that can achieve the highest SNR. Among all the mixing products, the 3rd-order components ($2f_0 \pm f_m$) are the target product. Note that the 2nd order mixing product ($f_0 \pm f_m$) offers higher signal power (2.35 Ghz and 2.4 Ghz in **Figure 3.3**). However, in practice, the

noise level at the proximity of f_0 is also higher due to the large phase noise of RF signal generators. In fact, the phase noise of the carrier f_0 easily overshadows the 2nd order mixing products ($f_0 \pm f_m$). The SNR at the 2nd order products, consequently, is much lower than that of the 3rd order.

The magnitude of current of the 3rd order mixing product, c_{3a}, can be calculated using equation (3.4):

$$c_{3a} = \frac{3C_0\gamma(1+\gamma)V_0^2V_m\omega_0}{4V_j^2} \tag{3.7}$$

With the current value obtained, we can then calculate the total power of the backscattered signal. The power of the 3rd order harmonic mixing products ($2f_0 \pm f_m$), P_3, can be obtained using:

$$P_3 = \frac{c_{3a}^2 R_r}{2} \tag{3.8}$$

Where R_r is the radiation resistance of the antenna on the sensor at the frequency $2f_0 \pm f_m$. Since the backscattered signal is an AM modulation of our target biosignal, the power of P_3 needs to be maximized. From equation (3.7) and (3.8), we can see that this can be accomplished by changing the parameters of the varactor, such as increasing the value of C_0 or γ. However, practically, the power of P_3 will not be determined so simple. Equation (3.8) does not take the antenna and the circuit structure into account, which actually plays the most critical role in determining the wireless backscattered power. The value of C_0 can significantly affect the matching of the circuit and thus it cannot be a very large capacitance. The value of γ and V_j is associated with the fabrication process of the varactor, which is

usually fixed. Therefore, the only way to maximize the backscattering power P_3 is to optimize the antenna and circuit design.

3.2 Basic of Antenna

In RF backscattering, the wireless fully-passive sensor receives an incident EM wave and generated a backscattered EM wave that incorporates useful information from the target biosignal. This communication between the sensor and external interrogator is completed through the antenna link. To better understand the design procedure of the sensor, some fundamental knowledge of the antenna is needed. A good reference is the book written by Balanis (Balanis 2016).

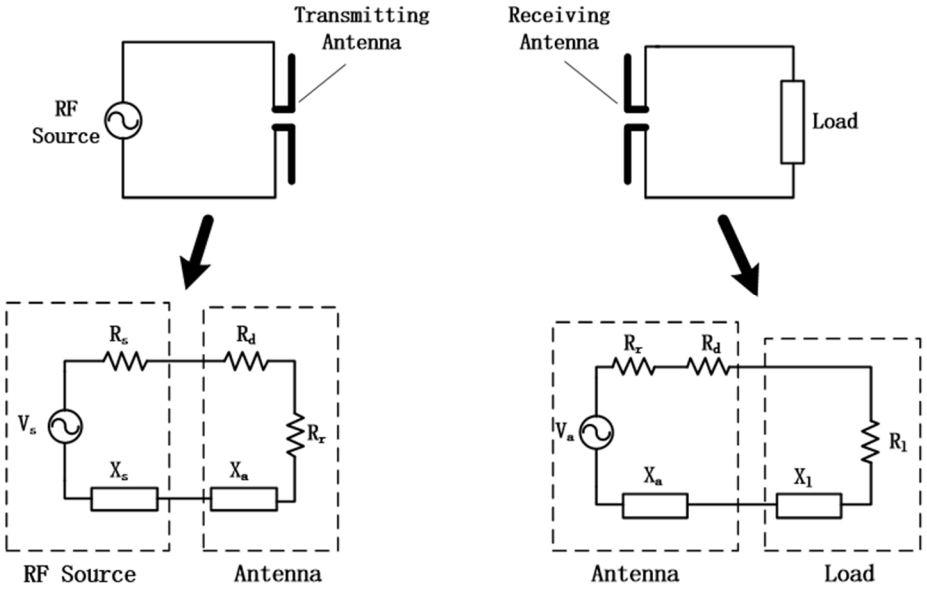

Figure 3.4. A basic model for antenna transmission. The Thevenin equivalent circuit model is used to represent transmitting and receiving antenna systems.

3.2.1 Antenna Impedance

Figure 3.4 shows a basic model representing the wireless communication between a transmitter and receiver. In the transmitting circuit, both the RF signal source and the transmitting antenna can be represented by a Thevenin equivalent circuit (Balanis 2016). Here, V_s is the voltage source in the RF generator, R_s and X_s are the resistance and reactance of the RF generator, respectively. The transmitting antenna can be represented by three components: R_d is the resistive loss, R_r is the radiation resistance, and X_a is the reactance of the antenna. The port impedance of the antenna Z_a, defined as the ratio of voltage to current, can be represented by:

$$Z_a = R_d + R_r + jX_a \tag{3.9}$$

Similarly, the output impedance of the RF generator can be represented by:

$$Z_s = R_s + jX_s \tag{3.10}$$

The power transferred from the RF source to the antenna can be expressed as:

$$P_a = \frac{1}{2} {I_s}^2 Z_a \tag{3.11}$$

The I_s is the current passing through the antenna, which is calculated by:

$$I_s = \frac{V_s}{Z_a + Z_s} = \frac{V_s}{R_d + R_r + R_s + j(X_a + X_s)} \tag{3.12}$$

From equation 3.12, the impedance of antenna and RF generator determine how much power can be transferred. The maximum power transfer occurs when the power source (RF generator) and the load (Antenna) achieves impedance conjugate matching:

$$R_s = R_d + R_r \tag{3.13}$$

$$X_s = -X_a \tag{3.14}$$

Under the impedance matching conditions, the power delivered to the antenna can be expressed as:

$$P_a = P_s = \frac{{V_s}^2}{8R_s} \tag{3.15}$$

The P_s represents the power dissipated in the RF generator as heat. Thus, when impedance matching is achieved, the power delivered to the antenna is determined only by the RF generator. For any RF generator, the maximum output power (P_s) is usually given by the manufacturer, which represents power output capability of the RF generator. In practice, commercial RF function generators usually have a pure resistive output impedance (X_s = 0), such as 50 Ohm, 75 Ohm, etc. To achieve impedance matching, the port impedance of the antenna also needs to be pure resistive (X_a = 0). When this happen, we say the antenna achieves resonance. Usually, an antenna resonates only at specific frequencies which are determined by the designer.

Under impedance matching condition, the actual power radiated by an antenna can be calculated by:

$$P_r = \frac{{V_s}^2}{8R_s}\left(\frac{R_r}{R_d + R_r}\right) = eP_a \tag{3.16}$$

Where:

$$e = \frac{R_r}{R_d + R_r} \tag{3.17}$$

The parameter e represents the radiation efficiency of the antenna. From equation (3.16), we can see that the antenna radiation resistance R_r is the parameter describing the radiation performance of an antenna. When external RF power is delivered to an antenna, a portion of the energy will be dissipated as heat through the ohmic loss (R_d). The remaining

energy will be radiated out from the antenna, which is represented by the antenna radiation resistance R_r. Therefore, when designing an antenna, under impedance matching condition, we want to maximize the radiation resistance R_r while minimizing the loss resistance R_d. In practice, this can be done through many methods, such as improving the conductivity, reducing the dielectric loss, or changing the geometry of the antenna.

Antennas used as receivers (**Figure 3.4** right) can also be represented by a Thevenin equivalent circuit. Here, the antenna itself can be replaced by an RF source with its inner impedance. No matter the antenna is used as a transmitter or a receiver, its port impedance (Z_a) remains the same. Thus, maximum power transfer to the load occurs when impedance matching between the antenna and the load is achieved:

$$R_l = R_d + R_r \tag{3.18}$$

$$X_l = -X_a \tag{3.19}$$

Where R_l and X_l are the resistance and reactance of the load. For the wireless sensor which receives the external RF energy, how well the impedance is matched determines how much energy can be transferred to the load by the sensor's antenna, and thus its optimization plays a crucial role in the design process. As can be seen from **Figure 3.1**, the load of the antenna in the wireless fully-passive sensor is a nonlinear network. To achieve proper impedance matching, a matching network is needed. It will be shown in the later section of this chapter that the design of the matching network greatly affects the power of the backscattered 3rd order mixing products.

3.2.2 Directivity and Gain of Antenna

An antenna can radiate RF power to its surrounding space. From the previous section we know that the total power radiated by an antenna is determined by the radiation resistance R_r, which can be expressed as:

$$P_r = \frac{1}{2} {I_s}^2 R_r \tag{3.20}$$

Assuming the antenna radiates the same amount of power in all directions, in other words, the antenna is an isotropic radiator. We can obtain the power density of the electromagnetic (EM) wave at a distance R from the antenna (Balanis 2016):

$$W_0 = \frac{P_r}{4\pi R^2} \tag{3.21}$$

Where W_0 is the power density of the EM wave radiated by an isotropic radiator and observed at distance R. Equation (3.21) suggests the radiated power of an isotropic antenna is uniformly distributed over a spherical surface with the antenna located at the center point. Generally, people are more interested in the radiation intensity along a given direction rather than the actual distance R. Thus, the radiation intensity of an antenna is expressed as:

$$U = R^2 W \tag{3.22}$$

For an isotropic radiator, the radiation intensity is:

$$U_0 = \frac{P_r}{4\pi} \tag{3.23}$$

If we plot the radiation intensity as a function of direction in a three-dimensional polar plot, the radiation pattern of an isotropic radiator will be a perfect sphere. However, a perfect radiator does not exist in the real world. Real antennas will always be directional,

which means they can have strong radiation in some direction while exhibiting very low radiation intensity in other directions. As an example, **Figure 3.5** shows the radiation pattern of a simple dipole antenna. As can be seen, the dipole has strong radiation intensity in the X or Y direction, but the radiation in the Z direction is almost zero. The directional characteristic of antennas is very useful in real applications. A highly directional antenna can achieve a very far transmission distance, such as the antenna on an artificial satellite.

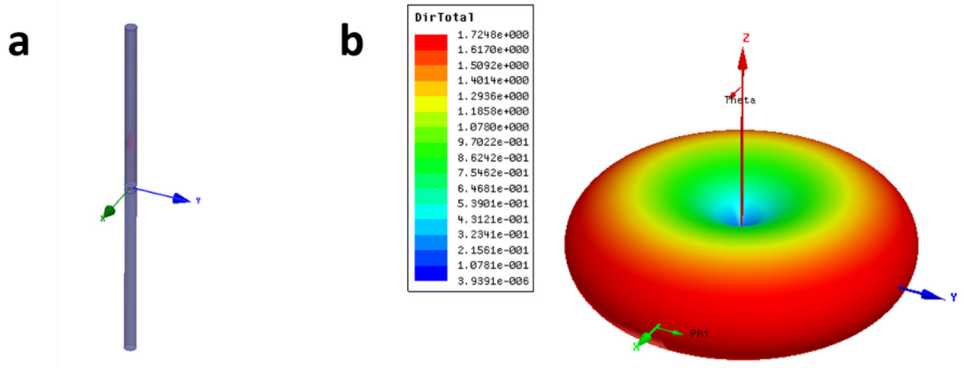

Figure 3.5 Radiation pattern of a dipole antenna.

To describe how directional an antenna is, the directivity, D, of an antenna is defined as (Balanis 2016):

$$D = \frac{U}{U_0} = \frac{4\pi U}{P_r} \tag{3.24}$$

Equation (3.24) suggests the directivity of an antenna in a given direction is equal to the ratio of the radiation intensity of the antenna in the direction to that of an isotropic radiator. When the direction is not specified, the directivity of an antenna refers to the

maximum directivity the antenna can achieve within all directions. For any antenna, the maximum directivity must be a number larger than 1 ($D_{max} > 1$).

Equation (3.15) gives the maximum deliverable power from an RF source. When impedance matching is achieved, the RF source can deliver all of this power to the antenna. However, when impedance matching is not achieved, the actual power transferred to the antenna will be much less. Imagining a portion of the power outputted from the RF source is reflected back, we can define a reflection coefficient Γ so that the reflected RF power can be represented by $\Gamma^2 P_s$. Thus, the actual power transferred to the antenna, P_a, can be expressed as:

$$P_a = (1 - \Gamma^2)P_s = (1 - \Gamma^2)\frac{{V_s}^2}{8R_s} \tag{3.25}$$

From equation (3.11) and (3.12), we have:

$$P_a = \frac{{V_s}^2 Z_a}{2(Z_a + Z_s)^2} \tag{3.26}$$

As mentioned before, RF sources usually have pure resistive output impedance, meaning $Z_s = R_s$. Therefore, we can obtain the value of Γ from equation (3.25) and (3.26):

$$\Gamma = \frac{Z_s - Z_a}{Z_s + Z_a} \tag{3.27}$$

The refection coefficient Γ is a very important parameter in RF design. It represents how well the impedance is matched between the antenna and the RF source. Under a perfect match, Γ = 0, suggesting all the power is absorbed by the antenna. In the worst case, for example, $Z_a = 0$, Γ = 1, suggesting all the power is reflected by the antenna. Thus, the lower

the Γ is, the better the impedance matching is achieved. To maximize power radiation, antenna designers generally need the Γ to be as low as possible.

Take equation (3.25) into equation (3.16):

$$P_r = eP_a = e(1 - \Gamma^2)P_s \tag{3.28}$$

Equation (3.28) represents the actual radiated power from an antenna taking the radiation efficiency and the impedance mismatching into account. In practical applications, the directivity, radiation efficiency, and impedance mismatching characteristics of an antenna can be expressed by a comprehensive figure of merit, which is called gain. There are two different definitions of gain. The first definition is the ratio of the radiation intensity of an antenna in a given direction to the radiation intensity that would be obtained if the power accepted by the antenna is radiated isotopically (Balanis 2016). This can be expressed as:

$$G = \frac{U}{(\frac{P_a}{4\pi})} = \frac{4\pi U}{P_a} \tag{3.29}$$

Where G is the gain of the antenna. Since $P_a = P_r/e$, we have:

$$G = \frac{4\pi U}{\frac{P_r}{e}} = e\frac{4\pi U}{P_r} = eD \tag{3.30}$$

Same as the definition of directivity, when no direction is specified, the gain refers to the maximum gain the antenna can achieve in all directions. From equation (3.30), this gain definition does not consider the effect of impedance mismatching. Therefore, a more practical definition of gain is expressed as (Balanis 2016):

$$G = \frac{U}{(\frac{P_s}{4\pi})} = \frac{4\pi U}{P_s} = e(1-\Gamma^2)D \tag{3.31}$$

This definition of gain includes the effect of both radiation efficiency and impedance mismatching. The gain defined by (3.31) is also referred to as absolute gain or realized gain. Since this definition can more accurately express the performance of antennas, it will be used to describe the gain from now on.

For a receiving antenna, another important parameter is the antenna effective area. The antenna effective area is defined as the ratio of the total power delivered to the load by the receiving antenna, to the power density of the incident wave. This can be expressed as:

$$A_e = \frac{P_l}{W} \tag{3.32}$$

Where A_e is the effective area of the receiving antenna, P_l is the total power delivered to the load, W is the power density of incident electromagnetic wave. The effective area of a receiving antenna is also related to its gain. This relationship can be expressed as:

$$A_e = \left(\frac{\lambda^2}{4\pi}\right) G \tag{3.33}$$

Where the λ is the wavelength of the incident electromagnetic (EM) wave.

3.3 Estimation of Backscattered Power

With some fundamental knowledge of antennas, now we can derive the power of the 3rd order harmonic mixing product backscattered from the wireless fully-passive sensor. First, assuming the external RF source is generating a single tone RF carrier signal with

the frequency f_0 and the power P_0, which is radiated out by the external antenna. Using equation (3.31), we can obtain the radiation intensity of the external antenna:

$$U_{1,f_0} = \frac{P_0 G_{1,f_0}}{4\pi} \tag{3.34}$$

Where U_{1,f_0} represents the radiation intensity of the incident RF carrier (f_0) by the external antenna (antenna 1). G_{1,f_0} represents the gain of the external antenna at the frequency f_0. Assuming the wireless fully-passive sensor is placed at a distance R from the external antenna, we can then calculate the power density of the incident EM wave at the location of the wireless sensor using equation (3.22):

$$W_{1,f_0} = \frac{P_0 G_{1,f_0}}{4\pi R^2} \tag{3.35}$$

This power will be accepted by the receiving antenna on the wireless sensor and delivered to the load (the non-linear network). The power delivered to the load can be estimated using equation (3.32) and (3.33):

$$P_{l,f_0} = W_{1,f_0} A_{2,f_0} = \frac{P_0 G_{1,f_0} G_{2,f_0} {\lambda_{f_0}}^2}{16\pi^2 R^2} \tag{3.36}$$

Where A_{2,f_0} is the effective area of the antenna on the wireless sensor at the frequency f_0. G_{2,f_0} represents the gain of the antenna on the sensor at the frequency f_0. λ_{f_0} is the wavelength of the incident EM wave. When the nonlinear network (varactors) receives the incident RF energy, it will mix the carrier signal with the biosignal to generate the 3rd order mixing product. For simplicity, we define a mixing coefficient k, which represents the ratio of the power of the generated 3rd order mixing product to the power

delivered to the varactor by the sensor's antenna. We can then write the power of the 3rd order mixing product generated from the varactor as:

$$P_{2f_0} = kP_{l,f_0} = \frac{kP_0 G_{1,f_0} G_{2,f_0} {\lambda_{f_0}}^2}{16\pi^2 R^2} \tag{3.37}$$

Where P_{2f_0} represents the power of the 3rd order mixing product. Note the actual frequency of the 3rd order mixing product is $2f_0 \pm f_m$, rather than $2f_0$. However, since f_m is very small compared to f_0, it can be neglected when designing the antenna. Thus, for simplicity, here we use $2f_0$ to represent the frequency of the backscattered signal. The actual value of the mixing coefficient *k* can be derived from equation (3.7) and (3.8), but this will make the expression too complex. Therefore, here we assume it is a known variable.

The generated 3rd order mixing product will be radiated by the antenna on the wireless sensor. The radiation intensity can be estimated using equation (3.31):

$$U_{2,2f_0} = \frac{P_{2f_0} G_{2,2f_0}}{4\pi} = \frac{kP_0 G_{1,f_0} G_{2,f_0} G_{2,2f_0} {\lambda_{f_0}}^2}{64\pi^3 R^2} \tag{3.38}$$

Where $U_{2,2f_0}$ represents the radiation intensity of the 3rd order mixing product by the wireless fully-passive sensor (antenna 2). $G_{2,2f_0}$ represents the gain of the antenna on the wireless sensor at the frequency $2f_0$. Again, using equation (3.22), we can obtain the power density of the backscattered EM wave at the location of the external interrogator:

$$W_{2,2f_0} = \frac{kP_0 G_{1,f_0} G_{2,f_0} G_{2,2f_0} {\lambda_{f_0}}^2}{64\pi^3 R^4} \tag{3.39}$$

The backscattered signal will be picked up by the external antenna and transmitted to the load for demodulation. Using equation (3.32) and (3.33), the power delivered to the load can be expressed as:

$$P_{l,2f_0} = W_{2,2f_0} A_{1,2f_0} = \frac{kP_0 G_{1,f_0} G_{1,2f_0} G_{2,f_0} G_{2,2f_0} {\lambda_{f_0}}^2 {\lambda_{2f_0}}^2}{256\pi^4 R^4} \tag{3.40}$$

Where $A_{1,2f_0}$ is the effective area of the external antenna at the frequency $2f_0$. $G_{1,2f_0}$ represents the gain of the external antenna at the frequency $2f_0$. λ_{2f_0} is the wavelength of the backscattered EM wave. Equation (3.40) can give a rough estimation of the backscattered power received at the external interrogator. In the practical design process, the values of k, G_{2,f_0}, and $G_{2,2f_0}$ are closely related to how the antenna and circuits are designed, and their values cannot be obtained very easily because of the complicated calculation involved. However, modern Computer Aid Design (CAD) software greatly simplifies the system design process. With the help of CAD software, optimization of the sensor can be achieved efficiently with direct visualization of results. Moreover, the result of CAD simulation can be much more accurate as sophisticated modeling methods, such as finite element analysis, are used to construct the complicated geometry structure of antennas. Therefore, in this thesis, the design and optimization of the sensor are accomplished with CAD software including HFSS and ADS. The detailed methods of using CAD simulation for wireless sensor design will be introduced in the next section.

It should also be noted that all the above derivations have assumed that the interaction between the external interrogator and the wireless sensor occurs in the far-field region of the antennas. In the near field, the above derivations will not be valid. The

boundary between the far-field and the near-field can generally be estimated by the equation $R = 2D^2/\lambda$, where D is the largest dimension of the antennas, and λ is the wavelength. Thus, to ensure both antennas work in the far-field region, the distance between the antennas needs to be larger than $2D^2/\lambda$. In practice, this is very easy to achieve because the sizes of the external antenna and the wireless sensor are both sufficiently small.

3.4 Simulation of the Backscattered Power

To determine the backscattered power, we will need to solve two problems: 1) the power transfer between the external antenna and the wireless sensor, and 2) the generation of the 3rd order mixing product by the varactor diodes. Calculating either of them by hand will be very difficult or inaccurate due to simplifications, luckily, CAD simulation tools can help us complete the computations easily. In this thesis, the power transmission between two antennas is obtained using a three-dimensional electromagnetic analysis tool, Ansys HFSS (High Frequency Structure Simulator). The mixing product of the varactor, on the other hand, is solved using the RF circuit simulation tool, Keysight ADS (Advanced Design Simulator).

First, a 3D model containing two antennas is constructed in HFSS to represent the wireless link between the external antenna and the sensor. **Figure 3.6a** shows an example of the 3D model constructed in HFSS. Note that the external antenna is placed above the wireless sensor at a fixed distance. The external antenna needs to operate at two frequencies: f_0 and $2f_0 \pm f_m$. This can be accomplished by using either a commercial dual-band chip antenna or a wideband spiral antenna. For the wireless sensor, the detailed design

will be given in the later chapter. Here an unoptimized sensor will be used just to demonstrate the designing procedures.

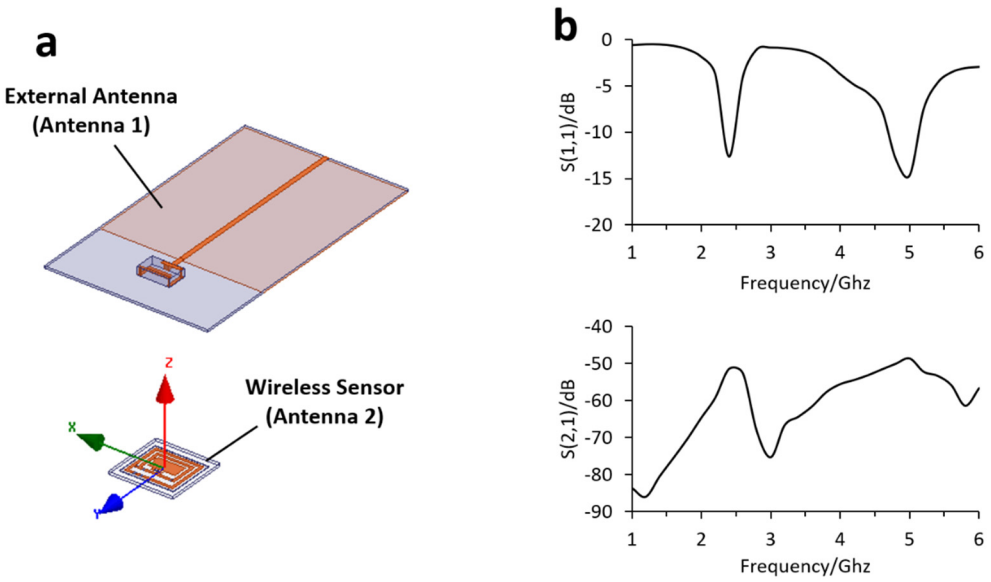

Figure 3.6 Simulation of the wireless transmission between antennas. (a) The 3D model of the wireless sensor and the external antenna constructed in HFSS. (b) The simulation result of S(1,1) and S(2,1) as a function of frequency.

The most important parameters from the HFSS simulation are the Scattering Matrix, also known as the S-parameters. For any systems/networks containing multiple input/output ports, the S-parameters can provide a complete description of the network as seen at its ports (Pozar 2009). Assuming an incident wave is input to the port n of an N-port network, V_n^+ represents the voltage incident to the port and V_n^- is the voltage reflected from the port. Then, the element in the Scattering matrix, $S_{i,j}$, is defined as (Pozar 2009):

$$S_{i,j} = \frac{V_i^-}{V_j^+}\Big|_{V_k^+=0\ for\ k\neq j} \tag{3.41}$$

The equation (3.41) means $S_{i,j}$ is calculated when all the ports have zero-incident wave except the port j. In other words, we assume all the other ports are connected to a matched load, except the port j. Thus, $S_{i,i}$ is equivalent to the reflection coefficient Γ, and $S_{i,j}$ represents the transmission coefficient from the port j to port i, when other ports are terminated with a matched load.

For the wireless backscattering method, since two antennas are involved, the system can be represented by a two ports S-parameter matrix. The S(1,1) represents the reflection coefficient of the external antenna and the S(2,1) represents the voltage transfer coefficient from the external antenna to the sensor. For a good design, we want the S(1,1) to be as low as possible while the S(2,1) to be as high as possible. **Figure 3.6b** shows the simulation result of the S(1,1) and S(2,1) as a function of frequency. As can be seen, the S(1,1) achieves the lowest value at around 2.4 GHz and 4.8 GHz, respectively, which is the result of the matching network at the external dual-band antenna. Similarly, S(2,1) achieves the highest value around the 2.4 GHz and 4.8 GHz, meaning the system performs best at these frequencies.

Besides the S-parameter matrix, another important result we can get from the HFSS simulation is the port impedance of the antenna on the wireless sensor. As described earlier, the port impedance of the antenna needs to be conjugate matched with the load of the antenna, i.e., the varactor network. For the varactor MA46H120 used in this work, its impedance is capacitive and around 60 Ohm in 2.4 GHz. Thus, the impedance of the antenna needs to be inductive and approximately 60 Ohm. Change of the varactor model

is possible, but the design of the antenna also needs to be changed accordingly to retain the impedance matching condition.

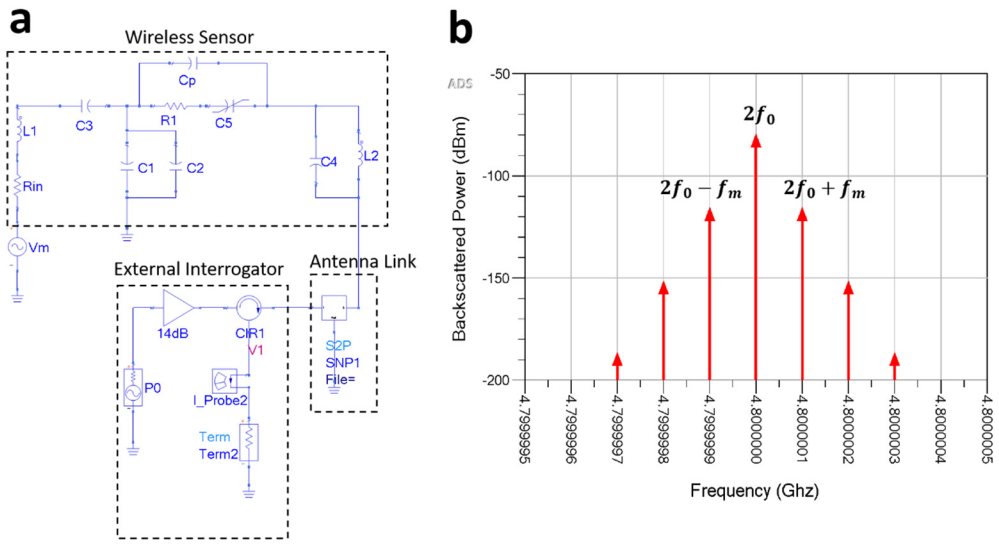

Figure 3.7 ADS circuit simulation. (a) The circuit model representing the RF backscattering system. (b) Simulated power spectrum showing the 3rd order mixing product ($2f_0 \pm f_m$) of the backscattered signal.

After the S-parameters of the antenna link is obtained we can then import them into the ADS circuit model to calculate the power of each harmonic mixing product generated by the varactor, including our interested parameter, the power of the 3rd order mixing product $2f_0 \pm f_m$. **Figure 3.7a** shows the circuit model constructed in ADS representing the RF backscattering system. For simplicity, the external interrogator is represented by an RF signal source, an amplifier, and a 50 Ohm load. The incident EM wave is generated by the RF source, amplified, and then transmitted to the wireless sensor. The signal

backscattered from the wireless sensor is received by the 50 Ohm load. A circulator is used to separate the incident and backscattered signal routes. The varactor is represented by a nonlinear capacitor whose parameters are determined from equation (3.2). The biosignal is represented by a voltage source V_{in}. R_{in} stands for the input impedance seen at the tissue electrodes interface. The capacitor C_4 and inductor L_2 form the impedance matching network. Communication between the external interrogator and the wireless sensor is described by a two ports S-parameter network, whose value is obtained through the HFSS simulation.

From the analysis in section 3.1, we know that multiple frequency components exist in the circuitry of the wireless sensor. Calculation of the backscattered 3rd order harmonic mixing product requires solving each frequency component within the circuit using Kirchhoff's Current Law (KCL) and Kirchhoff's Voltage Law (KVL), which is an extremely complicated task. However, this problem can easily be solved using the Harmonic Balance Simulator of the ADS software. **Figure 3.7b** shows the simulated power spectrum of the backscattered signal received by the external interrogator. For better illustration, only the frequency components around the $2f_0$ are shown. The 3rd order mixing product ($2f_0 \pm f_m$) are located symmetrically around the $2f_0$ component.

As mentioned before, we want to maximize the power of the backscattered 3rd order mixing product. The result shown in **Figure 3.7b** demonstrates a rather low power level of – 116 dBm, which is due to the unoptimized design of the wireless sensor. To improve the result, the antenna of the sensor will need to be redesigned to increase its gain, reduce the radiation loss, or obtain a better impedance matching. The matching element C_4 and L_2 also

greatly affect the backscattered power so their values need to be chosen carefully. In practice, the values of C_4 and L_2 are easily affected by parasitic elements, therefore, they should be determined through experiment rather than simulation. Lastly, the impedance at tissue-electrode interfaces, R_{in}, is often very large (at least 100 kOhm), and thus the wireless sensor needs to be compatible with huge input impedance. It will be shown in the later chapter that the performance of the wireless fully-passive sensor is independent of R_{in}.

CHAPTER 4

WIRELESS FULLY-PASSIVE NEURAL RECORDER

Wireless implantable neural interfaces can record high-resolution neuropotentials without constraining patient movement. Existing wireless systems often require intracranial wires to connect implanted electrodes to an external head-stage or/and deploy application-specific integrated circuits (ASIC), that are battery-powered or externally power-transferred, raising safety concerns such as infection, electronics failure, or heat-induced tissue damage. This chapter introduces a biocompatible, flexible, and implantable neural recorder capable of wireless acquisition of neuropotentials without wires, batteries, energy harvesting units, or active electronics. The recorder, fabricated on a thin polyimide substrate, features a small footprint of 9 mm x 8 mm x 0.3 mm, and is composed of passive electronic components. The absence of active electronics on the device leads to near-zero power consumption, inherently avoiding the catastrophic failure of active electronics. The wireless neural recorder is validated both *in vitro* in a tissue-simulating phantom and *in vivo* in an epileptic rat. The fully-passive wireless recorder was implanted under the rat scalp to measure neuropotentials from its contact electrodes. The implanted wireless recorder demonstrated its capability to capture low voltage neuropotentials, including somatosensory evoked potentials (SSEP) and interictal epileptiform discharges (IED). Wirelessly recorded SSEP and IED signals were directly compared to those from wired electrodes to demonstrate the efficacy of the wireless data. In addition, a CNN (Convolutional Neural Network)-based machine learning algorithm successfully achieved IED signal recognition accuracy as high as 100% and 91% in wired and wireless IED data,

respectively. These results strongly support the fully-passive wireless neural recorder's ability to measure neuropotentials as low as tens of microvolts. With further improvement, this wireless neural recording system may find wide applications in future brain-machine interface (BMI) systems.

4.1 Design and Fabrication

Figure 4.1a illustrates the overall schematic of the fully-passive wireless neural recording system, which incorporates two sub-systems 1) the wireless fully-passive sensor for acquiring neuropotentials and 2) the external interrogator for wireless data readout and display. Wireless communication between the two sub-systems is accomplished by utilizing the RF backscattering effect (H. N. Schwerdt, Miranda, and Chae 2012; Helen N. Schwerdt et al. 2011). The external interrogator generates and radiates a single-tone sine wave RF carrier (f_0). When the RF carrier reaches the planar antenna on the wireless fully-passive sensor, a modulator, i.e varactor diodes, modulates the RF carrier with neuropotentials (f_m) and the planar antenna reflects the modulated signal back, backscattering, to the external interrogator. Among many harmonic components, the 3rd order mixing product ($2f_0 \pm f_m$) presents the highest SNR which goes through a series of filtering and demodulating processes to extract the original neuropotential signals.

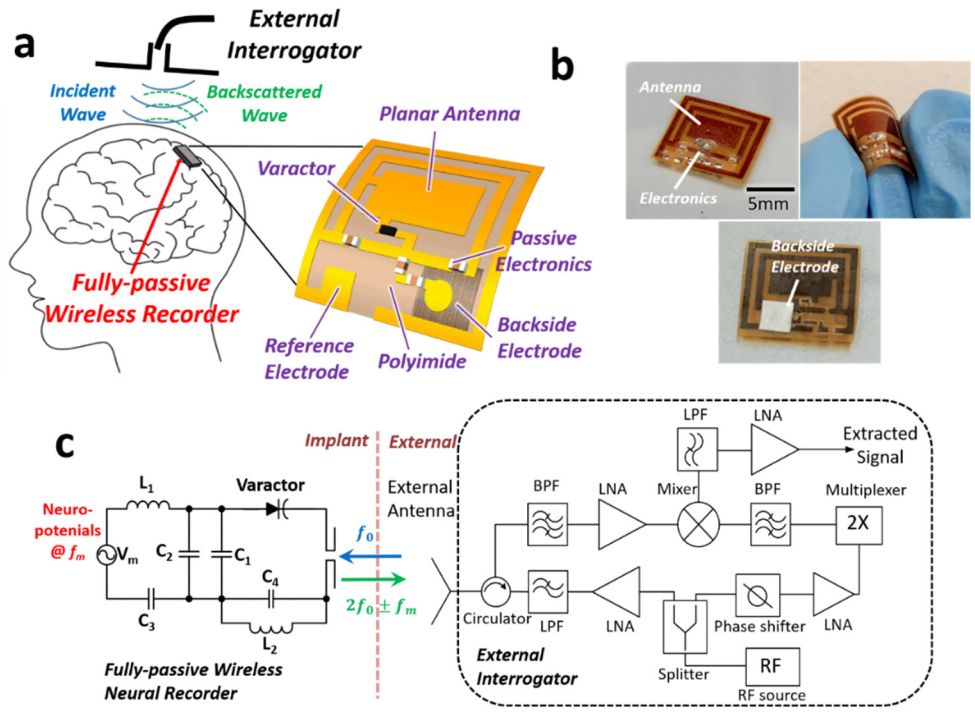

Figure 4.1. The full-passive wireless neural recorder. (a) The schematic of the fully-passive wireless neural recorder. The flexible recorder is implanted to collect neuropotentials (f_m) through its backside electrode. The external interrogator generates and shines an RF carrier (f_0) to the implanted neural recorder. The varactor diode mixes the RF carrier (f_0) with neuropotentials (f_m) to produce the 3rd order mixing product ($2f_0 \pm f_m$). This is subsequently backscattered to the external interrogator, where it undergoes a series of filtering and demodulating steps to extract the target neuropotentials. (b) Photographs of a fabricated fully-passive wireless neural recorder prototype, highlighting its size and flexibility. (c) Left: simplified equivalent circuit diagram of the recorder. Discrete passive electronic components include one varactor, two bypass capacitors C_1 and C_2, one RF choke inductor L_1, and one DC block capacitor C_3. V_m represents the target neuropotentials. Right: the

detailed structure of the external interrogator for extracting the neuropotentials from the backscattered 3rd order mixing product ($2f_0 \pm f_m$).

In this work, the varactor does not need to operate at a specific operational point precisely. The varactors produce nonlinear harmonics even at zero bias voltage. In practice, when we radiate the external RF carrier to the sensor, a small DC bias voltage of less than 100 mV will be generated due to the forward voltage applied on the varactor. This small DC bias voltage, however, has little influence on the overall performance of the sensor, therefore we can neglect it.

Figure 4.1c shows the simplified operation of the system. The external interrogator first generates and transmits a 2.32GHz RF carrier signal, denoted as f_0, to the implanted recorder. At this RF frequency, the capacitors C_1 and C_2 are equivalent to short circuits, resulting in only the RF carrier (f_0) excites the varactor diode. The inductor L_1 serves as an RF choke to isolate the neuropotentials V_m from the RF signal f_0. For low-frequency neuropotentials (<1000Hz, denoted as f_m), C_1 and C_2 are open circuits while L_1 becomes short circuits, allowing the neuropotentials (f_m) to directly reach the varactor diode. Hence, both the low-frequency neuropotentials (f_m) and the high-frequency RF carrier (f_0) appear at the varactor diode, enabling the mixing of the two signals. Many nonlinear harmonic components, including the 3rd order mixing product $2f_0 \pm f_m$, are backscattered from the planar antenna to the external interrogator to extract the target neuropotentials (f_m). The 3rd order harmonic component is chosen over others as its SNR is higher than others (Helen N. Schwerdt et al. 2011; Liu et al. 2019). The capacitor C_3 functions as a DC block to

protect the tissue from the DC component of the mixing products. The values of discrete electronic components are listed in **Table 4.1**.

Table 4.1 List of discrete electronic components on the neural recorder

Components	Model/Values
Varactor	MA46H120
C_1	33 pF
C_2	33 pF
L_1	27 nH
C_3	1 μF

The fully-passive wireless neural recorder was fabricated on a 90 μm thick polyimide substrate with the standard flexible PCB technology. The layout of the antenna and the circuitry was drawn using Altium Designer (Altium). The design file was sent out to a PCB manufacturer (Rush PCB Inc) for fabrication. The PCB consists of a 25 μm think polyimide substrate, an 18 μm thick copper layer, and a 50 μm thick polyimide overlay. The exposed metal pads use ENIG (electroless nickel immersion gold) surface finish. A 120 μm thick stainless-steel foil is cut into a 3mm x 3mm rectangular shape electrode and pasted at the backside of the recorder to form electrical contact with the tissue. Discrete electronic components, including varactor diodes, inductors, and capacitors are assembled on the sensor using conductive epoxy (12642-14, Electron Microscopy Science). The recorder is encapsulated with an 80 μm thick polyethylene film and coated with a 10 μm thick parylene-C layer.

Figure 4.1b shows photographs of the fabricated fully-passive flexible wireless neural recorder prototype, highlighting its biocompatibility, flexibility, and small footprint of 9 x 8 x 0.3 mm^3. **Figure 4.2a, b** illustrate the dimension of the antenna and circuit of the neural recorder. **Figure 4.2c** shows the stack-plot (profile) of the fabricated neural recorder prototype. Note the dimensions are not to scale.

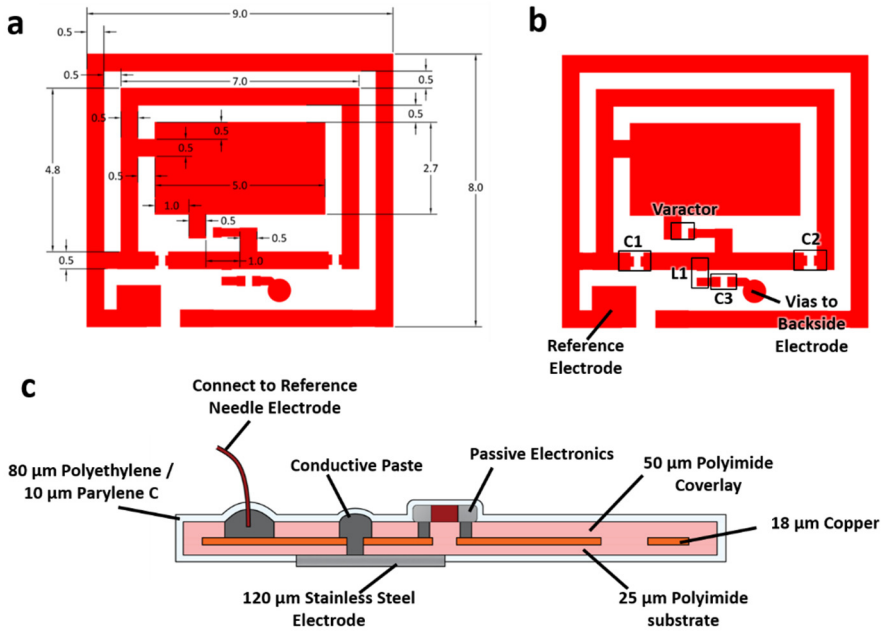

Figure 4.2. Design and fabrication of the fully-passive wireless neural recorder. (a) The layout of the planar antenna and circuitry. All critical dimensions are annotated with all values in mm. Locations of all the passive electronic components are marked in (b). (c) Layer stack plot of the recorder (dimensions are not to scale).

The fully-passive wireless recorder operates based on the RF backscattering method, no amplifier exists on the sensor capable of amplifying the signal strength before

or after the varactor's mixing. Consequently, the sensitivity of the recorder depends heavily on the design and optimization of the antenna and circuits. **Table 4.2** summarizes the characteristics of the targeted neuropotentials: SSEP and IED (Moncion et al. 2019; Ramantani et al. 2014).

Table 4.2: Characteristics of the target neuropotentials

Neuropotentials	Amplitude	Duration
IED	100 – 300 μV	50 – 500 ms
SSEP	10 – 20 μV	50 – 100 ms

To maximize the transmission of the 3rd order mixing products, we designed a unique single-layer planar antenna (**Figure 4.2a**) using the ANSYS HFSS (High Frequency Structure Simulator) and ADS (Advanced Design System, Keysight). **Figure 4.3a** shows the 3D simulation model, depicting the fully-passive wireless recorder inside a tissue-simulating phantom. The phantom model contains five different layers: scalp, skull, dura, gray matter, and white matter, using thickness, permittivity, and conductivity parameters (H. N. Schwerdt, Miranda, and Chae 2012; 2013). The neural recorder is placed between the dura and gray matter. An external dual-band antenna is placed 8 mm above the phantom to establish the wireless link. The S-parameter matrix from HFSS simulation is incorporated into the ADS circuit model in **Figure 4.3b**. In the circuit model, the voltage source V_m represents the collected neuropotentials and V_0 is the radiated RF power. The

impedance at the tissue-electrode interface, R_{in}, and major parasitic elements are included in the circuit model.

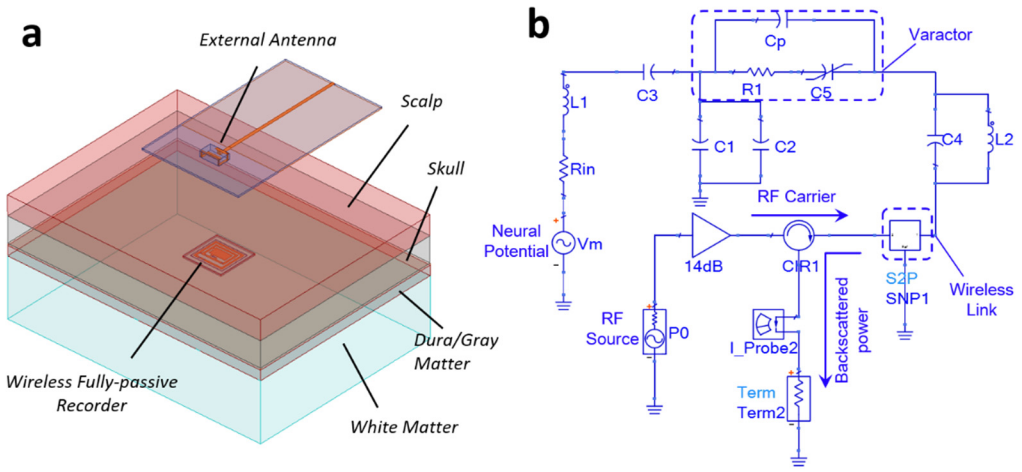

Figure 4.3. Simulation of the fully-passive wireless neural recorder. (a) 3D model of the fully-passive wireless neural recorder inside a five-layer tissue-emulating phantom. The model is constructed and simulated in HFSS. (b) Simplified ADS circuit model. The wireless link between the recorder and external antenna is modeled as a two ports S-parameters matrix, extracted from the HFSS simulation, and the backscattered power is obtained using the ADS harmonic balance simulator.

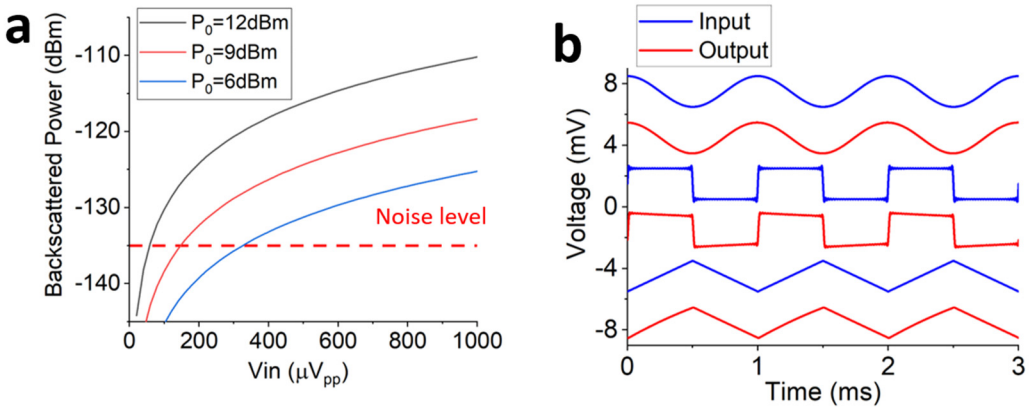

Figure 4.4. Simulation results of the fully-passive wireless neural recorder. (a) Simulated backscattered power as a function of the neuropotential amplitude at three different input RF power (P_0) levels. The red dashed line represents the anticipated noise level of -135 dBm. (b) Simulated temporal profiles of the output signals for sine, square, and triangle inputs (1 kHz, 2mV$_{pp}$). The output refers to the signal extracted at the external interrogator.

Figure 4.4a shows the simulated backscattered power at $2f_0 \pm f_m$ as a function of the neuropotential amplitude. We observe that the minimum detectable signal becomes approximately 60μV$_{pp}$ when P_0 = 12dBm. This value matches well with our experimental data, given later. It should be noted that the capacitor C_4 and inductor L_2 in **Figure 4.3b** are used for circuit impedance tuning, their value can greatly affect the backscattered power of the 3rd order mixing product. **Figure 4.5a** shows the backscattered power of the 3rd order mixing products ($2f_0 \pm f_m$) as a function of C_4 from 1 pF to 20 pF. The maximum power is achieved when C_4 = 11 pF, corresponding to the optimal impedance matching to the antenna. The resistor R_{in} represents the impedance at the tissue-electrode interface. As mentioned in the last chapter, the value of R_{in} is generally very large. Thus, it is necessary

for us to test the system performance under large R_{in}. **Figure 4.5b** shows the simulated backscattered power at $2f_0 \pm f_m$ as a function of R_{in}. The output of the system is independent of the input impedance. This result is expected, as the varactor always exhibit very large impedance, approximately open circuits, for low-frequency neuropotentials, which effectively compensates large R_{in}.

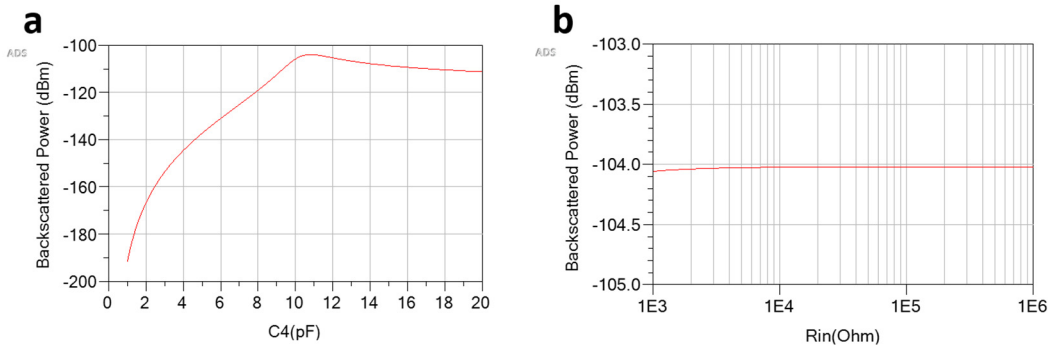

Figure 4.5. Design and optimization of the circuitry. (a) Simulated backscattered power at $2f_0 \pm f_m$ as a function of capacitor C_4. The maximum backscattered power is obtained at C_4 = 11 pF, when the circuit achieves optimized impedance to match with the planar antenna. In practice, the value of C_4 is empirically determined. (b) Simulated backscattered power at $2f_0 \pm f_m$ as a function of the input resistor R_{in}. The input resistor models the impedance at the tissue-electrode interface. The input resistor has little impact on the backscattered power as the varactor diode has a significantly larger impedance, closed to open circuits.

In the simulations above, the neuropotentials are treated as a single-tone sinusoidal signal to demonstrate the operation of the system. In practice, neuropotentials occupy multiple frequency bands. To better represent the actual neuropotentials, **Figure 4.4b**

shows the simulated output waveforms of the external interrogator for different input signal shapes, including sine, square, and triangle. As depicted, the output closely follows the input, regardless of the signal waveform, proving the efficacy of the external interrogator. The square and triangle waveforms are approximated in the frequency domain using 50 harmonics, and the output waveforms are obtained via the harmonic balance simulator of ADS. The detailed circuit model for simulation of the external interrogator is shown in (**Figure 4.6**).

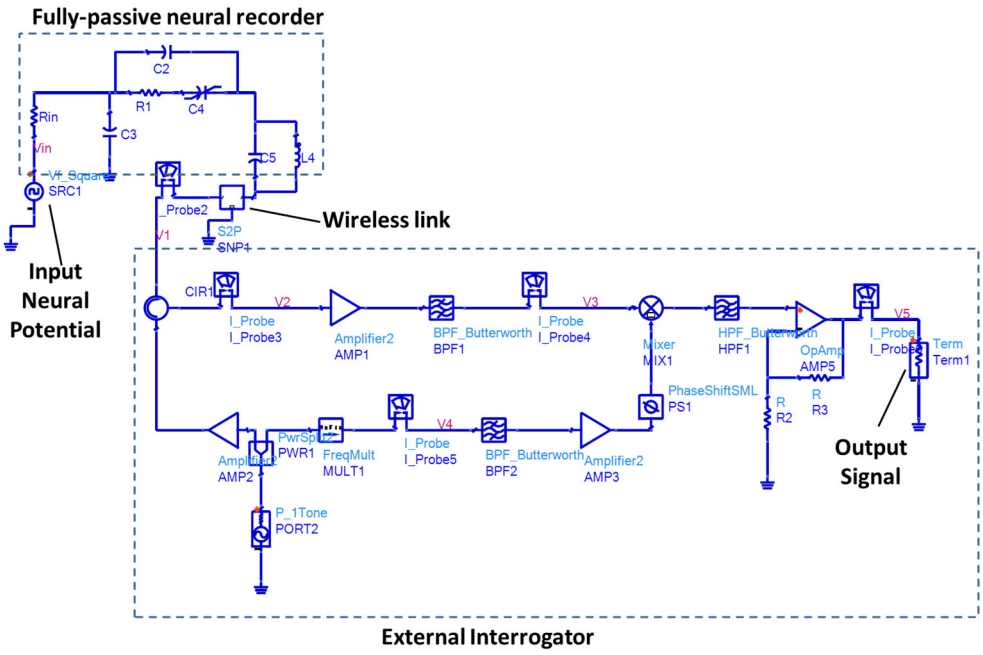

Figure 4.6. Circuit model for the simulation of the external interrogator. The emulated neural potential, including sine, square, and triangle wave, is approximated in the frequency domain using 50 harmonics. The output signal is calculated using the ADS harmonic balance simulator. The temporal waveform of the output signal is obtained with inverse FFT.

4.2 The External Interrogator

The external interrogator serves two functions: 1) transmitting a 2.33 GHz (f_0) RF carrier to the wireless fully-passive sensor and 2) receiving and demodulating the backscattered 4.66 GHz ($2f_0 \pm f_m$) EM wave to extract the original biopotentials (f_m). The RF source (RF function generator E4432B, Agilent) produces a 2.33 GHz (f_0) RF carrier with a tunable power amplitude, which is equally divided into two routes through a power splitter. One route doubles the frequency to be 4.66 GHz via a frequency multiplexer, for local oscillator (*LO*) of down-converter, demodulator. The second route amplifies and filters the RF carrier and passes the carrier to a dual-band (2.4 GHz/5 GHz) ceramic chip antenna (A10194, Antenova). The total radiated power from the antenna complies with the FCC regulations, by maximum at 30 dBm (1W) (Obeid et al. 2008). Concurrently, the dual-band antenna picks up the 4.66 GHz ($2f_0 \pm f_m$) backscattered harmonic products from the sensor. The circulator isolates the backscattered harmonic products from the RF carrier. A direct-conversion synchronous receiver extracts the biopotentials from the backscattered harmonic products (Abidi 1995), where the converter mixes 4.66 GHz *LO* with the processed backscattered harmonic products to down-convert the output to be f_m. The phase shifter provides phase tunability at the external interrogator between $2f_0 \pm f_m$ and *LO* ($2f_0$). Finally, the demodulated biopotentials (f_m) go through low-pass filtering and a 20 dB amplifier (SR560, Stanford Research System) to be visualized. The external interrogator is powered by 120V AC power.

4.3 Material and Method

4.3.1 Animal Preparation

All *in vivo* experimental procedures were approved by and carried out in compliance with the Institutional Animal Care and Use Committee (IACUC) at Florida International University (Approval No. 17-042). Wistar rats with weight > 460g were housed in standard cages and kept on a 12h-12h light-dark cycle. They were allowed continuous free access to food and water. Upon arrival from Charles River Laboratories (Wilmington, MA) they acclimated for one week before initiating any of the recordings. To prepare for the experiments, the rats were anesthetized with isoflurane (5% for induction, 1.5-2.5% during surgical procedures, 1 L/min O_2, 14.7 PSI). Rats were fixed in a stereotaxic device (Narishige, Japan) to implant the device and during the recording. Prior to starting neural recordings, the rats were sedated with a mixture of dexmedetomidine hydrochloride (Dexdomitor, 0.25 mg/kg, i.p.) and kept at low dose isoflurane (0.5%, 1 L/min O_2, 14.7 PSI). Body temperature was monitored throughout the experiment and maintained at approximately 36°C using a heating pad. The respiration rate was maintained between 50-60 breaths per minute while under isoflurane sedation.

4.3.2 *In vivo* Neuropotential Acquisition

Wireless Recorder Implantation

The schematics of experiment configuration for *in-vivo* SSEP and IED recordings are shown in **Figure 4.7** and **Figure 4.8**, respectively. The wired and wirelessly recordings were performed in sequential for SSEP recording (**Figure 4.7**) whereas they were

conducted concurrently for IED recording (**Figure 4.8**). Details of the two protocols are provided in the discussion section. In both cases, an incision of approximately 20 mm x 20 mm (dashed line in **Figure 4.7** and **Figure 4.8**) was made. The wireless recorder was placed on the skull and conductive paste was used to fix the recording electrode over the left S1HL (primary somatosensory cortex, hind limb region) area of the brain (Paxinos and Watson 2006). The rationale for selecting this region will be detailed in the next section. The entire wireless recorder was fixed to the skull with dental cement. Following this, the skin was placed over the implant and the incision was closed with biocompatible glue. The wired system used a stainless-steel needle as the recording electrode. In SSEP recording, the needle electrode was inserted subcutaneously proximal to the wireless recording electrode (not shown in **Figure 4.7**). In IED recording, the needle electrode was inserted subcutaneously near the wireless recording electrode (the distance between them was less than 2 mm, **Figure 4.8**). The reference electrodes of the recorder and the wired system were inserted subcutaneously over the contralateral (opposite) hemisphere of the rat. A robotic arm was also used to hold the external antenna in place, approximately 5 mm over the skin to establish wireless communication with the implanted recorder. An electrocardiogram (ECG) recording was used to calibrate the entire system as ECG generates significantly larger amplitude signals than target neuropotentials (Figure **4.11**).

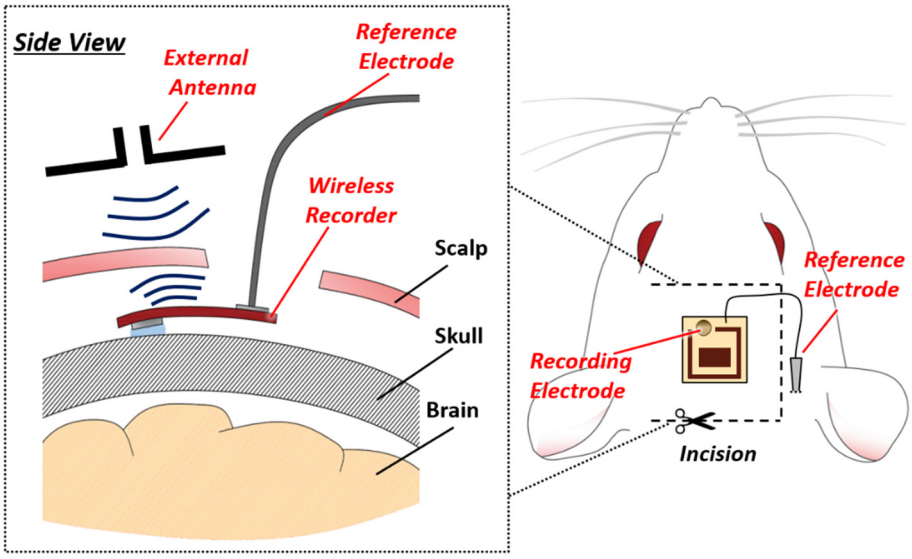

Figure 4.7. Schematic of the experimental setup for *in vivo* SSEP recording. The fully-passive wireless recorder was implanted subcutaneously to form the recording electrode on the rat skull. A stainless-steel reference electrode was inserted subcutaneously over the contralateral hemisphere of the rat. The wired SSEP recording electrode (not shown in the plot) was placed at the very proximity of the location where the wireless recording was performed for side-by-side comparison. The Black dashed line represents the incision made on the rat scalp.

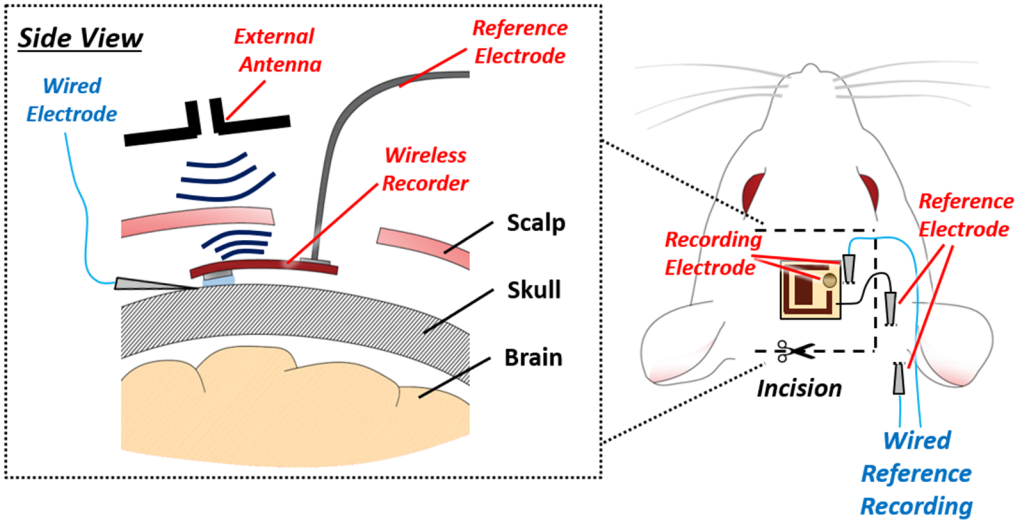

Figure 4.8. Schematic of the experimental setup for *in vivo* IED recording. A wired recording electrode, connecting to AD Instrument Bio Amp, was proximal to the wireless recorder <2 mm for synchronized wired IED recording. The reference electrodes for the wired and wireless recording systems were inserted subcutaneously over the contralateral (right) hemisphere of the rat.

SSEP Signal Recording

An established protocol was used to induce neural activation in the S1HL region of the brain (Moncion et al. 2019). Specifically, two needle stimulation electrodes were inserted subcutaneously in the rat's right hind paw to deliver electrical pulses (3 Hz, 2.5 mA, 0.5 ms duration, AM System Model 2100) and induce repetitive neural activation in the S1HL (Camp, Verhoye, and der Linden 2006; Valdés-Hernández et al. 2019). Given the small area of S1HL, it is difficult to perform simultaneous wired and wireless recordings of SSEP, and for this reason, the recordings were performed sequentially (Moncion et al. 2019). Three different RF power levels of 11, 9, and 7 dBm were used.

Each of these recordings, along with the wired recording, had a duration of approximately 10 minutes and was digitized at a 2 kHz sampling rate.

IED Signal Recording

The pilocarpine model was used to induce temporal lobe epilepsy (TLE) in rats of approximately 4 weeks of age, using a procedure similar to that carried out previously in (Song et al. 2015; Deshmukh et al. 2018). Upon reaching a state of spontaneously recurring seizures (SRSs), one of the subject rats was used for the *in vivo* experiments. To explore the effect of different RF power levels on the wireless recorder, we swept the RF power from 12 dBm to 6 dBm at a 2 dBm step. At each power level, wired and wireless recordings were continuously performed for 10 minutes with a 2 kHz sampling rate.

4.3.3 Neuropotential Signal Processing

SSEP Signal Processing

We followed the previous method of SSEP signal processing (Moncion et al. 2019). The wired and wireless signals were first band-pass filtered from 4-80 Hz, and then notch filtered between 35-45 Hz. The filtered signals were then segmented from -50ms to 250ms referenced to the onset of the recorded stimulation pulse. The SSEP was then obtained by averaging the neuropotential segments using MATLAB-based EEGLab software.

IED Signal Processing

The raw data were first band-pass filtered across 1-125 Hz to remove unwanted noise. The wireless data were further filtered to remove breathing artifacts. The IEDs in the wired data were identified and labeled, and those in the wireless data were synchronized

with the labeled IEDs. For each labeled IED, we marked the time of the negative peak as 0 ms and sliced the data into 600 ms segments (from 300 ms pre-peak to 300 ms post-peak).

4.3.4 IED Recognition via Machine Learning Algorithm

A machine learning algorithm was adopted to further evaluate the performance of the fully-passive wireless recorder. Studies have shown that the signal quality of the dataset has a significant impact on accuracy (Dodge and Karam 2016; Karahan et al. 2016). Hence, a supervised machine learning algorithm was used to analyze the IED signal identification accuracy in wired and wireless data as a function of RF power from 6 dBm to 12 dBm.

Training Dataset Preparation

The training dataset comprised sliced segments of labeled IEDs and noise. Each segment contained 400 points and the labeled IED segments were sliced from -85 ms to 115 ms referenced to the negative peak of the IED spike. The segments were then shifted with a gap of 10 points 10 times to generate 10 training slices. The total training dataset included 1540 wired IED slices, 468 wired noise slices, 110 wireless IED slices at 12dBm, and 468 wireless noise slices. All slices were labeled with 0 – noise and 1 – signal.

Model Configuration and Training

We adopted a simple yet robust machine learning model, where the 1st to 2nd and 3rd to 5th layers were convolutional neural networks and fully connected dense layers, respectively. The model was constructed and trained by Keras with TensorFlow backend. The training epochs were 100.

Recognition Process

A recognition scanning window, containing 400 data points, was created and scanned along each testing dataset at an interval of 20 data points. Notably, the data inside the window were fed to the trained model to obtain the recognition estimate (0 or 1). At every step of the scanning, the recognition values were added together and stored in a recognition array. After scanning, IEDs were identified from the recognition array to extract several parameters, such as signal energy, recognition value, and signal length to determine IEDs.

4.4. Experiment Results

4.4.1 Verification of the Fully-passive Wireless Recorder in Tissue-emulating Phantom

The fully-passive wireless neural recorder was first tested in a multi-layer tissue-simulating phantom (**Figure 4.9a**), representing skin, bone, dura, gray matter, and white matter, following our previous recipes (H. N. Schwerdt, Miranda, and Chae 2013; Ito et al. 2001) (see **Table 4.3**). The wireless recorder was placed between the dura and gray matter. **Figure 4.9b** illustrates the experimental setup. An arbitrary function generator (Agilent 33250A) supplied the emulated neuropotentials ($20\mu V_{pp}$-$2mV_{pp}$, 100Hz-1kHz) to the wireless neural recorder. A resistor (10 kΩ -1000 kΩ) was connected in series with the recorder to account for the input impedance at the electrode-tissue interface.

Table 4.3. Recipes for the five-layers tissue-emulating phantom

	Skin	Dura	Gray Matter	White Matter	Bone
DI Water	50 g	50 g	50 g	50 g	-
Agar	3 g	3 g	3 g	4.7 g	4 g
Sodium Chloride	0.075 g	0.1 g	0.075 g	0.067 g	-
Boric Acid	0.9 g	0.9 g	0.9 g	0.87 g	-
TX-151	2.5 g	2.5 g	2.5 g	3.3 g	2.4 g
Polyethylene Powder	20 g	15 g	10 g	25 g	26 g
Silicon Emulsion	-	-	-	-	50 g
Glycerol	-	-	-	-	40 g

The power of the 3rd order mixing product ($2f_0 \pm f_m$) at the external antenna was measured via a spectrum analyzer (Agilent 8563E). The external antenna was placed at three different heights (4 mm, 8 mm, and 13 mm) above the skin phantom. The RF power generated by the RF function generator was set at 12 dBm before amplification (26 dBm after amplified). We observe that the largest discrepancy between simulations and measurements is approximately 3 dB (**Figure 4.10a**), likely due to fabrication errors and parasitics in the circuits. The measurement confirms the wireless neural recorder's ability to receive the RF carrier, modulate it with emulated neuropotentials and backscatter the mixing product to the external interrogator.

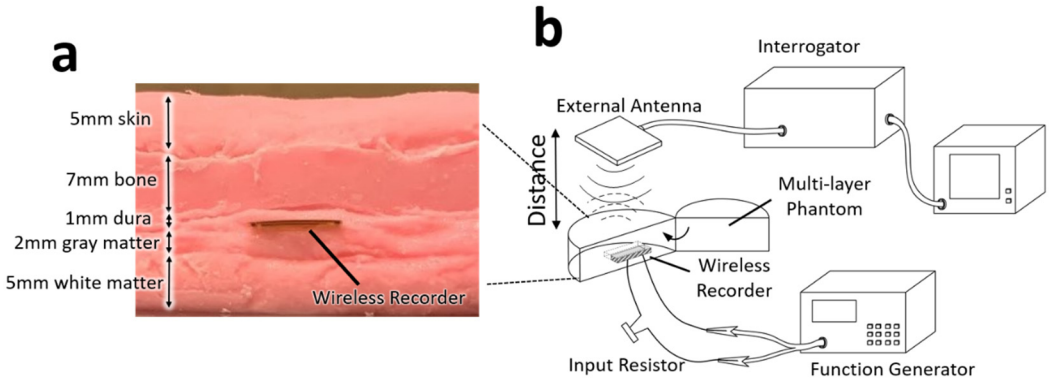

Figure 4.9. Testing setup of the fully-passive wireless neural recorder inside the tissue-emulating phantom. (a) Cross-section view of the fully-passive wireless recorder placed inside the multilayer tissue-emulating phantom, representing the skin, bone, dura, gray matter, and white matter, respectively. The wireless implant was placed between the dura and gray matter. (b) Schematic of the experimental setup. The function generator inputted emulated neuropotentials into the wireless neural recorder with a resistor representing the impedance at the tissue-electrode interface.

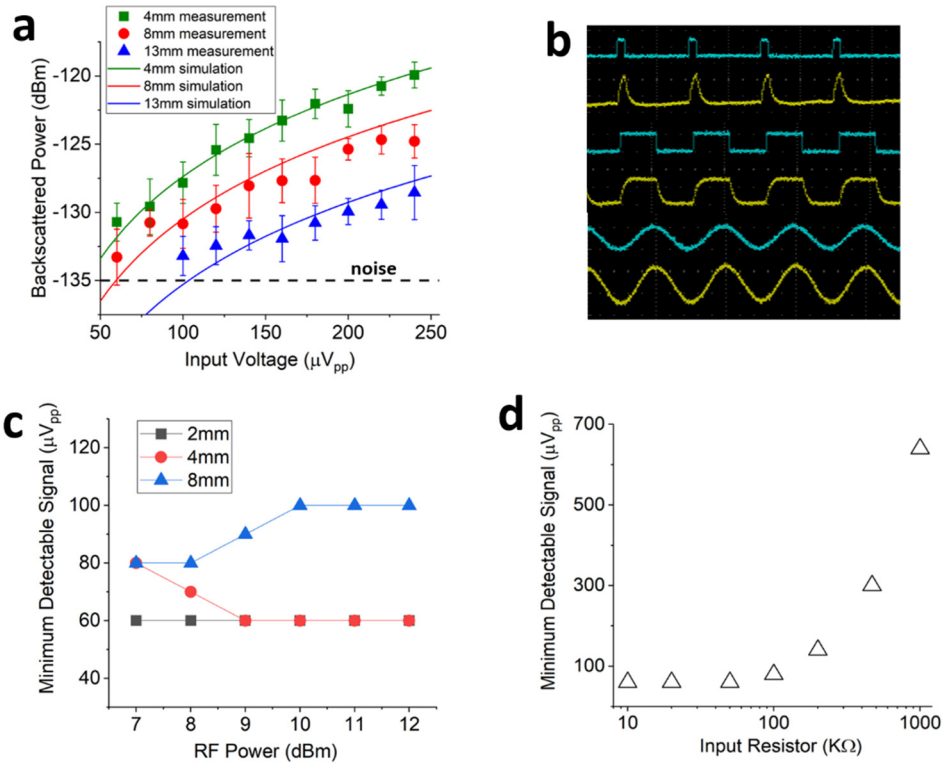

Figure 4.10. Characterization of the fully-passive wireless neural recorder inside the tissue-emulating phantom. (a) Measured and simulated power of the backscattered 3rd order mixing product ($2f_0 \pm f_m$) as a function of the input signal amplitude, at 4 mm, 8 mm, and 13 mm distances. The black dashed line represents the averaged noise level (-135 dBm). (b) Transient waveforms of the input and output signals. Blue: emulated neuropotentials (1 kHz, 2 mV_{pp}). Yellow: output signal extracted by the external interrogator. (c) The measured minimum detectable signal of the wireless recorder as a function of input RF power. The input emulated potential was a 1 kHz square wave. (d) Measured minimum detectable signal as a function of the input impedance. The minimum detectable signal remains less than 100 μV_{pp} when input impedance is less than 100 kΩ while it significantly increases as the impedance increases up to 1 MΩ.

Figure 4.10b compares temporal waveforms of the emulated neuropotential inputs and the outputs from the external interrogator, including pulse, square, and sine waves of 2 mV_{pp} at 1000 Hz. In all cases, the extracted output signals have a close resemblance to the input signals, demonstrating the effective operation of the wireless recorder for any arbitrary signal shape. Distortion of the output signals at sharp edges is due to low-pass filtering. **Figure 4.10c** shows the detection limit of the wireless reorder when the external antenna is placed at 2, 4, and 8 mm from the skin, respectively. The minimum detectable signal denotes the minimum input peak-to-peak amplitude to produce 2 dB SNR at the output. The minimum detectable signal improves as the RF power increases, as shown from the 2 mm and 4 mm data. The minimum detectable signal, on the other hand, actually suffers from the increased RF power, as shown in the 8 mm data. This is because higher RF power also results in a rise in the noise floor, leading to an unchanged or even decreased SNR. We recorded the minimum detectable signal as a function of the input resistance (**Figure 4.10d**). Due to the existence of noise, the minimum detectable signal of the wireless recorder increases from 60 μV_{pp} to 640 μV_{pp} as the input resistance increases from 10 kΩ to 1 MΩ. We suspect the noise mainly comes from the leakage current of the function generator and the environmental electromagnetic interference.

4.4.2 *In vivo* Recording

The implanted recorder was first calibrated by ECG by concurrent recordings of *in vivo* wired/wireless ECG signals (**Figure 4.11**). The close up on the ECG waveforms reveals that the wireless ECG overlaps well with the wired ECG, exhibiting negligible

delay, strongly supporting the fully-passive wireless recorder is capable of capturing *in vivo* biopotentials under a fully-implanted setting. The measured ECG also helps the alignment between the implanted wireless recorder and the external antenna.

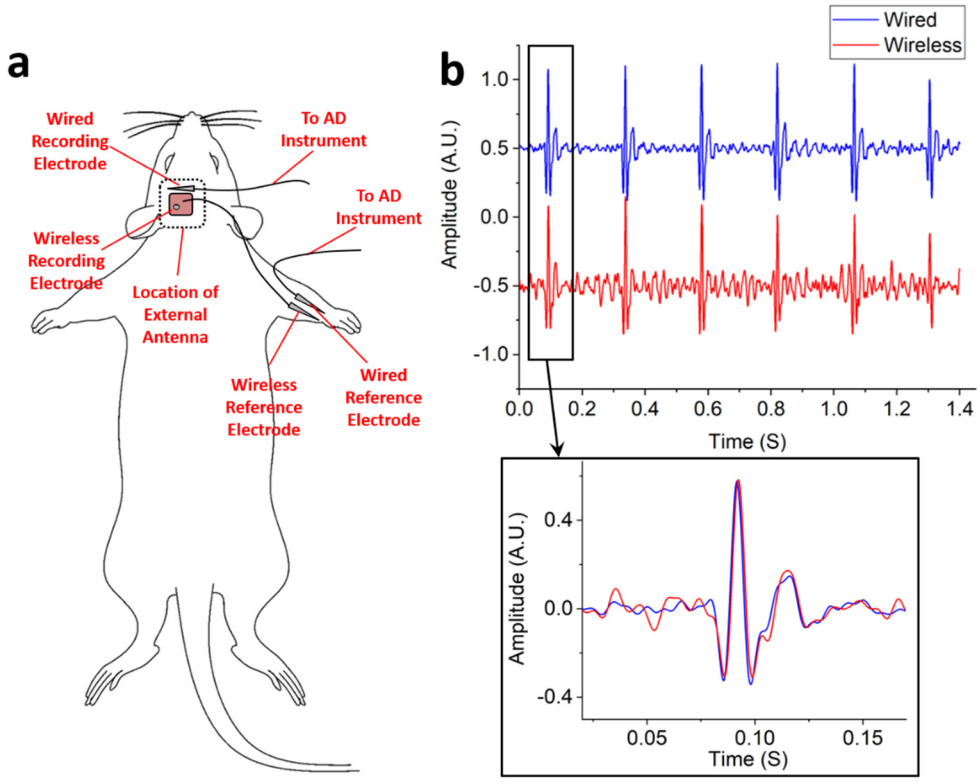

Figure 4.11. Calibration of the fully-passive wireless neural reorder using *in vivo* ECG. (a) Schematic of the experimental setup for *in vivo* ECG recordings. The fully-passive wireless sensor was implanted subcutaneously to enable electrical contact of the recording electrode with the rat skull. A wired electrode, connecting to AD Instrument Bio Amp, was placed right next to the wireless recorder for synchronized wired neural signal recording. The reference electrodes of both wired and wireless systems were carefully inserted subcutaneously in the contralateral (opposite side) right forelimb of the rat. The black dash

line shows the placement location of the external antenna. (b) *In vivo* ECG measured by wired and wireless systems. The ECG signal was used to calibrate the antenna alignment of the wireless system.

Wireless telemetry using RF backscattering requires precise alignment of the external antenna with the implanted neural recorder. For calibration of the antenna position, an electrocardiogram (ECG) recording was used. This was done because ECG generates larger amplitude signals (on the order of millivolts). After placing the implant as described in section 4.3.2, the reference electrode of each system was carefully inserted subcutaneously in the contralateral (right) forelimb of the rat. The AD Instruments Power Lab 8/35 and corresponding LabChart 7 software was used to record and digitize both signals at a 2 kHz sampling rate. The robotic arm discussed in section 4.3.2 was also used to gradually adjust the placement (both in x-y and z direction) of the external antenna until the ECG waveform (**Figure 4.11**) was distinguishable in the wireless recording and synchronized with that in the wired recording. Once this calibration was complete both reference electrodes (for the wireless and wired system) were carefully inserted subcutaneously in the contralateral (right) hemisphere of the rat brain. This was done to record the neuropotentials of interest. In the following discussion, the position of the external antenna was not changed.

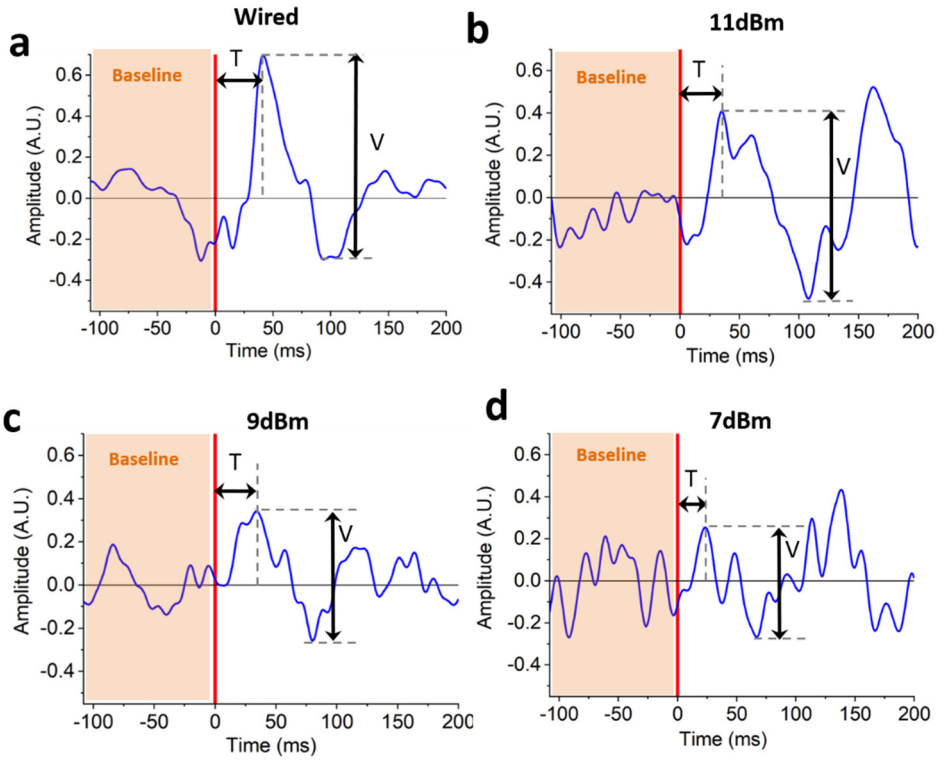

Figure 4.12. Fully-passive wireless SSEP recordings. (a) Normalized *in vivo* SSEP extracted from the wired recorder. (b-d) Normalized *in vivo* SSEP extracted from the fully-passive wireless recorder at the input RF power of 11 dBm (b), 9 dBm (c), and 7 dBm (d), respectively. The red lines at t=0 ms mark the location of the stimulation event (3 mA at the rat's right hind limb). V and T denote peak to peak amplitude of the evoked potentials and latency time from the positive peak to stimuli, respectively, as summarized in Table 4.4.

In vivo SSEP Acquisition

SSEP signals extracted from wired and wireless recordings are shown in **Figure 4.12**. The wired recorded SSEP signal (**Figure 4.12a**) depicts a distinct positive peak which

is followed by a negative peak with slightly smaller amplitude, agreeing well with previously published works(Moncion et al. 2019). Similar positive and negative peaks were also observed in the wireless SSEP (**Figure 4.12b-d**). For better analysis, two features, namely, the peak to peak amplitude (V) and the latency from stimulus trigger (T), were extracted and compared in **Table 4.4**.

Table 4.4. Wired and wireless *in vivo* SSEP recording summary

Recording	Total Number of Trials	Latency (T, ms)	Amplitude (V, A.U.)
Wired	2799	41	1
Wireless @11dBm	2999	35	0.89
Wireless @9dBm	2930	34	0.6
Wireless @7dBm	2908	24	0.55

The wireless SSEP amplitude shows an explicit drop as the RF power decreases, which agrees well with our simulation (**Figure 4.4**) as well as the phantom experiment (**Figure 4.10**). The wireless SSEP also marks consistent latency at 11 dBm and 9 dBm, marking around 35 ms in both cases. At 7 dBm, the latency starts to show deviation, dropping from 35 ms to 24 ms. From observing the temporal waveform, it is clear that the wireless SSEP at 7 dBm suffers from low SNR, which results in the positive and negative peaks becoming almost indistinguishable from the noise. For the wired SSEP, the latency is 41 ms, showing a 6 ms difference with that of the wireless SSEP (35 ms). Such discrepancy may come from our experiment procedures. Notably, due to the small area of

S1HL, we were not able to perform wired and wireless recordings simultaneously. Instead, we first conducted wired recordings, followed by wireless recordings. This may result in the wired and wireless electrodes placed not exactly at the same places, leading to the difference in recorded SSEP.

It should also be noted that SSEP typically has a very small amplitude of less than 20 μV_{pp}, beyond the minimum detectable signal of the wireless recorder (60 μV_{pp}). We were able to obtain SSEP by averaging thousands of stimulation trials (**Table 4.4**). Through averaging, the noise is canceled out and characteristic SSEP components are strengthened. The averaged wireless SSEP shows slightly larger fluctuation than the wired counterpart, the amplitude and latency demonstrate strong coherence with wired data, which strongly validates our results.

In vivo IED Acquisition

Figure 4.13a,b show the normalized temporal waveforms of the IED signal recorded by the wired system (AD Instrument Bio Amp) and the wireless recorder at various RF powers. The IED signal contains a rapid sharp negative component that last approximately 70 ms, and is followed by a positive slow wave of 100 ms duration. This type of IED can be classified as interictal spikes, which are typical of cryptogenic and benign forms of epilepsy(Based 2012). As shown in **Figure 4.13a**, the wired IED signals overlap well with each other, independent of the RF power, indicating that the wired IED data remains unchanged when the RF power is varied. In contrast, the amplitude and signal quality of the wireless IED show strong dependence upon the RF power. At 12 dBm, the wireless IED shows the closest resemblance to its wired counterpart. With the RF power

decreasing, the amplitude of wireless IED notably drops, until it is completely indistinguishable at 6 dBm. The dependency of wireless signal quality upon RF power agrees well with our simulations and *in vitro* validation results.

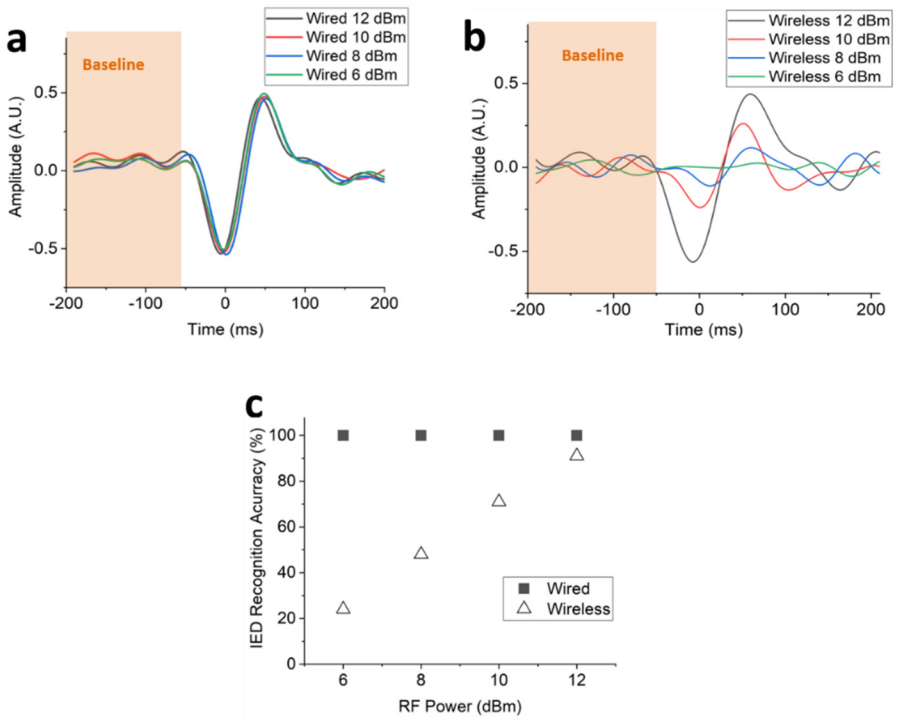

Figure 4.13. Fully-passive wireless IED recording. (a,b) Normalized temporal waveforms of a single IED activity recorded by the wired (a) and wireless system (b) as a function of RF power. The amplitude of the wireless IEDs increases with the RF power while that of the wired counterpart remains almost unchanged. (c) IED recognition accuracy using a machine learning algorithm. Labeled IED segments from wired and wireless data (12 dBm) were used to train the machine learning model. The accuracy marks 100% on the wired data whereas it dramatically improves on the wireless data as RF power increases, agreeing

well with the backscattering operation. Detailed IED recognition results are provided in Table 4.5.

Table 4.5. Comparison of labeled IED and machine learning recognized IED

RF power	Recording	Number of IED		Recording Time	Rate of IED	
		Labeled	Recognized		Labeled	Recognized
12 dBm	Wired	11	92	5 mins	0.04/s	0.31/s
	Wireless		113			0.38/s
10 dBm	Wired	17	150	10 mins	0.03/s	0.25/s
	Wireless		228			0.38/s
8 dBm	Wired	31	176	10 mins	0.05/s	0.30/s
	Wireless		147			0.25/s
6 dBm	Wired	42	180	10 mins	0.07/s	0.3/s
	Wireless		89			0.15/s

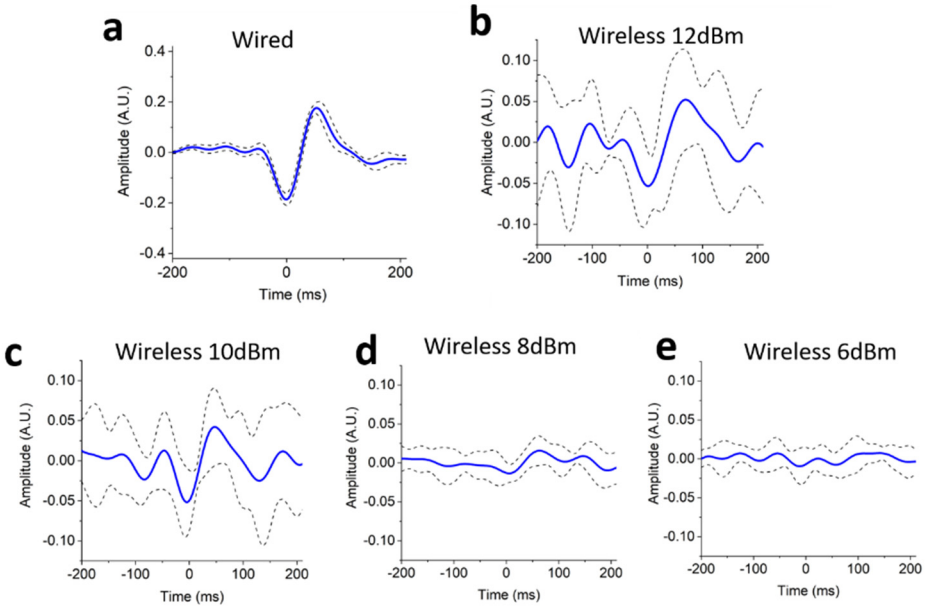

Figure 4.14. Mean and standard deviation of recorded IED. (a) Wired IED recorded by AD Instrument Bio Amp. (b-e) wireless IED recorded by fully-passive neural recorder. Blue straight line represents the mean of 7 independent IED signals, while black dashed line represents mean $\pm$ standard deviation.

The mean and standard deviation of 7 independent IED signals recorded from the wired and wireless recorders are shown in **Figure 4.14**. As expected, the wired recorder (AD Instrument Bio Amp) provides high SNR. The wireless IED at 12 dBm marks an averaged peak to peak amplitude of 0.11 and an averaged standard deviation of 0.053, yielding an SNR of approximately -1.34 dB, suggesting that the IED signal is overshadowed by the noise. In comparison, the wired IED has an averaged peak to peak amplitude of 0.362 and an averaged standard deviation of 0.018, which yields an SNR as high as 8.53 dB. The signal collected by the wired electrode, recorded by our AD amplifier,

marks high SNR, thus the IED recognition may be a simple classification task of noise vs signal; however, the wirelessly recorded signal imposes a challenge for the recognition of IED. As the fully-passive wireless recorder has little amplifying or digital coding capability, the wirelessly recorded IED signal is easily overshadowed by the noise and environmental artifacts. The low SNR of the wireless data results in a significant challenge to recognize IED using conventional signal processing methods, motivating us to adopt a machine learning based pattern recognition algorithm to enable IED signal recognition. Furthermore, our concurrent wired/wireless signal acquisition allows the wired data to be used as a reference. In a practical setting, however, when only wireless recording is performed, no reference will be available. Therefore, the machine learning IED recognition technique adopted in this work is essential to analyze the wireless data. For the training dataset, we included both wired and wireless signal samples so that the machine learning model can recognize not only high SNR IED signals, but also low SNR data. To ensure high recognition accuracy, only the best wireless IED signal, at 12 dBm, were used for training. **Figure 4.13c** illustrates the machine learning testing accuracy as a function of RF power. For the wired IED data, the testing accuracy remains at 100 % under all circumstances, which confirms the effectiveness of the developed machine learning model. For the wireless IED data, we observed the testing accuracy improves as a function of the RF power, from 24 % at 6 dBm to as high as 91% at 12 dBm. This result suggests that, although the wirelessly acquired temporal IED waveform is overshadowed by the noise and artifact, the machine learning algorithm can still recognize low SNR IED signal from the unwanted noise, marking recognition accuracy as a function of the RF power. The increase of

recognition accuracy with higher RF power also correlates well with our previous SSEP results. Detailed machine learning IED recognition results are provided in **Table 4.5**. It should be noted that the total number of IEDs recognized by the machine learning model, in both wired and wireless testing datasets, are significantly higher than what we labeled (see **Table 4.5**). This outcome is possibly due to 1) The training dataset of the labeled IED signal being limited and/or 2) the manual labeling is over-conservative. It should be noted that the rate of IED events was reported to be 0.15-0.3/s in (Lévesque, Behr, and Avoli 2015) and 0.15-0.4/s in (Bortel et al. 2010), which is close to our machine learning recognized IED rate. The large difference between the labeled and recognized IED rate suggests that our over-conservative manual labeling may have missed a large number of true IED signals.

4.5 Discussion

The *in vivo* recording of this work used both sequential (SSEP) and concurrent (IEDs) recording protocols. Specifically, the SSEP recordings focused on comparing averaged signals, meaning spontaneous neural activity is averaged out and only a time-locked evoked signal remains. This requires using comparable electrode configuration, but not concurrent recording with both systems. It is known that the latency and amplitude of the processed evoked potential can vary with animal, stimulation paradigm, and recording set up, however keeping these factors consistent between our wireless and wired recordings will lead to common characteristic components (positive peak followed by a negative peak) of SSEP. In this way, our wired recording data serve as a reference to evaluate the accuracy of our wireless system to reconstruct SSEP waveforms. In addition, a previous

work(Valdés-Hernández et al. 2019) where SSEPs were recorded with a high-resolution EEG mini-cap shows how the extracted evoked potential may vary with distance from the corresponding somatosensory area. This further supports the use of sequential recordings, as it allowed us to place the recording electrode over the appropriate cortical area (according to ref(Paxinos and Watson 2006), approximately 1.20 mm posterior to Bregma and 3 mm to the left of the midline) with the reference electrode in the same contralateral area and record in the same conditions with both systems.

On the other hand, IED recordings focused on spontaneously-occurring characteristic components of epilepsy, implying that every recording trial would result in different IED occurrences, as they might be generated by different irritative brain zones. Therefore, spontaneous background activity cannot be averaged out, forcing us to record the IEDs concurrently with both systems. Trivially, the waveform of the IEDs will be different as recorded by both systems. Our focus was not on the exact waveform, but on the capability to detect the IED peaks. The larger amplitude (hundreds of μV, peak-to-peak)(Song et al. 2015) of the IEDs allowed the tolerance of the distance between the wireless and wired electrode to be considered negligible (< 2 mm), supporting the similarity between the two signals despite the electrodes not being exactly identical.

It should be noted that the intended application for the presented wireless recorder is as a long-term implantable ECoG system. The tissue emulating phantom (**Figure 4.9**) was designed to emulate this environment. However the current dimension (9 mm x 8 mm) of the implant makes it very challenging to validate its functioning principles *in vivo* using a small animal like rat, as this requires us to open a craniotomy (practically removing the

entire skull and thus compromising physiology in this animal model). Our current *in-vivo* experiments (**Figure 4.7**, **Figure 4.8**) were used to validate the wireless signal transmission through the skin. The main objective of this work was to demonstrate the feasibility of neuropotential acquisition using the fully-passive wireless system, via SSEP & IED, as a function of signal power for a given wireless transmission. From both *in vitro* and *in vivo* data presented above, we conclude that fully-passive wireless system is very feasible through the skull-scalp interface.

Table 4.6 compares the specifications of our recorder with several other state-of-the-art neural recording systems. Several prior arts feature smaller footprints than ours, including the ultrasonic neural dust developed at Berkeley(Seo et al. 2016) (3 x 1 x 0.8 mm^3). The current footprint of our sensor may be significantly reduced by adopting advanced fabrication such as miro-3D printing as the antenna occupies a large footprint.

Unlike inductive or ultrasonic coupling, the wireless fully-passive recorder relies on electromagnetic waves for wireless telemetry. Electromagnetic waves show significant adsorption in the body primarily dominated by dielectric and conductivity properties of the tissue. This directly impacts the amount of electromagnetic power to radiate from the external interrogator. In other words, we need to radiate higher power of electromagnetic waves than inductive or ultrasonic waves at a given target power delivery. This method, however, is not to power the implant, but to collect the backscattered signal; the amount of power being radiated can be drastically lowered. Nevertheless, the fundamental nature of tissue adsorption of electromagnetic waves sometimes limits our applications.

Table 4.6. Specification of the proposed wireless neural recorder in comparison to other state-of-the-art systems

	Borton(Borton et al. 2013)	Sodagar(Sodagar et al. 2009)	Muller(Muller et al. 2014)	Lee(B. Lee et al. 2019)	Seo(Seo et al. 2016)	This work
Size	56 x 42 x 9 mm^3	15 x 14 mm^2	6.5 x 6.5 mm^2	19 x19 x 30 mm^3	3 x 1 x 0.8 mm^3	9 x 8 x 0.3 mm^3
Weight	44.5 g	275 mg	-	5.7 g	-	54 mg
No. of Channel	100	64	64	32	1	1
Power Source	Rechargeable battery	RF (70/200M)	RF (300M)	Inductive (13.56M)	Ultrasound (1.85M)	RF (2.32G)
Power Consumption	90.6 mW	14.4 mW	225 µW	35 mW	0	0
Minimum Detectable Signal	8.6 µVrms	8 µVrms	1.25 µVrms	3 µVrms	180 µVrms	21.2 µVrms
Working Distance	1 - 3 m	10 mm	12.5 mm	-	8.8 mm	15 - 21 mm

CHAPTER 5

WIRELESS MULTICHANNEL NEURAL RECORDER

The previous chapter presented a flexible, small-sized, fully-passive wireless neural recorder, its functionality has been validated through both *in vitro* and *in vivo* experiment. Although the results are very promising, the presented sensor also has many limitations. One major limitation is that the sensor has only one single recording channel. In practical application, physicians always need to acquire neural activities from multiple locations of the brain simultaneously. To meet this requirement, expanding the number of recording channels of the fully-passive neural recorder is essential. Existing wireless neural recording systems often utilize sophisticated digital integrated circuit (IC) to achieve the multichannel recording ability. However, as described in chapter 2, this approach usually leads to a large dimension and high power consumption of the wireless system. As the channel number increases, the problem of power consumption becomes more severe which eventually makes the system unsafe for long-term implantation. In this chapter, a novel passive wireless multichannel recording method will be presented. The multichannel recording ability is achieved through an inductor-capacitor delay line circuit and a diode switching array. By initiating the propagation of an electrical pulse along the LC delay line, the neural signals of each channel are sampled and wirelessly telemetered in a time-multiplexed manner. As no digital circuit is involved, the total power consumption of the wireless sensor is independent of the channel number. In other words, the developed wireless multichannel recorder will always have extremely low power consumption no matter how many channels are recorded simultaneously. This characteristic makes the

sensor a promising candidate for long-term neural recording applications. The chapter will first present the concept of the proposed multichannel neural recorder and discuss the key design considerations. Simulation results will also be presented to verify the operating principle. Next, a 16 channel passive wireless ECoG array prototype will be fabricated and validated *in vitro*.

5.1 Design of the Multichannel Recorder

Figure 5.1 shows the overall concept of the passive wireless multichannel neural recorder. Here, multiple inductors and capacitors are used to construct a delay line circuit, where each inductor-capacitor pair of the circuit will produce a small time delay. When an electrical pulse signal appears at the start of the delay line, the pulse will propagate through the delay line from node to node, arriving at each recording channel at a different time. Thus, the voltage of the pulse signal can be used to turn on each channel as it propagates through the delay line. Through a diode switching array, the neural signal inputted to each channel (represented by different colors in **Figure 5.1**) will sequentially be applied to the output of the delay line circuit in a time-multiplexed manner. Then, the output signal can be wireless recorded using the RF backscattering method as described in previous chapters. Note that in this method, no digital control signal is used to turn "on" or "off" the channel. All channels are turned on one by one as the pulse signal propagates through them.

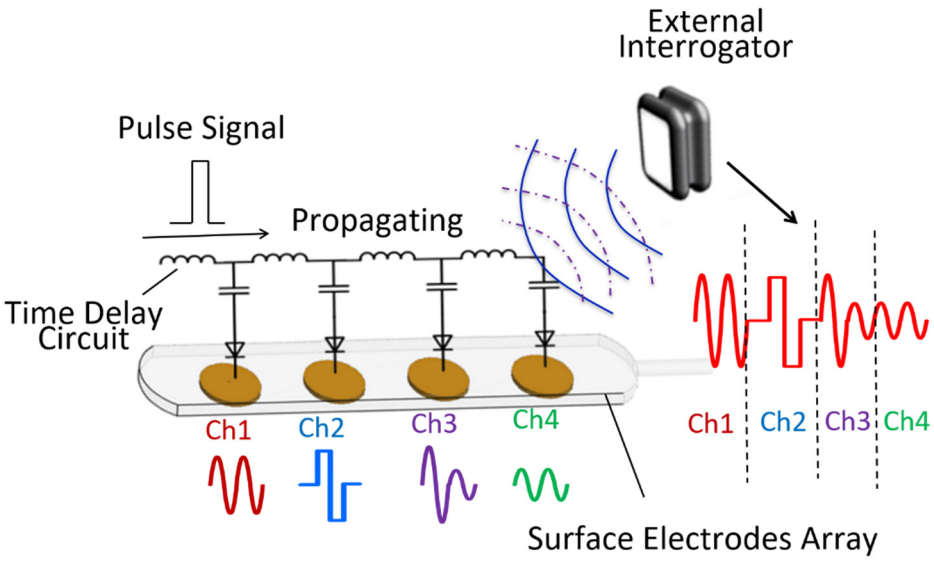

Figure 5.1 Schematic of the passive multichannel wireless neural recorder. The schematic shows a wireless fully-passive 4 channels electrode array based on the time-multiplexed method. The time delay circuit, composed of inductors, capacitors, and diodes, delivers a propagating pulse signal which alternately turns on channel 1-4. The output signal of the external interrogator contains the waveform of all channels in the corresponding time sequence.

The detailed design method of the wireless multichannel neural recorder will be described below. For simplicity, we will consider a 4 channel recorder. For a larger number of channels, the design method should remain the same.

5.1.1 The LC Delay Line Circuit

To enable simultaneous signal recordings on multiple channels, a switching mechanism based on an LC delay line circuit is developed. This mechanism does not require any conventional digital circuitry, clock, or controller to operate. Its power consumption does not increase with the expansion of recording channels. **Figure 5.2a** shows a simple LC delay line circuit. The circuit is composed of repeatedly connected inductor-capacitor pairs. When a pulse signal is inputted to the LC delay line circuit, it will propagate through the delay line. In other words, each node in the LC circuit network will have a similar waveform as the input pulse, only with a gradually increased time delay (**Figure 5.2b**). The time delay, t_d, is determined by the value of inductors and capacitors, which can be expressed as:

$$t_d = \sqrt{LC} \tag{5.1}$$

If all the capacitors and inductors have the same value, the LC delay line circuit can be viewed as a transmission line, meaning the pulse will propagate through the delay line with a constant speed (**Figure 5.2b**). Using this phenomenon, all the nodes inside the LC delay line circuit can be used as a controlling method to select different channels. For example, if let the node with the highest voltage to be selected “on” and turn all the other nodes “off”, then each node can be turned on in sequence as the pulse propagates through the line. This can be accomplished using a diode switching circuit, which will be explained in the later section.

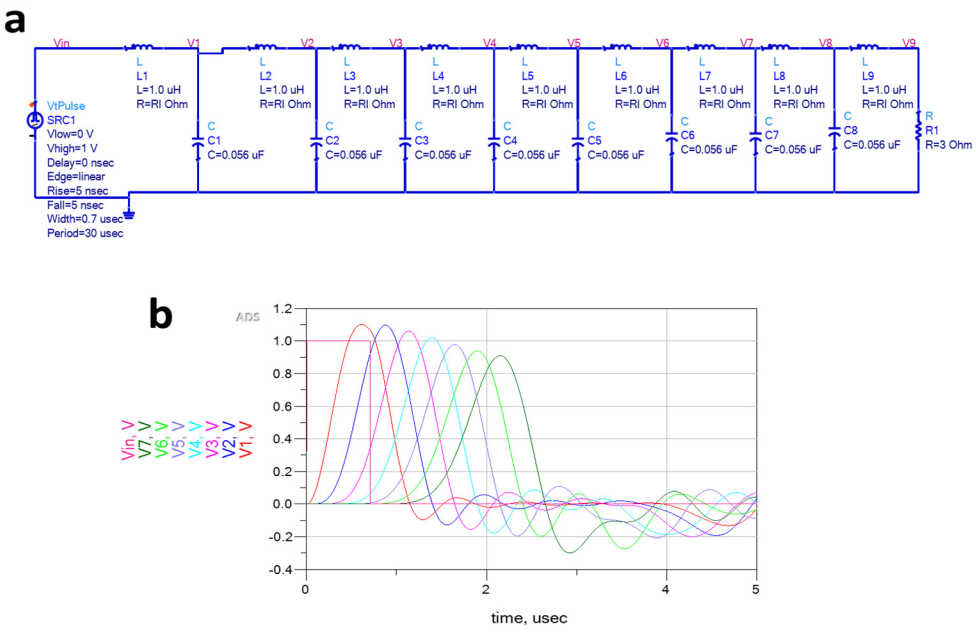

Figure 5.2. The LC delay line circuit. (a) Schematic of a simple LC delay line circuit. Each inductor-capacitor pair in the circuit generate a time delay for a propagating pulse signal. (b) ADS simulation of the circuit in response to a pulse input. Each colored curve represents the voltage signal measured at the corresponding node in (a). It can be seen that the input pulse is propagating from node to node with an attenuated amplitude.

When constructing the LC delay line circuit, the first step is to choose the right inductor. The important parameters of inductors are their sizes, inductance values, and DC resistance. Ideally, we want the inductor to have a small size, a high inductance value, and a DC resistance as low as possible. For an ideal inductor, the pulse can propagate indefinitely until it reaches the resistor R_1. However, an actual inductor always has finite conductivity, which results in energy dissipated as heat when the pulse propagates through the delay line circuit. As shown in **Figure 5.2b**, the amplitude of the pulse signal gradually

attenuates as it reaches more nodes. Therefore, the maximum achievable number of recording channels depends on how far the pulse can propagate. To minimize the loss, the DC resistance of the inductor needs to be as low as possible. **Figure 5.3** shows the effect of the inductor DC resistance on the pulse propagation in the LC delay line circuit. It can be seen that the propagating pulse will experience large attenuation even for a DC resistance as small as 0.7 Ohm. Therefore, in the actual design, the DC resistance of the inductor should not be larger than 100 mOhm. Generally, inductors with a small size will have higher DC resistance. When the size of the recorder is limited, sacrificing the DC resistance is unavoidable, which limits the maximum achievable channel number.

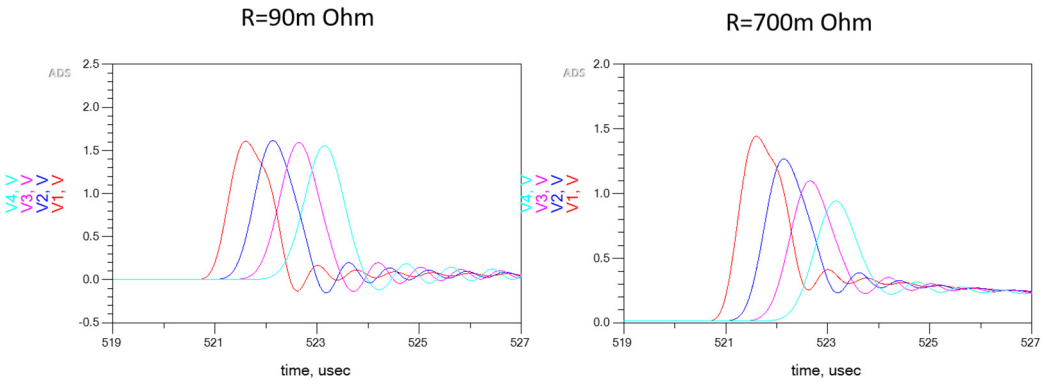

Figure 5.3 Effect of the inductor DC resistance. ADS simulation results show waveforms of the propagating pulse in the LC delay line circuit when the inductors have 90m Ohm DC resistance versus 700m Ohm. For 90m Ohm (left), the pulse amplitude at each node has very small attenuation, making it possible to achieve a large channel number. For 700m Ohm (right), a very clear attenuation of pulse amplitude can be observed. In this case, the maximum channel number is limited to only a few channels.

The inductance value mainly affects the delay time of the circuit. The delay time is a very crucial design parameter. In the later section, we will see that the delay time also means how long each channel is turned “on”. During this period, the output signal must be accurately sampled by the external readout system to reconstruct the input signal in the corresponding channel. Therefore, the delay time must be chosen based on how fast and accurate the data acquisition device can achieve. We want the delay time to be as large as possible to leave enough time for data acquisition. From equation (5.1), this can be achieved by increasing the value of either the capacitor or the inductor. However, the capacitor cannot be chosen very large because it also affects the shape of the pulse. Specifically, a large capacitor will result in a slow rise/fall of the pulse, which is undesirable because the rise/fall needs to be as fast as possible to enable a reliable switching from channel to channel. Thus, the only way to increase the delay time is to increase the inductor. In practice, however, large inductors are always accompanied by large sizes and low quality factor (high DC resistance), which is undesired. Therefore, a proper delay time must be determined from a comprehensive trade-off between the inductor quality, size, and the capability of the sampling device. In this work, we chose to use the 1 μH, 1.6 mm x 0.8 mm surface mount inductor manufactured by Taiyo Yuden (LBMF1608T1R0M). The capacitor is chosen as 0.056 μF. The resulted time delay is around 0.25 μs at each node. Thus, every two nodes can generate a 0.5 μs time delay, corresponding to a 2Mhz sampling frequency.

5.1.2 Pulse Generation

The functionality of the delay line circuit is based on the propagation of a pulse signal. Since there is no battery on the wireless sensor, the pulse signal is generated by an antenna. The multichannel wireless neural recorder needs two antennas to operate. One antenna (antenna 1) is used to create the propagating pulse signal; the other (antenna 2) is used as the backscattering antenna. Since these two antennas serve different purposes, they should be designed separately. Antenna 2 is the backscattering antenna, whose design method is the same as the signal channel recorder. Antenna 1 is used to receive external RF energy and accumulate voltage on a capacitor. This circuit is shown in **Figure 5.4a**. In practice, the voltage generated with one single diode is often not enough. Thus, diode voltage multiplier circuits can be used to increase the voltage. **Figure 5.4b** shows the circuit using three stages of the diode voltage multiplier to increase the voltage output of the antenna.

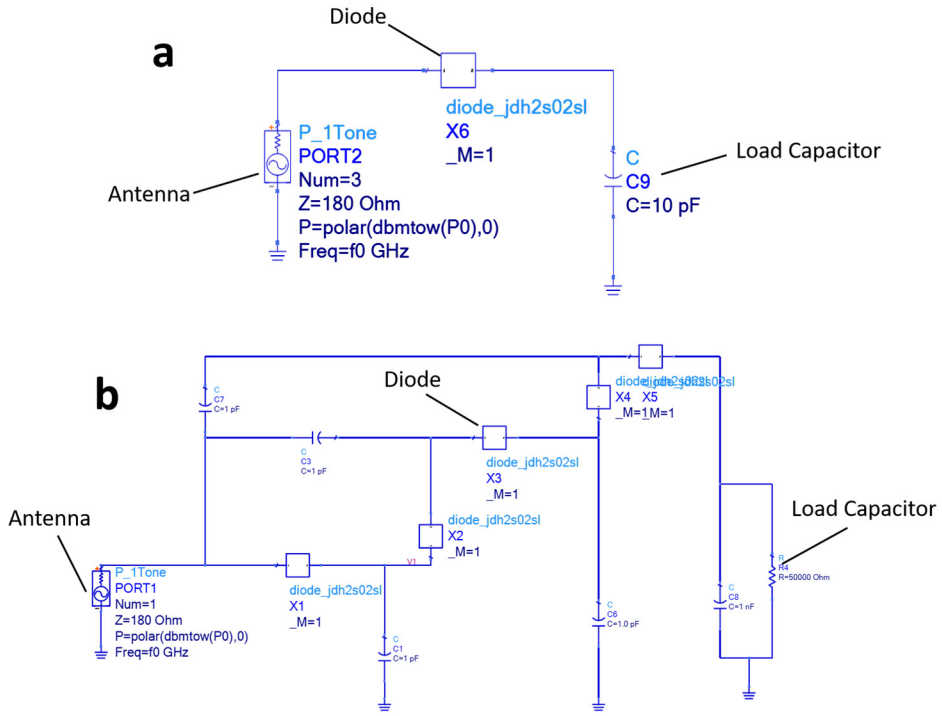

Figure 5.4. Antenna follow-up circuits for voltage accumulation. (a) The basic voltage regulator circuit consisting of a diode and a load capacitor. (b) The revised circuit adopting diode voltage multiplier circuits to increase the voltage on the load capacitor. In both (a) and (b), the antenna is represented by a single tone power source.

The design of antenna 1 greatly impacts the amplitude of the voltage on the load capacitor. To establish a reliable wireless link, we want the amplitude to be as high as possible. Thus, the optimization of antenna 1 is of critical importance. When designing antenna 1, many factors need to be considered, including its size, gain, material, and port impedance. The antenna size is primarily determined by the operating frequency. A higher frequency can reduce the overall footprint of the antenna. On the other hand, the higher frequency also results in greater loss of EM energy inside the tissue (skin, muscle, etc.).

Therefore, we need to make a trade-off between size and performance. For a very small antenna, its gain is usually much compromised. The antenna port impedance can also affect its output voltage. For an optimized output voltage, the port impedance needs to be matched with the antenna follow-up circuits. For example, the circuit in **Figure 5.4a** and **Figure 5.4b** needs to be matched with different port impedance. As the follow-up circuit is always capacitive, the port impedance of the antenna should be inductive. Because parasitic elements and fabrication errors are hard to estimate, it is better to leave some room for tuning impedance afterward. An example design of antenna 1 is shown in **Figure 5.5**. This antenna can be viewed as a dipole with two meandered arms. The substrate is FR4 and the metal trace is copper. It should be noted that there are two inductors required by the antennas: one inductor is placed next to the output port; the other provides a closed-loop circuit path for low-frequency signals. The port impedance of the antenna is near zero at DC frequency.

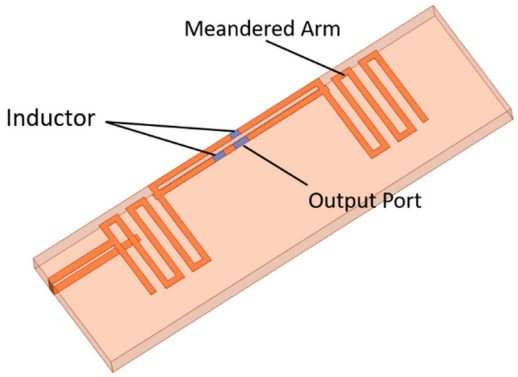

Figure 5.5. The geometry of the antenna for pulse generation. The antenna has two meandered arms and two inductors (represented by the blue rectangular). The output port connects the follow-up voltage accumulating circuit.

To generate a pulse signal that propagates through the LC delay line circuit, a P channel MOSFET is used as a switch to control the current discharging from the load capacitor. **Figure 5.6** shows the circuit to create the propagating pulse. Antenna 1 (A_1) receives external RF energy and accumulates voltage on two load capacitors C_1 and C_2 through the diode D_1 and D_2, respectively. The capacitor C_1 is 1 pF while the capacitor C_2 is several micro-farads. R_1 and R_2 are in kilo-ohms. When the incident EM wave is turned "on", the antenna A_1 continuously output a DC voltage at the node V_g and V_s. When the EM wave is turned "off", the voltage at V_g and V_s begin to drop due to the discharging of capacitor C_1 and C_2. Due to the difference in their capacitance values, V_g drops very fast while V_s drops very slow, increasing the voltage difference between the transistor gate and source (V_{gs}), turning "on" the PMOS transistor T_1. This will cause the voltage on C_2 to discharge through the transistor drain path. The external EM wave is then turned "on" again, turning "off" the transistor T_1 and creating a pulse-shaped signal at the input of the LC delay line circuit. Note the reason to use P channel transistors instead of N channel is that the external EM wave needs to be turned "on" when the pulse signal is propagating through the delay line so that the time-multiplexed multichannel signal can be measured using the RF backscattering method.

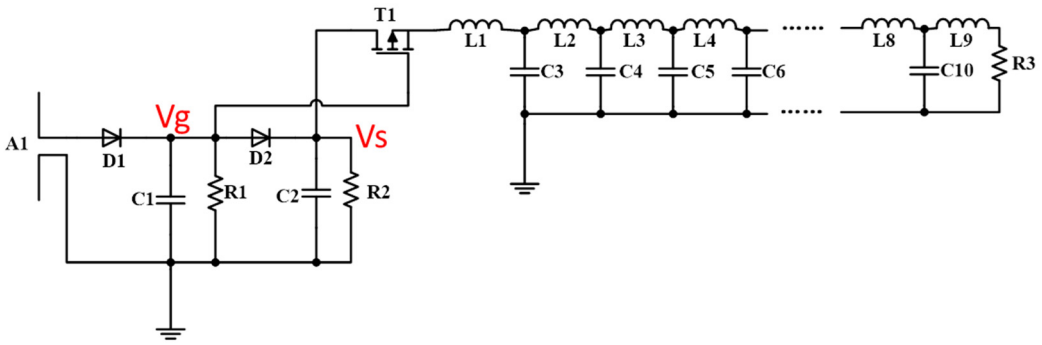

Figure 5.6. The basic pulse generation circuit. The voltage difference between V_g and V_s of the PMOS transistor T_1 is used to control the discharging of the capacitor C_2.

To repeatedly generate pulse signals, the incident EM wave needs to be periodically turned "on" and "off". This can be accomplished either by amplitude modulation (AM) or an RF switch (**Figure 5.7 a,b**). However, RF amplifiers usually have an inherent response time to the sudden change of waveform, which will result in an undesired time delay when turning "on" and "off" the incident RF signal. As the wireless telemetry is based on the RF backscattering method, the RF signal needs to be turned "on" before the propagating pulse signal reaches the first recording channel. As described previously, the time gap between each channel is only 0.5 μs. This means the RF signal should be turned "on" within 0.5 μs to guarantee valid wireless telemetry. In a practical system, achieving such a small response time is very difficult, therefore, we insert additional time delay units before the first channel to compensate for the response time of the system. For the two methods shown in **Figure 5.7**, the RF switch is a better choice because the switch can be placed after the amplifier, which effectively reduces the system delay. On the other hand, this requires the RF switch to have a high power handling capability.

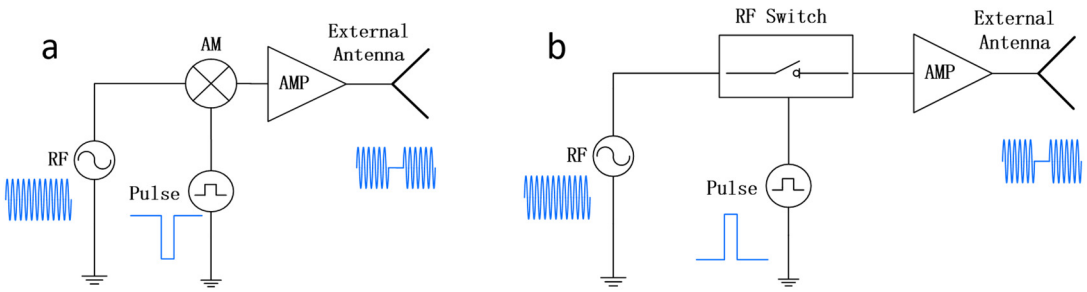

Figure 5.7. External RF modulation systems for generating a pulse signal on the wireless sensor. (a) The amplitude modulation (AM) method. (b) The RF switching method. Both methods can alternately turn "on" and "off" the incident RF signal.

The circuit in **Figure 5.6** works well in the ideal condition. In practice, however, parasitic elements, especially the parasitic capacitance, heavily impact whether the pulse signal can be successfully generated. The parasitic capacitance affects the antenna, and more importantly, the shape of the generated pulse signal. Two critical components are most affected by the parasitic capacitance: the diode and the PMOS transistor.

The parasitic capacitance of the diodes in **Figure 5.4** and **Figure 5.6** greatly affects the amplitude of the voltage accumulated on the load capacitor. This voltage should be as high as possible since it is used to turn on the PMOS transistor. The parasitic capacitance on the diode needs to be as small as possible. **Figure 5.8** shows a comparison of the accumulated voltage of a three-stage diode multiplier circuit when the diode has a 0.15 pF parasitic capacitance versus a 10 pF parasitic capacitance. As can be seen, when the diode has a 10 pF capacitance, the circuit does not work. Besides the parasitic capacitance, the forward voltage of the diode will result in an unwanted voltage drop, thus it should also be

as small as possible. Considering these factors, RF Schottky diodes are the best choice. For our design, we chose the JDH2S02Sl RF Schottky diode (Toshiba) for its small size, low capacitance, and low forward voltage.

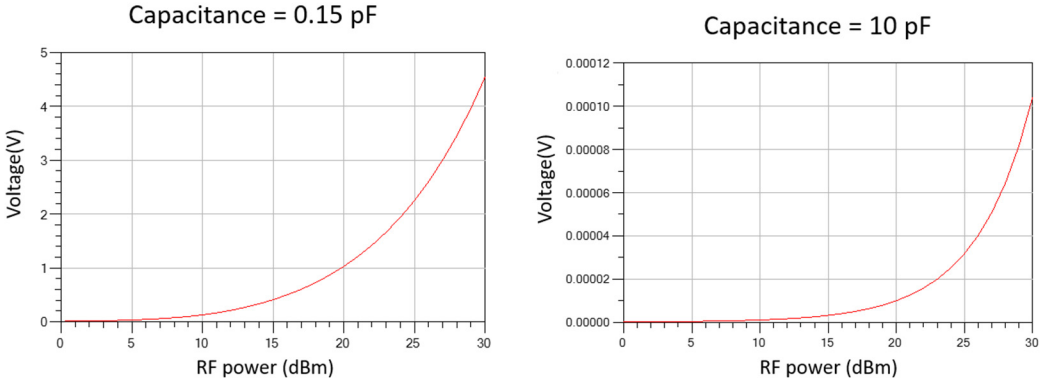

Figure 5.8. The effect of the diode parasitic capacitance. The figure shows simulation results of the voltage accumulated on the load capacitor through a three-stage diode multiplier circuit (Figure 5.4b). The circuit only works when the diode has a 0.15 pF (RF diode) parasitic capacitance. For a 10 pF parasitic capacitance, no voltage can be accumulated.

The capacitance between the source and gate port of the PMOS transistor (C_{gs}) is another critical parameter impacting the generation of the pulse signal. The C_{gs} should be as small as possible because a large C_{gs} will result in a slow rise time of V_{gs}, distorting or even preventing the generation of the pulse signal. **Figure 5.9** demonstrates the effect of C_{gs}. For a small parasitic capacitance C_{gs} (**Figure 5.9a**), the voltage on the gate terminal of the PMOS, V_g, drops quickly when the incident EM wave is turned "off", causing the

increase of V_{gs}. The sufficient increment of V_{gs} turned on the PMOS transistor, inducing the discharge of current from the load capacitor (C_2 in **Figure 5.6**), which cause the drop of V_s and creating a pulse signal that can propagate through the LC delay line circuit. For a large C_{gs} (**Figure 5.9b**), however, the drop of V_g is too slow to create sufficient amplitude of V_{gs} that can turn on the PMOS transistor, and thus no effective pulse signal is generated on the LC delay line circuit.

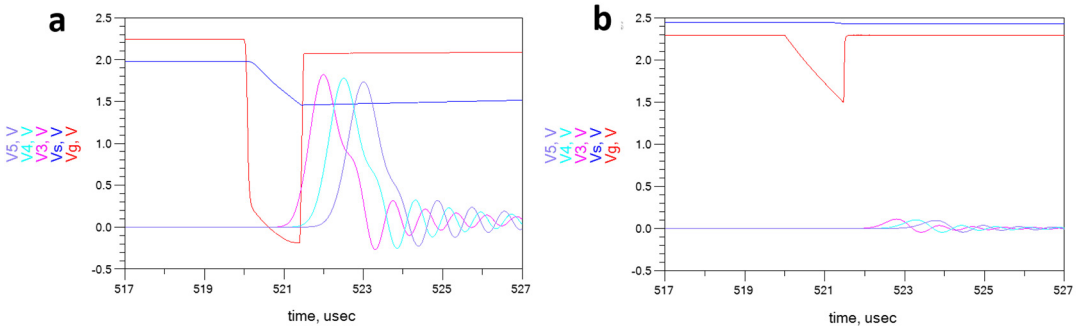

Figure 5.9. The effect of the input parasitic capacitance (C_{gs}) of the PMOS transistor. ADS simulation shows the waveform of the pulse signal generated by the circuit in Figure 5.6. The curve V3, V4, V5 represent the voltage signals measured at the nodes of the delay line circuit. (a) When C_{gs} is small (around 10 pF), a clear pulse signal can be seen propagating from node 3 to node 5. (b) When C_{gs} is large (around 120 pF), no distinct pulse signal is observed.

The input parasitic capacitance (C_{gs}) greatly affects the pulse generation, yet it is not the only critical specification. When choosing the PMOS transistor, we have to consider other specifications, including the footprint, threshold voltage V_{th}, and transconductance

g_m. In an ideal situation, we want the threshold voltage V_{th} and the capacitance C_{gs} to be small while the transconductance g_m to be large so that the generated pulse signal would have a large amplitude and a fast rise/fall time. In practice, however, these conditions usually cannot be all fulfilled because they contradict each other. For example, the transconductance of the transistor, g_m, can be expressed by:

$$g_m = \mu_n C_{ox} \frac{W}{L} (V_{GS} - V_{TH}) \tag{5.2}$$

Where μ_n is the mobility of electrons, C_{ox} is the gate oxide capacitance per unit area. W and L are the width and length of the gate. The μ_n, C_{ox}, V_{th}, and L are parameters related to the device fabrication process, their values are determined primarily by the technology node standard. For most commercial MOS transistors, these fabrication related parameters will not have a dramatic difference. Therefore, a high g_m is usually obtained from a large W. Yet, a large W will also lead to a large area of the gate, increasing the capacitance C_{gs}, which, as previously described, is undesired for the pulse generation. Therefore, for the circuit in **Figure 5.6**, choosing a perfect transistor is generally very difficult, a trade-off between C_{gs} and g_m has to be made to achieve an acceptable result.

The problem of the capacitance C_{gs} is also closely associated with the gate resistor (R_1 in **Figure 5.6**). The resistor at the gate port of the PMOS mainly affects three aspects of the circuit: 1) the gate voltage V_g; 2) the overall power consumption and 3) the discharging speed of the capacitor C_1. As mentioned before, we want the voltage V_g to have high amplitude and fast response to generate sufficient V_{gs} to turn on the transistor. Therefore, to increase the voltage and reduce power consumption, both the resistors R_1 and R_2 in **Figure 5.6** need to be large (50K-100K). However, a large R_1 also results in a very

slow discharging speed of the capacitor C_1. This is equivalent to a large parasitic capacitance C_{gs}. Thus, for the circuit shown in **Figure 5.6**, the resistor R_1 cannot be selected very large. From simulations, to effectively generate a propagating pulse signal, R_1 should be around 2K-5K Ohm. This small resistance value decreases the gate voltage V_g and increases the overall power consumption. For example, to create a 1.5 V propagating pulse, a 2K Ohm R_1 needs to consume 2 mW power, while a 50 KOhm R_1 only consumes 80 μW. The decreased gate voltage V_g has to be compensated through further optimization of the antenna, otherwise, the accumulated gate voltage will not be enough to effectively turn on the PMOS transistor.

As discussed above, although the circuit in **Figure 5.6** can be used to generate the pulse signal, the design still suffers from the large transistor parasitic capacitance as well as the small gate resistor. Using only one PMOS transistor, the gate voltage V_g is impossible to achieve both high amplitude and fast response speed, as these two factors contradict each other. However, we can revise the circuit to overcome these shortages. One method is to use additional transistors. An improved version of the circuit is shown in **Figure 5.10**. Three additional MOS transistors, including $PMOS_2$, $NMOS_1$, and $NMOS_2$, are inserted into the pulse generation circuit to improve the transition speed of the transistor while maintaining a high resistance at the gate terminal. The $PMOS_1$ transistor is used to control the discharging of the capacitor C_3 for generating the pulse signal. The two NMOS transistors are used to pull down the gate voltage of $PMOS_1$ when the external RF energy is turned "off". The fall time of V_g is controlled by the NMOS transistors and is independent of the gate resistor R_2 and the parasitic capacitance C_{gs}. **Figure 5.11** compares

the fall time of V_g before and after the NMOS transistors are added. The PMOS used here is the PMZ320UPE (Nexperia), which has a C_{gs} of 122 pF. The gate resistor R_2 is 50 KOhm. As can be seen, before the transistors are added (the circuit in **Figure 5.6**), the large C_{gs} and R_2 lead to the slow fall of V_g, impeding the pulse generation. However, after the transistors are added, the fall time of V_g significantly decreases. The transistor $PMOS_2$ is used as a voltage-controlled resistor to isolate the gate port of the $PMOS_1$ from the capacitor C_1. This is necessary because when V_g is pulled down, the overall resistance seen at the gate port of $PMOS_1$ is very small. This small resistance will draw a huge current from the antenna, hampering the voltage accumulation on any of the load capacitors (C_1, C_2, and C_3). As a result, V_g cannot return to the high level when the RF power is turned "on". The transistor $PMOS_2$ can effectively solve this problem. When RF power is "off", the voltage of V_c is pulled up by the voltage on the capacitor C_3, turning off the $PMOS_2$. The resistance between the source and the drain of $PMOS_2$ becomes very large, which isolates the capacitor C_1 from the small gate resistance of $PMOS_1$, enabling voltage accumulation when RF is turned "on". As the voltage on C_1 rises, V_c is pulled down and the transistor $NMOS_2$ is switched off, which causes the gate resistance of $PMOS_1$ to become large. The voltage V_g can be charged back to the high level through the transistor $PMOS_2$. **Figure 5.12** compares the waveform of V_g with and without adding the transistor $PMOS_2$.

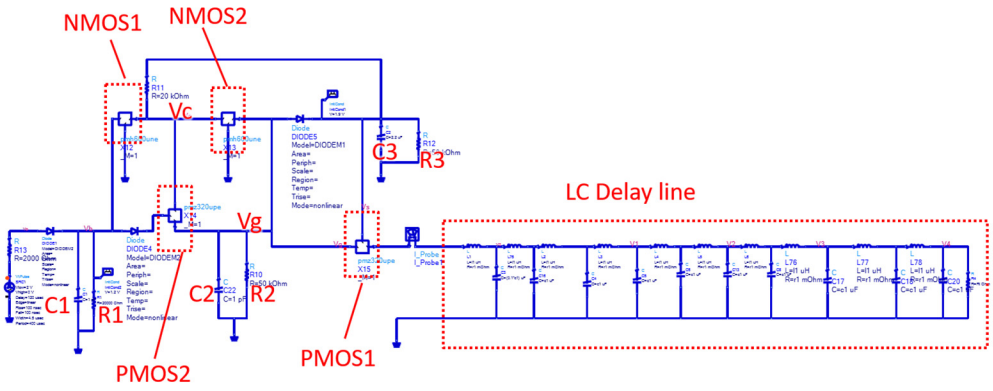

Figure 5.10. The revised circuit for pulse generation. Three additional transistors ($NMOS_1$, $NMOS_2$, and $PMOS_2$) are included to improve the fall speed of V_g without sacrificing the gate resistor R_2.

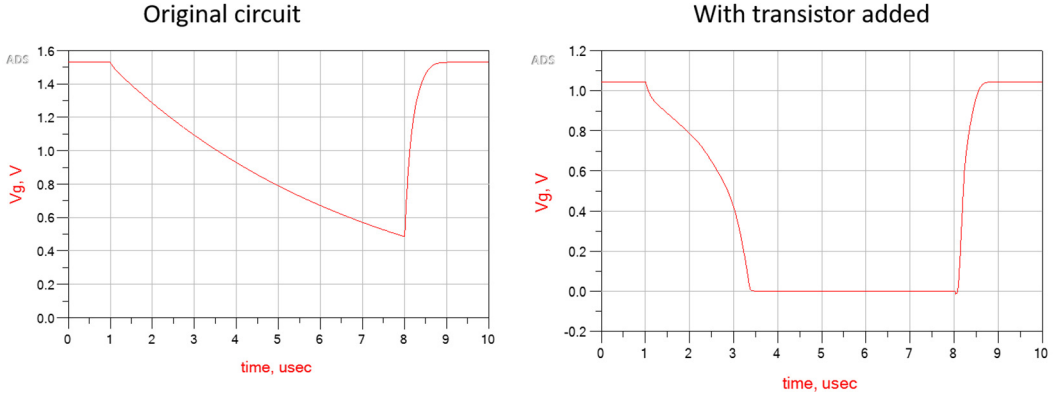

Figure 5.11. Adding transistors to improve the fall speed of V_g. In the original circuit, the fall time of V_g completely depends on the discharging speed of the capacitor C_{gs}. With transistors added, the V_g is pulled down by the NMOS transistors, thereby greatly shorten its falling time.

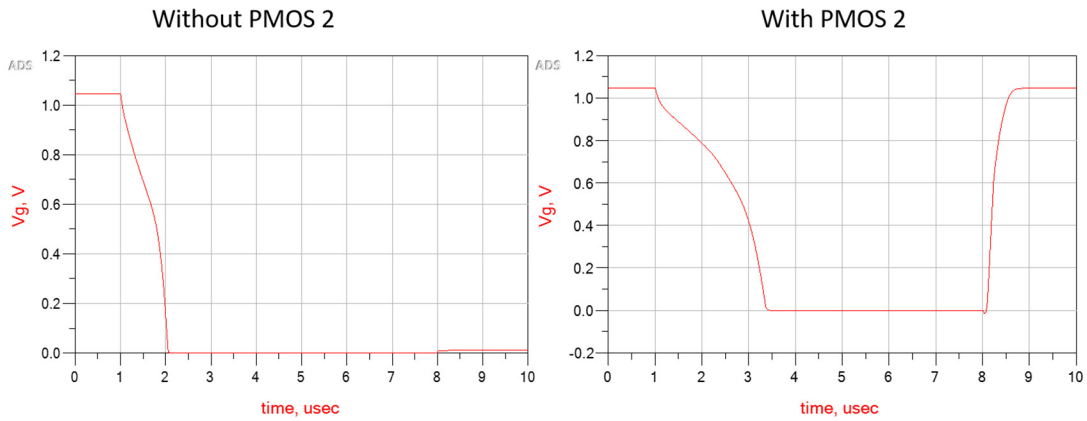

Figure 5.12. The isolation effect of the PMOS transistor. The transistor $PMOS_2$ in Figure 5.10 is necessary for the pulse generation. Without $PMOS_2$, the gate voltage V_g cannot recover to the high level when the incident RF power is turned "on". This is because the current output capability of the antenna is limited to a very small value (several mA). When the NMOS transistors pulled V_g to zero, the impedance seen at the gate of $PMOS_1$ is very small, which draws a large current from the antenna and prevents the rise of V_g. On the other hand, with the $PMOS_2$ inserted, the drain-source impedance of the inserted $PMOS_2$ effectively isolates the antenna from the gate port of $PMOS_1$, enabling V_g to be charged to the high level.

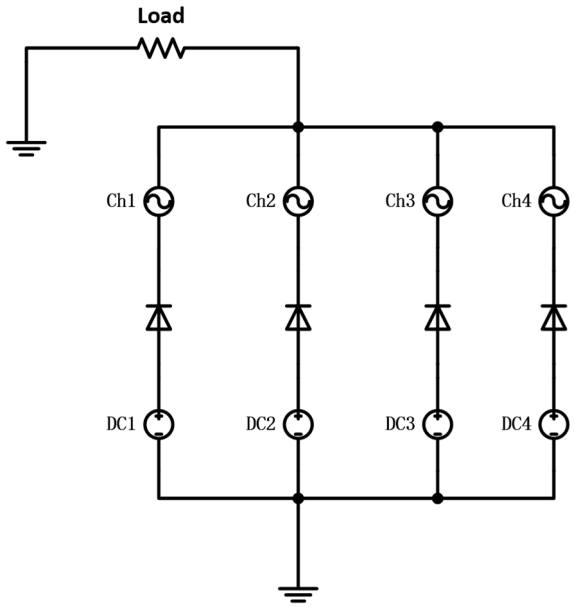

Figure 5.13. The basic diode switching circuit. DC bias voltages (DC1-DC4) are used to turn on different voltage sources (Ch1-Ch4). The channel with the highest DC bias will be turned on, and its signal will appear on the load resistor; all the other channels are turned off.

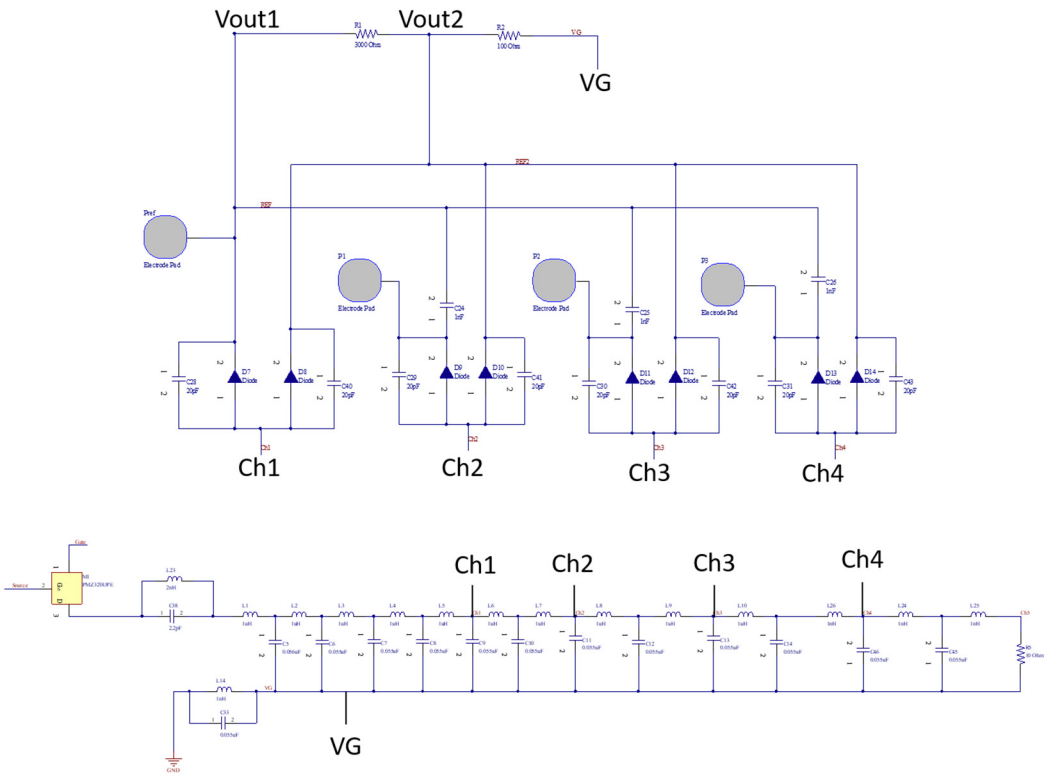

Figure 5.14. The diode switching circuit and its connection with the LC delay line. Nodes that are labeled with the same name are connected. In each channel, the signal is inputted from the electrode pad. All channels share one common reference electrode. Note that Ch1 is shorted to the reference electrode. The purpose of this arrangement is to enable the wireless telemetry system to directly measure the baseline signal and thus reduce the motion artifact.

5.1.3 Diode Switching Circuit

As mentioned in section 5.1.1, the pulse signal propagating through the LC delay line circuit can be used to turn on different channels. This is achieved through the diode switching circuit. **Figure 5.13** shows the simplified schematic of a four-channel diode

switching circuit. Each of the channels is controlled by a DC bias and a diode, and all the channels share one common load resistor. At any time, the channel with the highest DC bias will be turned on by the diode, causing the signal of the channel applied on the load resistor, while all the other channels are turned off. Thus, if the DC bias of each channel alternately reaches the highest voltage, the output signal on the load will change from channel to channel accordingly. Based on this principle, we developed the multichannel recording mechanism by integrating the diode switching circuit with the LC delay line. The propagating pulse is implemented as the bias to control the "on" and "off" of each recording channel.

Figure 5.14 shows the complete diode switching circuit integrated with the LC delay line. In each channel, the neural signal is recorded from the electrode (round pads in **Figure 5.14**), and two diodes are required. One diode is connected to the electrode (D_7, D_9, D_{11}, D_{13}), the other is connected to resistor R_2 (D_8, D_{10}, D_{12}, D_{14}). The purpose of using two diodes in each channel is to reduce the baseline offset. This can be explained in **Figure 5.15**. The V_{out1} and V_{out2} are signals measured at the output resistor R_1 and R_2, respectively. As shown in the plot, at different times, the output signal V_{out1} exhibits the waveform of different input channels (represented by different colors in **Figure 5.15**), switching from channel 1 to channel 4 in sequence. Yet, V_{out1} also contains a large baseline offset, which is directly coupled with the pulse signal in the LC delay line. Since the amplitude of the offset is much larger than that of the input neural signal, it can cause the amplifiers in the external wireless telemetry system to saturate. This baseline offset comes from the propagating pulse signal in the LC delay line, and it is very difficult to be completely

removed. However, we can reduce its impact. We use two diodes in each channel to construct a secondary pathway for the pulse signal. The diode D_8, D_{10}, D_{12}, D_{14} are connected in parallel and transport the pulse signal directly to the resistor R_2, creating the signal V_{out2}, which contains only the baseline offset (blue curve in **Figure 5.15**). Thus, the voltage across the resistor R_1, V_{out1}-V_{out2}, will contain all the input signals with a reduced baseline offset (red curve in **Figure 5.15**). This alleviates the problem of saturation in the external system. How much the baseline offset is removed can be controlled by tuning the resistance of R_1 and R_2. However, lowering the baseline offset too much can also decrease the input signal amplitude, thus a trade-off has to be made. In our design, we chose the resistor R_1 and R_2 to be 700 Ohm and 100 Ohm, respectively. These values can produce good offset attenuation while maintaining the amplitude of the input signals.

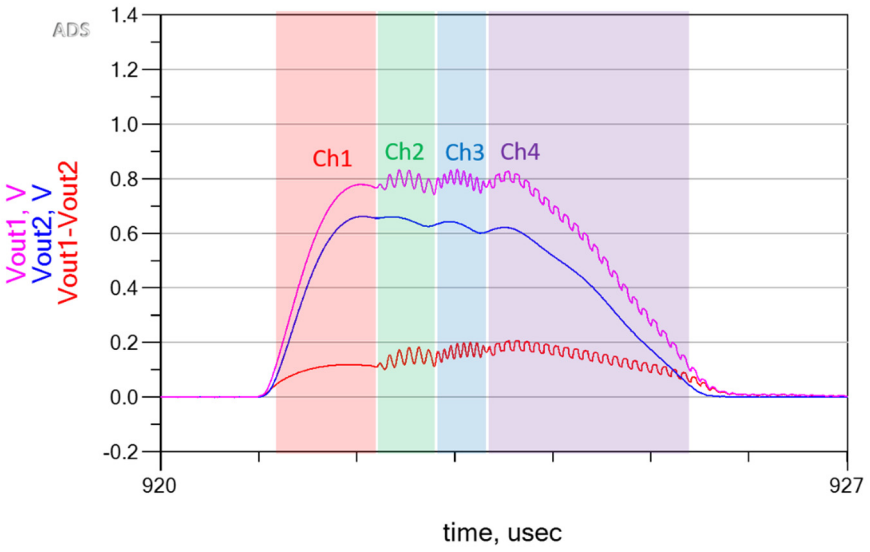

Figure 5.15. Output signals of the diode switching circuit. Note that output signal V_{out1} carries a large baseline offset, which tends to make the external wireless telemetry system saturated. To reduce the offset, a secondary signal pathway is constructed to create a second

output signal, V_{out2}, at the resistor R_2. The V_{out2} contains only the baseline signal. Thus, the voltage across R_1 (V_{out1}-V_{out2}) will contain all the input signals with a reduced baseline offset.

It should be noted that in the LC delay line circuit in **Figure 5.14**, the channels are separated by two inductor-capacitor pairs instead of one pair. The purpose of this arrangement is to create enough time delay between each channel. This can be seen in **Figure 5.16**. V_1 -V_4 represent the pulse signals measured at each channel node in the LC delay line circuit. Observing their waveforms, we can see that the channel selection is controlled by the relative voltage amplitude at each node. The output signal is switched to the channel that has the highest amplitude. However, there is also a clear transition region between each channel. A transition region is created when the channel is not fully turned on by the diode. This happens when the voltage difference between the "on" and "off" channels are too small, less than the forward voltage of the diode. Many factors can lead to an inadequate voltage difference, such as slow rise/fall time of the pulse and insufficient time delay between each channel. Thus, to reduce the transition region, we arrange two inductor-capacitor pairs between each channel. Adding more LC pairs can better isolate each channel, but it also increases the overall size of the device. Another point worth mentioning is that in **Figure 5.14** channel 1 is connected at the 5th inductor in the LC delay line circuit instead of the 1st. As mentioned earlier, this arrangement is made to compensate for the delay time (or response time) of the external system when RF power is turned "on" or "off". Due to the response time of amplifiers, mixers, and filters, the external

interrogator generally has around 1-1.5 μs time delay after the RF switch is turned "on" or "off". To make sure that the RF power is turned "on" before the pulse reaching the recording channels, we insert five LC time delay units before channel 1.

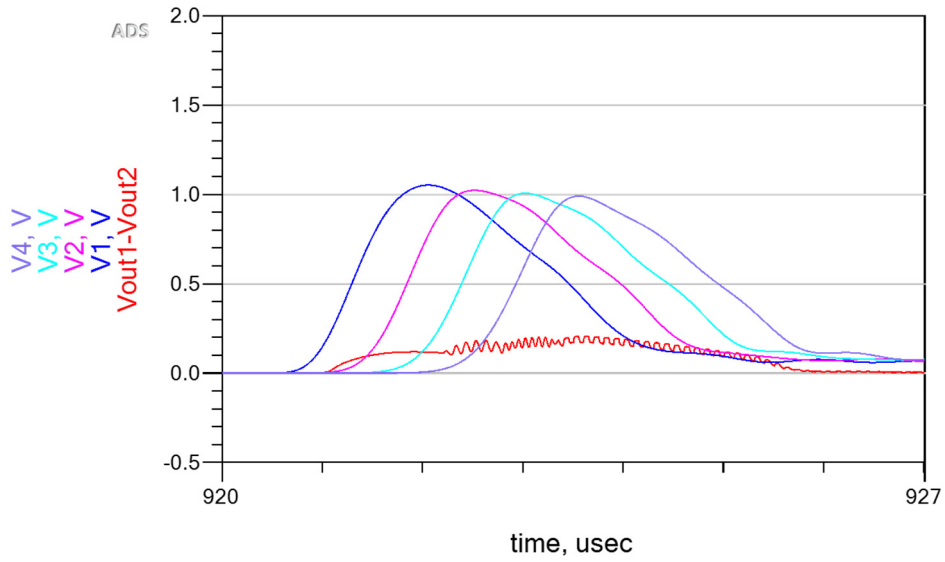

Figure 5.16. Relationship between the output signal and the propagating pulse in the LC delay line circuit. V_1-V_4 are the pulse signals measured at the channel node in the LC delay line.

It should also be noted that in **Figure 5.14**, all the diodes are connected in parallel with a capacitor. These capacitors are used to minimize the undesired RF signal generation at the diodes. When an external EM wave shines upon the sensor, RF signals will be generated not only at the output port of the antenna. In fact, every electronic component will be more or less affected by the EM wave. For diodes, due to their non-linearity, the RF signal will create an undesired DC bias across the diodes. Although those DC signals

are generally small (up to hundreds of millivolts), their existence can disturb the switching mechanism of the circuit. Connecting a capacitor in parallel with the diodes effectively solves this problem because the capacitor greatly diminishes the RF signal generation. The values of these capacitors are usually 20-30 pF.

In each channel, a capacitor is inserted between the recording electrode and the reference electrode (capacitor C_{24}, C_{25}, and C_{26} in **Figure 5.14**). The function of these capacitors is to construct a signal pathway. Through these capacitors, the pulse signal carries the input neuropotentials to the output resistor R_1 and R_2. Note that these capacitors need to be chosen carefully because they also affect the input impedance of the channels. If the input impedance is too small, the input neuropotentials will be attenuated due to the large impedance at the tissue-electrode interface. To maintain an acceptable input impedance, the value of those capacitors should not be larger than 1 nF.

5.1.4 Backscattering Antenna and Circuit

With the time-multiplexed multichannel signal generated at the output resistor R_1 (**Figure 5.14**), the last step is to wireless telemetry this signal using the RF backscattering method. To accomplish this, a second antenna (antenna 2) is required. The basic design principle of antenna 2 is the same as the single-channel neural recorder described in the previous chapter. However, we need to make sure that the two antennas (antenna 1 and antenna 2) can work together. This requires the two antennas have similar radiation pattern so that they can be aligned to the same external antenna and operate normally without affecting each other. **Figure 5.17** shows the design of antenna 2 and its location as referred to antenna 1. The two antennas are both designed and simulated in HFSS. Antenna 2 can

be viewed as a folded dipole. As it needs to operate at two frequencies (f_0 and $2f_0 \pm f_m$), several discrete components are used to achieve impedance matching at both frequencies.

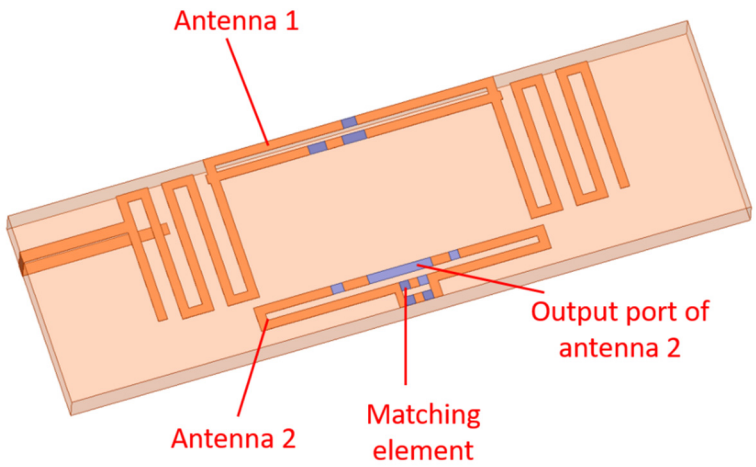

Figure 5.17. An example design of the antenna for RF backscattering. Antenna 2 and antenna 1 share one common substrate (FR4). The blue rectangular on the antennas represent discrete electronic components used for impedance matching.

Figure 5.18 shows the schematics of the fully-passive circuits for the RF backscattering operation. The basic circuit contains one varactor and one bypass capacitor (**Figure 5.18a**). This circuit has the simplest structure and its working principle and design method have been described in chapter 4. Since only one varactor is used, the performance of this circuit depends heavily on how well the backscattering antenna (antenna 2) is designed. This means antenna 2 needs to have a good gain and a good impedance matching with the circuit. To achieves these requirements, the size of antenna 2 cannot be very small. Generally, to achieve sub-millivolt neural recording sensitivity, the footprint of antenna 2

should be at least 15 mm in length. In addition, the working distance of the sensor is usually very short. Thus, although the circuit in **Figure 5.18a** has only two components, it has a rather poor performance. To improve this circuit, we can apply multiple varactor diodes to enhance the power of the mixing products. As shown in **Figure 5.18b**, three varactor diodes are connected in series with two capacitors, parallel with four inductors. As the inductors and capacitors have different impedance at high and low frequencies, the circuit will exhibit different structures for the RF and neural signals, respectively. For high-frequency RF signals, the three varactor diodes are arranged in series. For the low-frequency neural signals, they are arranged in parallel. This structure greatly increases the backscattered power of the 3rd order mixing product (approximately 20 dBm). Using multiple varactors, the size of antenna 2 can be largely reduced and the working distance of the sensor can be largely improved. In the later sections, it will be shown that a three varactors circuit can achieve a wireless working distance as large as 240 mm, while a two varactors circuit can shrink the size of the sensor to as small as 5 mm x 4 mm.

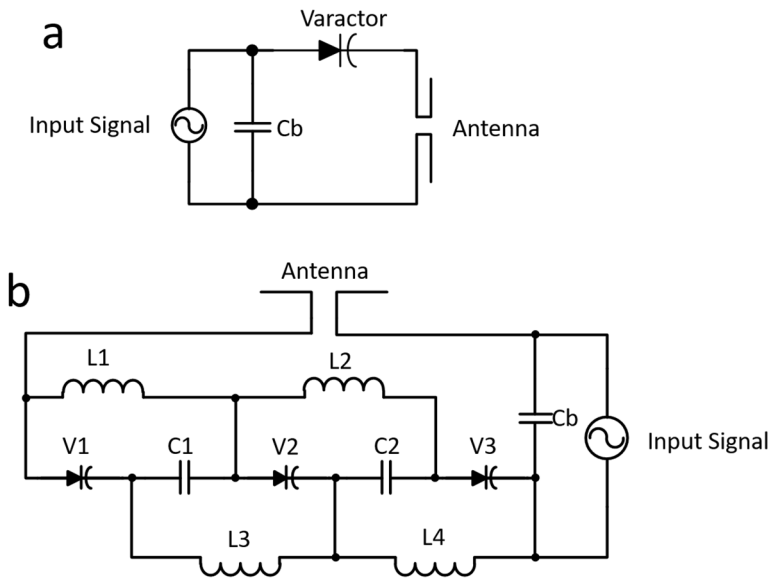

Figure 5.18. Schematics of the circuits for the RF backscattering operation. (a) The basic circuit containing one varactor and one bypass capacitor. (b) The improved circuit using three varactors to enhance the power of the mixing products. The input signals refer to the neuropotentials.

Figure 5.19 shows the actual layout of antenna 2. Here, two varactor diodes are used to enhance the RF backscattering operation. Note that the discrete components highlighted in the black box are the critical capacitors/inductors for impedance matching. The inductor L_s can greatly impact the backscattered power of the 3rd order mixing product, thus it needs to be tuned through experiments. As a starting value, L_s can be chosen as 5.1 nH. The two arms of antenna 2 are connected to the output port of the diode switching circuit (resistor R1 in **Figure 5.14)**.

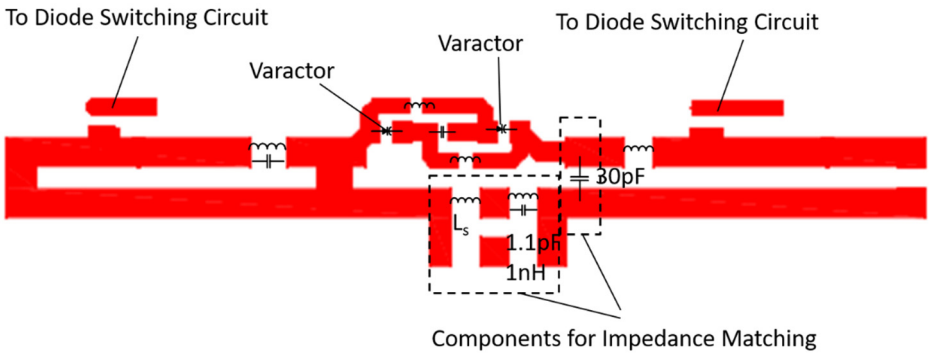

Figure 5.19. The layout of the antenna for RF backscattering. Two varactor diodes are used to enhance the RF backscattering operation. Besides the components shown in Figure 5.18, additional inductors/capacitors are added for impedance matching.

5.2 The External Interrogator

Figure 5.20 shows the block diagram of the external interrogator of the wireless multichannel neural recording system. It can be seen that most parts of the external interrogator remain the same as they are in the single-channel neural recorder. The major difference is the two switches: the RF switch and the analog switch. As demonstrated in **Figure 5.7**, the function of the RF switch is to turn "on" and "off" the incident EM wave so that a pulse signal can be generated at the LC delay line circuit of the sensor. The RF switch is controlled by an external voltage, which can be supplied from the output port of the data acquisition system (DAQ). The successful recording of multichannel signals relies on very well coordination between the RF switch and the DAQ. Initially, the output voltage of the DAQ is zero (low level), turning "on" the RF switch. The antenna starts to transmit RF power to the wireless multichannel recorder, accumulating voltage on its loading capacitors. When the output voltage of the DAQ becomes 5V (high level), the RF switch

is turned “off”. Within several microseconds, a pulse signal will be generated by the PMOS transistor on the recorder, which propagates through the LC delay line circuit, turning on each of the recording channels. Before the pulse reaches the first recording channel, the RF switch must be turned “on” by the DAQ to enable wireless telemetry of the multichannel signal through the RF backscattering method. In addition, the DAQ needs to sample the data point exactly at the time each channel is turned on. To achieve this very critical timing requirement, the DAQ should have the ability to time the start of data acquisition with an accuracy of less than tenths of nanoseconds. For the RF switch, its response time to the external control signal should be as fast as possible. As mentioned before, to reduce the system delay due to the slow response of the amplifiers, the RF switch should be placed after the amplifiers, which also requires the RF switch to have a relatively high power handling ability. Considering these factors, we chose to use the ZSWA4-63DR+ RF Switch (Mini-circuits). This RF switch has a fast switching time of 400 ns and a rather high power handling of up to 33 dBm. Note that the 400 ns delay is from the RF switch along. The actual delay of the entire external interrogator system is between 1-1.5 μs. To account for this delay, additional LC pairs are used in the LC delay line circuit, as shown in **Figure 5.14**.

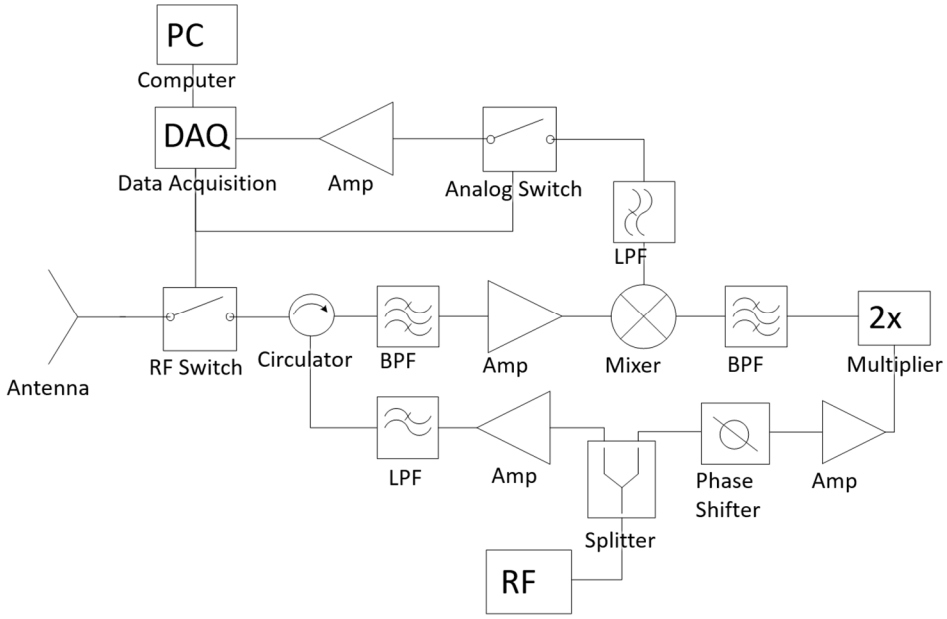

Figure 5.20. Block diagram of the external interrogator for wireless multichannel neural recording.

In **Figure 5.20**, an analog switch is placed just before the preamp. The purpose of this switch is to isolate the preamp from the RF switch. When the RF switch is turned "on" or "off", the output signal of the mixer will generate a large DC shift, which is resulted from the sudden power change at the RF port of the mixer. If not isolated, this large DC shift will be amplified by the preamp, causing the preamp to saturate or even damaging the preamp. To avoid this problem, an analog switch is used to shut down the signal path to the preamp just before the DC shift occurs. The actual analog switch should be chosen as a single pole double throw (SPDT) switch so that when the signal path is closed, the preamp can still be provided with the same DC level from a charging capacitor in the second path.

The data acquisition system (DAQ) is used to digitalize the output signal of the multichannel recorder and transfer those data to a PC for visualization. As mentioned

before, the DAQ needs to have a fast sampling rate and accurate control of the sampling start time. We chose to use the multifunctional DAQ NI 6361 (National Instrument). This DAQ system has a maximum sampling frequency of 2M Hz, and its timing resolution is as accurate as 10 ns. The DAQ system is controlled by a custom Labview program. To initiate the multichannel recording, the DAQ system will first output a pulse signal to turn off both the RF switch and the analog switch. The output signal is also used as the trigger for starting the data acquisition. After the pulse is generated, the system waits for several microseconds, and then starts to sample the first data point, which corresponds to the neural signal from channel 1; the second data point corresponds to channel 2, the third corresponds to channel 3, and so on. After all the channels are sampled for enough time, the Labview program process the data to visualize the signal waveform of each channel.

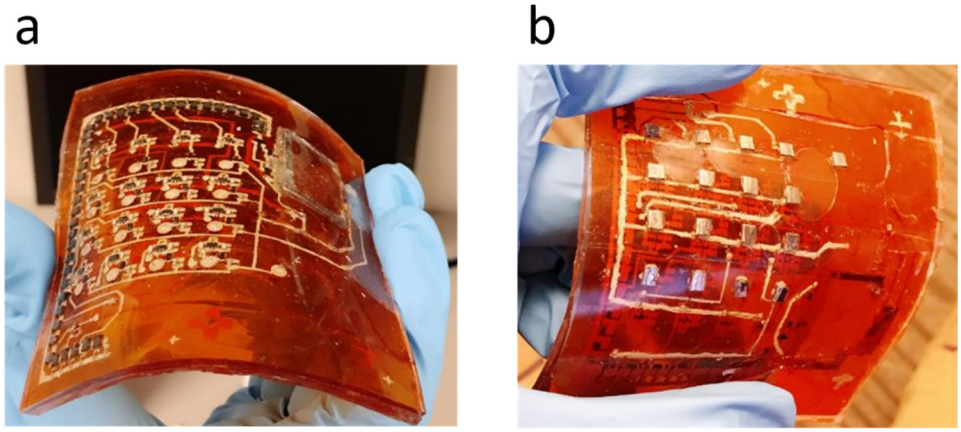

Figure 5.21. Images of a fabricated 16 channels passive wireless ECoG array. (a) The front side of the array contains all the electronics needed for wireless telemetry. (b) The backside of the array has 17 electrodes, of which 16 are used for neural recording and one is used for reference.

5.3 Device Fabrication and Verification

Based on the proposed passive wireless multichannel neural recording method, we fabricated a 16 channel wireless ECoG array prototype. **Figure 5.21** shows the front and back of the fabricated 16 channel wireless ECoG array prototype. The device was fabricated on a polyimide substrate. The circuit was constructed by screen printing conductive epoxy (EP21TDCSMed). All the passive electronic components were assembled using the same conductive epoxy. Totally 17 electrodes were placed on the backside of the device. 16 of the electrodes are used for recording and one is used as the reference electrode. All the electrodes were made from titanium foil and were connected to the front side circuits through vias. A layer of PDMS encapsulated and insulated the entire array, exposing only the backside titanium electrodes. Note all electronic components for wireless telemetry have been integrated and no additional circuit or battery is needed.

The wireless ECoG array was verified *in vitro* using emulated signals generated by an arbitrary function generator. Due to the limited number of input signal sources, we can only generate three different input signals simultaneously. Thus, to verify the functionality of each recording channel, we performed several tests. In each test, the function generators input emulated neural signals into different channels. The device was tested in air and the external antenna was placed 20 mm above the device. Before actual recording, the wireless output signal waveform is first verified using an oscilloscope to determine the actual time delay of the system.

Figure 5.22 – Figure 5.25 show the temporal waveforms of input and output signals recorded from four different testings of the fabricated wireless ECOG array. In test 1 **(Figure 5.22)**, three different shaped emulated signals, including square, sine, and pulse waves, each with 2 mV peak to peak amplitude, are inputted to channel 1, 3, and 5, respectively. Channel 7 and 9 are turned off (shorted to ground). Other channels are invalid. It can be seen that for all the channels, the wireless output signals closely follows the input signals despite some phase difference. Similarly, in test 2 – test 4, the input signals are connected to different channels, yet in all tests, we observe a good correspondence between the input and output signals. Overall, out of the 16 channels, we find that 11 channels are working properly, demonstrating strong coherence between input and output signals, whereas the other 5 channels do not function properly. These 5 channels lost their functions probably due to some unexpected damage of the circuit during the fabrication process, causing the breakage of electrical connections. To quantify the signal integrity and crosstalk between each channel, **Figure 5.26** summarizes the measured SNR and channel-channel isolation of the 11 working channels. Overall, the fabricated wireless ECOG array achieves at least 22 dB SNR in each channel and provides at least 8 dB channel-channel isolation. These results prove that our proposed wireless passive multichannel recording method is indeed feasible. The fabricated ECoG array is flexible and has extremely low heat generation. With further optimization, it has the potential to replace conventional wired ECoG electrode array, enabling long-term implantable wireless ECoG recording in future neurosurgical applications.

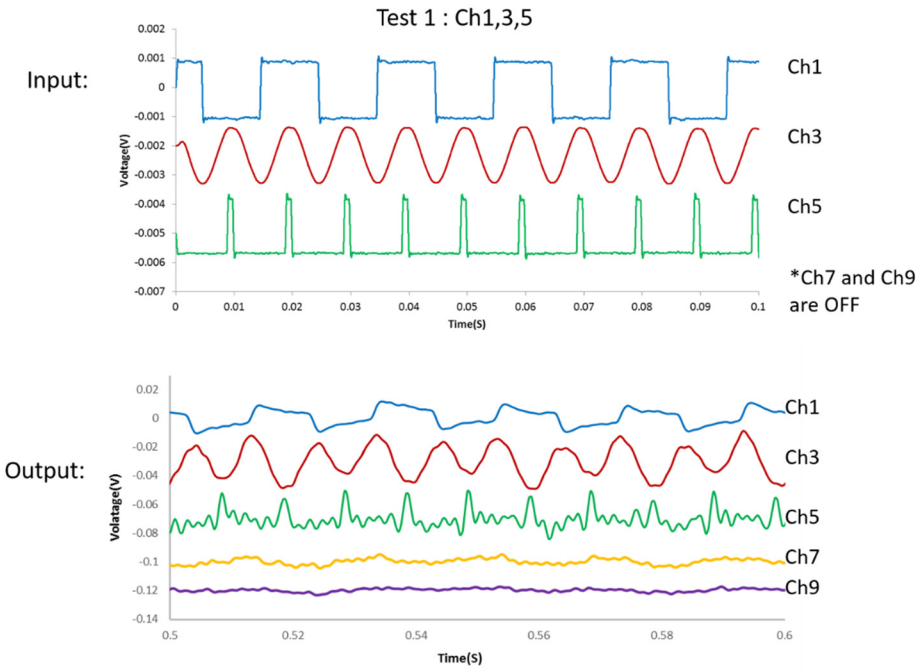

Figure 5.22. Test 1 of the fabricated 16 channels wireless ECoG array prototype. Temporal waveforms show the input and output signals at Ch 1, 3, 5, 7, and 9. Ch 7 and 9 are shorted to ground. For all the channels, the output signals follow the input signals well, despite the phase difference.

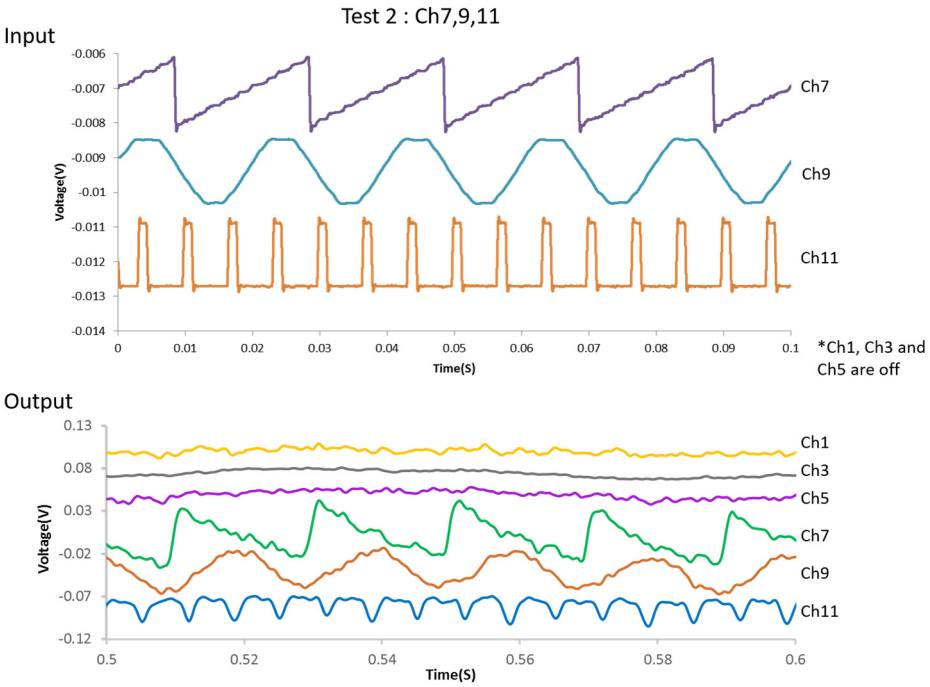

Figure 5.23. Test 2 of the fabricated 16 channels wireless ECoG array prototype. Temporal waveforms show the input and output signals at Ch 1, 3, 5, 7, 9, and 11. Channel 1,3 and 5 are shorted to the ground.

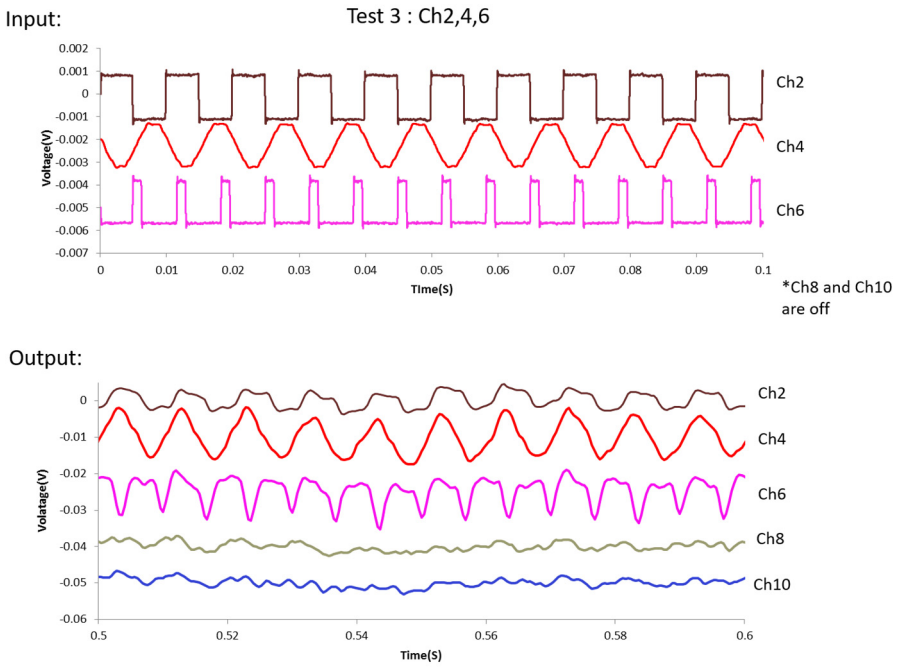

Figure 5.24. Test 3 of the fabricated 16 channels wireless ECoG array prototype. Temporal waveforms show the input and output signals at Ch 2, 4, 6, 8, and 10. Ch 8 and 10 are shorted to the ground.

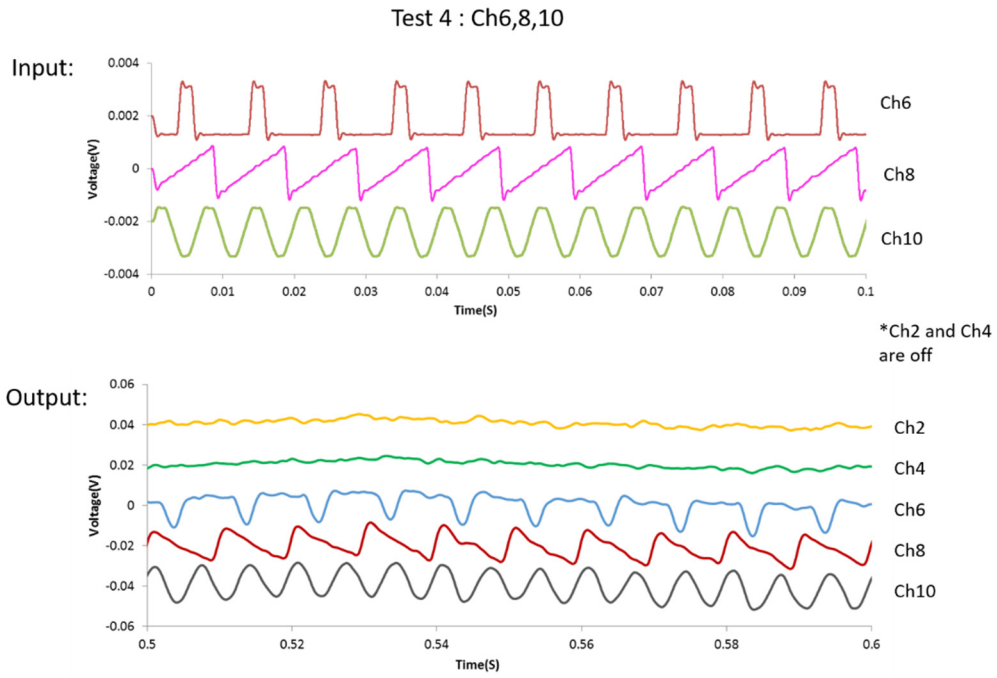

Figure 5.25. Test 4 of the fabricated 16 channels wireless ECoG array prototype. Temporal waveforms show the input and output signals at Ch 2, 4, 6, 8, and 10. Ch 2 and 4 are shorted to the ground.

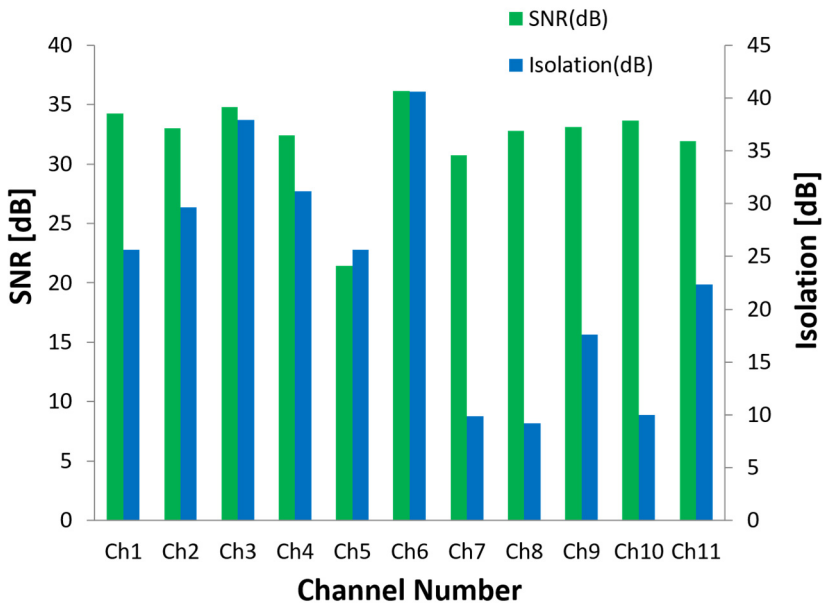

Figure 5.26. Summary of the measured SNR and channel-channel isolation for channel 1 - channel 11. Within the 11 working channels, the wireless ECOG array achieves at least 22 dB SNR and 8 dB channel-channel isolation.

CHAPTER 6

WIRELESS FULLY-PASSIVE ACQUISITION OF BIOPOTENTIAL

The wireless fully-passive recorders presented in previous chapters are intended to be implanted inside the skull for neuropotential acquisition. Our proposed wireless fully-passive sensors can also be used to measure other types of biosignals, especially, the body biopotentials, including Electrocardiogram (ECG), Electromyogram (EMG), and Electrooculogram (EOG). All of these signals are very useful as they can provide vital information about organs and help doctors to diagnose a number of diseases and abnormalities.

In this chapter, we present a small-size, light-weight, flexible sensor, capable of acquiring biopotentials in real-time in a wireless and fully-passive manner, offering up to 240 mm wireless communication by consuming nearly zero power, except the parasitics. The RF backscattering effect described in the last chapter is used to establish wireless communication. However, there are several differences between the neural recorder and the biopotential sensor. The neural recorder targets to record neural signals of the brain. All design parameters and implementation methods are geared toward implantation in the body, specifically inside the brain. The biopotential sensor, however, aims to measure body potentials on the skin. This results in large differences in the design parameters. For instance, the implant antenna depends heavily on the dielectric constant (permittivity) of its surrounding material. The permittivity of body tissue is as high as 50, while that of air is close to 1. To enable fully-passive wireless biopotential recording in air, the design, simulation, and verification needs to be redone from the scratch. On the other hand, the

size of the device is larger as it does not need to be implanted. The larger footprint also results in a longer wireless communication distance between the sensor and the external antenna. The wireless fully-passive biopotential sensor is fabricated on a 90 μm-thick flexible polyimide substrate with a footprint of 18 x 15 x 0.5 mm^3. Using an array of varactor diodes to enhance the mixing operation, the sensor achieves wireless communication up to 240 mm distance. A deep learning algorithm is applied to analyze the signal quality of wirelessly acquired data, along with the data from commercially-available wired sensor counterparts. Wired and wireless data show a < 3% discrepancy in deep learning testing accuracy for ECG and EMG signals. Wireless acquisition of EOG further demonstrates accurate tracking of horizontal eye movement, indicating successful detection of biopotentials signal as low as 250 μV_{PP}. These findings support that the real-time wireless fully-passive acquisition of on-body biopotentials is feasible. The sensor may find various uses for future clinical research.

6.1 Wireless Fully-passive Biopotential Sensor

Figure 6.1 shows the schematic of the wireless fully-passive biopotential sensor. Like the neural recorder, the system contains two parts: 1) the wireless fully-passive sensor (**Figure 6.1a**) for acquiring biopotentials and 2) the external interrogator (**Figure 6.1b**) for wireless data readout and display. The major modification on the sensor is the structure of the antenna and the circuitry.

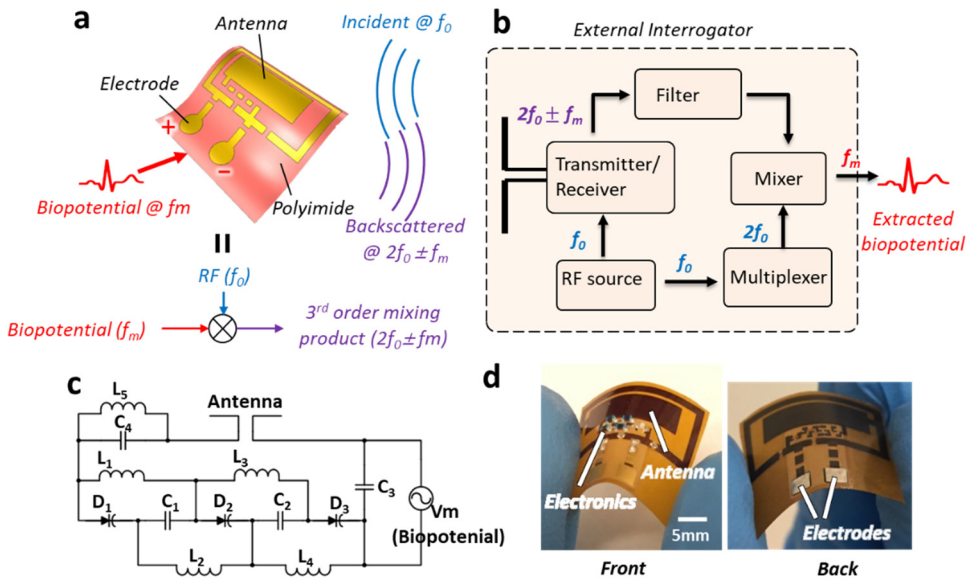

Figure 6.1. Wireless fully-passive biopotential sensor. (a) The schematic of the sensor. Fabricated on a polyimide substrate, the sensor is constructed entirely by passive components, including a planar antenna, varactors, inductors, and capacitors. (b) The simplified structure of the external interrogator. RF source generates the carrier (f_0) to be transmitted to the sensor as well as to be used in synchronous demodulation. The backscattered mixing products, including 3rd order ($2f_0 \pm f_m$), go through a series of filters and amplifiers to reach a down-converting mixer where the 3rd order product ($2f_0 \pm f_m$) is mixed with $2f_0$ to extract the biopotentials (f_m). (c) Equivalent electronic circuit model diagram of the sensor. Voltage source V_m represents low frequency (f_m) biopotentials collected at the electrodes. An integrated antenna on the sensor feeds RF carrier (f_0) to the varactor diodes array and simultaneously forms a short-circuit path for low-frequency biopotentials (f_m), enabling mixing of the two signals. (d) Photos of a fabricated and assembled sensor on a polyimide substrate, having a footprint of 18 x 15 x 0.5 mm^3. The 65 μm-thick polyimide substrate contains an antenna, discrete surface mount electronic

components, including varactor diodes, and contact electrodes located at the backside to collect biopotentials.

To maximize signal power at the 3rd order mixing products ($2f_0 \pm f_m$), the antenna and electronics of the sensor need to be designed uniquely. The design requirements of the antenna are vastly different from any traditional antennas that possess 50 or 75 ohms impedance (Pozar 2009). As no resistive load exists, the unique RF backscattering wireless communication leads to zero power consumption of the electronics on the sensor, neglecting parasitic ohmic loss on metal traces. No existing antenna pattern satisfy the need; instead, we designed a unique antenna aiming to deliver the following characteristics: 1) the antenna has optimized gain at two frequency bands (f_0, 2.33 GHz, and $2f_0$, 4.66 GHz) and 2) port impedance at both frequencies are largely inductive to match the capacitance of varactors (which will be described later). The antenna is constructed and simulated in High Frequency Structure Simulator (HFSS, Ansoft).

Figure 6.1c shows the schematic of the equivalent circuit diagram of the sensor. The circuit contains two paths for high-frequency and low-frequency signals, respectively. At RF frequency (f_0), capacitors C_1, C_2, and C_3 have low impedance, equivalent to short circuits. Inductors L_1 — L_4, are equivalent to open circuits. Therefore, the RF signal from the antenna is directly outputted to the varactor diodes D_1 — D_3. At low frequency (f_m), the capacitors C_1 — C_3 are open circuits while the inductors L_1 — L_4 are short circuits, respectively. Consequently, the low-frequency biopotential signal is simultaneously coupled to each of the varactor diodes D_1 — D_3. By using three varactor diodes rather than

one, the equivalent impedance of the circuits at f_0 is increased by three times, making the impedance match easier to achieve. L_5 and C_4 further help the impedance matching, their values are determined experimentally.

The estimation of backscattered power is accomplished using the harmonic balance simulation in Advanced Design System (ADS, Keysight, **Figure 6.2**), where the nonlinear behavior of varactor diodes, parasitic elements, and the HFSS simulation data of the antenna link are all taken into account.

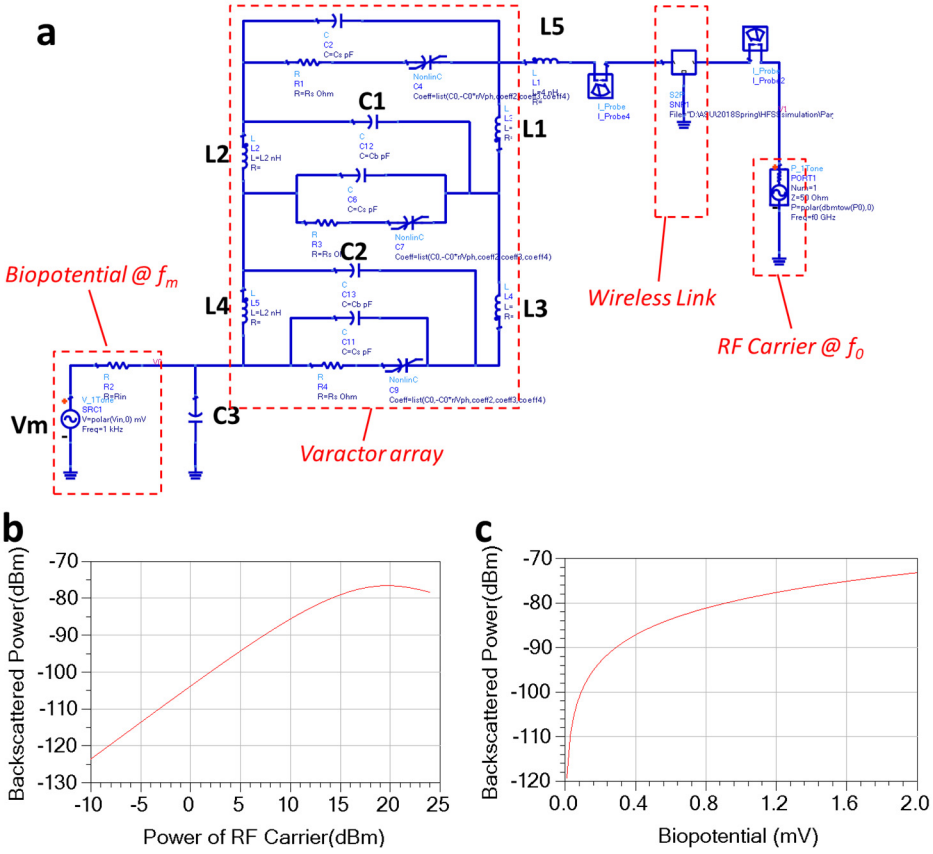

Figure 6.2. Simulation of the wireless fully-passive biopotential sensor. (a) Equivalent circuit model constructed in ADS (Advanced Design System, Keysight). The two ports S-

parameter matrix models the wireless link between the external antenna and the integrated antenna of the sensor. The S-parameter data at the f_m, f_0, and $2f_0$ are imported from HFSS simulation results. The varactors are modeled as nonlinear capacitors whose capacitance is controlled by the voltage applied on terminals. The parasitic parallel capacitance, serial resistance, and inductance are also included. Biopotential signals are represented by a voltage source with large (>1M Ohm) input impedance. The ADS simulation model uses Harmonic Balance simulation to calculate the 3rd order harmonic mixing products picked up at the external antenna. (b, c) Simulation results of the backscattered power of the 3rd order harmonic mixing product ($2f_0 \pm f_m$) as a function of RF carrier power (b) and input biopotential amplitude (c). In (b) the input biopotential is 2 mV_{pp} and in (c) the RF power is 25 dBm. The distance between the sensor and the external antenna is fixed at 50 mm.

The wireless fully-passive sensor is fabricated using standard flexible PCB technology. The layout of the antenna and the circuitry is drawn using Altium Designer (Altium). The design file is sent out to a PCB fabrication service company (Rush PCB Inc) for fabrication. Fabricated sensor PCB consists of a 1 mil polyimide substrate, a 0.7mil copper layer, and a 2 mils polyimide coverlay. The exposed metal pads use ENIG (electroless nickel immersion gold) surface finish. Discrete electronic components, including varactor diodes, inductors, and capacitors are assembled on the sensor using conductive epoxy (12642-14, Electron Microscopy Science). After the assemble, the sensor is coated with a 10um thick parylene-C. A fully assembled senor has a total footprint

of 18 x 15 x 0.5 mm^3. **Figure 6.1d** shows photos of an assembled wireless fully-passive sensor, demonstrating its small size and high flexibility.

6.2 The External Interrogator

The external interrogator for wireless telemetry has the same structure as the one which is described in Chapter 4. The block diagram of the external interrogator is shown in **Figure 6.3**. In short, the RF source (RF function generator E4432B, Agilent) produces a 2.33 GHz (f_0) RF carrier with a tunable power amplitude, which is equally divided into two routes through a power splitter. One route doubles the frequency to be 4.66 GHz via a frequency multiplexer, for local oscillator (*LO*) of down-converter, demodulator. The second route amplifies and filters the RF carrier, and passes the carrier to a dual-band (2.4 GHz/5 GHz) ceramic chip antenna (A10194, Antenova). The dual-band antenna picks up the 4.66 GHz ($2f_0 \pm f_m$) backscattered harmonic products from the sensor. The circulator isolates the backscattered harmonic products from the RF carrier. A direct converter mixes 4.66 GHz *LO* with the processed backscattered harmonic products to down-convert the output to be f_m. The phase shifter provides phase tunability at the external interrogator between $2f_0 \pm f_m$ and *LO* ($2f_0$). The output signal of the external Interrogator is recorded by a Data Acquisition (DAQ) system (USB-6361, National instrument) at 360 (ECG) and 1000 (EMG and EOG) Hz sampling rates, respectively. The DAQ transfers the recorded biopotential data to an external PC, where they are digitally filtered before being displayed in a LabView (National Instrument). Three different types of biopotentials are considered as measurement targets: ECG, EMG, and EOG. Their amplitude and frequency range are

listed in **Table 6.1**. Parameters of the digital filter are selected based on the frequency characteristics of each type of biopotentials, which are detailed in the result section.

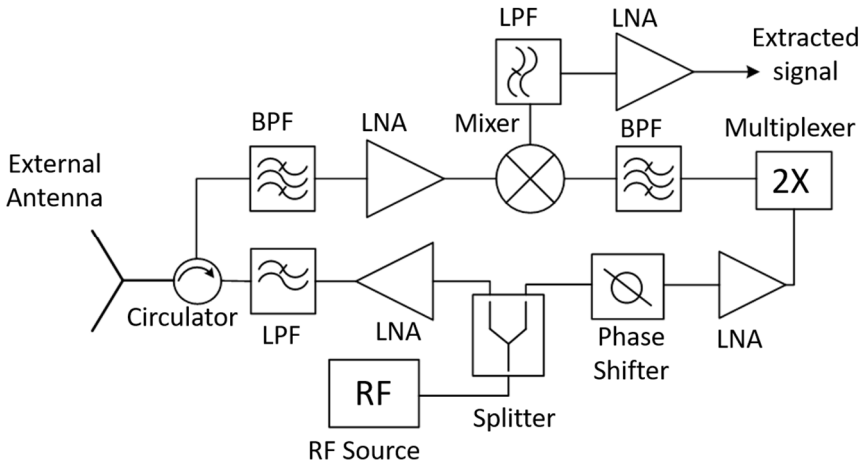

Figure 6.3. Structure of the external interrogator for wireless fully-passive biopotential recording.

Table 6.1. Amplitude and frequency range of target biopotentials

Biopotentials	Amplitude Range	Frequency Range
Electrocardiogram (ECG)	1 — 5 mV	0.5 — 20 Hz
Electromyogram (EMG)	0.1 — 10 mV	50 — 200 Hz
Electrooculogram (EOG)	0.1 — 1 mV	0 — 30 Hz

6.3 Material and Method

6.3.1 Study Design

We studied the efficacy and accuracy of the wireless fully-passive biopotential sensor to collect biopotentials such as ECG, EMG, and EOG. Ground truth measurements were taken by commercially-available sensors. To demonstrate the feasibility, we recruited volunteers to attach the wireless sensors onto specific locations of their bodies to collect biopotentials. Randomization was not applicable and investigators were not blinded. All participants provided informed consent, and the studies were approved by the Arizona State University Institutional Review Board (IRB).

6.3.2 Biopotential Recording Protocols

ECG: The standard practice for ECG acquisition measures biopotentials at bipolar leads, (lead I, II, III in a three-electrode system), in which lead II is the most frequently viewed lead in clinical practices (Hockman, Mauck Jr, and Hoff 1966) and is chosen as our target. Two electrodes are placed on the subject's right shoulder and lower edge of the left ribcage (RA and LL), respectively (**Figure 6.4**). The wireless fully-passive sensor is attached to the subject's left chest using a medical double-sided tape, and the two leads are connected to the sensor. A wired ECG sensor (AD8232, Sparkfun) is placed in parallel to record the ECG signal concurrently for real-time data comparison. A reference electrode (LA) is placed on the subject's left shoulder (not shown in **Figure 6.4**) to provide the reference potential for the wired sensor.

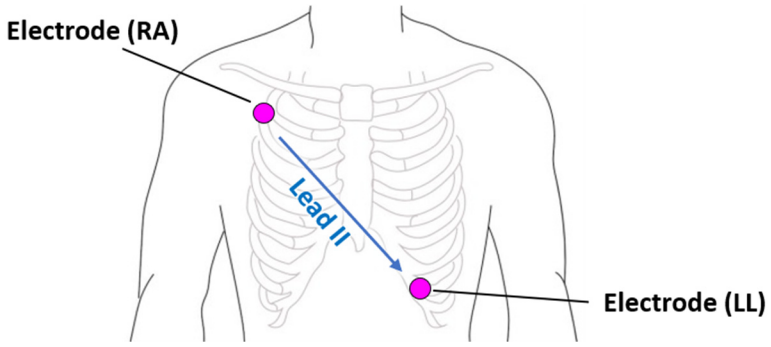

Figure 6.4 Electrodes placement position for the wireless ECG acquisition. The two measurement electrodes RA (right arm) and LL (left leg) are connected to the wireless fully-passive sensor as well as a commercial wired sensor through electrical leads. A third electrode placed at the left shoulder (not shown in the plot) provides reference potential for the commercial sensor. This setup measures the Lead II ECG.

EMG: EMG signals are measured at three commonly used muscles on the participants' limbs, including biceps brachii, extensor digitorum, and tibialis anterior, as shown in **Figure 6.5**. The testing subject performs the following practices to generate EMG signals at the target muscles: 1) biceps — bending the elbow to 90 degrees; 2) extensor digitorum — bending the wrist upward; 3) tibialis anterior — pulling the foot upward. For each of the practice, the subjects perform the muscle contraction for 5 seconds, relax the muscles for 10 seconds, and then repeat 3 times to complete one cycle. The subjects perform the cycle 6 times, with approximately 1 minute resting between each cycle. A commercial one-channel EMG sensor (Myoware Muscle Sensor) is used to record wired EMG data for reference. In all EMG testings, the inter-electrode distance (IED) is set as 40 mm. Increasing the IED will not produce stronger signal amplitude(Beck et al. 2005). The

recorded EMG signals are passed through a 20 Hz high-pass filter to remove motion artifacts(Potvin and Brown 2004).

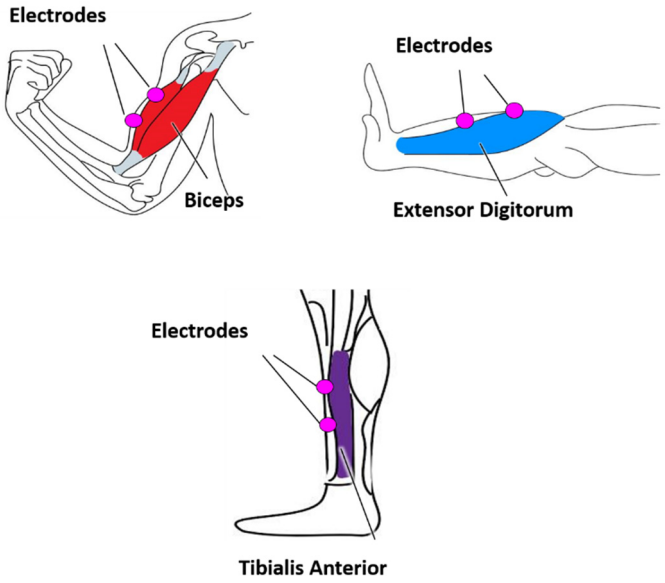

Figure 6.5. Schematic of electrodes placement for the wireless fully-passive EMG recording. The colored region highlights the target muscles, including biceps (red), extensor digitorum (blue), and tibialis anterior (violet). Electrodes are connected to the wireless sensor via electrical leads. A commercial one-channel wired EMG sensor is used for reference.

EOG: Standard EOG measurement needs five electrodes(López et al. 2016): two electrodes are placed beside the external canthus of each eye for measuring horizontal eye movement (channel 1); two electrodes are placed just above and below either one of the eyes to measure vertical movement (channel 2). The reference electrode is usually placed

on the forehead. This work targets only the horizontal channel. An electrode (+) is placed beside the external canthus of the left eye; the reference electrode (-) is placed at the center of the forehead (**Figure 6.6**). Both electrodes are connected to the wireless fully-passive sensor through electrical leads. To minimize the impact of artifacts associated with motion or other sources, the wireless sensor is placed and fixed on the bench, where the external antenna is placed 30mm above the sensor.

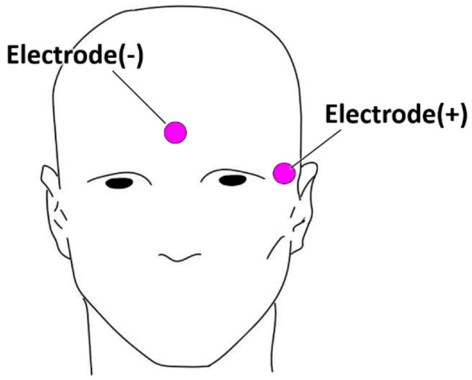

Figure 6.6. Electrode placement for the wireless fully-passive acquisition of horizontal EOG.

All the electrodes used for biopotential recording are commercial disposable electrodes (H124SG, Corvidien). The diameter of the electrodes is 24 mm, thus the impedance to the skin is expected to be small. We characterized the minimum detectable signal of the wireless system as a function of the impedance (**Figure 6.7**), demonstrating 140 μV_{pp} for an input resistance as high as 120 KΩ, high enough to measure the body biopotentials.

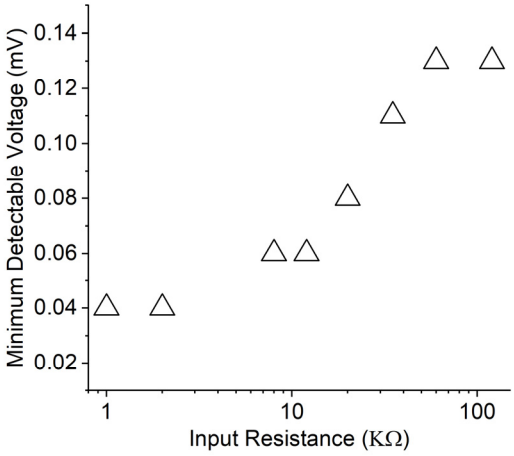

Figure 6.7. The measured minimum detectable voltage of the sensor as a function of input resistance. The input resistance represents the impedance at the electrode-skin interface. The radiated RF power from the antenna is 28 dBm, the input signal is a 1 kHz square wave.

6.3.3 Signal Analysis by Deep Learning

Recent advances in the deep learning technique have shown its promising potential in the field of biopotential signal analysis, such as ECG classification(Kiranyaz, Ince, and Gabbouj 2016; Schmidhuber 2015). Inspired by the structure of biological neural networks, deep learning is an algorithm that attempts to abstract useful information from the raw data by using multiple processing layers that consist of complex structures, including dense layers, convolutional neural networks (CNN) layers, and so on. Many studies have pointed out that the signal quality of the raw data inputted to a deep learning model has a significant impact on final testing accuracy(Karahan et al. 2016; Dodge and Karam 2016). A supervised deep learning algorithm is adopted in our study as a tool for signal quality

analysis and comparison between the data from a commercially-available wired sensor and that from the wireless fully-passive sensor.

We develop a deep learning algorithm on a Laptop computer. Various deep learning models on Keras are used to analyze the biopotentials. ECG and EMG, whose signal shape rather complex, require two 1D CNN layers with three full-connection dense layers. A simple-shaped EOG only demands three full-connection dense layers (**Figure 6.8**). Each model is trained by 30 epochs of training data set, followed by being tested with the testing data set to obtain testing accuracy. In addition, various slicing methods have been used, depending upon the characteristics of biopotentials and sampling frequency.

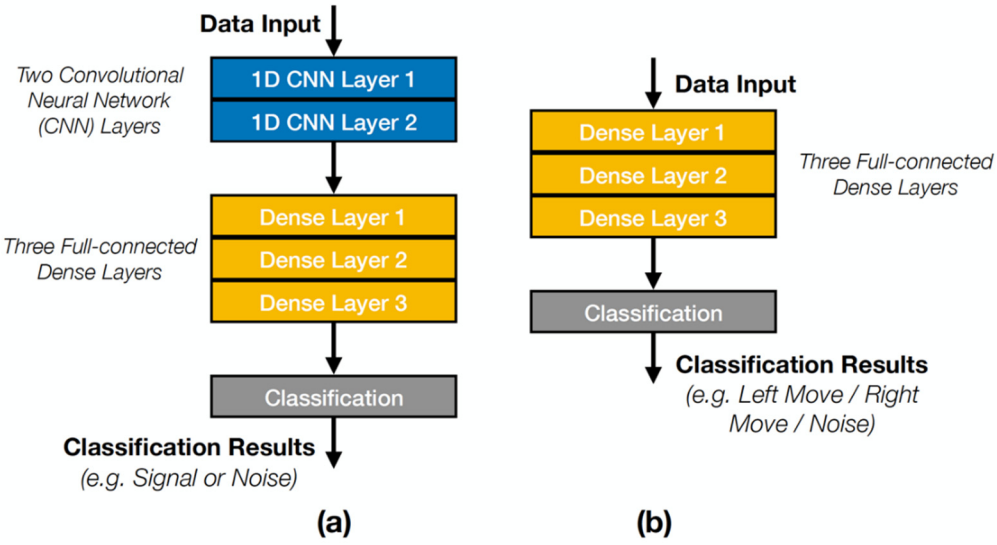

Figure 6.8. Structure diagram of the deep learning model for biopotential analysis. The structure (a) is used for analyzing the ECG and EMG signals which are composed of rather complex shapes. The 1D CNN is able to recognize the signal changes in a short time period, making it ideal for the ECG and EMG signal analysis. For ECG signal analysis, the 1st

CNN layer has 36 1x5 convolutional kernels, and the 2nd CNN layer has 72 1x5 convolutional kernels. For EMG signal analysis, the 1st CNN layer has 256 1x7 convolutional kernels, and the 2nd CNN layer has 512 1x7 convolutional kernels. The dense layer is the most basic method in deep learning, allowing simple classifications of the input data. The results from CNN layers are fed to three dense layers and then the model gives out the final classification results. The structure (b) is used for analyzing the EOG signal. For simple-shaped signals the deep learning model is preferred to be simple, otherwise, the model may run into the overfitting challenge. The model for EOG analysis adopts three dense layers for the classification.

The deep learning algorithm aims to detect the QRS complex in ECG data. The typical duration of the QRS complex is less than 200 ms, thus a segment length of 555.6 ms (200 points, 360 Hz sampling rate) is chosen to capture the complete QRS features. To ensure the continuity of the analysis, the segment is shifted with a shifting length of 138.9 ms (50 points, 360 Hz sampling rate), producing 150 overlapped points between two adjacent segments. The algorithm is used to distinguish EMG from the background noise. EMG signals are continuous and have a rather random temporal shape, which makes them challenging to distinguish from noise. To achieve the best classification ability from the algorithm, the segment length and shift are chosen as 1 second (1000 points, 1000 Hz sampling rate) and 0.25 seconds (250 points), respectively. In EOG testing, the deep learning algorithm slices EOG and noise separately. The EOG signals are precisely sliced at the points when a change of eye potential occurs. The duration of the potential change

spans approximately 1 second, which aligns with the length of one sliced segment (1000 points, 1000 Hz). The noise segments are sliced where the eye potential remains relatively constant and the length of the noise segments is chosen as 1 second (1000 points). Segment shifting is not applied in EOG signal analysis.

All sliced segments are labeled manually, normalized, and followed by random arrangement. The training and testing data sets use 70% and 30% of the raw data, respectively.

6.4 Experiment Results

6.4.1 Benchtop characterization

The verification of the wireless fully-passive sensor is first performed on benchtop with an emulated signal (**Figure 6.9**) via an arbitrary function generator (33250A, Agilent). The power of the 3rd order mixing product ($2f_0 \pm f_m$), collected at the external interrogator, measures the efficacy of backscattering via spectrum analyzer (HP 8563E, Agilent). The power of backscattered products depends upon the radiation power of the external interrogator and the spatial distance from the sensor to the interrogator. For initial testing, the emulated signal is set as a sine wave of $2mV_{pp}$ at 1 kHz. As the amplitudes of the two mixing products ($2f_0 + f_m$ and $2f_0 - f_m$) are identical, we measure only the upper sideband ($2f_0 + f_m$).

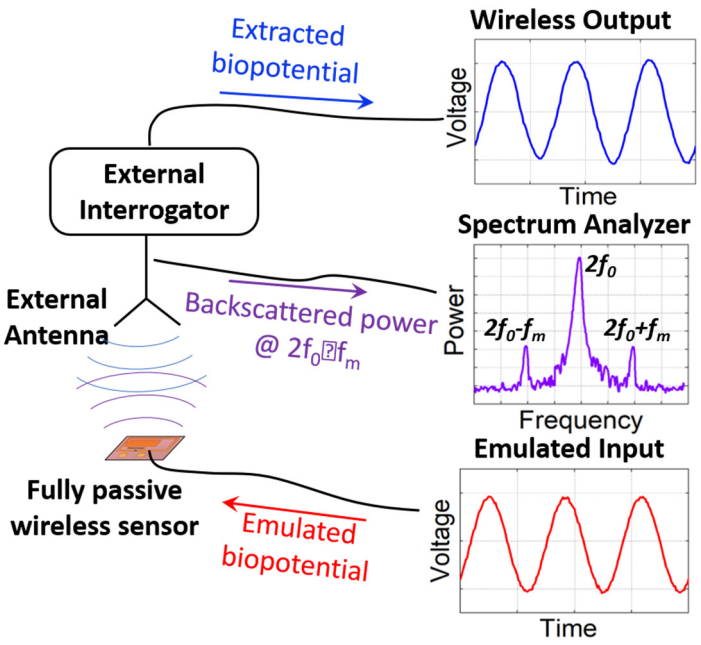

Figure 6.9. Experiment setup of benchtop characterization of the wireless fully-passive sensor. An arbitrary function generator inputs emulated biopotentials to the sensor through electrical leads. The RF backscattering wireless telemetry is verified both in the time and frequency domain.

Figure 6.10a shows the power of the backscattered mixing product drops with the decrease of radiation power of the external interrogator at various distances (60 mm, 120 mm, 240 mm). The minimum detectable power, determined by the noise level of the spectrum analyzer, marks approximately -130 dBm. To comply with FCC regulation, the maximum radiation power remains at 30 dBm(Obeid et al. 2008). An ADS circuit model marks the simulation predictions. The power of the backscattered product decreases by 13-15 dB as the transmission distance doubles, agreeing well with the EM wave free-space propagating model(McClaning 2012). For a 2 mV_{pp} sine wave input signal, the sensor

demonstrates a working distance of 240 mm. The maximum working distance for the device to reliability measures biopotentials will be discussed in the next section. **Figure 6.10b** shows the temporal waveforms of output at different input shapes, including sine, square, and triangle. All three differently shaped signals exhibit the minimum discrepancy with inputs, demonstrating the sensor's capability to reliably extract both simple (sine) and complicated (square and triangle) waveforms.

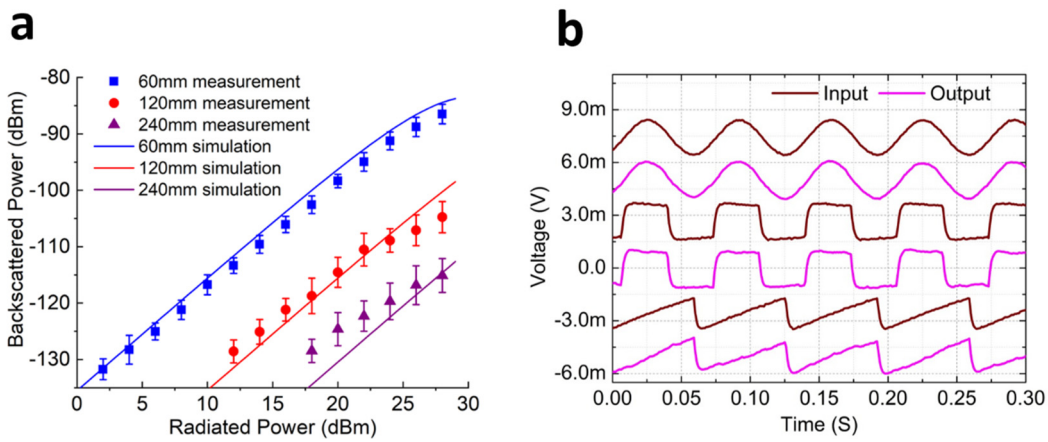

Figure 6.10. Results of the benchtop characterization of the wireless fully-passive biopotential sensor. (a) Measured and simulated spectrum power of the backscattered 3rd order mixing product, 2f0 ± fm, as a function of the external antenna radiation power at 60, 120, and 240 mm wireless distances, using an emulated biopotential of 2 mVpp at 1 kHz. The error bar represents the standard deviation. (b) Temporal profiles of the emulated inputs and extracted wireless outputs show almost all types of inputs can be extracted by the wireless fully-passive telemetry (emulated inputs (brown) are 2 mVpp and 15 Hz periodic sine, square, and triangle wave, respectively, whereas wireless outputs (pink) are normalized and offset to facilitate the comparison).

6.4.2 Electrocardiogram (ECG)

Figure 6.11a shows the normalized temporal ECG waveforms recorded from the wireless fully-passive (red) and wired (blue) sensors, respectively, in 3 seconds. Both waveforms are filtered by a 0.3~30 Hz bandpass filter and a 60 Hz notch filter. The signal distortion due to the filters can be negligible as ECG spans primarily 0.5~20 Hz(C.-H. Lin 2008). Correlation analysis between the two waveforms produces a correlation coefficient as high as 0.8762, with a root-mean-square error (RMSE) as low as 0.0279. Both waveforms clearly show the QRS complex and T wave. However, the P wave, which has a small amplitude of less than 250 μV_{pp}, is barely distinguishable in the wirelessly recorded waveform. The wireless ECG data also exhibits a noticeable baseline distortion, possibly resulted from the breathing activity of participants. For temporal ECG features, measurement results from wired/wireless sensors show little discrepancy. For instance, the QTc interval measured by the wired and wireless sensor is 0.370 sec and 0.362 sec, respectively. The 8 ms difference is within the acceptable accuracy since the standard manual determination of QTc has an accuracy level of as large as 20-40 milli-sec(Goldenberg, Moss, and Zareba 2006). This supports that the wireless sensor may be useful for diagnosing diseases and abnormalities such as Torsades de pointes (TdP)(Yap and Camm 2003) and acute destabilized heart failure (ADHF)(Breidthardt et al. 2007).

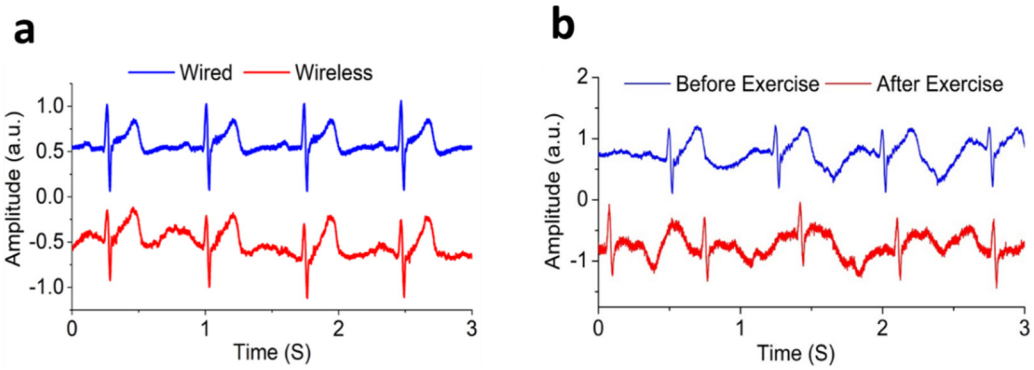

Figure 6.11. Wireless fully-passive acquisition of Electrocardiogram (ECG). (a) ECG signals recorded from the wireless fully-passive sensor in comparison with the output of a commercial wired ECG sensor that is recorded simultaneously. Both signals are normalized. The unit of amplitude is arbitrary unit (a.u.). (b) Wireless fully-passive recording of ECG before/after the participant performs a 5-minute jogging exercise.

To induce a change in heartbeat rhythm, the participant performs a jogging practice at 6~7 km/h for 5 minutes. The heartbeat rate of the participant changes from 80/minutes to 94/minutes after the short-term jogging practice, as shown in **Figure 6.11b**. The recorded wireless ECG data contains an undesirable baseline distortion introduced by breathing activity and other motion artifacts. The artifacts undoubtedly harm the ECG signal integrity, impeding accurate feature extractions from recorded data. To reduce the effect of artifacts, a 16^{th}-order polynomial fitting is adapted to remove the baseline drifting curve (**Figure 6.12**).

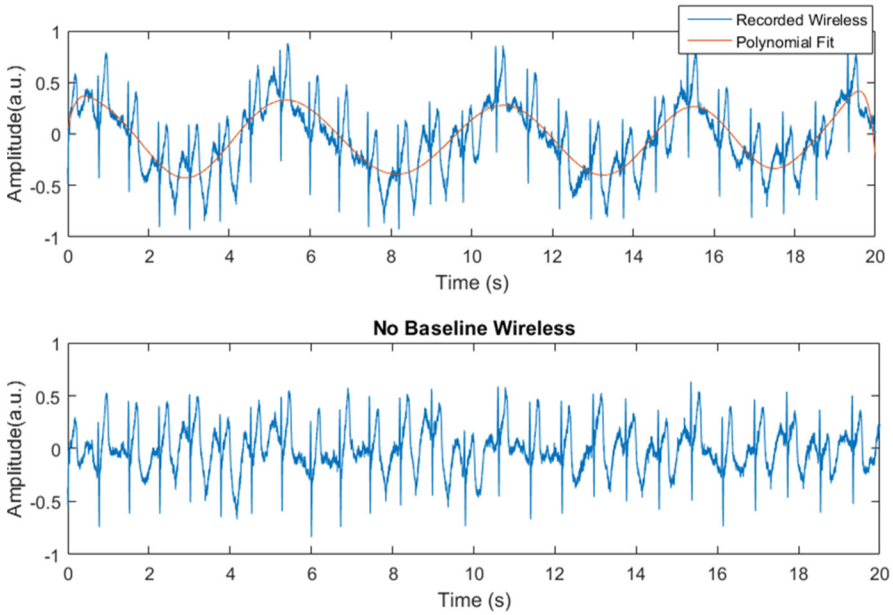

Figure 6.12. Polynomial fitting method to remove baseline drifting and reduce artifacts in the wireless ECG measurement. (a) Wireless ECG waveform before baseline removal. The low-frequency baseline drift of the wireless data originates from testing the participant's breathing activity (artifacts). The red straight line shows the baseline drifting curve estimated with a 16th-order polynomial fitting in MATLAB. Subtracting this curve from (a) yield baseline removed wireless waveform (b). Using this method, the impact of breathing artifact is largely reduced.

The wireless fully-passive sensor is further evaluated by analyzing the signal quality as a function of the wireless transmission distance and angle. The ECG signal quality is assessed by using 1) the accuracy of heartbeat rate measurement and 2) the testing accuracy of the applied deep-learning model which distinguishes ECG features from background noise**. Figure 6.13a** shows the testing accuracy and error as the wireless transmission distance varies from 100 mm to 370 mm. At a given distance, both the

commercial wired sensor and wireless fully-passive sensor record participants' ECG continuously for 10 minutes. The numbers of heartbeat in each group of data are counted and compared. Within 270 mm distance, the wireless heartbeat measurement shows very small errors (<0.5%) during the continuous 10 minutes recording. The heartbeat miscount occurs only once or twice in approximately seven hundred times when the QRS features are shadowed by artifacts. At distances larger than 270 mm, the heartbeat measurement error of the wireless sensor exhibits an exponential increase, which is primarily due to the SNR loss. Meanwhile, the deep learning analysis reveals that when the distance remains less than 240 mm, the testing accuracy of the wireless ECG is comparable to that of the wired counterpart, with <3% discrepancy. At over 240 mm distance, such discrepancy is amplified more than three times, resulting in the testing accuracy of the wireless data dropping to below 90%. As distances increase over 320 mm, the testing accuracy of the wireless data suffers a sudden drop to as low as 60%, suggesting a significant degradation of ECG data quality.

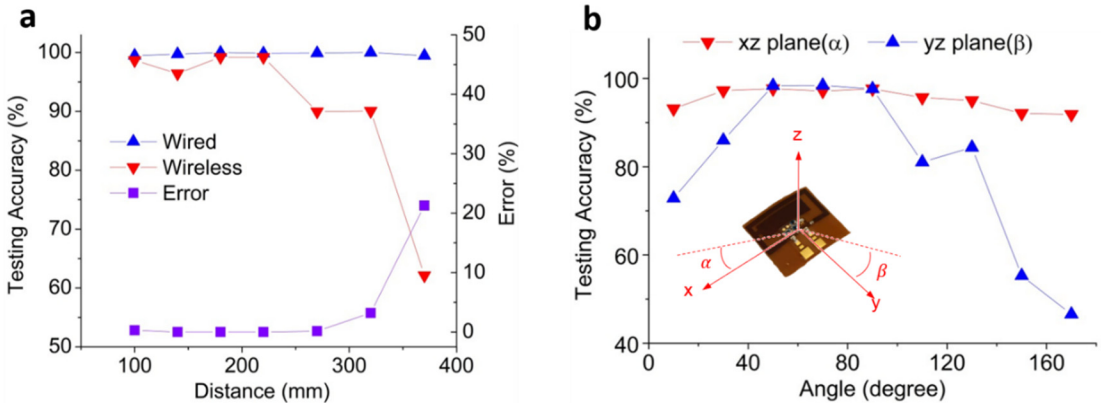

Figure 6.13. Distance and angle dependence of the wireless fully-passive biopotential sensor. (a) The signal quality of the wireless and wired ECG data as a function of wireless distances. A higher deep learning testing accuracy represents better signal quality, i.e., less noise and distortion. The error represents the percentage of miscounted heartbeat in the wireless data, comparing to the wired counterpart. (b) The signal quality of the wireless ECG data varies as a function of the angle between the external antenna and the sensor. The Inlet shows the coordinate used in this measurement. The labeled angle represents the direction where the external antenna locates.

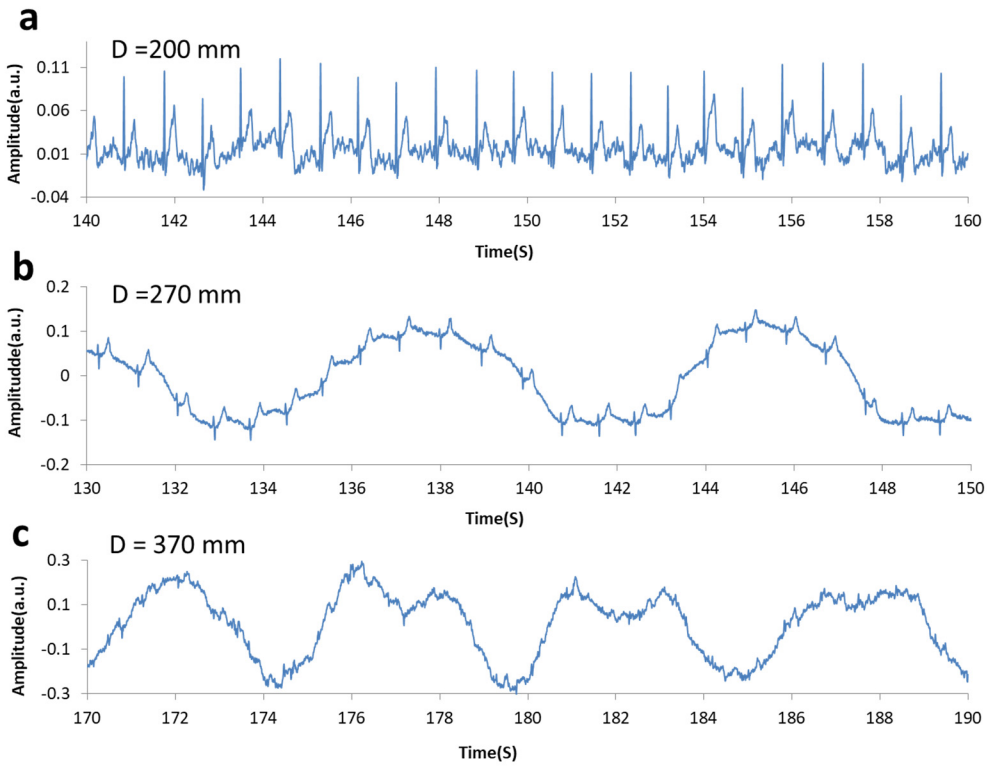

Figure 6.14. Artifact and noise of the wireless ECG at different distances. (a)The waveform of wireless ECG measured at D = 200 mm. At this distance, the ECG signal features are easily distinguishable. Although the breathing artifact exists, their amplitudes are insignificant comparing to the target signal. (b) Wireless ECG waveform at D = 270 mm. A clear breathing pattern can be seen in the ECG baseline. As the amplitude of the ECG signal attenuates with the increase of distance, motion artifacts begin to dominate the waveform. (c) The wireless ECG waveform at D = 370 mm. At this distance, the SNR of wireless ECG drops to a level that features of ECG (P, QRS, and T wave) become almost indistinguishable from noise and artifacts.

A further observation at the ECG temporal profile shows that the drop of deep learning testing accuracy may correlate to the amplitude of the signal, artifacts, and noise (**Figure 6.14**). Below 240 mm, the ECG features are easily distinguishable in the wireless data. The artifacts exist, yet their amplitudes are insignificant comparing to that of the target signal. Over 240 mm, as signal amplitude attenuates, the artifacts begin to dominate the waveform. When the distance reaches beyond 320 mm, the SNR drops to a level that the features of ECG (P, QRS, and T wave) become almost indistinguishable from noise and artifacts. Thus, we summarize that the wireless fully-passive sensor has a working distance of 240 mm, where the sensor maintains its best performance in both heartbeat detection and deep learning analysis. Due to the elimination of any kind of power source on the sensor, our operating distance cannot compete with what is offered by battery-powered devices. Comparing to other recently developed battery-free, flexible sensors that have similar footprints(Fonseca et al. 2006; J. Kim et al. 2016; Xu et al. 2014), our sensor achieves the highest operating distance. This attractive feature may facilitate the application of the sensor in more practical settings.

The signal quality of ECG is also a function of antenna radiation angle, the angle between the external antenna and the antenna on the wireless fully-passive sensor. Both the sensor and external antenna are designed to have maximum gain perpendicular to their surface plane (90 degrees, z-axis in **Figure 6.13b**). **Figure 6.13b** shows the variation of deep learning testing accuracy as the radiation angle changes in the two vertical planes (XZ plane and YZ plane), at a given distance of 140 mm. The testing accuracy in the XZ plane is rather independent of angle change, maintaining > 90% for the entire angle span (0 –

180 degrees). In the YZ plane, the testing accuracy exhibits strong dependency on angle arrangement, achieving the best results in the range of 50 – 90 degrees. Different angular response in the two vertical planes possibly originates from the intrinsic radiation pattern of the external dual-band antenna (A10194, Antenova).

6.4.3 Electromyogram (EMG)

Figure 6.15 shows normalized wired/wireless EMG waveforms measured at biceps brachii, extensor digitorum, and tibialis anterior muscle, respectively, during one cycle of the muscle contraction practice. In all cases, the wireless EMG show excellent correspondence with the wired counterparts. Zooming in on the waveforms further reveals that the wireless data almost overlap with the wired data. The good correspondence between the wired and wireless data comes primarily from the remarkable reduction of low-frequency noise and motion artifacts, which are filtered out by the 20 Hz high-pass filter, thereby improving the wireless signal fidelity. It should also be noted that during the 6 cycles of muscle contraction practices, EMG data recorded at the three muscles exhibit different SNRs. As shown in **Table 6.2**, EMG measured at the biceps brachii have the best signal quality, where wired and wireless data achieve an average SNR of 25 and 21 dB, respectively. In comparison, the average SNRs at the extensor digitorum is 16 dB and 14 dB for wired and wireless measurements, respectively. At the tibialis anterior muscle, the averaged SNRs become 7 dB (wired) and 6 dB (wireless), and only 1 in 6 cycles of EMG data achieve the SNR over 10 dB. The degradation of signal quality at the tibialis anterior muscle may be explained by the uncertainty of electrode location over or across the

innervation zone. Previous studies(Rainoldi, Melchiorri, and Caruso 2004; Saitou et al. 2000) have shown that the amplitude of the EMG signal reaches the lowest when electrodes are placed over the innervation zone. Moreover, different individuals may have different innervation zone distribution(Saitou et al. 2000).

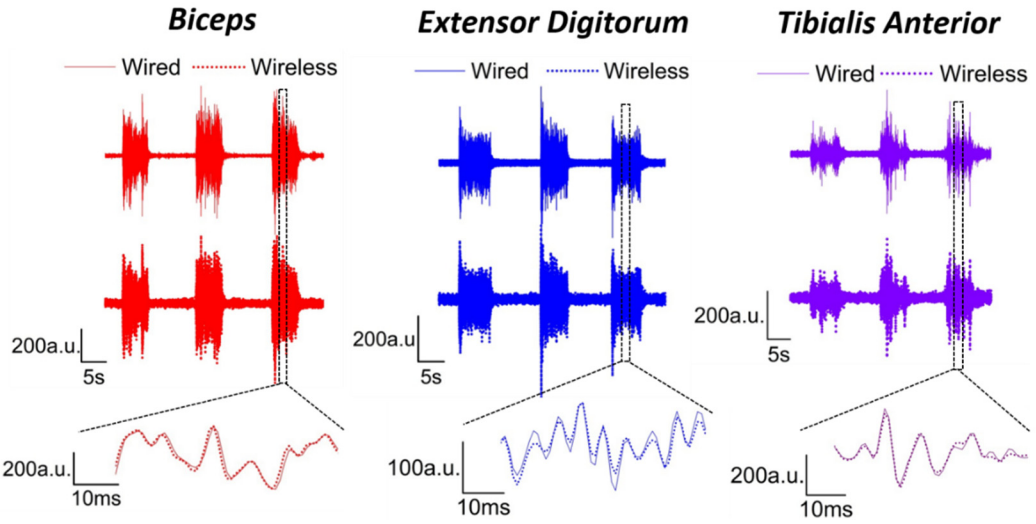

Figure 6.15. Wireless fully-passive acquisition of Electromyography (EMG). Data shows the EMG signal of biceps (red), extensor digitorum (blue), and tibialis anterior (violet) from the wired/wireless sensors for 45 seconds. Straight lines (top) represent EMG recorded from the commercial wired sensor, while dotted lines (middle) depict their wireless counterparts. Bottom plots show the zoom-in of EMG signals in the marked regions. Data from the wireless/wired sensors are normalized and aligned to demonstrate their closeness to each other.

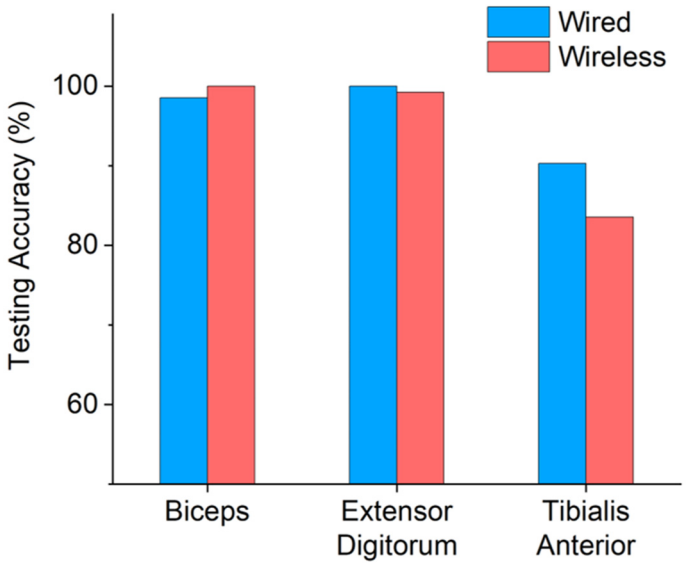

Figure 6.16. EMG signal quality analysis by the deep learning algorithm. The deep learning algorithm trains the computer to distinguish EMG signals from noise. For each muscle, the training data set comes from 270 seconds of EMG recording.

Table 6.2. SNR and feature extraction of wireless EMG

		SNR(dB)		RMS		MAV		IAV		WL	
	Cycle	Wire	Wire-less	Wire	Wire-less	Wire	Wire-less	Wire	Wire-less	Wire	Wire-less
Biceps Brachii	1	21.36	18.69	0.532	0.530	0.501	0.499	200.2	199.5	17.33	17.73
	2	24.68	22.28	0.540	0.538	0.508	0.506	203.1	202.4	17.64	18.89
	3	26.99	22.73	0.526	0.513	0.493	0.480	197.4	191.9	18.07	19.23
	4	24.57	19.76	0.526	0.527	0.496	0.496	198.2	198.6	18.23	19.63
	5	27.70	20.93	0.526	0.522	0.493	0.489	197.3	195.8	19.01	20.35
	6	24.52	21.07	0.524	0.523	0.492	0.491	196.6	196.3	19.10	20.45
	mean	24.97	20.91	0.529	0.526	0.497	0.494	198.8	197.4	18.23	19.38
	SD	2.237	1.514	0.006	0.008	0.006	0.009	2.444	3.602	0.714	1.013
Extensor Digitorum	1	15.08	12.27	0.556	0.552	0.532	0.528	212.6	211.3	33.78	31.74
	2	15.92	13.97	0.555	0.556	0.529	0.530	211.6	212.0	35.52	33.72
	3	15.94	14.75	0.537	0.539	0.511	0.513	204.3	205.1	34.68	33.29
	4	15.41	14.21	0.544	0.543	0.517	0.516	206.6	206.2	34.12	32.50
	5	15.89	14.51	0.551	0.543	0.526	0.518	210.6	207.0	33.47	31.56
	6	15.54	14.34	0.552	0.552	0.527	0.527	210.7	210.9	33.16	31.57
	mean	15.63	14.01	0.549	0.548	0.524	0.522	209.4	208.8	34.12	32.40
	SD	0.348	0.892	0.007	0.007	0.008	0.007	3.227	2.986	0.864	0.935
Tibialis Anterior	1	6.72	4.77	0.528	0.524	0.506	0.502	202.5	200.7	31.35	24.47
	2	3.55	2.19	0.531	0.532	0.510	0.509	203.8	203.4	32.20	25.82
	3	6.05	7.39	0.524	0.531	0.503	0.507	201.3	202.7	30.85	23.00
	4	5.50	5.65	0.532	0.538	0.531	0.516	205.2	206.5	29.96	23.15
	5	8.68	6.58	0.530	0.529	0.510	0.509	204.0	203.6	30.24	25.74
	6	12.76	11.55	0.522	0.527	0.503	0.507	201.2	202.9	28.45	23.84
	mean	7.21	6.35	0.528	0.530	0.510	0.508	203.0	203.3	30.51	24.34
	SD	3.190	3.113	0.004	0.005	0.011	0.005	1.604	1.877	1.288	1.235

SNR - signal to noise ratio, RMS - root mean square, MAV - mean absolute value

IAV – integral of absolute value, WL- wavelength, SD – standard deviation

The signal quality of the wired and wireless EMG data is further quantified by deep learning analysis. **Figure 6.16** shows the quality assessment of EMG data using deep learning testing accuracy. At biceps brachii and extensor digitorum muscles, both the wired and wireless EMG data show a very high (>98.5%) testing accuracy, indicating that at these two muscles, the wired and wireless sensors produce high-quality EMG data, well distinguished from the noise. A decrease of EMG SNR from 21~25 dB to 14~16 dB, does not yield a significant difference in the testing accuracy. At tibialis anterior, however, a clear drop of testing accuracy is observed. The wired and wireless EMG signal testing accuracy decrease by 10% and 17%, respectively. It is obvious that an SNR degradation from 14~16 dB to 6~7 dB has resulted in difficulty for the deep learning model to identify EMG signals from noise. Comparing with the case of extensor digitorum, although the wired and wireless EMG data of tibialis anterior exhibit less discrepancy in SNR, 1 dB over 2 dB, their discrepancy in testing accuracy actually increases from 1.5 % to 7%, suggesting that the deterioration of signal quality in the wireless EMG data is larger than that in the wired counterpart. Those results support that the wireless sensor delivers EMG measurement accuracy for a signal with SNR of 14dB or above.

In applications such as neuroprosthesis or movement recognition, feature extraction is an essential step in EMG signal analysis. To evaluate the potential implementation of the wireless sensor in those fields, we compare four commonly used features extracted from the wired and wireless EMG of biceps brachii, extensor digitorum, and tibialis anterior muscles. These features include(Chan and Green 2017; Phinyomark, Limsakul, and Phukpattaranont 2009; Zardoshti-Kermani et al. 1995): mean absolute value (MAV),

root mean square (RMS), integral of absolute value (IAV), and wavelength (WL), listed in **Table 6.2**. MAV, RMS, and IAV of all three muscles show very small errors (<3%) between the wired and wireless results. On the other hand, the WL of wireless EMG shows a significant increase of error at tibialis anterior, 25%, as compared with the other two muscles, <8%, suggesting feature extraction accuracy of the wireless sensor drops when the measurement signal has a low SNR. This result agrees well with the deep learning analysis in the previous section. Therefore, we conclude that the wireless sensor is capable of reliable EMG acquisition upon an SNR of over 14 dB. For such EMG signals, the wireless sensor may offer high accuracy, less than 8% error, so that EMG features can be used in EMG pattern recognition. Further study needs to be performed to confirm the practical implementation of the sensor, which will remain as our future work.

6.4.4 Electrooculogram (EOG)

EOG measures the inherent electrical potential between the cornea and retina(Bulling et al. 2011). This potential changes as the eyes move, producing the EOG signal which can be used to track eye movement. **Figure 6.17a** shows the normalized EOG signal when the participant rotates his eyeballs left and right, performing saccade. The angle of this rotation, according to previous studies, is approximately 60 degrees(Darrell and Pentland 1993). The recorded signal is filtered by a 3-30 Hz band-pass filter to reduce baseline shifting. As the participant rotates his eyeball left, the EOG shows a sharp rise of electrical potential, which gradually declines when the movement stops. As the participant rotates the eyeballs right, the EOG demonstrates the opposite trend. According to reference

articles(Bulling et al. 2011), the amplitude of EOG signals is typically 5-20 μV_{pp}/degree, suggesting the wireless sensor is capable of measuring EOG signal in the range of 0.12-1.2 mV_{pp}, generated by 60 degrees of eye movement.

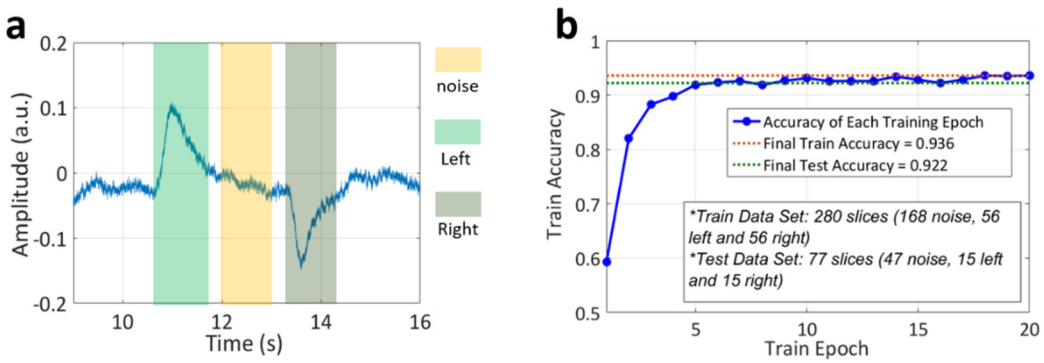

Figure 6.17. Wireless fully-passive acquisition of Electrooculography (EOG). (a) The waveform of the wireless recorded EOG signal when the participant moves his eyes left and right. The colored region represents the segments of data used to train the deep learning model. (b) EOG signal analysis using the deep learning algorithm. EOG Training data set is labeled as shown in (a). One training epoch represents one pass of the complete data set into the deep learning training model. The inlet details the composition of the training and testing data set.

The quality of EOG signals is analyzed using the deep learning algorithm. To guarantee a sufficient window length, the left and right eye movements are labeled as in **Figure 6.17a**. One complete left or right movement includes both the sudden rise and fall of the signal and the gradual recovery that follows. When the EOG signal stabilizes, it is labeled as noise. **Figure 6.17b** shows the process of training the deep learning model using

the wireless measured EOG data. The training accuracy improves very quickly with the increase of training epochs, and only 5 epochs are required from beginning to close convergence. This fast training suggests that the EOG data collected by the wireless sensor have a high quality so that they are learned by the deep learning model easily. Training accuracy reaches a maximum value of 93.6% while the testing accuracy achieves as high as 92.2%, which further validates the performance of the deep learning model trained by our wireless EOG data(Hsu, Chang, and Lin 2003).

A real-time eye tracking trial is performed with a pre-programmed dot moving on a computer screen. **Figure 6.18** shows that the EOG signal closely follows the path of the moving target. The position change of the target dot from 0 to 1 corresponds to approximately 18 degrees of eye rotation, demonstrating the wireless sensor successfully records EOG signals as low as ~250 μV_{pp}. It should be noted that the successful detection of EOG largely contributes to the sensor being placed off the body as well as the external antenna being located relatively close to the sensor, 30mm. When the sensor, however, sits on the body and the wireless transmission distance becomes large, detecting weak biopotentials, ~250 μV_{pp}, is a challenge, as shown by the P wave in ECG measurement (**Figure 6.11**). The recorded EOG waveform also shows that the amplitude of EOG signals changes even when the eyes do not move. Previous studies have reported similar baseline drift with commercially-available wired EOG recording equipment. (Belov et al. 2010; Bulling et al. 2011; Iwasaki et al. 2005). The causes of this phenomenon include the change of skin resistance (Heide et al. 1999), electrode polarization, and background interfering (Bulling et al. 2011).

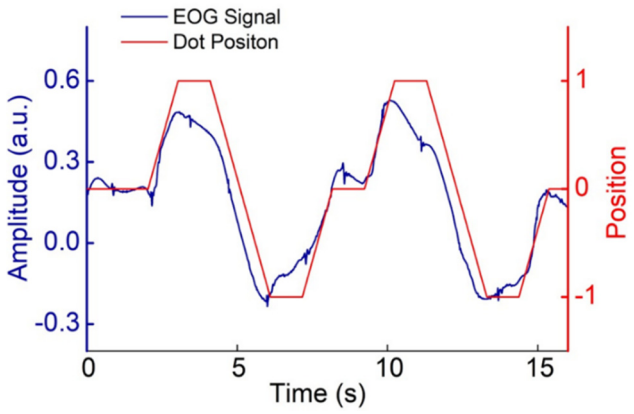

Figure 6.18. The wireless recorded EOG signal of the participant's eyes tracking a moving dot on a computer screen. The target dot is programmed to move horizontally within an 18.5 inches width computer monitor. The participant focuses his gaze upon the moving dot while the wireless EOG signal and the location of the dot are recorded simultaneously. The Red line represents the movement trail of the dot, where the location "0", "1" and "-1" represent the center, left, and right end of the monitor, respectively.

6.5 Discussion

The sensor presented in this chapter is intended to be placed on the participants' skin for the measurement of body biopotentials. -30 ~ 50 °C may be considered as a reasonable temperature range, which falls within the general operating range of all the passive electronic components (varactors, inductors, and capacitors) of the sensor. Within -30 ~ 50 °C temperature range, the temperature has little impact on the value of the passive components due to the extremely low temperature coefficients (Cockbain and Harrop 1968; Groves et al. 1996). Consequently, the temperature effect has little impact on the

performance of our sensor. We encapsulated the entire sensor by a 10μm-thick parylene-C, thus the humidity effect may not be very large as well.

The antenna radiation pattern is dependent upon the permittivity of its surrounding material. When the humidity changes from 0 to 100 % the permittivity of air remains almost constant (Zarnik and Belavic 2012), suggesting the antenna performance may remain relatively unchanged as a function of the humidity. A prior study has also shown that temperature change from -30 to 60 °C results in a merely 0.2 dB variation on the antenna gain(Mayer, Kress, and Migl 2001).

The overall cost of the current system is primarily dominated by the equipment used in the external interrogator. However, the cost can be substantially reduced by replacing the equipment with custom-designed monolithic microwave integrated circuits (MMIC). The antenna of the sensor can be further miniaturized by adopting 3D printing technology to print sophisticated 3D antenna structures. This may allow us to minimize the footprint of the antenna while maintaining or even enhancing its performance. Besides biopotential recordings, the sensor presented here may also find applications in other research fields such as cultured cell stimulation or AC impedance measurement(Liu et al. 2017; Pan et al. 2019; Zou et al. 2016). Having a near-zero power consumption, the sensor may be attractive for many biosensing applications where temperature change needs to be minimized, such as Surface Plasmonic Resonance (SPR)(Choi and Chae 2009; R. Wang et al. 2014; 2011).

CHAPTER 7

WIRELESS FULLY-PASSIVE ICP MONITORING

Previous chapters have introduced wireless fully-passive sensors for the acquisition of electrical biosignals, including the neuropotentials and body biopotentials. For the RF backscattering method, measuring electrical biosignals is simple since they are directly applied onto the varactor diodes, which leads to the generation of the 3rd order mixing product. However, the RF backscattering method cannot be directly implemented for wireless telemetry of other non-electrical biosignals, such as the pressure. To bridge this gap, this chapter introduces the design, fabrication, and verification of a wireless fully-passive intracranial pressure (ICP) sensor. To enable wireless telemetry of pressure, a resistive pressure transducer is fabricated to convert the pressure to resistance. This resistance information is then converted to an electrical signal using a photodiode and a Wheatstone Bridge circuit. Finally, this electrical signal can be wirelessly acquired using the RF backscattering method. We adopted a new antenna and circuit structure, which successfully shrink the size of the proposed wireless pressure sensor to as small as 5 mm x 4 mm. Since the RF backscattering method introduced in the previous chapters are greatly affected by the wireless transmission distance and motion artifacts, it cannot accurately measure the absolute signal amplitude. To overcome this challenge, we modify the structure of the Wheatstone Bridge circuit and make use of two different signal frequencies to compensate for the effect of artifact and antenna distance, which enables us to achieve wireless fully-passive acquisition of absolute pressure value. The fabricated wireless ICP sensor was first verified *in vitro* using a benchtop setup. *In vivo* test was then conducted by

implanting the sensor onto the skull of a rat to measure the pressure change induced by thoracic compression using a blood pressure (BP) cuff. Both the *in vitro* and the *in vivo* tests showed strong evidence that the wireless fully-passive pressure sensor can accurately record pressure change as small as 10 mmH_20. Different from capacitive pressure sensors that are based on the LC resonance circuit, the resistive pressure sensor is not sensitive to change of permittivity in the external environment, greatly reducing the baseline drift as compared to the capacitive pressure sensor. To our knowledge, the proposed wireless ICP sensor is the smallest resistive pressure sensor reported to date. Besides the small size, our wireless sensor is battery-free and has very little power consumption. These characteristics make the sensor very attractive to be used as an implant for long term ICP monitoring.

This chapter will first present the design and working principle of the wireless fully-passive ICP sensor. Next, detailed fabrication steps of the sensor will be given. Lastly, we will demonstrate the preliminary *in vitro*/*in vivo* testing results of the sensor.

7.1 Design of the Wireless Fully-passive ICP Sensor

7.1.1 System Overview

Figure 7.1 shows the 3D schematics of the wireless fully-passive ICP sensor. The sensor is fabricated on a 10 μm thick parylene-C substrate. The front side of the sensor contains all the passive electronics, including resistors, capacitors, inductors, varactor diodes, and a photodiode. The antenna and the circuits are fabricated by sputtering thin gold film (120 nm) onto the parylene substrate. A stainless steel wire (50 um diameter and 15 mm length) is connected to enhance the performance of the antenna. At the backside

of the sensor, a conductive elastomer is used as the sensing element of the pressure from the external environment. The conductive elastomer sits on top of a pair of interdigitated electrodes to form a piezoresistive pressure sensor. When pressure is applied, the elastomer deforms, and the resistance between the electrodes changes. A pipet tip is placed on top of the conductive elastomer and fixed with epoxy. This pipet tip forms the interface between the tissue and the sensor. The sensor does not contain any battery, amplifier, or high power-consuming digital circuit; only passive electronic components are used. Because of this characteristic, the sensor has a very small size and very low power consumption. The frontside and backside of the sensor are connected through vias made from conductive silver paste. All the electronics are covered with water-resistant epoxy for protection from water. The fabricated sensor has a total dimension of 5 mm x 4 mm.

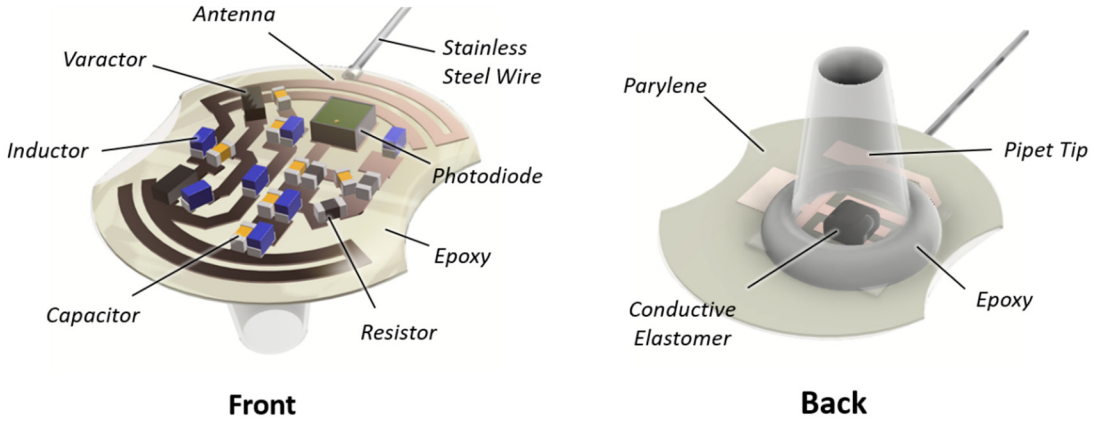

Figure 7.1. The 3D schematics of the wireless fully-passive ICP sensor. The front side of the sensor contains all the passive electronics. The backside of the sensor contains a pressure sensing resistor (PSR) made from a conductive elastomer and a pair of

interdigitated electrodes. A pipet tip sits on the pressure sensing resistor to form the interface between the sensor and the tissue

The simplified working principle of the wireless fully-passive ICP sensor is shown in Figure 7.2. The sensor utilizes both the IR and RF energy to accomplish the wireless telemetry of pressure. An external IR emitter radiates a modulated IR (Infrared) signal to the sensor. The photodiode receives the IR energy and converts it to an electrical signal. This electrical signal is then applied to a Wheatstone bridge circuit, where R_v represents the pressure sensing resistor (PSR). The PSR converts the change of external pressure to the change of resistance R_v. This resistance change is then converted to an electrical signal by the Wheatstone bridge circuit. Thus, the output signal of the Wheatstone bridge circuit, V_m, reflects the value of external pressure.

The output signal of the Wheatstone bridge circuit, V_m, is wirelessly measured using the RF backscattering method. The external interrogator generates an RF carrier signal f_0 and transmits f_0 to the sensor through an electromagnetic wave. The sensor receives the incident EM wave and mixes it with the output signal of the Wheatstone bridge circuit. The mixing product is then backscattered to the external interrogator. The external interrogator receives the backscattered signal and demodulates it to extract V_m. The pressure information is then calculated from the extracted signal.

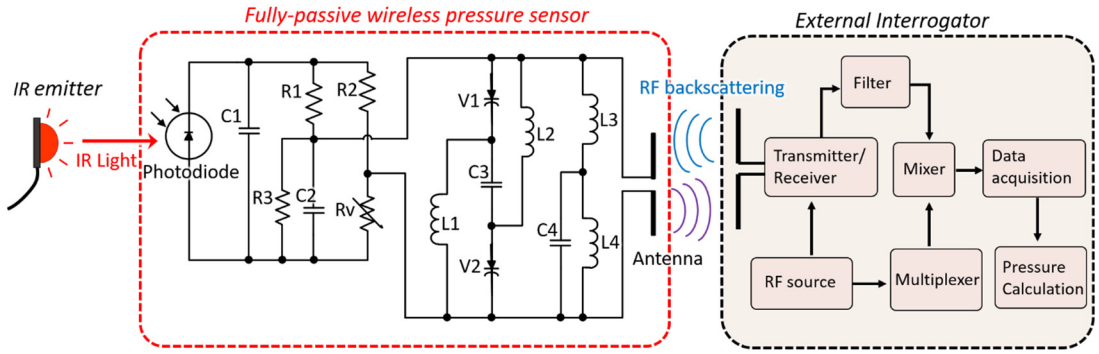

Figure 7.2. Working principle of the wireless fully-passive ICP sensor.

7.1.2 The Backscattering Antenna

Figure 7.3a shows the structure of the backscattering antenna and circuits. Both the antenna and the circuits are fabricated on a 10 µm thick parylene-C substrate. Thin gold film (200nm) is sputtered onto the parylene substrate and patterned using standard photolithography and wet etching process to form the conductive traces. The design requirement of the backscattering antenna is the same as the neural recorder and the biopotential sensor. In short, the antenna operates at two frequencies: both f_0 (2.4 GHz) and $2f_0$ (4.8 GHz). We want to maximize the gain of the antenna at these frequencies, at the same time, the port impedance of the antenna needs to be matched to the following-up varactor mixing circuits. Since the size of the antenna has been shrunk down to 5 mm x 4 mm, the gain of the antenna is further undermined as compared to that of the neural recorder/biopotential sensor. Thus, in order to remain an acceptable gain of the antenna, we need to reduce the resistive loss as much as possible. The conductivity of the sputtered thin gold film is very low, resulting in very poor performance of the sensor. The highlighted area in **Figure 7.3a** marks the location of the antenna, where high conductivity is required.

To increase the conductivity, stainless steel wires (diameter 50 μm) are adhered to the highlighted antenna traces using conductive epoxy. The attached stainless steel wire has a short tail around 15 mm (not shown in **Figure 7.3a**) For the other conductive traces, high conductivity is not critical so the thin gold film suffices. **Figure 7.3b** shows the 3D model of the antenna constructed in HFSS. For simplicity, the detailed circuit structure is neglected, only the antenna port and the impedance matching elements are taken into consideration.

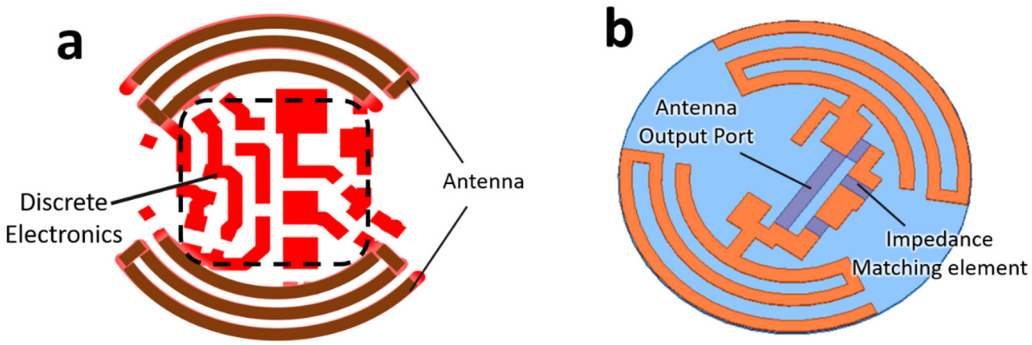

Figure 7.3. The backscattering antenna of the wireless fully-passive ICP sensor. (a) The layout of the antenna and the circuits. Highlighted traces mark the location of the antenna, where high conductivity is required. These traces are enhanced by adhering stainless steel wires. (b) 3D model of the antenna constructed in HFSS. For simplicity, all the discrete electronic components are neglected, only the antenna and the impedance matching networks are considered.

7.1.3 The Varactor Mixing Circuit

Figure 7.4 shows the schematic of the varactor mixing circuits. The circuit uses two varactor diodes as the harmonic mixer to produce the 3rd order mixing products. The principle of using multiple varactor diodes as a mixer has been explained in Chapter 6. Basically, the circuit comprises two paths for high-frequency and low-frequency signals, respectively. At RF frequency (f_0), capacitors C_1 is equivalent to short circuits. Inductors L_1, L_2 are equivalent to open circuits. Thus, for the RF signal, the varactor diodes are connected in series. At low frequency (f_m), capacitors C_1 is open circuits while inductors L_1 and L_2 are short circuits. Therefore, for low-frequency signals, the varactor diodes are connected in parallel. This arrangement increases the total impedance of the varactor mixing circuit at the RF frequency, making the impedance matching much easier to achieve. As mentioned in the previous chapter, using multiple varactor diodes greatly enhances the backscattering power of the 3rd order mixing product, achieving a nearly 20 dB improvement. For a very small antenna size such as 5 mm x 4 mm, the circuit using a single varactor diode (**Figure 4.1**) will not work anymore, and using multiple varactors is the only option. The inductor L_3, L_4, and the capacitor C_5 are components for impedance matching. Specifically, L_4 and C_5 form a parallel resonance LC circuit that exhibits high impedance at the frequency $2f_0 \pm f_m$ but low impedance at the frequency f_0. The values for L_4 and C_5 are 1nH and 1.1 PF, respectively. The inductor L_3 is used for impedance matching at the frequency f_0. The value of L_3 is usually between 1-8 nH. Due to the existence of parasitic inductance/capacitance, the value of L_3 is determined by experiment.

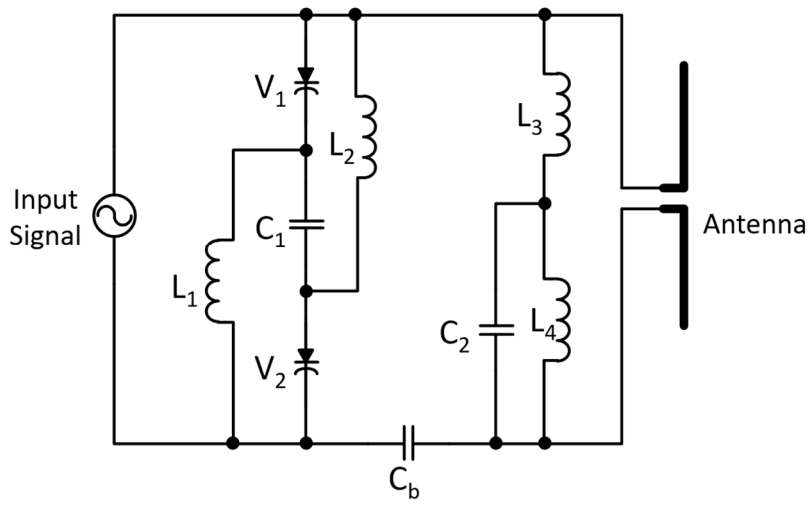

Figure 7.4. The varactor mixing circuit of the wireless fully-passive ICP sensor. The input signal refers to the signal generated by the Wheatstone Bridge Circuit.

Figure 7.5 shows the circuit model constructed in ADS to estimate the backscattered power of the 3rd order mixing product. Note that this simulation model does not account for the Wheatstone bridge circuit and the pressure sensing element. Only the impedance matching and the mixing performance of the two varactor diodes are considered. Same as before, the varactors are represented by nonlinear capacitors whose capacitance is controlled by the voltage applied. The backscattered power of the 3rd order mixing product is obtained through the ADS harmonic balance simulation. The wireless link between the sensor and the external antenna is first simulated by HFSS and then imported to the ADS circuit model as a two-port S parameter matrix. To achieve the best result, parameters of the circuit and the antenna dimensions are repeatedly tuned until the desired performance is achieved.

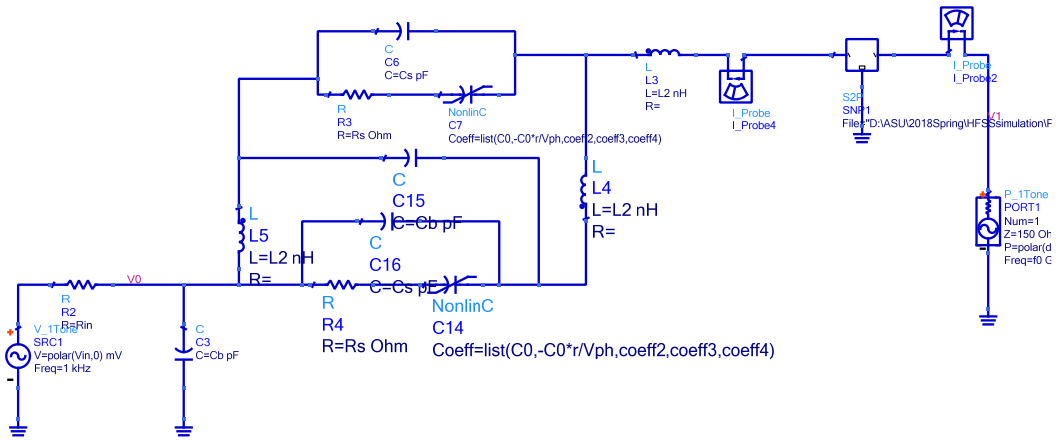

Figure 7.5. ADS circuit model for simulation of the wireless backscattering operation. The simulation uses the ADS harmonic balance simulator to estimate the backscattered power of the 3rd order mixing product. The antenna wireless link is represented by a two-port S-parameter matrix obtained from HFSS simulation.

7.1.4 The Wheatstone Bridge Circuit

Figure 7.6a shows the schematic of the Wheatstone Bridge Circuit. The circuit is used to measure the resistance value of the PSR (R_v in **Figure 7.6a**). In order to make the circuit functional, a voltage source is needed. We use a photodiode to receive and convert the external IR energy into an electrical signal. The generated signal is then inputted to the Wheatstone Bridge circuit for resistance measurement.

Assume the photodiode generates a voltage signal V_s. Neglecting all the capacitors in the circuit, the output signal of Wheatstone bridge, V_g, can be expressed as:

$$V_g = V_1 - V_2 = \left(\frac{R_3}{R_1 + R_3} - \frac{R_v}{R_2 + R_v}\right) V_s \tag{7.1}$$

Therefore, the value of R_v can be solved if we know V_g/V_s. In practical, however, the value of V_s cannot be easily obtained as it is closely related to the power of the external IR light. This means the external environment and the location of the IR source can all affect the value of V_s. Similarly, the absolute value of V_g is also very difficult to obtain because the RF backscattering method cannot accurately measure the absolute value of an electrical signal.

To overcome the above problem, a capacitor C_2 is connected in parallel with R_3 in the Wheatstone Bridge circuit. Also, IR Signal is modulated by two different frequencies: a low-frequency f_1 and a high-frequency f_2. At the low-frequency f_1, the output signal of the Wheatstone bridge circuit, V_{g1}, can be expressed as:

$$V_{g1} = \left(\frac{Z_1}{R_1 + Z_1} - \frac{R_v}{R_2 + R_v}\right) V_s \tag{7.2}$$

Where Z_1 is the complex impedance of C_2 and R_3 in parallel at the frequency f_1. Due to the existence of the capacitor C_2, the impedance Z_1 is frequency-dependent. Similarly, at frequency f_2, we have:

$$V_{g2} = \left(\frac{Z_2}{R_1 + Z_2} - \frac{R_v}{R_2 + R_v}\right) V_s \tag{7.3}$$

Where Z_2 is the complex impedance of C_2 and R_3 in parallel at the frequency f_2. Since frequency is the only variable in the Wheatstone Bridge circuit, the amplitude of the IR signal remains the same. Thus, the amplitude V_s does not change.

Take the ratio of V_{g1} / V_{g2}, then we have:

$$\frac{V_{g1}}{V_{g2}} = \frac{\left(\frac{Z_1}{R_1 + Z_1} - \frac{R_v}{R_2 + R_v}\right)}{\left(\frac{Z_2}{R_1 + Z_2} - \frac{R_v}{R_2 + R_v}\right)} \tag{7.4}$$

Both the signal V_{g1} and V_{g2} will be wirelessly telemetered through the RF backscattering operation. At the output of the external interrogator, we can obtain the wireless recovered signals V_{wg1} and V_{wg2}. As mentioned before, V_{wg1} and V_{wg2} can be easily affected by the position of the antenna and the IR emitter, therefore, their absolute values have no meaning. However, the waveform of the wireless recovered signal is accurate, meaning we have $V_{g1}/V_{g2} = V_{wg1}/V_{wg2}$. Therefore, we can accurately measure the ratio:

$$Ratio = \frac{V_{wg1}}{V_{wg2}} = \frac{\left(\frac{Z_1}{R_1 + Z_1} - \frac{R_v}{R_2 + R_v}\right)}{\left(\frac{Z_2}{R_1 + Z_2} - \frac{R_v}{R_2 + R_v}\right)} \tag{7.5}$$

Since Z_1 and Z_2 are known, we can solve the equation (7.5) to obtain the resistance value R_v. Z_1 and Z_2 are complex impedance, therefore the equation above may have multiple solutions. To avoid this, the value of resistors and capacitors need to be chosen carefully. **Figure 7.6b** shows the simulation result of the ratio (V_{g1} / V_{g2}) as a function of the variable resistor R_v. The resistor R_1 and R_2 are set as 3 KOhm, R_3 is 7 KOhm, and C_4 is 47 nF. It can be observed that the ratio of V_{g1}/V_{g2} has a monotonous relationship with R_v. Thus, we can use the ratio to obtain the absolute pressure value, which is independent of the position of the antenna or the IR emitter.

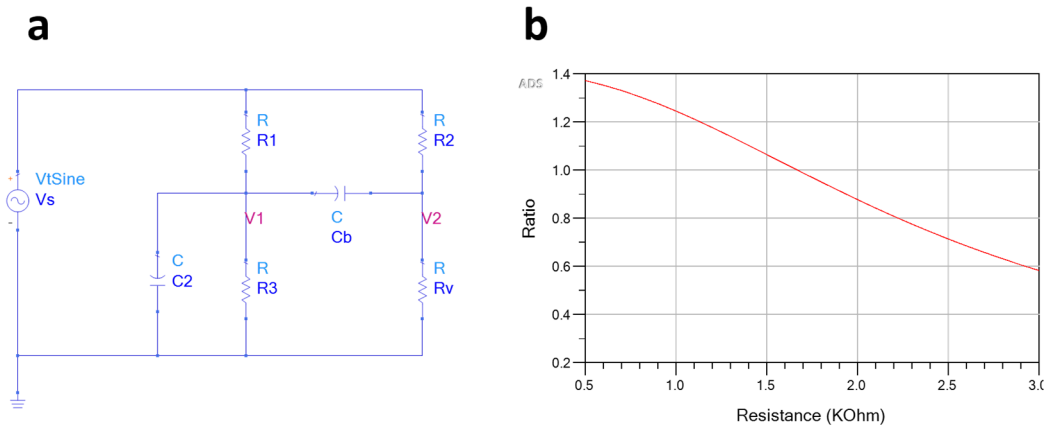

Figure 7.6. Modified Wheatstone Bridge the circuit for absolute pressure measurement. (a) Schematic of the Wheatstone Bridge Circuit. A Capacitor C_3 is added to the circuit to introduce frequency variation. R_v represents the PSR on the sensor. (b) Simulation result of the V_{g1}/V_{g2} as a function of the R_v. A monotonous relationship can be obtained if the circuit is designed correctly.

7.2 Fabrication of the Wireless Fully-passive ICP Sensor

7.2.1 Fabrication of the Pressure Sensing Resistor (PSR)

The PSR comprises a pair of interdigitated electrodes and a piece of conductive elastomer. When external pressure is applied, the elastomer deforms and the resistance between the interdigitated electrodes will change. **Figure 7.7a** shows the layout of the PSR. Each of the two interdigitate electrodes is made from a 200 μm width gold line which is sputtered onto the parylene-C substrate. The separation between the electrode is 200 μm. The conductive elastomer sits on top of the two center fingers of the electrodes (**Figure 7.7b**). Since a pipet tip will be installed later, the size of conductive elastomer should not be larger than 1 mm x 1 mm to ensure its fit into the pipet tip. Each of the interdigitated

electrodes is also connected to a pad (not shown in **Figure 7.7**). These pads will be connected with wires and used for testing of the PSR.

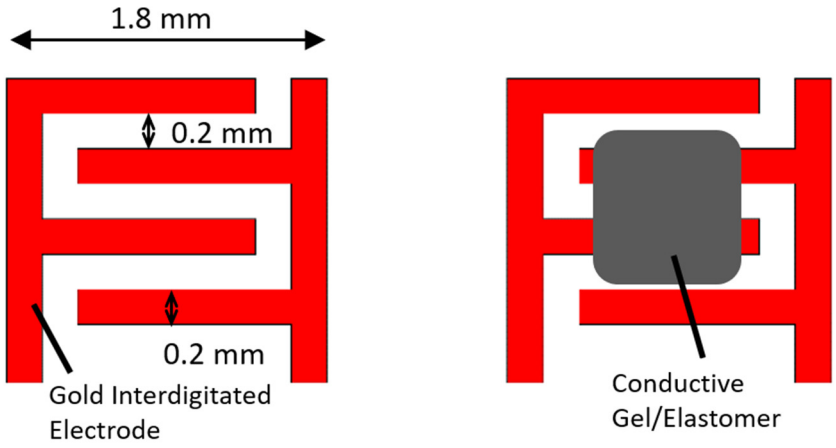

Figure 7.7. Schematic of the PSR. (a) The layout of the gold interdigitated electrodes. (b) Placement of the conductive elastomer.

The PSR is fabricated using the standard photolithography process. **Figure 7.8** depicts the cross-section view of the fabrication process. The detailed fabrication steps are listed below:

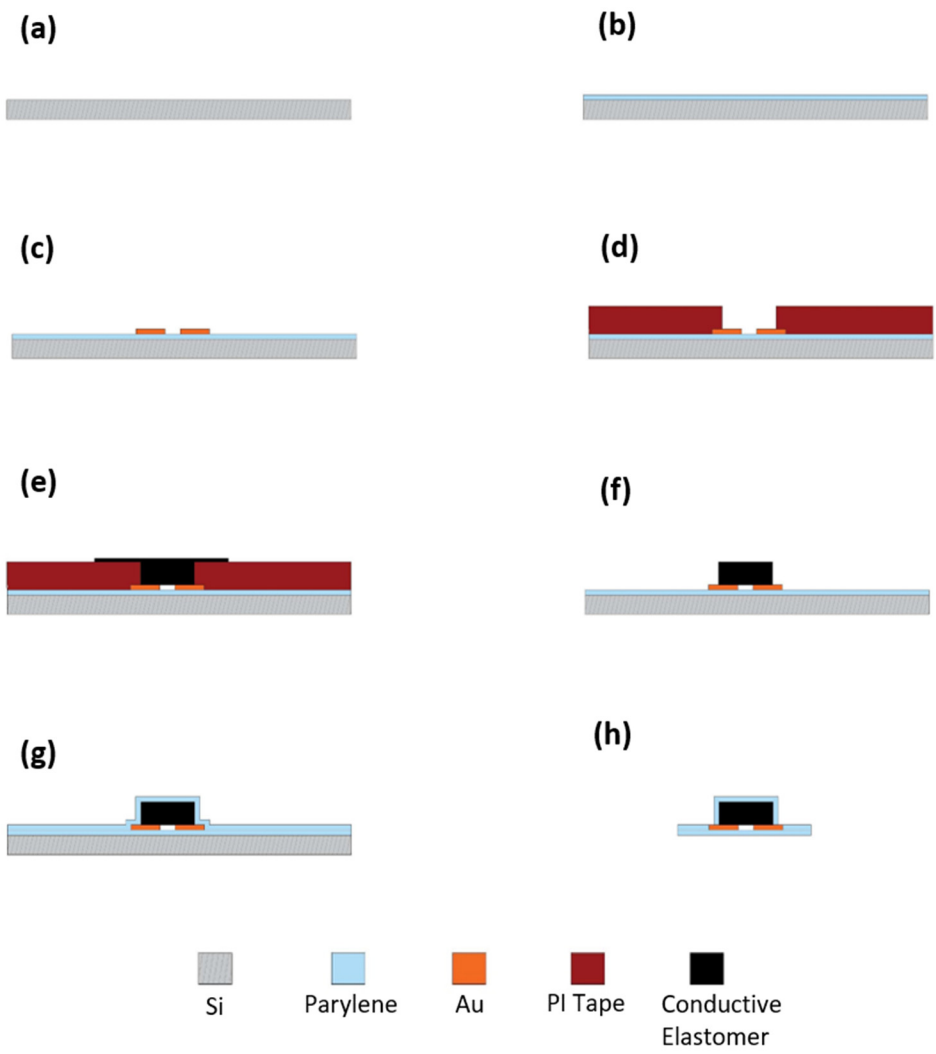

Figure 7.8. Cross-section view of the fabrication process of the PSR. (a) The fabrication process starts with a clean silicon wafer. (b) A 10 μm thick parylene-C film is deposited onto the wafer. (c) A layer of thin gold film (120 nm) is sputtered onto the parylene-C substrate and patterned with the standard photolithography process. (c-f) Polyimide tapes are used to pattern the conductive elastomer. (g) Another 10 μm thick parylene-C film is deposited to encapsulate the conductive elastomer. (h) The fabricated PSR is peeled off from the silicon wafer.

1) A silicon wafer is precleaned with acetone, IPA, and distilled (DI) H_2O. The cleaned wafer is deposit with a 10 μm thick parylene-C film. This parylene-C film forms the substrate of the wireless fully-passive ICP sensor (**Figure 7.8b**).
2) The surface of the parylene-C film is cleaned by an oxygen plasma cleaner for 3 minutes to remove contaminants. After the surface treatment, a conductive gold film (120 nm) is deposited onto the parylene-C film using a sputter. The wafer is then placed into a spin coater. A layer of hexamethyldisilazane (HMDS) is first spin-coated at 3000 rpm and baked at 100˚C for 30 seconds to promote the adhesion of photoresist. AZ 4330 photoresist is then spin-coated at 2500 rpm (~4.5um thick) and cured at 100˚C for 60 seconds. The wafer is held for 30 minutes for rehydration and then exposed with 400 mJ/cm^2 ultraviolet (UV) light for 1 minute through a polyester photomask. The exposed photoresist is developed in AZ MIF 300 developers for 2 minutes, rinsed in H_2O, and dried using N_2 gas to generate the desired pattern. The gold thin film is wet etched by emerging the wafer in the gold etchant for 20 seconds. The wafer is then rinsed with acetone, IPA, and water to remove the remaining photoresist (**Figure 7.8c**).
3) To pattern the conductive elastomer, a layer of double-sided tape (Scotch) is stacked with a layer of polyimide tape (Kapton) to create a total thickness of 200 μm. The combined tape is cut and pasted onto the parylene-C film, exposing only a 1 mm x 1 mm area at where the conductive elastomer sits. Note

the polyimide tape should be at the bottom to avoid leaving any remnant when peeled off (**Figure 7.8d**).

4) Conductive elastomer MED10-4280 (Nusil) is applied to the exposed area of the wafer. The conductive elastomer is firmly pressed by a glass slide to ensure its contact with the gold interdigitated electrodes (**Figure 7.8e)**.
5) The tape is carefully peeled off, leaving only the conductive elastomer sitting on top of the gold interdigitated electrodes. Excessive conductive elastomer is carefully cleaned by laboratory tissue (**Figure 7.8f**).
6) Another 10 μm thick parylene-C film is coated on the wafer to completely encapsulate the conductive elastomer (**Figure 7.8g**).
7) Finally, the parylene-C substrate of the PSR is cut and peeled off from the silicon wafer **(Figure 7.8h)**. The parylene-C film covering the testing pads is removed and two stainless steel wires are connected to the pads using conductive epoxy (12642-14, Electron Microscopy Science).

7.2.2 Fabrication and Assemble of the Wireless ICP Sensor.

Same as the PSR, the antenna and circuits of the wireless fully-passive ICP sensor are fabricated on the parylene-C substrate using the standard photolithography process. **Figure 7.9a** shows a picture of the antenna and circuits fabricated on a parylene-C film, highlighting a very small footprint of 5 mm x 4 mm. Note that the discrete electronic components are not assembled. After the antenna and circuits are fabricated, two 0.3 mm diameter through-hole vias are drilled using a computer-aided PCB milling machine

(LPKF). The vias are then filled with conductive epoxy (12642-14, Electron Microscopy Science) to form electrical connections to the backside of the parylene-C substrate.

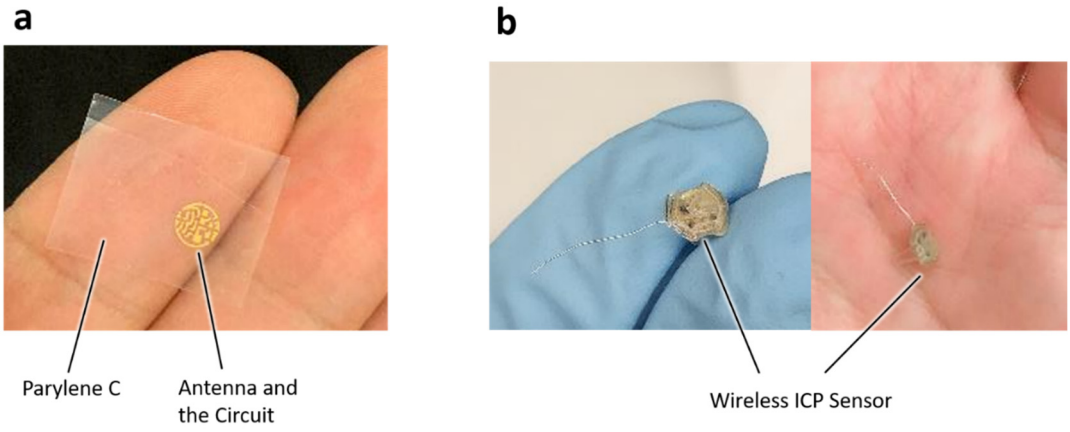

Figure 7.9. Fabricated wireless fully-passive ICP sensor. (a) Photo of the antenna and circuit fabricated on the parylene-C substrate. Discrete electronic components and the PSR are not assembled. (b) Photo of a completely assembled wireless fully-passive ICP sensor.

As mentioned before, to enhance the conductivity of the antenna, thin (50 um diameter) stainless steel wires (AM system) are pasted onto the gold traces using conductive epoxy. The stainless wire leaves a short tail (~15mm) out of the sensor to further improve the performance of the antenna. All discrete electronic components, including the inductors, capacitors, resistors, a photodiode, and varactors, are assembled onto the circuits using conductive epoxy (12642-14, Electron Microscopy Science). After the pressure sensing resistor (PSR) is fabricated and tested, it is pasted at the backside of the antenna using a double-sided tape. Conductive epoxy is used to connect the PSR to the vias. A 1000 μL pipet tip is cut and placed on top of the conductive elastomer and fixed with

waterproofed epoxy. Care should be taken when assembling the pipet tip to ensure the conductive elastomer not touching the wall of the pipet tip. Finally, the electronics at the front side of the wireless sensor are completely encapsulated by the waterproofed epoxy. **Figure 7.9b** shows the photos of a fully assembled wireless fully-passive ICP sensor. The sensor occupies a total footprint of 5mm x 4mm, neglecting the 15 mm stainless steel tail. The height of the backside pipet tip is around 4 mm.

7.3 The External System

7.3.1 The External Interrogator

Figure 7.10 shows the structure of the external interrogator for wireless fully-passive ICP measurement. Most components of the external interrogator remain the same as that of the neural recorder and the biopotential sensor. The major differences are the inclusion of the data acquisition system (DAQ), together with the Infrared (IR) driver and emitter. The DAQ has two functions: 1) Generating AC signals at two different frequencies to modulate the IR emitter and 2) Sampling and recording the wireless recovered output signal demodulated from the backscattered 3rd order mixing product. As described in section 7.1.4, to wireless measure the absolute pressure value, the IR signal needs to be modulated by both a low-frequency signal (f_1) and a high-frequency signal (f_2). In addition, the data recording should be synchronized with the two signals so that they can easily be separated and processed to calculate the pressure information. To achieve this, we program the DAQ to output analog signals at two channels. Channel 1 outputs a periodical signal composed of sine waves of two frequencies (f_1 and f_2), while channel 2 outputs a square

wave that is synchronized with channel 1 to mark the time when the frequency is changed. The signal of channel 1 is connected to the IR driver circuit to modulate the IR emitter. The signal of channel 2 is used as a digital trigger for the DAQ to commence data sampling. The DAQ system is connected to a PC, where the wireless signal is visualized and processed to obtain the absolute pressure value.

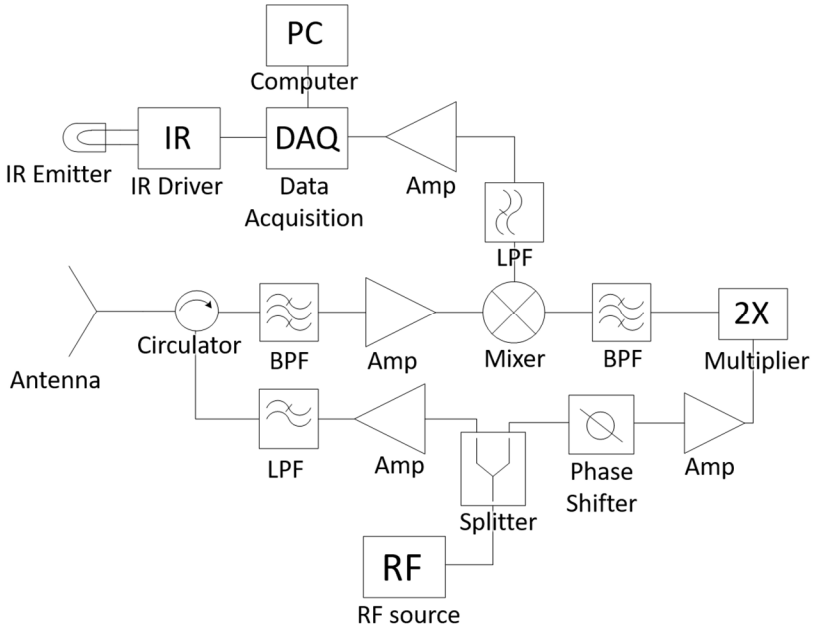

Figure 7.10. Block diagram of the external interrogator for wireless ICP monitoring.

7.3.2 The External IR Generator

The structure of the IR generator is shown in **Figure 7.11**. The IR energy is generated by an array of 4 IR photodiodes (SFH 4248, OSRAM). Each of the photodiodes has a maximum radiation intensity of 100 mW/sr. An array of 4 photodiodes can provide sufficient IR energy for our application. If higher IR energy is needed, the number of

photodiodes can be increased. The photodiodes are driven by AC currents at two different frequencies (f_1 and f_2). Each of the photodiodes needs 1.5V, 100 mA to operate. Thus, they cannot be directly driven by the data acquisition system. To increase the current output capability, we used an NMOS transistor to construct the IR driving circuit as shown in **Figure 7.11**. The resistor R_i is used to regulate the current, its value needs to be determined by the following equations:

$$R_i = \frac{V_{dd} - V_f}{nI_f} \tag{7.6}$$

Where V_f and I_f refers to the forward voltage and current of the IR photodiode, respectively; n is the number of photodiodes; V_{dd} is the DC supply voltage. Since we use a 5V power supply and an array of 4 IR photodiodes, the R_i is calculated to be 8.75 Ohm. As can be seen, the resistance of R_i is very small, and thus parasitic resistance of the circuit will greatly impact the function of the circuit. To reduce the parasitic resistance, we fabricated the circuit on a printed circuit board (PCB). All the electronic components are soldered onto the board. The gate of the NMOS transistor is connected to the output channel 1 of the data acquisition system (DAQ). To create a sinusoid shaped IR signal, the DAQ is programmed to output 0.2 V_{pp} sine waves of two frequencies (f_1 and f_2) with a 1.1 V DC bias.

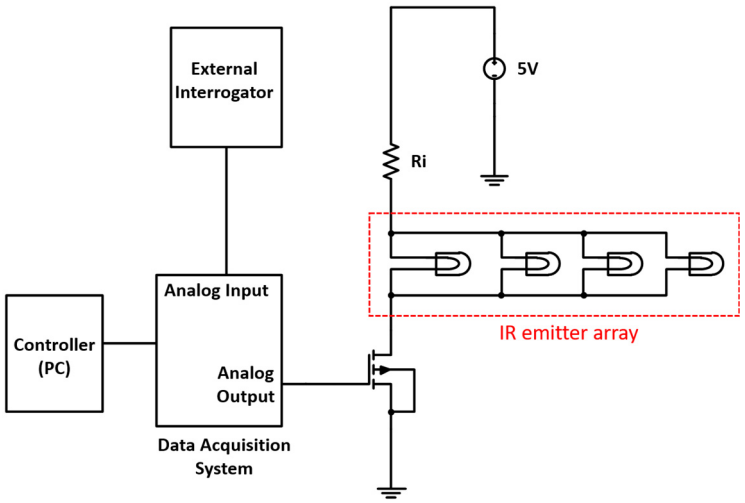

Figure 7.11. Structure of external IR generator.

7.4 Experiment Results

7.4.1. Testing of the Pressure Sensing Resistor (PSR)

The PSR was tested before it was assembled with the antenna and the wireless circuit. For the convenience of testing, the interdigitated electrodes are connected to two 3mm x 3 mm pads for wire bonding (not shown in **Figure 7.7**). After fabrication of the PSR (**Figure 7.8**), the parylene-C coating covering the pads was removed with a razor blade to expose the conductive pads. Two PFA coated stainless steel wires (A-M Systems) are connected to the pads using conductive paste (the coating at the connection part of the wire was removed). The conductive paste was then covered by epoxy for insulation. **Figure 7.12** shows the experiment setup for testing the PSR. The PSR was placed inside a small water tank. The bottom of the tank connects to a 300 mm height graduated cylinder through a PVC tube. The pressure inside the water tank is controlled by the height of the water column inside the graduated cylinder. The two stainless wires of the PSR were drawn out

from the tube and then connected to an LCR meter (Agilent E4980A) for measurement of resistance.

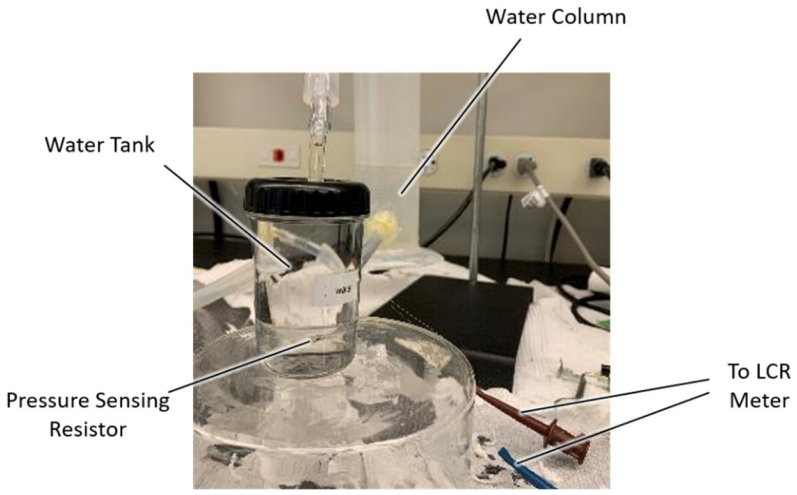

Figure 7.12. Experiment setup for testing the pressure sensing resistor (PSR).

Figure 7.13a shows the measured resistance of two fabricated PSR sensors as a function of the pressure change from 50 to 300 mmH_2O. Each data point shows the mean values of three consecutive testing results. As can be seen, the two fabricated PSR sensors have vastly different initial resistance R_0 at 50 mmH_2O. As the pressure increase, the resistance of both PSRs decreases, proving their pressure sensing capability. The different initial resistance of the fabricated PSR may come from many factors, such as the nonuniformity of the conductive elastomer, the size difference of the elastomer, and the variation of contact resistance between the elastomer and the interdigitated electrodes. Thus, the initial resistance of a fabricated PSR can have large variation and it is hard to give an accurate estimation. Based on our experience, most PSRs will have an initial

resistance between 500 – 5KOhm. **Figure 7.13b** shows the normalized relative pressure change (R/R_0) of the two PSRs as a function of the pressure. It can be seen that despite the different initial resistance, the two fabricated PSRs exhibit a similar change of relative resistance as the pressure increases. Overall, this testing result shows that the fabricated PSRs can successfully measure pressure change as small as 10 mmH_2O.

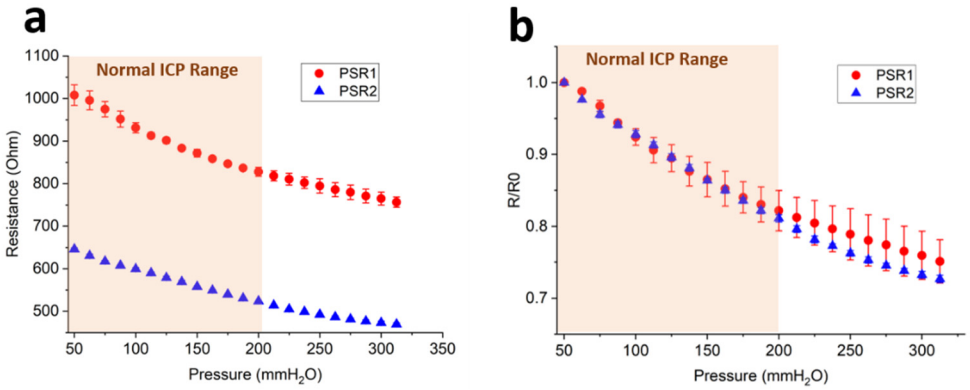

Figure 7.13. PSR testing results. (a) Measured resistance of two fabricated PSRs as a function of the pressure. (b) Normalized relative resistance (R/R_0) as a function of the pressure. The highlighted area marks the normal ICP range (0-203 mmH_2O).

7.4.2. In Vitro Verification of the Wireless Fully-passive ICP Sensor

Figure 7.14a shows the benchtop setup for *in vitro* verification of the wireless ICP sensor. The wireless ICP sensor was attached to the inner wall of the water tank. The bottom of the water tank connects to a 300 mm height graduated cylinder through a PVC tube. The pressure is controlled by the height of the water column inside the graduated cylinder. To establish wireless communication with the sensor, an external antenna was placed close to the water tank. The distance between the antenna and the wireless ICP

sensor was kept at 5 mm. An external IR LED array was placed next to the antenna to radiate IR energy to the ICP sensor. The distance between the IR emitter and the wireless ICP sensor was kept around 30 mm. To reduce the EM interference on the IR generation, the IR emitter and its cables were encapsulated with aluminum foil.

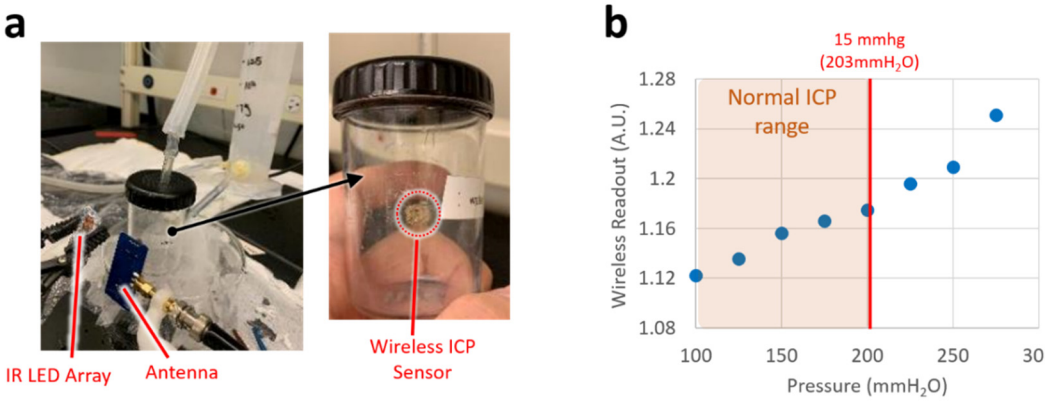

Figure 7.14. *In vitro* verification of the wireless fully-passive ICP sensor. (a) Photos show the experimental setup for testing the wireless ICP sensor. (b) Wireless readout as a function of the pressure. The red line shows the threshold of the normal ICP.

Figure 7.14b shows the measured wireless readout as a function of the pressure. The wireless readout refers to the ratio of V_{wg1} / V_{wg2} as described in equation (7.5). As the pressure increase from 100 mmH_2O to 300 mmH_2O, we can see a clear increase of wireless readout, suggesting the resistance of PSR decreasing, which corresponds well with our PSR measurement result. This result shows the fabricated wireless ICP sensor can indeed measure the pressure change through the combination of the PSR and the RF backscattering method.

7.4.3. In Vivo Verification of the Wireless Fully-passive ICP Sensor

The *in vivo* verification of the wireless fully-passive ICP sensor was conducted in a rat model. All experimental procedures were approved by and carried out in compliance with the Institutional Animal Care and Use Committee (IACUC) at Arizona State University. A Wistar rat with a weight of 360g was housed in standard cages and kept on a 12h-12h light-dark cycle. To prepare for the surgery, the rat was anesthetized with isoflurane (5% for induction, 1.5-2.5% during the surgical procedure, 1 L/min O_2, 14.7 PSI). The rat was fixed with stereotaxy and a surgical incision was made on the scalp to expose the skull. A burr hole with a 2 mm diameter was made on the skull using a surgical drill. The wireless ICP sensor was implanted by inserting the pipet tip into the burr hole (**Figure 7.15a,b**). The tapered shape of the tip enables the sensor to be firmly inserted into the burr hole. After the sensor was implanted, the external antenna and the IR emitter were placed on top of the sensor. The distance between the external antenna and the sensor was approximately 5 mm. The alignment between the sensor and the external antenna was adjusted until a clear output signal can be seen in the Labview program. After a good alignment was obtained, the locations of the antenna and IR emitter were not changed.

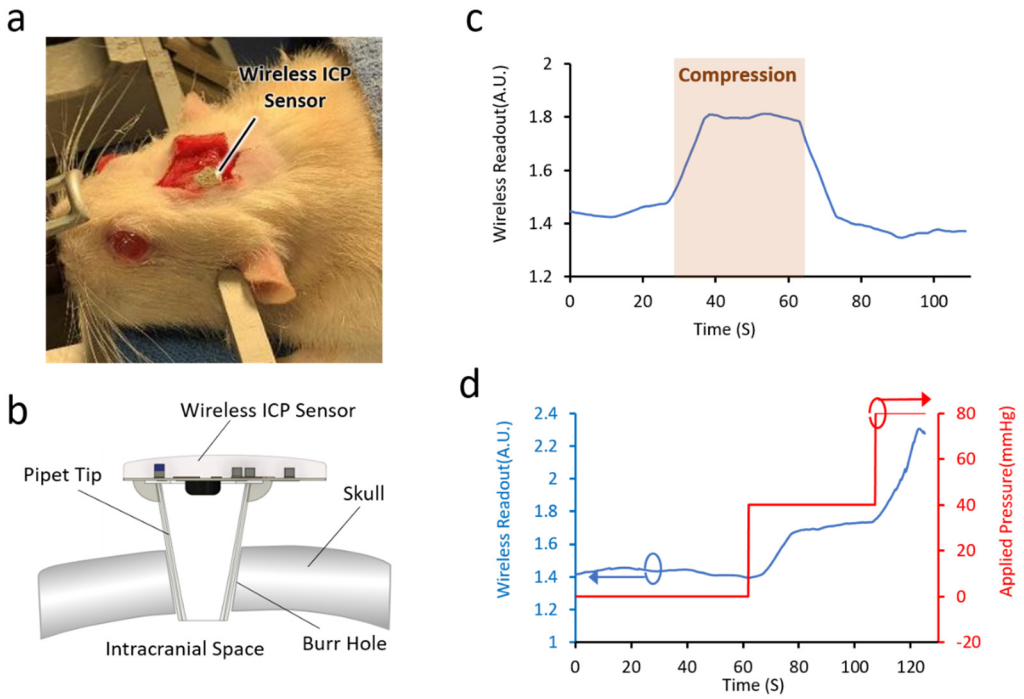

Figure 7.15. *In vivo* verification of the wireless fully-passive ICP sensor. (a) Photo of the wireless ICP sensor implanted on the rat skull through a burr hole. (b) Cross-section view of the ICP sensor implanted on the rat skull. The tapered shape of the pipet tip enables it to be firmly inserted into the burr hole. (c) Wireless readout of the system recorded during thoracic compression on the rat body. (d) Wireless signal recorded during the pressure change induced by a BP cuff.

We first measure the change of pressure through thoracic compression. **Figure 7.15c** shows the real-time recorded wireless readout (the ratio of V_{wg1} / V_{wg2}) when thoracic compression was applied to the rat body manually. As seen in the plot the wireless output signal shows a clear rise from 1.4 to 1.8, which is resulted from the pressure increase in the rat intracranial space. When the compression stops, the wireless readout gradually return

to 1.4, suggesting the wireless sensor ICP sensor was able to track the intracranial pressure returning to its original value. The result also shows that the sensor has a slow response time of more than 10s. The slow response time indicates the sensor may not be able to measure a rapid change of pressure but is more suited for applications where pressure change is slow, such as the ICP monitoring.

Another thoracic compression was conducted by using a blood pressure (BP) cuff to apply different pressure onto the rat body. **Figure 7.15d** shows the recorded wireless signal as the pressure of the BP cuff increases from 0 to 40 and 80 mmHg. The wireless signal shows a very well correspondence with the applied pressure, proving the functionality of the wireless ICP sensor. Note that in **Figure 7.15d**, the applied pressure refers to the pressure of the BP cuff. The actual intracranial pressure of the rat should be much smaller.

In summary, both the *in vitro* and *in vivo* experiments have verified the functionality of the developed wireless fully-passive ICP sensor. With its small size, low power consumption, and resistive pressure sensing mechanism, the proposed sensor may eventually be implemented as a chronic neural implant for safe and reliable long-term ICP monitoring.

CHAPTER 8

WIRELESS PASSIVE STIMULATION OF CARDIAC CELL

As mentioned in chapter 1, electrical stimulation delivers effective treatment in many clinical fields, such as restoring paralyzed limbs(Peckham and Knutson 2005), inhibiting epilepsy(Yamamoto et al. 2002), suppressing pain(Fregni et al. 2006), correcting abnormal heart rhythm(S. Y. Lee, Cheng, and Liang 2011), and restoring vision(Walter et al. 2005). Existing wireless stimulators generally require bulky coils or rechargeable batteries, and they deliver relatively low stimulation current which is insufficient for high-current demanding applications such as cardiac tissue stimulation. This chapter presents a battery-free RF microwave powered wireless stimulator, having a footprint of 25 mm x 42 mm x 1.6 mm, featuring low power consumption and high current delivery of up to 60 mA to stimulate engineered cardiac tissues. An external antenna, which is modulated by an inverted pulse to directly control the stimulating waveform, shines 2.4 GHz RF to the wireless passive stimulator. The wireless passive stimulator contains an onboard antenna to receive the incoming modulated RF signal, a multistage diode multiplier to accumulate electric charges, and a transistor to control the timing respectively. Comprising only one active component, the stimulator exhibits very low power consumption, yet it is capable of generating output current as high as 60 mA. To test the stimulator, neonatal ventricular rat cardiomyocytes are seeded on electrically conductive gelatin-based hybrid hydrogels to form cardiac tissues. The engineered tissues demonstrate synchronous contractions immediately upon wireless stimulation. The stimulator output voltage and current profiles match the tissue contraction frequency within 0.5-2 Hz, confirming the efficacy of the

wireless passive stimulator to precisely control the beating frequency of cardiomyocytes. Such characteristic is further shown based on Ca^{2+} puffs that are synchronized with the stimulator output. The cardiac tissue beating frequency shows negligible differences when comparing the wireless stimulator and the reference wired stimulator. Viability and cardiac specific immuno-stained images illustrate no major cell death and disruptions in cellular phenotype, i.e., sarcomere and troponin-I organization, upon applying wireless stimulation. Overall, our results indicate the promising potential of the proposed wireless passive stimulator for cardiac tissue engineering applications and induction of preciously controlled synchronous contractions.

This chapter will primarily describe the design of passive wireless stimulator, implementation of the stimulator, and characterization of the wireless stimulator using emulated loads. Then, we will discuss the preparation of engineered cardiac tissue constructs, and fabrication of a custom-made bioreactor. Finally, we present the measured results of wireless stimulations on the engineered cardiac tissues, side by side compared to the wired configuration.

8.1 Design of the Passive Wireless Stimulator

The preferred electrical signal parameters for stimulation of engineered cardiac tissue have been described by a published protocol(Tandon et al. 2009). Briefly, a monophasic square wave pulse with relatively short duration is sufficient to excite the cardiac tissue; the stimulation frequency is in the range of several hertz, depending on the heart beating rate; large stimulating current, at least 60mA(Hirt et al. 2014; Tandon et al.

2011), is required. While a wire connected electrical system can easily achieve those parameters, they are challenging specifications for a wireless system. In addition, for an implantable device, the maximum power dissipation of the device and the maximum allowable external RF energy need to be within the safety regulation(Wolf 2008). **Table 8.1** summarizes our target design parameters of the wireless stimulator for engineered cardiac tissues.

Table 8.1: Design requirement of the wireless stimulator

Design parameters	Requirements
Stimulating current	$> 60\text{mA}$
Frequency	0.5Hz-2Hz
External RF power	$< 30\text{dBm}$
Channel number	1
Heat dissipation	$< 40\text{mW/cm2}$
Battery	No

Wireless implantable systems can generally be classified into two different kinds. One kind is active systems, which utilize sophisticated integrated circuitry (IC) and implanted battery to achieve complex functionality. For active systems, power consumption, reliability, size, and cost are the critical concerns that limit their realization in the clinical setting(P. J. Chen et al. 2008; Kaiser 2006). Passive systems, on the other hand, have a much simplified structure with minimum power dissipation, making them safer for implantation and less likely to malfunction(H. N. Schwerdt, Miranda, and Chae

2015). Due to these reasons, we choose a passive stimulator configuration with relatively simple structure. **Figure 8.1a** shows the circuit diagram of the passive stimulator, which utilizes a multistage diode voltage multiplier to accumulate electric charges. Only one active component (P-channel MOSFET) is used as a switch to control the output.

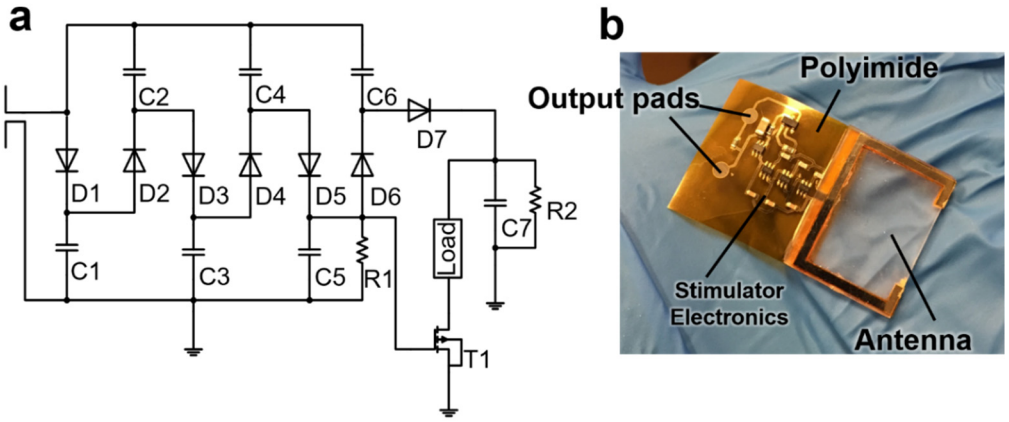

Figure 8.1. The passive wireless stimulator. (a) The equivalent circuit diagram of the stimulator. (b) Photograph of a fabricated stimulator.

The circuit operates in two states. In the charging state, the voltage accumulated on the capacitor C5 and C7 is almost equal, the gate-source voltage of the PMOS is near zero ($V_{gs}\approx 0$), turning "off" the transistor. In the meantime, the circuit charges the capacitor C7 through the multistage diode multiplier until the voltage across C7 reaches 8~20V. The total power consumption of the circuit during this state is mainly contributed by the heat dissipation of resistor R1 and R2, which can be calculated using:

$$P_{total} = \frac{{V_{c5}}^2}{{R_1}^2} + \frac{{V_{c7}}^2}{{R_2}^2} \tag{8.1}$$

We used R1 of 22 kΩ and R2 of 300 kΩ, and C5 of 200 pF and C7 of 30 μF, respectively, contributing a total power consumption of approximately 2.9~18mW. In the discharging state, C5 and C7 discharge their accumulated charges at a different speed, determined by their capacitance and resistance values. As a result, C5 discharges much faster than C7, increasing the gate-source voltage of the PMOS, which eventually became larger than the threshold voltage (V_{gs}>V_{th}), turning "on" the transistor. During this state, the Drain-Source current of the pMOS can be expressed as:

$$I_d = \frac{1}{2}\mu_n C_{ox}\frac{W}{L}(V_{c7} - V_{c5} - V_{th} - I_d R_{load})^2 \quad (8.2)$$

where μ_n, C_{ox}, W and L are parameters determined by the MOS fabrication process, V_{th} is the threshold voltage, and R_{load} is the resistance of the load (the cardiac tissue). The stimulating current is determined by the voltage across C7 and C5 (V_{c7} and V_{c5}) and the resistance of the cardiac tissue. The "on" state of the circuit is controlled to maintain only a few milliseconds, and it is reactivated at a frequency of only a few hertz. In consequence, power consumption during the "on" state is negligible as compared to that in the "off" state. Therefore, the total power consumption of the stimulator is 2.9~18mW. In our experimental settings, 2.9mW is sufficient to excite cardiac tissue contraction. It should be noted that in the current setting, the 18mW maximum power consumption is primarily determined by R1 and R2. Increasing the value of R1 and R2 can significantly decrease the power consumption of the stimulator. For example, increasing R1 and R2 by 10 times will reduce the power consumption to merely 1.8 mW. As the stimulator has a dimension of several centimeters, the design requirement on heat dissipation can easily be satisfied.

The two states of the circuits are controlled by the external RF transmitter. Two popular methods exist to wirelessly deliver RF power: inductive coupling and electromagnetic (RF) coupling. A comparison of the two methods is well studied(Zhang and Chae 2011). Generally speaking, inductive coupling performs better in close distance and high power requiring settings whereas RF coupling is better suited for power-limited, long-range applications. Since the stimulator demands low power, RF coupling allows us to implement the wireless stimulator. The wireless stimulator demands high voltage (8~20V) to deliver high current on the cardiac tissue. At a given transmitting power, RF coupling delivers higher DC voltage than inductive coupling does, especially at a prolonged distance. Additionally, inductive coupling features that the external coil scales dramatically large as the working distance increases(Harrison 2007) whereas RF coupling demonstrates the size of the external antenna is rather independent upon the working distance. **Figure 8.2** shows the simulated efficiency of electromagnetic coupling between two antennas. Comparing this to the inductive coupling reported by a previous article(Harrison 2007), it can be seen that inductive coupling achieves higher efficiency at a close distance, less than 4 of z/d_{ant}, whereas the electromagnetic coupling, as shown in **Figure 8.2**, shows better performance at a longer distance, more than 4 of z/d_{ant}. We also notice that for both coupling methods, the coupling efficiency increases as the distance decrease. However, when the distance between the two antennas becomes too close, the efficiency of the electromagnetic coupling begins to drop. Another disadvantage of inductive coupling is that the size of the transmitting coil is directly affected by the coupling distance. The size of the transmitting coil needs to increase significantly as the

coupling distance increases. For electromagnetic coupling, on the other hand, the size of the antenna is only determined by its operating frequency(Balanis 2016) and is impacted little by the distance.

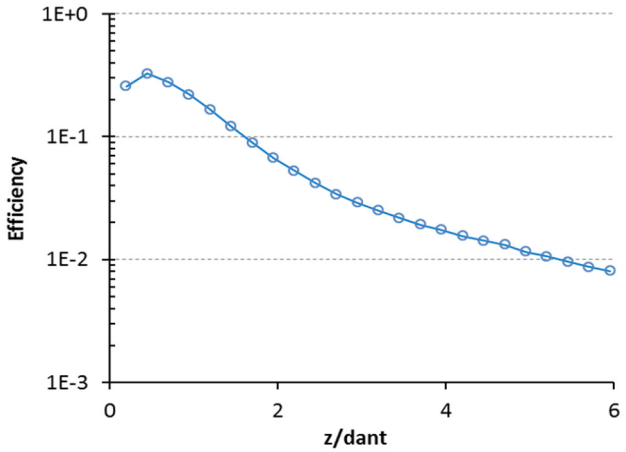

Figure 8.2. HFSS simulation of the electromagnetic coupling efficiency between two antennas. The transmitting and receiving antennas are two 2.4 GHz, 18cm x 20cm planner antennas. The X-axis shows the z/d_{ant}, which is the ratio of the distance (between two antennas) over the antenna diameter.

Figure 8.1b shows the photograph of the fabricated passive wireless stimulator, including the antenna and circuits. The wireless stimulation circuit was fabricated on a 25 μm thick polyimide film. All the metal traces were formed by a thin chrome-gold-chrome film (Cr/Au/Cr, 20/200/20nm), deposited by an RF sputter. Discrete components were mounted using biocompatible conductive sliver paste (ED21TDCSMED, Masterbond). The total size of the stimulator is 25 mm x 42 mm x 1.6 mm, including the on-board antenna.

The RF carrier frequency is chosen to be 2.45 GHz through the tradeoff between the size of the onboard antenna and the skin depth penetration into the body. High frequency is preferred to minimize the size of the antenna as well as to achieve the desired characteristics such as input impedance and radiation pattern. On the other hand, high frequency results in a significant loss within tissues surrounding the implant(Chow, Morris, and Irazoqui 2013). Based on our previous work(H. N. Schwerdt, Miranda, and Chae 2012; 2013; Abbaspour-Tamijani et al. 2008), 2.45 GHz was found to be the optimized frequency for the on-board antenna. Typically, the impedance of the antenna should be matched to the load so that the maximum power could be transferred to the load(Balanis 2016). For our system, however, this is not the primary consideration. The passive stimulator has low energy consumption during its operation, leading to a less significant impedance matching. This critical feature allows for reducing the size of the onboard antenna. The antenna also needs to exhibit low impedance at low frequency, which is a critical requirement for the following circuits. Taking these into considerations, we designed the antenna using the finite element method (FEM) in High Frequency Structure Simulator (HFSS). **Figure 8.3** shows the geometry and simulation results of the antenna. We used PDMS for the antenna dielectric material as PDMS is a well-known flexible and biocompatible material that has a relatively low dielectric loss (δ=0.0015-0.0035). The detailed steps for fabricating the PDMS based onboard antenna are shown in **Figure 8.4.**

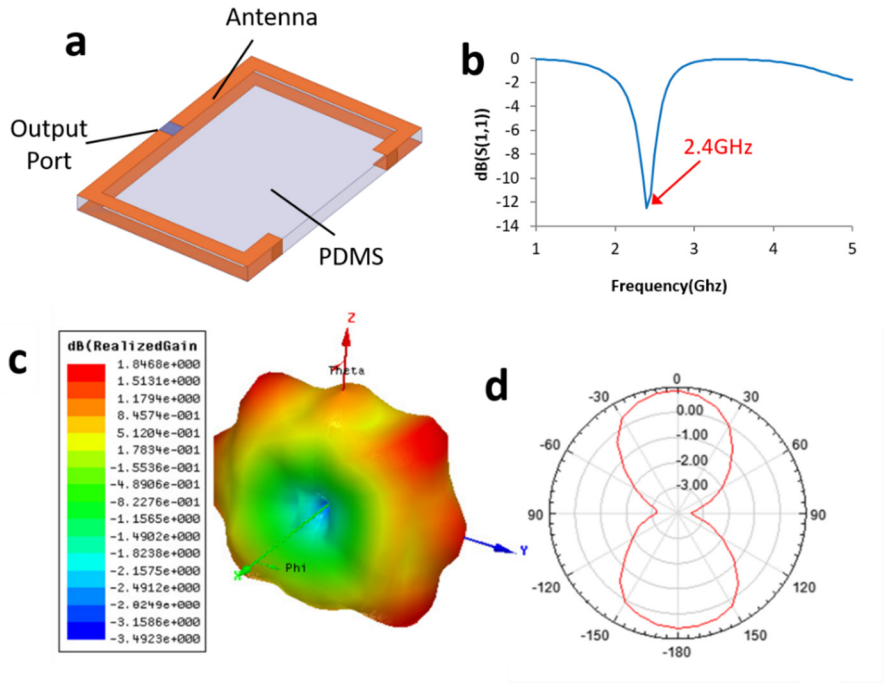

Figure 8.3. Design of the antenna of the wireless passive stimulator. (a) The 3D model of the antenna constructed in HFSS. The antenna is optimized at 2.4 GHz. A folded diode structure is adopted to maximize the gain and provide a short circuit path for low-frequency signals. The output port of the antenna (blue rectangular) connects the subsequent diode voltage multiplier circuit. (b) S(1,1) of the antenna when it is connected to a 300 Ohm load, showing the antenna resonant at 2.4 GHz. The passive stimulator has very low energy consumption during its operation, and thus the impedance matching is less significant. This critical feature allows for reducing the size of the onboard antenna. (c) 3D polar plot of the antenna gain. The designed antenna has a gain of 0.8-1.12 dB along the z-axis. (d) Antenna radiation pattern in the x-z plane.

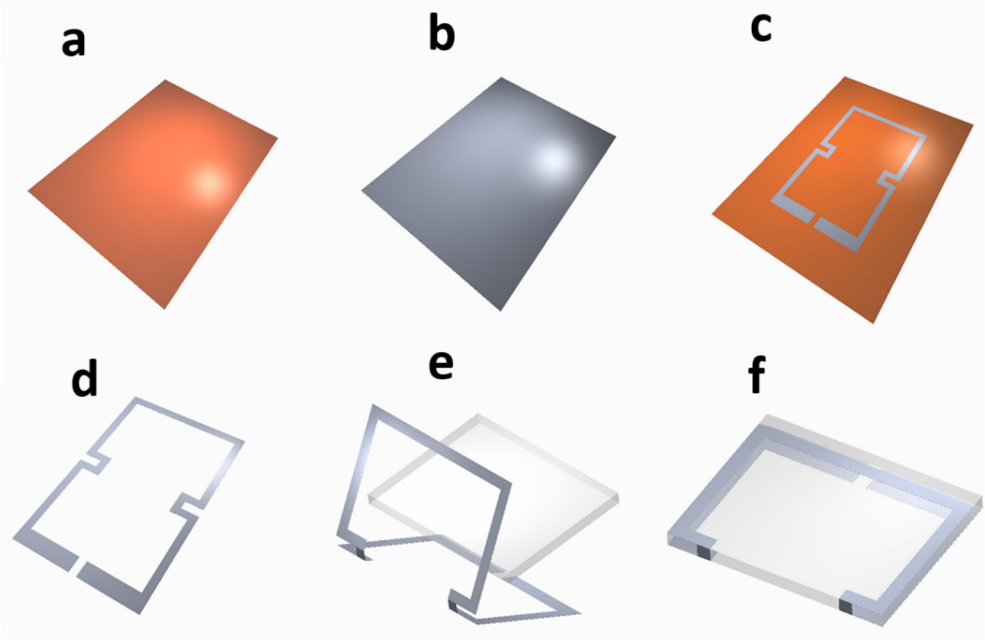

Figure 8.4. Fabrication procedures of the onboard antenna. (a) A 25 μm thick Kapton polyimide film (DuPont) is cut to a 45 mm x 60 mm rectangular. The film is then wiped with acetone and cleaned using an RF plasma cleaner. (b) A thin chrome-gold-chrome (20nm/200nm/20nm) film is deposited onto the polyimide film using RF sputtering (EMITECH K675X). (c) The deposited metal film is patterned by photolithography and then wet-etched to form the geometry shape of the antenna. (d) The antenna is manually cut off using a razor blade (e) The antenna is folded along the PDMS substrate (25 mm x 22 mm x 1.6 mm). (f) The metal traces and the PDMS substrate are bonded together using silicone epoxy (MED2-4213, Nusil).

8.2 The External Transmitter

Figure 8.5 illustrates the schematic of the external transmitter. An inverted pulse modulates a 2.45 GHz RF carrier through amplitude modulation. The modulated signal is

amplified then radiated from the external antenna. When the modulated RF reaches the stimulator, the transistor will turn “on” or “off”, controlled by the modulated RF, activating the charging/discharging of the onboard capacitors. Thus, the input inverted pulse controls the output pulse of the stimulator. The frequency and pulse width of the inverted pulse was set to be 0.5-2 Hz and 2 milliseconds, whereas the high and low level of the inverted pulse was set at 2.8 V and 0 V, respectively. The pulse and the RF carrier was generated by an arbitrary waveform (Agilent 33250A) and an RF signal generator (Agilent E4432B), respectively. The modulation depth of the RF generator was set at 32.5%. The modulated signal was amplified by a low noise power amplifier (MPA-24-20, RF bay). The radiating external antenna is a 2.45 GHz 10 mm x 10 mm ceramic chip antenna (A10194, Antenova). We set the maximum power of the RF signal generator to be 30 dBm, guided by the Federal Communication Commission (FCC) regulation(Obeid et al. 2008). The actual radiating power from the external antenna was less than 30 dBm.

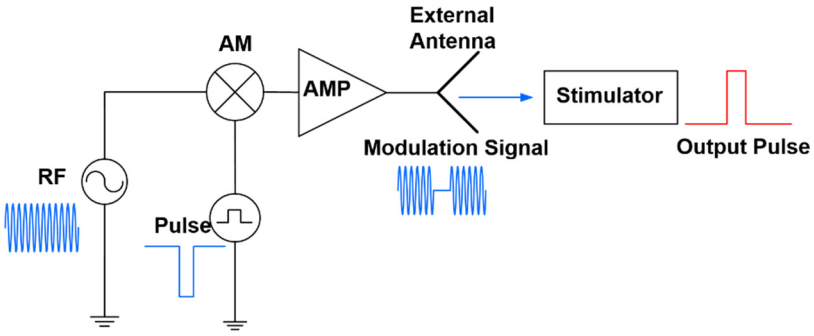

Figure 8.5. Schematic of the external transmitter for generating modulated RF pulses.

8.3 Material and Method

8.3.1. Isolation of Cardiomyocytes.

Cardiomyocytes were isolated from the ventricular region of a 2-day old neonatal rat based on a previously well-established protocol(Saini et al. 2015). The isolated cells were used to form the cardiac tissue constructs and subsequent external stimulation experiments. Briefly, the heart pieces were placed in 0.05% trypsin solution (without EDTA) prepared in Hank's balanced salt solution (HBSS) for 14-16 h at 4°C. After trypsinization, the heart pieces were neutralized in cardiac specific culture media, containing fetal bovine serum (10%), L-glutamine (1%), 100 units/mL of penicillin/streptomycin (antibiotics), and Dulbecco's modified eagle medium (DMEM). Afterward, the tissue pieces were treated with collagenase to isolate the cardiomyocytes population.

8.3.2. Preparation of Gold Nanorods (GNRs)-incorporated Gelatin Methacrylate (GelMA) Hybrid Hydrogels.

We formed the cardiac tissues by seeding cardiomyocytes on top of a GNRs-embedded gelatin methacrylate (GelMA) (10% wt/v of GelMA and 1 mg/mL of GNRs) hydrogel due to its excellent cell-responsiveness, *i.e.* adhesion, retention, ease of microfabrication as well as electrical conductivity as demonstrated in our recently published work(Navaei et al. 2017). In detail, due to the significantly lower electrical conductivity of the pure GelMA hydrogel compared to GelMA-GNR constructs, we were not able to induce external electrical stimulation (either wired or wireless) on cardiac cells

seeded on pure GelMA tissue constructs. Therefore, we selected the GelMA-GNR cardiac tissue construct to conduct wireless stimulation. The isolated cardiomyocytes were seeded on top of the GelMA hydrogel instead of encapsulation within the matrix. This was in part due to the sufficient supply of nutrients to the cells on top of the matrix throughout the culture period. Additionally, in our previous studies(Saini et al. 2015), we demonstrated that cardiomyocytes in mono-culture maintain a round morphology and do not spread when encapsulated within GelMA hydrogel, and in fact, they required to be co-cultured with helper cells such as cardiac fibroblasts. Apart from these, our studies have also shown that even cardiomyocytes seeded on top of the GelMA hydrogel penetrate approximately 15 to 20 μm inside the hydrogel(Navaei et al. 2016). Therefore, there is truly no significant difference between seeding cardiomyocytes on the GelMA hydrogel as compared to encapsulation within a very thin layer of GelMA hydrogel matrix (~50 μm). As the focus of this study was to assess the functionalities and feasibility of the wireless stimulator to contract cardiac cells, we utilized a cell-seeded tissue model with only a mono-culture of cardiomyocytes to test our hypothesis.

Gelatin methacrylate (GelMA)(Saini et al. 2015) and GNRs(Navaei et al. 2016) were each synthesized according to our previous studies. To synthesize GelMA-GNR (1 mg/mL) hydrogels, first a 0.5% w/v solution of photoinitiator (PI) in Dulbecco's phosphate-buffered saline (DPBS) was prepared (80 ºC), then GelMA (10% w/v) solution was fully dissolved in the PI solution. Next, GNRs were purified and mixed with the GelMA solution. Subsequently, 15 μL of GelMA-GNR prepolymer solution was placed between 150 μm tall spacers and covered by TMSPMA-coated glass slides(Saini et al. 2015). The hybrid

constructs were formed through photopolymerization by exposure to UV light (800mW, 360nm-480nm) for 25 s and immediately submerged in DPBS to avoid dehydration. To prepare the cardiac tissues, one million cardiomyocytes were seeded on each GelMA-GNR hydrogel construct in a 24 well plate, and the samples were subsequently submerged in cardiac specific media(Navaei et al. 2016).

8.3.3. Bioreactor Preparation.

Electrical stimulation on cardiac tissues was conducted in a custom-made bioreactor chamber based on established protocols(Tandon et al. 2009). Briefly, the bioreactor chamber was fabricated by placing two parallel carbon electrodes (5 mm length) on a plastic petri dish (6 mm diameter) with 1 cm spacing. The carbon electrodes were fixed using silicone adhesive. Platinum wires were attached to the carbon electrodes at the opposite ends and were fully covered by silicone adhesive to prevent contact with media. After fabrication, the entire chamber was washed with 70% ethanol and sterilized under UV light for 1 hour. Wired stimulation was applied via an arbitrary waveform generator (BK PRECISION 4052) as the control condition to our fabricated wireless stimulator. Based on the protocols, the stimulation waveform was chosen to be a pulsatile signal with 2 milli-sec duration at three different frequencies (0.5, 1, and 2 Hz) for both wired and wireless stimulation conditions.

8.3.4. Electrochemical Impedance Spectroscopy.

For any electrical system, the output voltage and current are usually strongly influenced by the electrical property of the load. In our stimulation experiment, the impedance of the cardiac tissue constructs, carbon electrodes, and the culture media together determine the voltage-current relationship. Therefore, the total impedance of the bioreactor chamber needed to be characterized and included in design considerations. In this regard, the electrical impedance of the bioreactor was measured using a precision LCR meter (4980A, Agilent) at 20~10 kHz, with 1, 5, and 10 V input signal amplitudes.

8.3.5. Cell Viability Assay.

Live/Dead standard kit (Life Technology, USA) was utilized on day 8 of culture to investigate the impact of applied electrical pulses on cell survival. Tissue samples were placed in the electrical stimulation chamber under stimulation at 2 Hz for 30 min, and fluorescent images were acquired using an inverted microscope (Observer Z1, Zeiss, Germany).

8.3.6. Cardiac Specific Phenotype and Cytoskeleton Organization of Cultured Cells.

To confirm the formation of cardiac tissue with intact cytoskeleton and mature cardiac phenotypes, the constructs were stained for F-actin fibers and cardiac-specific markers including sarcomeric α-actinin, troponin-I, and connexin 43 (Cx43) respectively. The samples were collected on day 8 of culture and stained based on well-established protocols(Navaei et al. 2016). Briefly, the cells were primarily fixed using

paraformaldehyde (PF) solution (4% v/v), treated with Triton X-100 (0.5% v/v) for 45 min to permeabilize cells' membrane, and subsequently blocked in goat serum (10% v/v). The primary antibodies specific to each cardiac protein (sarcomeric α-actinin, troponin-I, and Cx43) (Abcam, USA) were added to each sample, followed by staining for secondary antibodies, Alexa Fluor-488 for sarcomeric α-actinin, and 594 for troponin-I and Cx43 (Life Technologies, USA). Cells' nuclei were stained with a 0.1% v/v of 4',6-diamidino-2-phenyl indole dihydrochloride (DAPI) for 20 min. Z-stack fluorescent images were taken using a fluorescent microscope (Observer Z1, Zeiss, Germany) equipped with ApoTom2 enabling 3D imaging.

8.3.7. Intracellular Calcium Transient Assays.

Calcium ions (Ca^{2+}) transients were stained, according to our recent work(Saini et al. 2015), to demonstrate the frequency of the calcium puffs and investigate their synchronicity to the applied wireless stimuli.

8.3.8. Data acquisition and evaluation of tissue contraction.

Electrical voltage output to the bioreactor under the wired and wireless stimulations was monitored and recorded using a data acquisition card (NI6216, National Instrument) and visualized in NI Signal Express. The stimulation current was obtained by measuring the voltage drop at a 1 Ohm resistor which was in series with the bioreactor. Synchronous contractions of the cells were recorded in real-time using an optical microscope equipped with a physiological incubator (37 °C, 5 % CO_2). The excitation threshold voltage was

defined as the minimal voltage required to induce synchronous contractility in the tissue. The wired and wireless excitation thresholds were obtained by slowly decreasing the output amplitude/power of the function generator/RF power source while simultaneously monitoring cell contraction in real-time under the microscope until the minimum voltages were recorded (0.5, 1, and 2 Hz frequencies). Once the synchronous tissue beating was observed, real-time videos were captured by using an inverted microscope equipped with an AxioCam MRm camera (Zeiss, Germany), and simultaneously the stimulator output voltage and current were recorded. The recorded videos were processed with a custom-written MATLAB code(S. B. Kim et al. 2011) to generate representative beating signals, which were subsequently compared to the recorded voltage and current waveforms. Both wired and wireless stimulations were conducted on 6 different cardiac tissue samples.

8.3.9. Statistical Analysis.

The statistical analysis was performed using GraphPad PRISM 6 software. Particularly, student t-test (Two-tailed) was used to investigate the difference between the data sets, and *p* value less than 0.05 was considered to be significant.

8.4. Experiment Results and Discussion

8.4.1 Wireless Passive Stimulator Characterization.

The performance of the wireless stimulator was primarily evaluated by measurement of the output voltage onto the custom-made bioreactor filled with cell culture media. The output pads of the wireless stimulator are connected to the carbon electrodes in

the bioreactor through platinum wires (**Figure 8.6**). The external antenna was placed 5 mm above the stimulator. The output voltage was collected between the two electrodes in the bioreactor, which was recorded simultaneously along with the input. **Figures 8.7a** shows the input and output voltage signal of a 2 Hz, 2 millisecond pulse. It is clear that the output follows the input with a negligible delay. When the input signal reaches the high level, *i.e.,* 2.8 V, the radiating RF power is maximum. On the other hand, when the input becomes low, *i.e.,* 0 V, the RF power becomes nearly zero. These different RF power levels control the "On" and "Off" states of the PMOS on the stimulator, charging and discharging the capacitor, which subsequently generates the output pulse signal. **Figure 8.7a** shows monophasic pulses output. A biphasic pulse can be produced using a switching structure(McDermott 1989). However, this requires complex digital circuits and power rectifiers. As described in the protocol(Tandon et al. 2009), a monophasic pulse with a short pulse duration (2ms) and a long period (500-1000ms) is sufficient to excite the cardiac tissue and does not cause irreversible chemical reaction between the electrode-electrolyte interface.

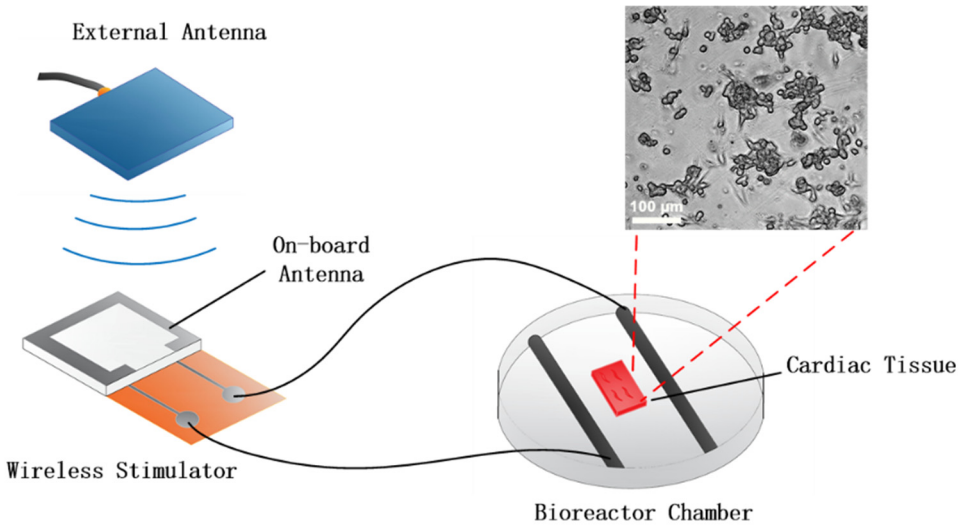

Figure 8.6. Experiment setup of cardiac tissue stimulation. Output pads of the wireless stimulator are connected to the carbon electrodes in the bioreactor via platinum wires. The bioreactor is placed under the microscope for real-time monitoring of cell contractions. The electrical output of the wireless stimulator is a pulse signal with 0.5~2Hz frequency and 2ms pulse width. The amplitude of the pulse is set to be 2-10V.

Figure 8.7b, a close-up of **Figure 8.7a**, shows that the output waveform presents a non-ideal square wave upon the input of a square wave. The high level voltage dropped over time and the low level voltage remained non-zero. Such behavior is due to the electrical impedance property of the load, the bioreactor. As the stimulator produces pulse outputs via the discharging of capacitors, the load impedance influences the pulse waveform. Also, the bioreactor itself contains a very large capacitive impedance (0.9-5 mF) at low frequencies(Tandon et al. 2009; Serena et al. 2009), whereas the wireless stimulator has a relatively large output impedance (20 kΩ). These results in large time constants ($\tau \cong$ 18 sec) for the bioreactor to discharge its stored charges, thus the voltage stays above zero.

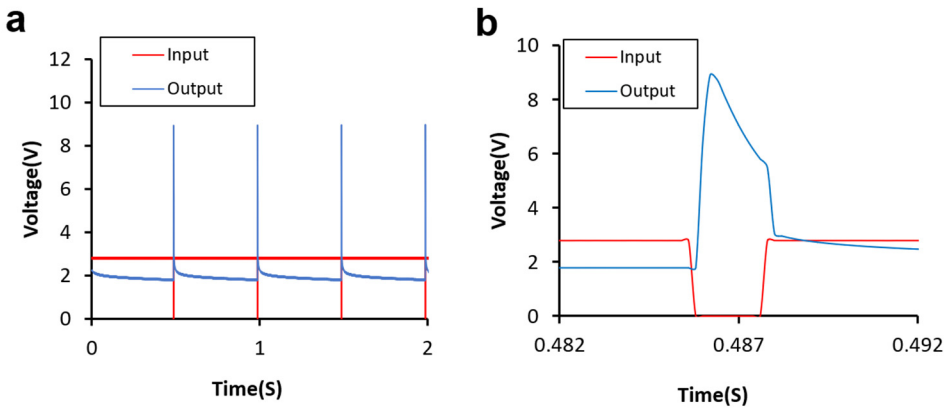

Figure 8.7. Characterization of the passive wireless stimulator using a custom made bioreactor. (a) Measured input/output voltage waveform of the stimulator. (b) A close-up of the input/output waveform shown in (a).

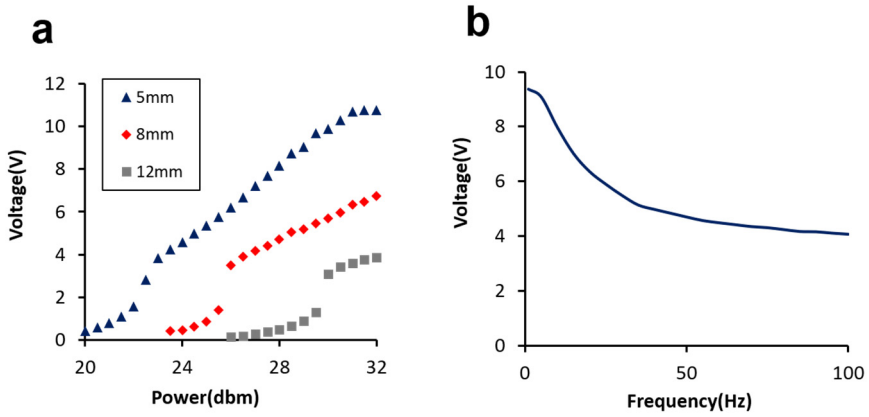

Figure 8.8. Impact of the wireless transmission distance and the stimulation frequency. (a) Stimulation amplitude as a function of the RF power under different wireless transmission distances. (b) Stimulation amplitude as a function of the frequency.

Several parameters impact the output amplitude of the stimulator. **Figure 8.8a** shows the output amplitude as a function of the RF power, set by the RF signal generator, at different wireless transmission distances. The output amplitude increases as the power increases or the distance decreases. The maximum output voltage achieved is 10.7 V at 5 mm. We also notice the distinct discontinuities of the curves when the output amplitudes were approximately 2.5 V, regardless of the wireless transmission distances. Those discontinuities may originate from the transition of the PMOS from "on" to "off". As the available RF power decreases, V_{gs} of the PMOS becomes near its threshold voltage, V_{th}. When the V_{gs} becomes higher than V_{th}, approximately 2.5 V, the PMOS turns "on" effectively. However, when the V_{gs} fails to reach V_{th}, the PMOS turns "off", leading to a decrease in the output amplitude.

The output amplitude of the stimulator is also a function of the stimulation frequency (**Figure 8.8b**). The stimulation period, the inverse of frequency, determines the available time for the stimulator to accumulate electrical charges. Thus, as the frequency increases the output amplitude decreases.

Human tissue is largely capacitive(Schwan and Kay 1957), requiring that the wireless stimulator be carefully evaluated at different capacitive loads. Both the amplitude and waveform of the stimulator output depend upon the impedance of the load. To characterize the loading effect, the output amplitude was evaluated when the stimulator was connected to a pure resistive load (**Figure 8.9a**) and a capacitive load (**Figure 8.9b**). The output voltage and current were recorded as a function of resistance (10-5000 Ω) at 5, 8, and 13 mm distances. The output voltage amplitude dropped quickly as the resistance

decreased, primarily due to the finite power delivery capability of the wireless communication. For the capacitive load, the stimulator was connected to a capacitor in parallel with a resistor to account for the realistic resistive loss, in addition to the capacitive effect. The output voltage was recorded as the capacitance changed from 10 nF to 10 µF (**Figure 8.9b**). The voltage was independent of the capacitance of less than 1 µF. Beyond 1 µF, the voltage began to drop slowly. These results demonstrate that the wireless stimulator is capable of delivering pulse signals of several volts on low resistive and high capacitive loads.

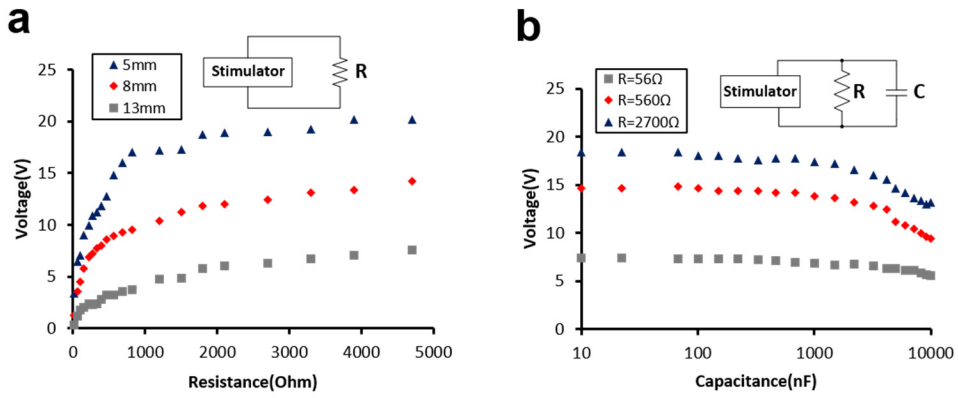

Figure 8.9. Characterization of the wireless stimulator on resistive/capacitive load. The amplitude of the pulses generated by the wireless stimulator is affected by both (a) pure resistive load and (b) capacitive load.

Figure 8.10a shows the temporal output voltage waveforms of the stimulator, derived on 56, 560, and 2700 Ω loads. The waveform variation was due to the differences in the discharging current of the capacitors. The large output current, for the low resistance

(R=56 Ω), allows the electric charges stored on the onboard capacitors to be depleted quickly, resulting in the dropping of output voltage before the pulse duration ends. For the high resistance (R=2700 Ω), on the other hand, the small output current is insufficient to stabilize the output voltage during the whole pulse duration. The output voltage, for the medium load (R=560 Ω), was maintained at a relatively stable level. **Figure 8.10b** shows the output waveforms at 10 nF, 2 µF, and 10 µF loading capacitors, with a 560-Ohm resistor in parallel. The loading effect became clear as the capacitance increases, as shown in the discharging behavior. The output voltage kept dropping until all the electric charges were completely discharged.

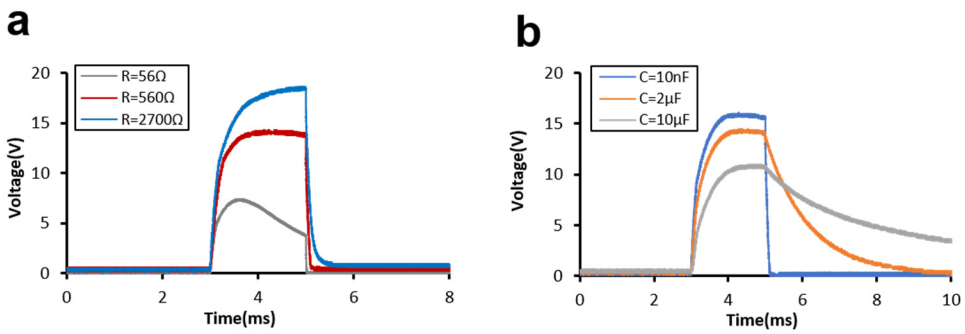

Figure 8.10. Effect of the load on the stimulation waveform. (a) The temporal voltage waveforms of the stimulator on different loading resistors. (b) The temporal voltage waveforms of the stimulator on different loading capacitors.

8.4.2. Electrical Stimulation of Cardiomyocytes.

External electrical stimulation was applied to the cardiac tissue constructs between the two carbon electrodes of the bioreactor chamber, on day 8 of the culture (**Figure 8.11a**).

The cells demonstrated spread and elongated morphology (**Figure 8.11b**). The impedance of the bioreactor was measured using an LCR meter (Agilent E4980A), at 20-10000 Hz with 1, 5, 10 V input voltage amplitudes. **Figure 8.11c** shows the Nyquist plot of the bioreactor impedance, from which we extracted simplified equivalent circuit parameters, R_p and constant phase element (CPE), the parallel resistance of the electrolyte (cell culture media), and a non-ideal capacitor, respectively (**Table 8.2**).

Table 8.2: Impedance of the bioreactor chamber

Voltage (V)	Frequency (Hz)	CPE (F)	Rp (Ω)
1	20	2.40E-5	128.2
	1000	6.17E-8	86.5
5	20	2.14E-5	116.7
	1000	6.06E-8	85.8
10	20	1.81E-5	110.1
	1000	5.79E-8	86.7

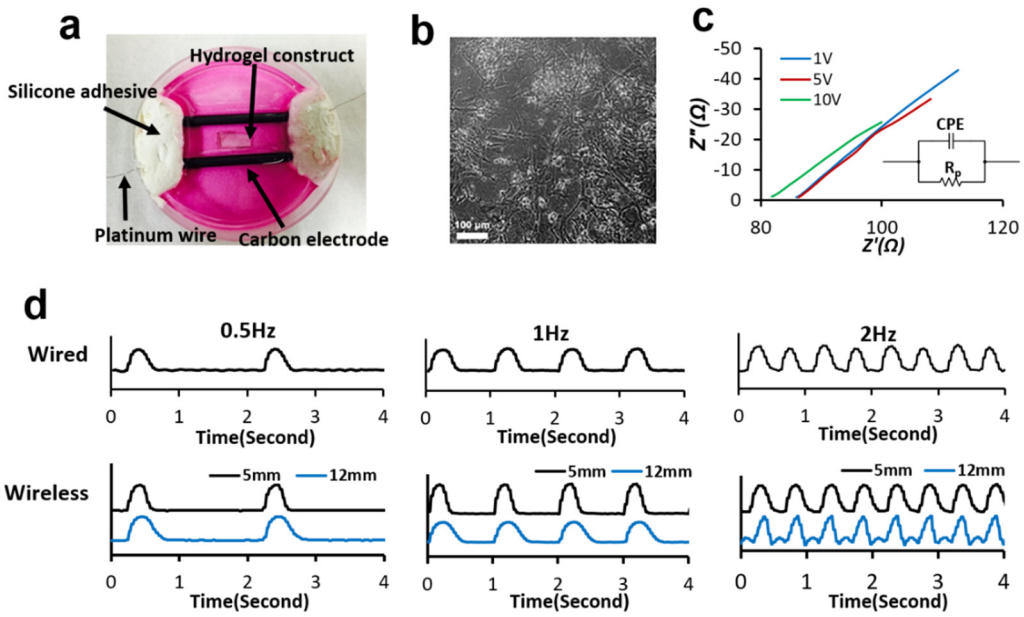

Figure 8.11. Wireless passive stimulation of cardiomyocytes. (a) Photograph of the cardiac tissue placed in the bioreactor chamber. (b) Phase-contrast image of the cardiomyocytes on day 8. (c) Measured Nyquist plot of the bioreactor chamber under various input voltages. The inlet shows the simplified equivalent circuit of the bioreactor chamber. The values of CPE and R_p are given in Table 8.2. (d) Comparison of cell beating signals under the wired and wireless stimulations.

The impedance measurement confirmed that the bioreactor was highly capacitive (20 μF) at low frequency. We chose the lowest frequency of 20 Hz, limited by the LCR meter (E4980A, Agilent). At high frequency, the bioreactor showed lower capacitive behavior, thus the short period pulse can stimulate cardiac tissues. To evaluate the capability of the wireless stimulator to induce synchronous cellular contractions within the tissue constructs as compared to that of a conventional wired setup, the samples were

stimulated using the wireless setup, placing the external antenna close (5 mm) and far from the stimulator (1.2 cm). **Figure 8.11d** shows the recorded cell beating signals under the wired (control) and wireless stimulations of 2 millisecond pulses at 0.5, 1, and 2 Hz, respectively. The y-axis values are arbitrary numbers correlated to the "pixel movement" in the recorded videos, representing the extracted beating signals of cardiac cells, therefore no unit or title is assigned to the y-axis. The cell contraction patterns under the wireless stimulation at both antenna locations (5 mm and 1.2 cm away from the stimulator) were consistent with that of the wired stimulation, demonstrating cardiac cell beating in synchrony with the external electrical pulses.

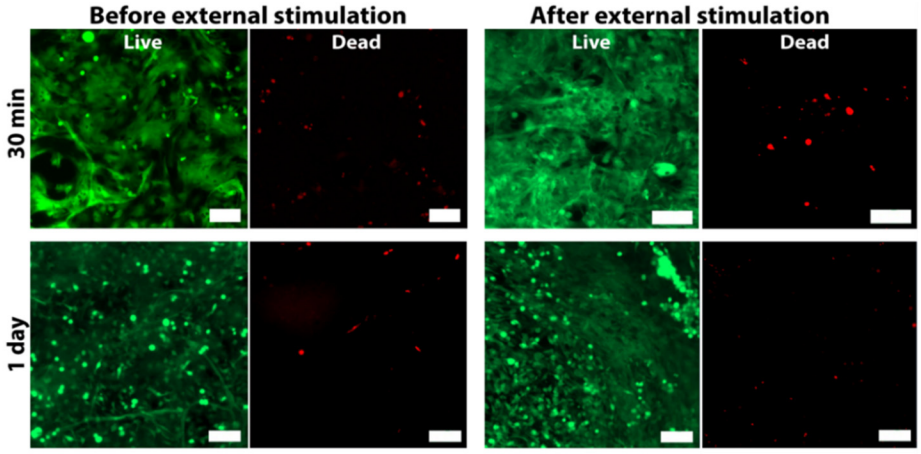

Figure 8.12. Cell viability assays for confirming the safety of wireless passive stimulation. The fluorescent images show live (green) and dead (red) cells before and after 30 minutes / 1 day continuous wireless electrical stimulation. All the scale bars are 100 μm.

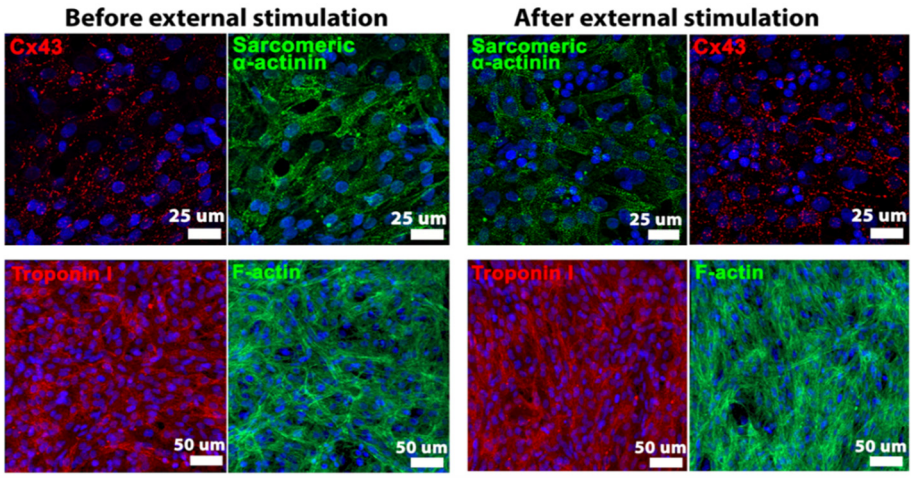

Figure 8.13. Analysis of cardiac tissue construct. Up: Z-stack immuno-stained images of sarcomeric α-actinin (green) and Cx43 (red) cardiac-specific markers before and after 30 minutes wireless stimulation. Down: F-actin (green) and troponin-I (red) stained before and after 30 minutes wireless stimulation.

We assessed the cellular survival before and after wireless stimulations in two different settings including 30 minutes with 2 Hz (short-term) and 1 day with 1 Hz (long-term) to verify that the wireless stimulation incurred no significant influence on cell viability. The short-term stimulation was designed based on the highest frequency (2 Hz) that was used in our study, and the long-term stimulation was consistent with previously published studies(Tandon et al. 2009). As can be seen in **Figures 8.12**, most cells were viable upon stimulation (30 min stimulation at 2 Hz). Viability images of the cardiac constructs after 1 day of wireless stimulation also confirmed no significant cell death. The tissue constructs were also analyzed for cytoskeleton organization and the expression of cardiac-specific proteins, namely sarcomeric α-actinin, troponin-I, and Cx43, before and

after 30 minutes wireless stimulation. As shown in **Figure 8.13**, the cells maintained an intact cytoskeleton organization (F-actin fibers), integrated sarcomere structures and troponin-I networks, along with well-established Cx43 gap junctions in presence of wireless stimulations. These findings confirmed that the electrical stimulation led to no significant alterations in cardiac cells survival, cytoskeleton organization, cardiac-specific phenotype, and cellular connectivity.

Figure 8.14 shows the electrical characterization of wired vs. wireless stimulation (5mm) set up. We primarily compared the output voltage and current waveforms from the wired and wireless stimulators (**Figure 8.14a, b**). As can be seen in the graph, the pulse amplitudes of wired and wireless stimulations were both approximately 3 V, and the voltage to current ratio agreed well with the measured impedance in table II. Obviously, cardiac cells exhibited synchronous beating only when output current exceeded 60 mA. This high value is beyond the output capability of all the previously reported wireless stimulator(Ziaie et al. 1997; Schulman 2008; E. Lee et al. 2009; Arfin et al. 2009). We observed that both voltage and current profiles dropped quickly in wireless stimulations, whereas in wired stimulations they remained at a stable level. This phenomenon is primarily caused by the differences in the current driving capability of the wired and wireless devices. The output current of the wired stimulator, directly driven by the arbitrary function generator, was continuously provided by the instrument internal power supply. On the other hand, the output current of the wireless stimulator came from the discharging of the capacitor, which ran off its stored charges quickly and resulted in a quick drop in both output voltage and current. Although the wireless stimulating waveform exhibited

some inconsistency with its wired counterparts, it was sufficient to induce well-controlled synchronous contractility in cardiac tissue.

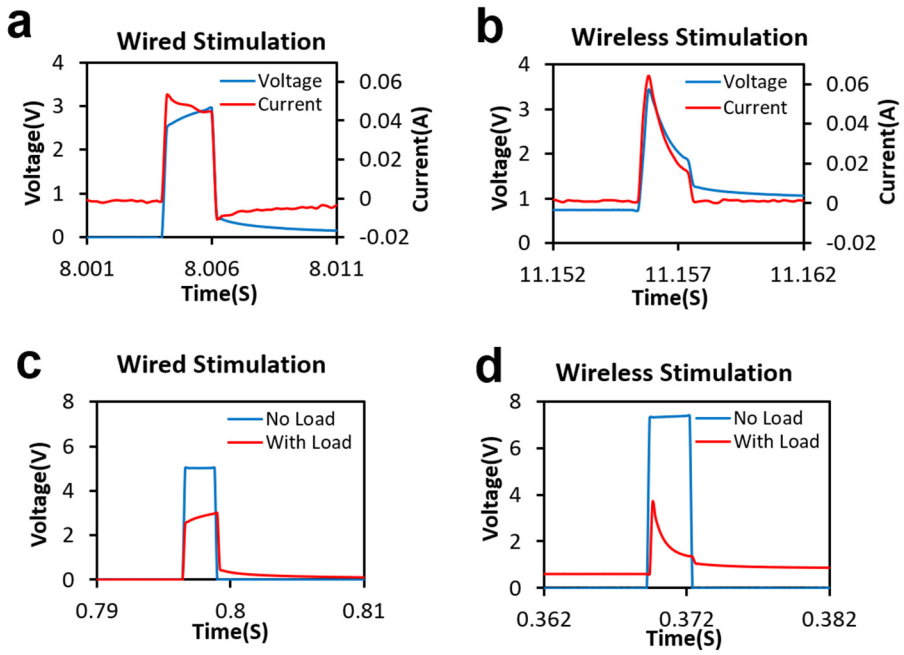

Figure 8.14. Comparison of the electrical output of the wired/wireless stimulator. (a,b) The waveform of voltage and current outputted from the wired (a) and wireless (b) stimulator to the bioreactor. The wireless output signal shows a clear capacitor discharging process. (c,d) The load effect on the wired / wireless stimulator. Due to the load effect, output voltage in both wired (c) and wireless (d) stimulation dropped when the bioreactor was connected.

Figure 8.14c, d compares the output voltage profile recorded from the wired and wireless stimulators before and after connecting the bioreactor. In both cases, the stimulation voltage dropped when the bioreactor was connected. Tandon(Tandon et al.

2009) suggested that this phenomenon is caused by the low current rating of the stimulating device. Therefore, the accurate electrical stimulating parameters (stimulating voltage and current) need to be measured in-situ. As mentioned earlier, the output pulse signal in wireless stimulation remained non-zero because of the high capacitive property of the bioreactor and the large output resistance of the wireless stimulator (approximately 20 kΩ). As for the wired stimulator, this phenomenon did not occur because the function generator has a notably lower output resistance (50 Ω), which enabled the bioreactor to quickly discharge its stored charges and return the voltage level back to zero.

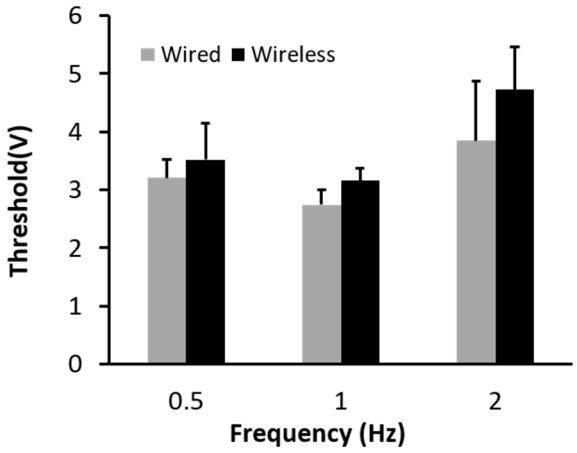

Figure 8.15. Comparison of the excitation voltage threshold of wired / wireless stimulations. No significant difference was observed between wired and wireless stimulations (p<0.05).

Figure 8.15 shows measured excitation threshold voltages for wired and wireless stimulators. As the frequency became higher, the excitation threshold increased, consistent with the prior studies(Tandon et al. 2009). We observed that the threshold voltages of

wireless stimulations were slightly above the values obtained from the wired stimulation. We speculate that this is due to the different output pulse waveforms as shown in **Figure 8.14a, b**. The quick drop of the wireless output voltage can lead to lower efficacy on the contraction of cardiomyocytes compared to the wired stimulation with the same output amplitude. The wireless stimulator may have an edge over wired counterparts in its compatibility for implantation and potential applications such as cardiac regenerating therapy(Kharaziha et al. 2016). In fact, confirmation of cardiomyocytes stimulation using the wireless stimulator, with a consistent regime as compared to wired stimulation, is a significant advantage of our study over prior studies(Tandon et al. 2009; Hirt et al. 2014; Serena et al. 2009; Radisic et al. 2004; Tandon et al. 2011).

8.4.3. Assessment of Intracellular Calcium Ions (Ca^{2+}) Transients.

Calcium ions (Ca^{2+}) have been known to play a central role in regulating the contraction of cardiomyocytes. Ca^{2+} ions release from the intracellular pools into the actin-myosin complexes (contractile machinery of the heart muscle cells) and initiate the contraction process(Bers 2000). As cardiomyocytes beat, the concentration of Ca^{2+} ions increases sharply, creating puffs with the same frequency of beating(Takahashi et al. 1999).

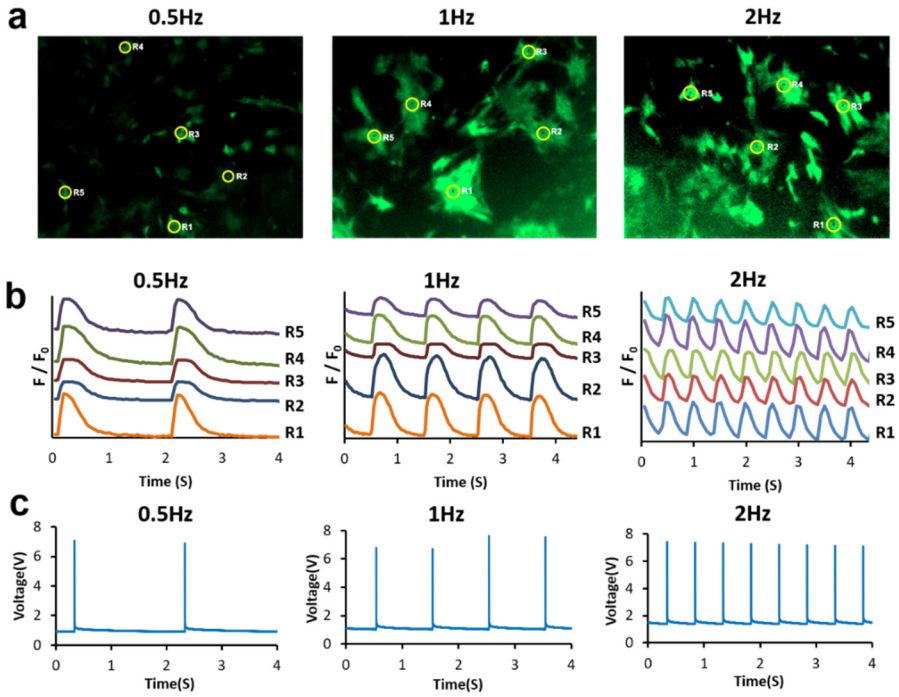

Figure 8.16. Analysis of intracellular calcium transient under passive wireless stimulation. (a) Fluorescent imaging showing Ca^{2+} ion transients (green). (b) Extracted signals of intracellular Ca^{2+} ions concentration changes (F/F_0) within the cultured cardiomyocytes (R1 to R5 are five different selected regions of interest). (c) Measured stimulator output waveforms at 0.5, 1, and 2 Hz stimulating frequencies.

Figure 8.16a and b represent the fluorescent images and the extracted calcium transient signals at 5 different regions of interest (R1 to R5) of each sample at 0.5, 1, and 2 Hz wireless stimulation (5mm). All the defined regions demonstrated synchronized calcium puffs, in synchrony with the stimulator output voltage signals (**Figure 8.16c**).

Table 8.3: Comparison of the prior wireless stimulator with this work

Spec	(Ziaie et al. 1997)	(E. Lee et al. 2009)	(Arfin et al. 2009)	(H. M. Lee, Park, and Ghovanloo 2013)	This work
Powering method	Inductive coupling	Rechargeable battery	Inductive coupling	Inductive coupling	RF coupling
External coil/antenna size	9 x 8.5 cm	-	17 x 17 cm	4 x 4 cm	1 x 1cm
Maximum Stimulating current	10mA	10mA	1mA	2.8mA	60mA
Maximum Power consumption	55mW	21.6mW	50µW	-	18mW
Application	Muscle Stimulation	Muscle stimulation	Brain Stimulation	Brain Stimulation	Cardiac tissue stimulation

Table 8.3 compares the presented stimulator and prior arts on wireless stimulation systems. The wireless stimulator, developed herein, delivers the highest stimulating current as compared to other works. In addition, RF coupling greatly reduces the size of the external transmitting antenna to as small as 1cm x 1cm, which is the smallest among other reported wireless stimulating systems. However, the large footprint of current stimulator is still one of the challenges limiting its future application. Currently, the onboard antenna occupies a large area because the performance of the antenna is strongly associated with its electrical length. As the antenna becomes smaller, many of its important characteristics will be sacrificed, such as radiation resistance, efficiency, and directivity. Therefore,

reducing the antenna size without sacrificing the performance of the stimulator requires more design optimization. The 12 mm wireless working distance of the stimulator needs to be improved for further practical applications. Several mitigations exist, including optimized multistage charging/discharging circuits, and directivity enhancement of the antenna. Evaluating the wireless stimulator in a tissue-emulating phantom also conveys a more realistic performance evaluation, which remains a subject of our future study.

Overall, the proposed RF powered passive wireless stimulator demonstrated excellent efficacy, for the first time, to stimulate synchronous contractility in engineered cardiac tissues. The cells beating curves generated under wired and wireless stimulations showed consistent agreements with the stimulation regimes. Recorded electrical signal during the stimulation delivered a current output value of higher than 60 mA, which is the highest among existing passive wireless stimulators. The stimulator contains only one on-board active electronic component, PMOS, to regulate the stimulating behavior. The total power consumption, 18 mW, is determined by the two on-board resistors. We may further lower the power consumption, down to less than 1 mW by increasing the value of the resistors. These results suggest a promising potential of the proposed stimulator for cardiac tissue stimulation, as well as many other clinical and research applications.

CHAPTER 9

CONCLUSION

This thesis described the design, fabrication, and verification of several wireless fully-passive sensors for biosignal acquisitions. These sensors utilize a novel RF backscattering method to accomplish wireless telemetry of different kinds of biosignals, including neuropotentials, biopotentials, and intracranial pressure (ICP). Without using any battery or any digital electronics, the developed wireless fully-passive sensors have many attractive features, such as small size, high flexibility, biocompatible, and near-zero power consumption. Thus, these sensors are envisaged for long-term, continuous monitoring of the user's physiological signals. The RF backscattering method is based on the non-linear mixing operation of the varactor diodes. Both theoretical calculations and CAD simulation models are introduced to analyze the basic principle of the sensor and estimate the power of the backscattered signal (Chapter 3). The design of a small-sized (9 mm x 8 mm), flexible, wireless fully-passive neural recorder is introduced in Chapter 4. Simulation and *in vitro* verification of the sensor demonstrates a sensitivity of 60 μV_{pp} when it is implanted inside a tissue-emulating phantom. *In vivo* verification is also carried out by implanting the neural recorder subcutaneously onto a rat skull. Wirelessly recorded neural signals, including SSEPs and IEDs, shows well correspondence with those from a wired electrode. In addition, a machine learning algorithm is used to analyze the wireless IED data, showing a recognition accuracy as high as 91%, which strongly support the recorder capability to measure neuropotentials as low as tens of microvolts. To expand the number of recording channels, a wireless, passive, multichannel neural recording mechanism based on an

inductor-capacitor delay line circuit is proposed in Chapter 5. The LC delay line circuit alternately turns on each recording channel as a pulse signal propagates through it, enabling wireless acquisition of multichannel neural signals in a time-multiplexed manner. The working principle of the system is discussed and verified by CAD simulations. Furthermore, a 16 channel wireless passive ECoG array prototype is fabricated and tested using emulated signals. Output signals of 11 channels show good correspondence with the input, achieving at least 22 dB SNR and 8 dB channel-channel isolation. To measure the body biopotentials, a small, flexible, and wearable wireless fully-passive biopotential sensor is introduced in Chapter 6. The sensor adopts an improved antenna and circuit structure. Simulation and benchtop characterization of the sensor shows a significantly improved working distance of up to 240 mm. Realtime wireless acquisitions of various biopotentials, including ECG, EMG, and EOG, are conducted on volunteer subjects, which demonstrates the sensor accurate detection of biopotentials as low as 250 μV_{pp}. Besides measuring electrophysiological signals, a wireless fully-passive sensor for intracranial pressure (ICP) monitoring is also developed (Chapter 7). With a custom-fabricated pressure sensing resistor (PSR) and a modified Wheatstone Bridge circuit, the wireless ICP sensor is able to measure absolute pressure value using the RF backscattering method. A further optimized antenna and circuit structure reduces the total footprint of the sensor to 5 mm x 4 mm. The sensor is successfully verified *in vitro* through measurement of water columns, and *in vivo* through real-time recording of the ICP in a rat in response to external pressure. Lastly, the development of a passive wireless stimulator for engineered cardiac cells is introduced in Chapter 8. The RF powered wireless stimulator is fabricated on a flexible polyimide

substrate. Composing only one PMOS transistor, the stimulator consumes very little power, yet it demonstrates excellent efficacy to stimulate engineered cardiac tissues, inducing their synchronous contraction. The output current of the stimulator is shown to be larger than 60 mA during stimulation, which is the highest among existing passive wireless stimulators. These results indicate the promising potential of the wireless passive stimulator for cardiac tissue engineering applications

Despite the promising results, the wireless fully-passive sensors presented by this thesis still faces several limitations and challenges before their real clinical applications. Due to the lack of any digital coding techniques, the wireless fully-passive sensors generally have relatively low SNR as compared to active systems. In addition, motion artifacts can greatly interfere with the wireless output signal, impairing the signal integrity of the sensors. However, these challenges can be largely mitigated if additional functions, such as the electronic chopping, are included in the circuit. Although the accuracy of the wireless fully-passive sensors is not ideal, they offer unparalleled advantages in safety and reliability. Thus, they are strong candidates for medical applications that require high safety rather than complex functionality.

The technology introduced by this thesis aims at providing a convenient, long-term, safe, and reliable method for biosignal acquisition. The successful development of this technology may ultimately result in substantial improvement in the well-being of patients. For example, patients with severe neurological disorders sometimes require to be hospitalized for continuous cortex recording for several days in order to capture the pre-seizure signals. The sensors introduced in this thesis may eventually enable this procedure

to be done at the patient home in an easy and safe way without any constraints on the patient's activities. In addition, this technology may become useful tools to accelerate our understanding of numerous chronic diseases and neurological disorders.

REFERENCES

Abbaspour-Tamijani, A., M. F. Farooqui, B. C. Towe, and J. Chae. 2008. "A Miniature Fully-Passive Microwave Back-Scattering Device for Short-Range Telemetry of Neural Potentials." In *2008 30th Annual International Conference of the IEEE Engineering in Medicine and Biology Society*, 129–32. https://doi.org/10.1109/IEMBS.2008.4649107.

Abidi, A. A. 1995. "Direct-Conversion Radio Transceivers for Digital Communications." *IEEE Journal of Solid-State Circuits* 30 (12): 1399–1410. https://doi.org/10.1109/4.482187.

Albulbul, Anas. 2016. "Evaluating Major Electrode Types for Idle Biological Signal Measurements for Modern Medical Technology." *Bioengineering* 3 (3): 20.

AlGhatrif, Majd, and Joseph Lindsay. 2012. "A Brief Review: History to Understand Fundamentals of Electrocardiography." *Journal of Community Hospital Internal Medicine Perspectives* 2 (1): 14383.

Antes, Sebastian, Christoph A. Tschan, Michael Heckelmann, David Breuskin, and Joachim Oertel. 2016. "Telemetric Intracranial Pressure Monitoring with the Raumedic Neurovent P-Tel." *World Neurosurgery* 91: 133–48.

Arfin, Scott K., Michael A. Long, Michale S. Fee, and Rahul Sarpeshkar. 2009. "Wireless Neural Stimulation in Freely Behaving Small Animals." *Journal of Neurophysiology* 102 (1): 598–605. https://doi.org/10.1152/jn.00017.2009.

Babiloni, Claudio, Roberta Lizio, Nicola Marzano, Paolo Capotosto, Andrea Soricelli, Antonio Ivano Triggiani, Susanna Cordone, Loreto Gesualdo, and Claudio Del Percio. 2016. "Brain Neural Synchronization and Functional Coupling in Alzheimer's Disease as Revealed by Resting State EEG Rhythms." *International Journal of Psychophysiology* 103: 88–102.

Balanis, Constantine A. 2016. *Antenna Theory: Analysis and Design*. John Wiley & Sons.

Barrese, James C., Naveen Rao, Kaivon Paroo, Corey Triebwasser, Carlos Vargas-Irwin, Lachlan Franquemont, and John P. Donoghue. 2013. "Failure Mode Analysis of Silicon-Based Intracortical Microelectrode Arrays in Non-Human Primates." *Journal of Neural Engineering* 10 (6): 066014.

Based, Complex Neurobiological Mechanisms. 2012. "Interictal Epileptiform Discharges in Partial Epilepsy." *Jasper's Basic Mechanisms of the Epilepsies* 80: 213.

Beck, Travis W., Terry J. Housh, Glen O. Johnson, Joseph P. Weir, Joel T. Cramer, Jared W. Coburn, and Moh H. Malek. 2005. "The Effects of Interelectrode Distance on Electromyographic Amplitude and Mean Power Frequency during Isokinetic and

Isometric Muscle Actions of the Biceps Brachii." *Journal of Electromyography and Kinesiology* 15 (5): 482–95. https://doi.org/10.1016/j.jelekin.2004.12.001.

Behfar, Mohammad H., Emily Abada, Lauri Sydänheimo, Ken Goldman, Aaron J. Fleischman, Nalin Gupta, Leena Ukkonen, and Shuvo Roy. 2016. "Inductive Passive Sensor for Intraparenchymal and Intraventricular Monitoring of Intracranial Pressure." In *2016 38th Annual International Conference of the IEEE Engineering in Medicine and Biology Society (EMBC)*, 1950–54. IEEE.

Bellman, Matthew J., T.-H. Cheng, Ryan J. Downey, and Warren E. Dixon. 2014. "Stationary Cycling Induced by Switched Functional Electrical Stimulation Control." In *2014 American Control Conference*, 4802–9. IEEE.

Bellner, Johan, Bertil Romner, Peter Reinstrup, Karl-Axel Kristiansson, Erik Ryding, and Lennart Brandt. 2004. "Transcranial Doppler Sonography Pulsatility Index (PI) Reflects Intracranial Pressure (ICP)." *Surgical Neurology* 62 (1): 45–51.

Belov, D. P., S. Yu Eram, S. F. Kolodyazhnyi, I. E. Kanunikov, and O. V. Getmanenko. 2010. "Electrooculogram Detection of Eye Movements on Gaze Displacement." *Neuroscience and Behavioral Physiology* 40 (5): 583–91. https://doi.org/10.1007/s11055-010-9299-z.

Berger, Mitchel S., and George A. Ojemann. 1992. "Intraoperative Brain Mapping Techniques in Neuro-Oncology." *Stereotactic and Functional Neurosurgery* 58 (1–4): 153–61.

Bers, Donald M. 2000. "Calcium Fluxes Involved in Control of Cardiac Myocyte Contraction." *Circulation Research* 87 (4): 275–81. https://doi.org/10.1161/01.RES.87.4.275.

Besnoff, J. S., T. Deyle, R. R. Harrison, and M. S. Reynolds. 2013. "Battery-Free Multichannel Digital ECG Biotelemetry Using UHF RFID Techniques." In *2013 IEEE International Conference on RFID (RFID)*, 16–22. https://doi.org/10.1109/RFID.2013.6548130.

Bhadra, Narendra. 2015. "Physiological Principles of Electrical Stimulation." In *Implantable Neuroprostheses for Restoring Function*, 13–43. Elsevier.

Bi, Hua. 2018. "Electrodiagnostics in Today's Practice." *Review of Optometry* 155 (3): 52–58.

Bjerknes, Silje, Inger Marie Skogseid, Terje Sæhle, Espen Dietrichs, and Mathias Toft. 2014. "Surgical Site Infections after Deep Brain Stimulation Surgery: Frequency, Characteristics and Management in a 10-Year Period." *PloS One* 9 (8): e105288.

Bortel, Aleksandra, Maxime Lévesque, Giuseppe Biagini, Jean Gotman, and Massimo Avoli. 2010. “Convulsive Status Epilepticus Duration as Determinant for Epileptogenesis and Interictal Discharge Generation in the Rat Limbic System.” *Neurobiology of Disease* 40 (2): 478–89.

Borton, David A., Ming Yin, Juan Aceros, and Arto Nurmikko. 2013. “An Implantable Wireless Neural Interface for Recording Cortical Circuit Dynamics in Moving Primates.” *Journal of Neural Engineering* 10 (2): 026010. https://doi.org/10.1088/1741-2560/10/2/026010.

Breidthardt, Tobias, Michael Christ, Miriam Matti, Delia Schrafl, Kirsten Laule, Markus Noveanu, Tujana Boldanova, et al. 2007. “QRS and QTc Interval Prolongation in the Prediction of Long-Term Mortality of Patients with Acute Destabilized Heart Failure.” *Heart*, March. https://doi.org/10.1136/hrt.2006.102319.

Brimioulle, Serge, Jean-Jacques Moraine, Danielle Norrenberg, and Robert J. Kahn. 1997. “Effects of Positioning and Exercise on Intracranial Pressure in a Neurosurgical Intensive Care Unit.” *Physical Therapy* 77 (12): 1682–89.

Brocker, David T., and Warren M. Grill. 2013. “Principles of Electrical Stimulation of Neural Tissue.” In *Handbook of Clinical Neurology*, 116:3–18. Elsevier.

Bulling, A., J. A. Ward, H. Gellersen, and G. Troster. 2011. “Eye Movement Analysis for Activity Recognition Using Electrooculography.” *IEEE Transactions on Pattern Analysis and Machine Intelligence* 33 (4): 741–53. https://doi.org/10.1109/TPAMI.2010.86.

Buzsáki, György, Costas A. Anastassiou, and Christof Koch. 2012. “The Origin of Extracellular Fields and Currents—EEG, ECoG, LFP and Spikes.” *Nature Reviews Neuroscience* 13 (6): 407.

Camp, N. Van, M. Verhoye, and A. Van der Linden. 2006. “Stimulation of the Rat Somatosensory Cortex at Different Frequencies and Pulse Widths.” *NMR in Biomedicine: An International Journal Devoted to the Development and Application of Magnetic Resonance In Vivo* 19 (1): 10–17.

Canac, Nicolas, Kian Jalaleddini, Samuel G. Thorpe, Corey M. Thibeault, and Robert B. Hamilton. 2020. “Pathophysiology of Intracranial Hypertension and Noninvasive Intracranial Pressure Monitoring.” *Fluids and Barriers of the CNS* 17 (1): 1–21.

Chae, Moosung, Wentai Liu, Zhi Yang, Tungchien Chen, Jungsuk Kim, Mohanasankar Sivaprakasam, and Mehmet Yuce. 2008. “A 128-Channel 6mw Wireless Neural Recording Ic with on-the-Fly Spike Sorting and Uwb Tansmitter.” In *2008 IEEE International Solid-State Circuits Conference-Digest of Technical Papers*, 146–603. IEEE.

Chan, Adrain DC, and Geoffrey C. Green. 2017. “Myoelectric Control Development Toolbox.” *CMBES Proceedings* 30 (1).

Chang, Won-Du. 2019. “Electrooculograms for Human–Computer Interaction: A Review.” *Sensors* 19 (12): 2690.

Changa, Abhinav R., Barry M. Czeisler, and Aaron S. Lord. 2019. “Management of Elevated Intracranial Pressure: A Review.” *Current Neurology and Neuroscience Reports* 19 (12): 99.

Chari, Aswin, Debayan Dasgupta, Alexander Smedley, Claudia Craven, Edward Dyson, Samir Matloob, Simon Thompson, Lewis Thorne, Ahmed K. Toma, and Laurence Watkins. 2017. “Intraparenchymal Intracranial Pressure Monitoring for Hydrocephalus and Cerebrospinal Fluid Disorders.” *Acta Neurochirurgica* 159 (10): 1967–78.

Chen, Cen, Xue Bai, Yahui Ding, and In-Seop Lee. 2019. “Electrical Stimulation as a Novel Tool for Regulating Cell Behavior in Tissue Engineering.” *Biomaterials Research* 23 (1): 25.

Chen, Lisa Y., Benjamin C.-K. Tee, Alex L. Chortos, Gregor Schwartz, Victor Tse, Darren J. Lipomi, H.-S. Philip Wong, Michael V. McConnell, and Zhenan Bao. 2014. “Continuous Wireless Pressure Monitoring and Mapping with Ultra-Small Passive Sensors for Health Monitoring and Critical Care.” *Nature Communications* 5 (1): 1–10.

Chen, P. J., D. C. Rodger, S. Saati, M. S. Humayun, and Y. C. Tai. 2008. “Microfabricated Implantable Parylene-Based Wireless Passive Intraocular Pressure Sensors.” *Journal of Microelectromechanical Systems* 17 (6): 1342–51. https://doi.org/10.1109/JMEMS.2008.2004945.

Chen, Po-Jui, Saloomeh Saati, Rohit Varma, Mark S. Humayun, and Yu-Chong Tai. 2010. “Wireless Intraocular Pressure Sensing Using Microfabricated Minimally Invasive Flexible-Coiled LC Sensor Implant.” *Journal of Microelectromechanical Systems* 19 (4): 721–34.

Chen, Ritchie, Andres Canales, and Polina Anikeeva. 2017. “Neural Recording and Modulation Technologies.” *Nature Reviews Materials* 2 (2): 1–16.

Cheng, Kuang-Wei, Xiaodan Zou, Jia Hao Cheong, Rui-Feng Xue, Zhiming Chen, Lei Yao, Hyouk-Kyu Cha, San Jeow Cheng, Peng Li, and Lei Liu. 2012. “100-Channel Wireless Neural Recording System with 54-Mb/s Data Link and 40%-Efficiency Power Link.” In *2012 IEEE Asian Solid State Circuits Conference (A-SSCC)*, 185–88. IEEE.

Chestek, Cynthia A., Vikash Gilja, Paul Nuyujukian, Ryan J. Kier, Florian Solzbacher, Stephen I. Ryu, Reid R. Harrison, and Krishna V. Shenoy. 2009. "HermesC: Low-Power Wireless Neural Recording System for Freely Moving Primates." *IEEE Transactions on Neural Systems and Rehabilitation Engineering* 17 (4): 330–38.

Cho, Sung-Hoon, Lawrence Cauller, Will Rosellini, and Jeong-Bong Lee. 2010. "A MEMS-Based Fully-Integrated Wireless Neurostimulator." In *2010 IEEE 23rd International Conference on Micro Electro Mechanical Systems (MEMS)*, 300–303. IEEE.

Choi, Seokheun, and Junseok Chae. 2009. "A Regenerative Biosensing Surface in Microfluidics Using Electrochemical Desorption of Short-Chain Self-Assembled Monolayer." *Microfluidics and Nanofluidics* 7 (6): 819.

Chow, E. Y., M. M. Morris, and P. P. Irazoqui. 2013. "Implantable RF Medical Devices: The Benefits of High-Speed Communication and Much Greater Communication Distances in Biomedical Applications." *IEEE Microwave Magazine* 14 (4): 64–73. https://doi.org/10.1109/MMM.2013.2248586.

Christoff, Kalina, Justin M. Ream, and John DE Gabrieli. 2004. "Neural Basis of Spontaneous Thought Processes." *Cortex* 40 (4–5): 623–30.

Chung, Ha Uk, Bong Hoon Kim, Jong Yoon Lee, Jungyup Lee, Zhaoqian Xie, Erin M. Ibler, KunHyuck Lee, Anthony Banks, Ji Yoon Jeong, and Jongwon Kim. 2019. "Binodal, Wireless Epidermal Electronic Systems with in-Sensor Analytics for Neonatal Intensive Care." *Science* 363 (6430).

Cockbain, A. G., and P. J. Harrop. 1968. "The Temperature Coefficient of Capacitance." *Journal of Physics D: Applied Physics* 1 (9): 1109.

Coosemans, Johan, Bart Hermans, and Robert Puers. 2006. "Integrating Wireless ECG Monitoring in Textiles." *Sensors and Actuators A: Physical* 130: 48–53.

Creel, Donnell J. 2019. "The Electrooculogram." In *Handbook of Clinical Neurology*, 160:495–99. Elsevier.

Darrell, Trevor, and Alexander Pentland. 1993. *Recognition of Space-Time Gestures Using a Distributed Representation*. Vision and Modeling Group, Media Laboratory, Massachusetts Institute of Technology.

Dementyev, A., and J. R. Smith. 2013. "A Wearable UHF RFID-Based EEG System." In *2013 IEEE International Conference on RFID (RFID)*, 1–7. https://doi.org/10.1109/RFID.2013.6548128.

Deshmukh, Abhay, Jared Leichner, Jihye Bae, Yinchen Song, Pedro A. Valdés-Hernández, Wei-Chiang Lin, and Jorge J. Riera. 2018. "Histological Characterization of the

Irritative Zones in Focal Cortical Dysplasia Using a Preclinical Rat Model." *Frontiers in Cellular Neuroscience* 12.

DiMarco, Anthony. 1999. "Diaphragm Pacing in Patients with Spinal Cord Injury." *Topics in Spinal Cord Injury Rehabilitation* 5 (1): 6–20.

DiMarco, John P., and John T. Philbrick. 1990. "Use of Ambulatory Electrocardiographic (Holter) Monitoring." *Annals of Internal Medicine* 113 (1): 53–68.

Dodge, S., and L. Karam. 2016. "Understanding How Image Quality Affects Deep Neural Networks." In *2016 Eighth International Conference on Quality of Multimedia Experience (QoMEX)*, 1–6. https://doi.org/10.1109/QoMEX.2016.7498955.

Drost, Gea, Dick F. Stegeman, Baziel G. M. van Engelen, and Machiel J. Zwarts. 2006. "Clinical Applications of High-Density Surface EMG: A Systematic Review." *Journal of Electromyography and Kinesiology*, Special Section (pp. 541–610): 2006 ISEK Congress, 16 (6): 586–602. https://doi.org/10.1016/j.jelekin.2006.09.005.

Dunn, Laurence T. 2002. "Raised Intracranial Pressure." *Journal of Neurology, Neurosurgery & Psychiatry* 73 (suppl 1): i23–27.

Fakhry, Samir M., Arthur L. Trask, Maureen A. Waller, and Dorraine D. Watts. 2004. "Management of Brain-Injured Patients by an Evidence-Based Medicine Protocol Improves Outcomes and Decreases Hospital Charges." *Journal of Trauma and Acute Care Surgery* 56 (3): 492–500.

Fonseca, Michael A., Mark G. Allen, Jason Kroh, and Jason White. 2006. "Flexible Wireless Passive Pressure Sensors for Biomedical Applications." In *Tech. Dig. Solid-State Sensor, Actuator, and Microsystems Workshop (Hilton Head 2006)*, 37–42.

Fregni, Felipe, Paulo S. Boggio, Moises C. Lima, Merari J. L. Ferreira, Tim Wagner, Sergio P. Rigonatti, Anita W. Castro, et al. 2006. "A Sham-Controlled, Phase II Trial of Transcranial Direct Current Stimulation for the Treatment of Central Pain in Traumatic Spinal Cord Injury." *PAIN* 122 (1–2): 197–209. https://doi.org/10.1016/j.pain.2006.02.023.

Fye, W. Bruce. 1994. "A History of the Origin, Evolution, and Impact of Electrocardiography." *The American Journal of Cardiology* 73 (13): 937–49.

Garcia-Conde, Mario, Julio Plata-Bello, Liberto Brage-Martin, and Lucia Martin-Viota. 2017. "External CSF Shunts." In *Textbook of Pediatric Neurosurgery*, edited by Concezio Di Rocco, Dachling Pang, and James T. Rutka, 1–27. Cham: Springer International Publishing. https://doi.org/10.1007/978-3-319-31512-6_32-1.

Geeraerts, Thomas, Jacques Duranteau, and Dan Benhamou. 2008. “Ocular Sonography in Patients with Raised Intracranial Pressure: The Papilloedema Revisited.” *Critical Care* 12 (3): 1–2.

Glick, Roberta P., Josh Niebruegge, Sang H. Lee, Osbert Egibor, Terry Lichtor, and Noam Alperin. 2006. “Early Experience from the Application of a Noninvasive Magnetic Resonance Imaging-Based Measurement of Intracranial Pressure in Hydrocephalus.” *Neurosurgery* 59 (5): 1052–61.

Goldenberg, Ilan, Arthur J. Moss, and Wojciech Zareba. 2006. “QT Interval: How to Measure It and What Is ‘Normal.’” *Journal of Cardiovascular Electrophysiology* 17 (3): 333–36. https://doi.org/10.1111/j.1540-8167.2006.00408.x.

Groves, Rob, Ken Stein, Dave Harame, and Dale Jadus. 1996. “Temperature Dependence of Q in Spiral Inductors Fabricated in a Silicon-Germanium/BiCMOS Technology.” In *Proceedings of the 1996 Bipolar/BiCMOS Circuits and Technology Meeting*, 153–56. IEEE.

Harary, Maya, Rianne GF Dolmans, and William B. Gormley. 2018. “Intracranial Pressure Monitoring—Review and Avenues for Development.” *Sensors* 18 (2): 465.

Harrison, R. R. 2007. “Designing Efficient Inductive Power Links for Implantable Devices.” In *2007 IEEE International Symposium on Circuits and Systems*, 2080–83. https://doi.org/10.1109/ISCAS.2007.378508.

Heide, W., E. Koenig, P. Trillenberg, D. Kömpf, and D. S. Zee. 1999. “Electrooculography: Technical Standards and Applications. The International Federation of Clinical Neurophysiology.” *Electroencephalography and Clinical Neurophysiology. Supplement* 52: 223–40.

Helbok, Raimund, DaiWai M. Olson, Peter D. Le Roux, and Paul Vespa. 2014. “Intracranial Pressure and Cerebral Perfusion Pressure Monitoring in Non-TBI Patients: Special Considerations.” *Neurocritical Care* 21 (2): 85–94.

Hirt, Marc N., Jasper Boeddinghaus, Alice Mitchell, Sebastian Schaaf, Christian Börnchen, Christian Müller, Herbert Schulz, et al. 2014. “Functional Improvement and Maturation of Rat and Human Engineered Heart Tissue by Chronic Electrical Stimulation.” *Journal of Molecular and Cellular Cardiology* 74 (September): 151–61. https://doi.org/10.1016/j.yjmcc.2014.05.009.

Hochberg, Leigh R., Mijail D. Serruya, Gerhard M. Friehs, Jon A. Mukand, Maryam Saleh, Abraham H. Caplan, Almut Branner, David Chen, Richard D. Penn, and John P. Donoghue. 2006. “Neuronal Ensemble Control of Prosthetic Devices by a Human with Tetraplegia.” *Nature* 442 (7099): 164–71.

Hockman, Charles H., H. Page Mauck Jr, and Ebbe C. Hoff. 1966. “ECG Changes Resulting from Cerebral Stimulation: II. A Spectrum of Ventricular Arrhythmias of Sympathetic Origin.” *American Heart Journal* 71 (5): 695–700.

Hsu, Chih-Wei, Chih-Chung Chang, and Chih-Jen Lin. 2003. “A Practical Guide to Support Vector Classification.”

Israel, Carsten W, Gerian Grönefeld, Joachim R Ehrlich, Yi-Gang Li, and Stefan H Hohnloser. 2004. “Long-Term Risk of Recurrent Atrial Fibrillation as Documented by an Implantable Monitoring Device: Implications for Optimal Patient Care.” *Journal of the American College of Cardiology* 43 (1): 47–52. https://doi.org/10.1016/j.jacc.2003.08.027.

Ito, Koichi, Katsumi Furuya, Yoshinobu Okano, and Lira Hamada. 2001. "Development and Characteristics of a Biological Tissue-equivalent Phantom for Microwaves." *Electronics and Communications in Japan (Part I: Communications)* 84 (4): 67–77.

Iwasaki, Masaki, Christoph Kellinghaus, Andreas V. Alexopoulos, Richard C. Burgess, Arun N. Kumar, Yanning H. Han, Hans O. Lüders, and R. John Leigh. 2005. “Effects of Eyelid Closure, Blinks, and Eye Movements on the Electroencephalogram.” *Clinical Neurophysiology* 116 (4): 878–85.

Jeon, Sang-Beom, Younsuck Koh, H. Alex Choi, and Kiwon Lee. 2014. “Critical Care for Patients with Massive Ischemic Stroke.” *Journal of Stroke* 16 (3): 146.

Jiang, Hanjun, Yanshu Guo, Zeliang Wu, Chun Zhang, Wen Jia, and Zhihua Wang. 2018. “Implantable Wireless Intracranial Pressure Monitoring Based on Air Pressure Sensing.” *IEEE Transactions on Biomedical Circuits and Systems* 12 (5): 1076–87.

Jung, Julien, Romain Bouet, Claude Delpuech, Philippe Ryvlin, Jean Isnard, Marc Guenot, Olivier Bertrand, Alexander Hammers, and François Mauguière. 2013. “The Value of Magnetoencephalography for Seizure-Onset Zone Localization in Magnetic Resonance Imaging-Negative Partial Epilepsy.” *Brain* 136 (10): 3176–86.

Kaiser, S. T. J. 2006. “Passive Telemetric Readout System.” *IEEE Sensors Journal* 6 (5): 1340–45. https://doi.org/10.1109/JSEN.2006.881395.

Karahan, S., M. Kilinc Yildirum, K. Kirtac, F. S. Rende, G. Butun, and H. K. Ekenel. 2016. “How Image Degradations Affect Deep CNN-Based Face Recognition?” In *2016 International Conference of the Biometrics Special Interest Group (BIOSIG)*, 1–5. https://doi.org/10.1109/BIOSIG.2016.7736924.

Keith, Michael W., P. Hunter Peckham, Geoffrey B. Thrope, Kathy C. Stroh, Brian Smith, James R. Buckett, Kevin L. Kilgore, and James W. Jatich. 1989. “Implantable

Functional Neuromuscular Stimulation in the Tetraplegic Hand." *The Journal of Hand Surgery* 14 (3): 524–30. https://doi.org/10.1016/S0363-5023(89)80017-6.

Kennedy, Harold L. 1992. "Ambulatory (Holter) Electrocardiography Technology." *Cardiology Clinics* 10 (3): 341–59.

Khan, Marium Naveed, Hussain Shallwani, Muhammad Ulusyar Khan, and Muhammad Shahzad Shamim. 2017. "Noninvasive Monitoring Intracranial Pressure–a Review of Available Modalities." *Surgical Neurology International* 8.

Kharaziha, Mahshid, Adnan Memic, Mohsen Akbari, David A. Brafman, and Mehdi Nikkhah. 2016. "Nano-Enabled Approaches for Stem Cell-Based Cardiac Tissue Engineering." *Advanced Healthcare Materials* 5 (13): 1533–53. https://doi.org/10.1002/adhm.201600088.

Khodagholy, Dion, Jennifer N. Gelinas, Thomas Thesen, Werner Doyle, Orrin Devinsky, George G. Malliaras, and György Buzsáki. 2015. "NeuroGrid: Recording Action Potentials from the Surface of the Brain." *Nature Neuroscience* 18 (2): 310.

Kiefer, Michael, Sebastian Antes, Melanie Schmitt, Inga Krause, and Regina Eymann. 2011. "Long-Term Performance of a CE-Approved Telemetric Intracranial Pressure Monitoring." In *2011 Annual International Conference of the IEEE Engineering in Medicine and Biology Society*, 2246–49. IEEE.

Kilgore, Kevin L., Harry A. Hoyen, Anne M. Bryden, Ronald L. Hart, Michael W. Keith, and P. Hunter Peckham. 2008. "An Implanted Upper-Extremity Neuroprosthesis Using Myoelectric Control." *The Journal of Hand Surgery* 33 (4): 539–50.

Kim, Jeonghyun, Anthony Banks, Zhaoqian Xie, Seung Yun Heo, Philipp Gutruf, Jung Woo Lee, Sheng Xu, et al. 2018. "Miniaturized Flexible Electronic Systems with Wireless Power and Near-Field Communication Capabilities." *Advanced Functional Materials* 25 (30): 4761–67. https://doi.org/10.1002/adfm.201501590.

Kim, Jeonghyun, Giovanni A. Salvatore, Hitoshi Araki, Antonio M. Chiarelli, Zhaoqian Xie, Anthony Banks, Xing Sheng, et al. 2016. "Battery-Free, Stretchable Optoelectronic Systems for Wireless Optical Characterization of the Skin." *Science Advances* 2 (8): e1600418. https://doi.org/10.1126/sciadv.1600418.

Kim, Sang Bok, Hojae Bae, Jae Min Cha, Sang Jun Moon, Mehmet R. Dokmeci, Donald M. Cropek, and Ali Khademhosseini. 2011. "A Cell-Based Biosensor for Real-Time Detection of Cardiotoxicity Using Lensfree Imaging." *Lab on a Chip* 11 (10): 1801–7. https://doi.org/10.1039/c1lc20098d.

Kim, Sung-Min, Seung Hyun Kim, Dae-Won Seo, and Kwang-Woo Lee. 2013. "Intraoperative Neurophysiologic Monitoring: Basic Principles and Recent Update." *Journal of Korean Medical Science* 28 (9): 1261–69.

Kiourti, Asimina, Cedric WL Lee, Junseok Chae, and John L. Volakis. 2016. “A Wireless Fully Passive Neural Recording Device for Unobtrusive Neuropotential Monitoring.” *IEEE Trans. Biomed. Engineering* 63 (1): 131–37.

Kipke, Daryl R., Rio J. Vetter, Justin C. Williams, and Jamille F. Hetke. 2003. “Silicon-Substrate Intracortical Microelectrode Arrays for Long-Term Recording of Neuronal Spike Activity in Cerebral Cortex.” *IEEE Transactions on Neural Systems and Rehabilitation Engineering* 11 (2): 151–55.

Kiranyaz, S., T. Ince, and M. Gabbouj. 2016. “Real-Time Patient-Specific ECG Classification by 1-D Convolutional Neural Networks.” *IEEE Transactions on Biomedical Engineering* 63 (3): 664–75. https://doi.org/10.1109/TBME.2015.2468589.

Klein, Cliff S., Sheng Li, Xiaogang Hu, and Xiaoyan Li. 2018. “Editorial: Electromyography (EMG) Techniques for the Assessment and Rehabilitation of Motor Impairment Following Stroke.” *Frontiers in Neurology* 9. https://doi.org/10.3389/fneur.2018.01122.

Kobetic, Rudi, Byron E. Marsolais, Ronald J. Triolo, Dwight T. Davy, Richard Gaudio, and Scott Tashman. 2003. “Development of a Hybrid Gait Orthosis: A Case Report.” *The Journal of Spinal Cord Medicine* 26 (3): 254–58.

Kobetic, Rudi, Curtis S. To, John R. Schnellenberger, Musa L. Audu, Thomas C. Bulea, Richard Gaudio, Gilles Pinault, Scott Tashman, and Ronald J. Triolo. 2009. “Development of Hybrid Orthosis for Standing, Walking, and Stair Climbing after Spinal Cord Injury.” *Journal of Rehabilitation Research & Development* 46 (3).

Lang, Erhard W., Klaus Paulat, Christoph Witte, Jürgen Zolondz, and H. Maximilian Mehdorn. 2003. “Noninvasive Intracranial Compliance Monitoring: Technical Note and Clinical Results.” *Journal of Neurosurgery* 98 (1): 214–18.

Larson, P. J., and B. C. Towe. 2011. “Miniature Ultrasonically Powered Wireless Nerve Cuff Stimulator.” In *2011 5th International IEEE/EMBS Conference on Neural Engineering (NER)*, 265–68. https://doi.org/10.1109/NER.2011.5910538.

Le Roux, Peter. 2016. “Intracranial Pressure Monitoring and Management.” In *Translational Research in Traumatic Brain Injury*. CRC Press/Taylor and Francis Group.

Lee, Byunghun, Yaoyao Jia, S. Abdollah Mirbozorgi, Mark Connolly, Xingyuan Tong, Zhaoping Zeng, Babak Mahmoudi, and Maysam Ghovanloo. 2019. “An Inductively-Powered Wireless Neural Recording and Stimulation System for Freely-Behaving Animals.” *IEEE Transactions on Biomedical Circuits and Systems* 13 (2): 413–24.

Lee, Byunghun, Mukhesh K. Koripalli, Yaoyao Jia, Joshua Acosta, M. S. E. Sendi, Yoonsu Choi, and Maysam Ghovanloo. 2018. "An Implantable Peripheral Nerve Recording and Stimulation System for Experiments on Freely Moving Animal Subjects." *Scientific Reports* 8 (1): 6115.

Lee, Cedric WL, Asimina Kiourti, Junseok Chae, and John L. Volakis. 2015. "A High-Sensitivity Fully Passive Neurosensing System for Wireless Brain Signal Monitoring." *IEEE Transactions on Microwave Theory and Techniques* 63 (6): 2060–68.

Lee, E., E. Matei, J. Gord, P. Hess, P. Nercessian, H. Stover, T. Li, and J. Wolfe. 2009. "A Biomedical Implantable FES Battery-Powered Micro-Stimulator." *IEEE Transactions on Circuits and Systems I: Regular Papers* 56 (12): 2583–96. https://doi.org/10.1109/TCSI.2009.2034052.

Lee, H. M., H. Park, and M. Ghovanloo. 2013. "A Power-Efficient Wireless System With Adaptive Supply Control for Deep Brain Stimulation." *IEEE Journal of Solid-State Circuits* 48 (9): 2203–16. https://doi.org/10.1109/JSSC.2013.2266862.

Lee, S. Y., C. J. Cheng, and M. C. Liang. 2011. "A Low-Power Bidirectional Telemetry Device With a Near-Field Charging Feature for a Cardiac Microstimulator." *IEEE Transactions on Biomedical Circuits and Systems* 5 (4): 357–67. https://doi.org/10.1109/TBCAS.2011.2126570.

Lévesque, Maxime, Charles Behr, and Massimo Avoli. 2015. "The Anti-Ictogenic Effects of Levetiracetam Are Mirrored by Interictal Spiking and High-Frequency Oscillation Changes in a Model of Temporal Lobe Epilepsy." *Seizure* 25: 18–25.

Lin, Andrew L., and Edward K. Avila. 2017. "Neurologic Emergencies in the Cancer Patient: Diagnosis and Management." *Journal of Intensive Care Medicine* 32 (2): 99.

Lin, Chia-Hung. 2008. "Frequency-Domain Features for ECG Beat Discrimination Using Grey Relational Analysis-Based Classifier." *Computers & Mathematics with Applications* 55 (4): 680–90. https://doi.org/10.1016/j.camwa.2007.04.035.

Lissy, Dawn, and Sahana Kukke. 2001. "Preliminary Performance of a Surgically Implanted Neuroprosthesis for Standing and Transfers—Where Do We Stand?" *Development* 38 (6): 609–17.

Liu, Shiyi, Xueling Meng, Jianwei Zhang, and Junseok Chae. 2019. "A Wireless Fully-Passive Acquisition of Biopotentials." *Biosensors and Bioelectronics*, 111336.

Liu, Shiyi, Ali Navaei, Xueling Meng, Mehdi Nikkhah, and Junseok Chae. 2017. "Wireless Passive Stimulation of Engineered Cardiac Tissues." *ACS Sensors* 2 (7): 1006–12. https://doi.org/10.1021/acssensors.7b00279.

Loeb, Gerald E., Raymond A. Peck, William H. Moore, and Kevin Hood. 2001. "BION™ System for Distributed Neural Prosthetic Interfaces." *Medical Engineering & Physics* 23 (1): 9–18. https://doi.org/10.1016/S1350-4533(01)00011-X.

Loeb, Gerald E., Frances J. R. Richmond, and Lucinda L. Baker. 2006. "The BION Devices: Injectable Interfaces with Peripheral Nerves and Muscles." *Neurosurgical Focus* 20 (5): 1–9. https://doi.org/10.3171/foc.2006.20.5.3.

López, A., F. J. Ferrero, M. Valledor, J. C. Campo, and O. Postolache. 2016. "A Study on Electrode Placement in EOG Systems for Medical Applications." In *2016 IEEE International Symposium on Medical Measurements and Applications (MeMeA)*, 1–5. https://doi.org/10.1109/MeMeA.2016.7533703.

Lozano, Andres M., Nir Lipsman, Hagai Bergman, Peter Brown, Stephan Chabardes, Jin Woo Chang, Keith Matthews, Cameron C. McIntyre, Thomas E. Schlaepfer, and Michael Schulder. 2019. "Deep Brain Stimulation: Current Challenges and Future Directions." *Nature Reviews Neurology* 15 (3): 148–60.

Lu, Zhiyuan, Kai-yu Tong, Henry Shin, Sheng Li, and Ping Zhou. 2017. "Advanced Myoelectric Control for Robotic Hand-Assisted Training: Outcome from a Stroke Patient." *Frontiers in Neurology* 8. https://doi.org/10.3389/fneur.2017.00107.

Luo, Shiyu, Haonan Xu, Yi Zuo, Xiaogang Liu, and Angelo H. All. 2020. "A Review of Functional Electrical Stimulation Treatment in Spinal Cord Injury." *Neuromolecular Medicine*, 1–17.

Maguire, Yael G., Mikhail G. Shapiro, Thaddeus R. Cybulski, Joshua I. Glaser, Dario Amodei, P. Benjamin Stranges, Reza Kalhor, David A. Dalrymple, Dongjin Seo, and Elad Alon. 2013. "Physical Principles for Scalable Neural Recording." *Frontiers in Computational Neuroscience* 7: 137.

Marom, Tal, Abraham Goldfarb, Eyal Russo, and Yehudah Roth. 2010. "Battery Ingestion in Children." *International Journal of Pediatric Otorhinolaryngology* 74 (8): 849–54.

Martins, Mariane Barreto Brandão, Francis Vinicius Fontes de Lima, Ronaldo Carvalho Santos Júnior, Arlete Cristina Granizo Santos, Valéria Maria Prado Barreto, and Eduardo Passos Fiel de Jesus. 2012. "Cochlear Implants: Our Experience and Literature Review." *International Archives of Otorhinolaryngology* 16 (4): 476–81.

Mayer, Rupert, Horst-Dieter Kress, and Josef Migl. 2001. "Antenna Performance Measurements at Extreme Temperatures." *EUROPEAN SPACE AGENCY-PUBLICATIONS-ESA SP* 467: 377–82.

McClaning, Kevin. 2012. *Wireless Receiver Design for Digital Communications*. IET.

McDermott, H. 1989. “An Advanced Multiple Channel Cochlear Implant.” *IEEE Transactions on Biomedical Engineering* 36 (7): 789–97. https://doi.org/10.1109/10.32112.

Meng, Xu, Kevin D. Browne, Shi-Min Huang, Constance Mietus, D. Kacy Cullen, Mohammad-Reza Tofighi, and Arye Rosen. 2012. “Dynamic Evaluation of a Digital Wireless Intracranial Pressure Sensor for the Assessment of Traumatic Brain Injury in a Swine Model.” *IEEE Transactions on Microwave Theory and Techniques* 61 (1): 316–25.

Mestais, Corinne S., Guillaume Charvet, Fabien Sauter-Starace, Michael Foerster, David Ratel, and Alim Louis Benabid. 2015. “WIMAGINE: Wireless 64-Channel ECoG Recording Implant for Long Term Clinical Applications.” *IEEE Transactions on Neural Systems and Rehabilitation Engineering: A Publication of the IEEE Engineering in Medicine and Biology Society* 23 (1): 10–21. https://doi.org/10.1109/TNSRE.2014.2333541.

Miller, Robert V. 1958. “ELECTROMYOGRAPHY—Uses and Limitations.” *California Medicine* 89 (4): 250–52.

Mobini, Sahba, Liudmila Leppik, and John H. Barker. 2016. “Direct Current Electrical Stimulation Chamber for Treating Cells in Vitro.” *Biotechniques* 60 (2): 95–98.

Moncion, Carolina, Lakshmini Balachandar, Satheesh Bojja Venkatakrishnan, Jorge J. Riera, and John Volakis. 2019. “Fully-Passive Wireless Implant for Neuropotential Acquisition: An In Vivo Validation.” *IEEE Journal of Electromagnetics, RF and Microwaves in Medicine and Biology*.

Muller, Rikky, Hanh-Phuc Le, Wen Li, Peter Ledochowitsch, Simone Gambini, Toni Bjorninen, Aaron Koralek, Jose M. Carmena, Michel M. Maharbiz, and Elad Alon. 2014. “A Minimally Invasive 64-Channel Wireless MECoG Implant.” *IEEE Journal of Solid-State Circuits* 50 (1): 344–59.

Mulpuru, Siva K., Malini Madhavan, Christopher J. McLeod, Yong-Mei Cha, and Paul A. Friedman. 2017. “Cardiac Pacemakers: Function, Troubleshooting, and Management: Part 1 of a 2-Part Series.” *Journal of the American College of Cardiology* 69 (2): 189–210.

Navaei, Ali, Nathan Moore, Ryan T. Sullivan, Danh Truong, Raymond Q. Migrino, and Mehdi Nikkhah. 2017. “Electrically Conductive Hydrogel-Based Micro-Topographies for the Development of Organized Cardiac Tissues.” *RSC Advances* 7 (6): 3302–12. https://doi.org/10.1039/C6RA26279A.

Navaei, Ali, Harpinder Saini, Wayne Christenson, Ryan Tanner Sullivan, Robert Ros, and Mehdi Nikkhah. 2016. “Gold Nanorod-Incorporated Gelatin-Based Conductive

Hydrogels for Engineering Cardiac Tissue Constructs." *Acta Biomaterialia* 41 (September): 133–46. https://doi.org/10.1016/j.actbio.2016.05.027.

Neihart, Nathan M., and Reid R. Harrison. 2005. "Micropower Circuits for Bidirectional Wireless Telemetry in Neural Recording Applications." *IEEE Transactions on Biomedical Engineering* 52 (11): 1950–59.

Neumiller, Joshua J. 2013. "Review of the Treatment & Management of Hydrocephalus." *US Pharm* 3: 20.

Nicolas-Alonso, Luis Fernando, and Jaime Gomez-Gil. 2012. "Brain Computer Interfaces, a Review." *Sensors* 12 (2): 1211–79.

Nopper, Reinhard, Remigius Niekrawietz, and Leonhard Reindl. 2009. "Wireless Readout of Passive LC Sensors." *IEEE Transactions on Instrumentation and Measurement* 59 (9): 2450–57.

Obeid, D., G. Issa, S. Sadek, G. Zaharia, and G. El Zein. 2008. "Low Power Microwave Systems for Heartbeat Rate Detection at 2.4, 5.8, 10 and 16 GHz." In *2008 First International Symposium on Applied Sciences on Biomedical and Communication Technologies*, 1–5. https://doi.org/10.1109/ISABEL.2008.4712623.

Ordookhanian, Christ, Meena Nagappan, Dina Elias, and Paul E. Kaloostian. 2018. "Management of Intracranial Pressure in Traumatic Brain Injury." *Traumatic Brain Injury: Pathobiology, Advanced Diagnostics and Acute Management*, 177.

Pan, Yuxiang, Ning Hu, Xinwei Wei, Lin Gong, Bin Zhang, Hao Wan, and Ping Wang. 2019. "3D Cell-Based Biosensor for Cell Viability and Drug Assessment by 3D Electric Cell/Matrigel-Substrate Impedance Sensing." *Biosensors and Bioelectronics* 130: 344–51.

Parastarfeizabadi, Mahboubeh, and Abbas Z. Kouzani. 2017. "Advances in Closed-Loop Deep Brain Stimulation Devices." *Journal of Neuroengineering and Rehabilitation* 14 (1): 79.

Parmar, Paresh, S. Sumaria, and S. Hashi. 2011. "Stroke: Classification and Diagnosis." *The Pharmaceutical Journal* 3: 200–204.

Party, Intercollegiate Stroke Working. 2012. *National Clinical Guideline for Stroke*. Vol. 20083. Citeseer.

Pasquina, Paul F., Melissa Evangelista, A. J. Carvalho, Joseph Lockhart, Sarah Griffin, George Nanos, Patricia McKay, et al. 2015. "First-in-Man Demonstration of a Fully Implanted Myoelectric Sensors System to Control an Advanced Electromechanical Prosthetic Hand." *Journal of Neuroscience Methods*, Brain Computer Interfaces;

Tribute to Greg A. Gerhardt, 244 (April): 85–93. https://doi.org/10.1016/j.jneumeth.2014.07.016.

Paxinos, George, and Charles Watson. 2006. *The Rat Brain in Stereotaxic Coordinates: Hard Cover Edition*. Elsevier.

Peckham, P. Hunter, and Jayme S. Knutson. 2005. "Functional Electrical Stimulation for Neuromuscular Applications." *Annual Review of Biomedical Engineering* 7 (1): 327–60. https://doi.org/10.1146/annurev.bioeng.6.040803.140103.

Petrosian, A. A., D. V. Prokhorov, W. Lajara-Nanson, and R. B. Schiffer. 2001. "Recurrent Neural Network-Based Approach for Early Recognition of Alzheimer's Disease in EEG." *Clinical Neurophysiology* 112 (8): 1378–87.

Pfurtscheller, Gert, Gernot R. Müller, Jörg Pfurtscheller, Hans Jürgen Gerner, and Rüdiger Rupp. 2003. "'Thought'--Control of Functional Electrical Stimulation to Restore Hand Grasp in a Patient with Tetraplegia." *Neuroscience Letters* 351 (1): 33–36.

Phinyomark, Angkoon, Chusak Limsakul, and Pornchai Phukpattaranont. 2009. "A Novel Feature Extraction for Robust EMG Pattern Recognition." *ArXiv:0912.3973 [Cs]*, December. http://arxiv.org/abs/0912.3973.

Ponce, F. A. 2014. "Electrostimulation." In *Encyclopedia of the Neurological Sciences (Second Edition)*, edited by Michael J. Aminoff and Robert B. Daroff, 1110–11. Oxford: Academic Press. https://doi.org/10.1016/B978-0-12-385157-4.00743-0.

Potvin, J. R., and S. H. M Brown. 2004. "Less Is More: High Pass Filtering, to Remove up to 99% of the Surface EMG Signal Power, Improves EMG-Based Biceps Brachii Muscle Force Estimates." *Journal of Electromyography and Kinesiology* 14 (3): 389–99. https://doi.org/10.1016/j.jelekin.2003.10.005.

Pozar, David M. 2009. *Microwave Engineering*. John Wiley & Sons.

Quiñones-Hinojosa, Alfredo, Russ Lyon, Rose Du, and Michael T. Lawton. 2005. "Intraoperative Motor Mapping of the Cerebral Peduncle during Resection of a Midbrain Cavernous Malformation: Technical Case Report." *Operative Neurosurgery* 56 (suppl_4): ONS-E439-ONS-E439.

Raboel, P. H., Jr Bartek, M. Andresen, B. M. Bellander, and B. Romner. 2012. "Intracranial Pressure Monitoring: Invasive versus Non-Invasive Methods—a Review." *Critical Care Research and Practice* 2012.

Radisic, Milica, Hyoungshin Park, Helen Shing, Thomas Consi, Frederick J. Schoen, Robert Langer, Lisa E. Freed, and Gordana Vunjak-Novakovic. 2004. "Functional Assembly of Engineered Myocardium by Electrical Stimulation of Cardiac

Myocytes Cultured on Scaffolds." *Proceedings of the National Academy of Sciences* 101 (52): 18129–34. https://doi.org/10.1073/pnas.0407817101.

Rainoldi, A., G. Melchiorri, and I. Caruso. 2004. "A Method for Positioning Electrodes during Surface EMG Recordings in Lower Limb Muscles." *Journal of Neuroscience Methods* 134 (1): 37–43. https://doi.org/10.1016/j.jneumeth.2003.10.014.

Ramantani, Georgia, Matthias Dümpelmann, Laurent Koessler, Armin Brandt, Delphine Cosandier-Rimélé, Josef Zentner, Andreas Schulze-Bonhage, and Louis Georges Maillard. 2014. "Simultaneous Subdural and Scalp EEG Correlates of Frontal Lobe Epileptic Sources." *Epilepsia* 55 (2): 278–88.

Ramantani, Georgia, Louis Maillard, and Laurent Koessler. 2016. "Correlation of Invasive EEG and Scalp EEG." *Seizure* 41: 196–200.

Recio, Albert C., and Anna C. Schneider. 2011. "46 - Electrical Stimulation." In *Pain Procedures in Clinical Practice (Third Edition)*, edited by Ted A. Lennard, Stevan Walkowski, Aneesh K. Singla, and David G. Vivian, 559–66. Saint Louis: Hanley & Belfus. https://doi.org/10.1016/B978-1-4160-3779-8.10046-6.

Rijkhoff, Nico JM. 2004. "Neuroprostheses to Treat Neurogenic Bladder Dysfunction: Current Status and Future Perspectives." *Child's Nervous System* 20 (2): 75–86.

Rodríguez-Tapia, Bernabe, Israel Soto, Daniela M. Martínez, and Norma Candolfi Arballo. 2020. "Myoelectric Interfaces and Related Applications: Current State of EMG Signal Processing–A Systematic Review." *IEEE Access* 8: 7792–7805. https://doi.org/10.1109/ACCESS.2019.2963881.

Roeleveld, K., D. F. Stegeman, H. M. Vingerhoets, and A. van Oosterom. 1997. "Motor Unit Potential Contribution to Surface Electromyography." *Acta Physiologica Scandinavica* 160 (2): 175–83.

Rolston, John D., Dario J. Englot, Susannah Cornes, and Edward F. Chang. 2016. "Major and Minor Complications in Extraoperative Electrocorticography: A Review of a National Database." *Epilepsy Research* 122: 26–29.

Rolston, John D., David Ouyang, Dario J. Englot, Doris D. Wang, and Edward F. Chang. 2015. "National Trends and Complication Rates for Invasive Extraoperative Electrocorticography in the USA." *Journal of Clinical Neuroscience* 22 (5): 823–27.

Sahakian, Barbara J., Annette B. Bruhl, Jennifer Cook, Clare Killikelly, George Savulich, Thomas Piercy, Sepehr Hafizi, Jesus Perez, Emilio Fernandez-Egea, and John Suckling. 2015. "The Impact of Neuroscience on Society: Cognitive Enhancement

in Neuropsychiatric Disorders and in Healthy People." *Philosophical Transactions of the Royal Society B: Biological Sciences* 370 (1677): 20140214.

Saini, Harpinder, Ali Navaei, Alison Van Putten, and Mehdi Nikkhah. 2015. "3D Cardiac Microtissues Encapsulated with the Co-Culture of Cardiomyocytes and Cardiac Fibroblasts." *Advanced Healthcare Materials* 4 (13): 1961–71. https://doi.org/10.1002/adhm.201500331.

Saitou, Kenji, Tadashi Masuda, Daisaku Michikami, Ryuhei Kojima, and Morihiko Okada. 2000. "INNERVATION ZONES OF THE UPPER AND LOWER LIMB MUSCLES ESTIMATED BY USING MULTICHANNEL SURFACE EMG." *Journal of Human Ergology* 29 (1–2): 35–52. https://doi.org/10.11183/jhe1972.29.35.

Schmidhuber, Jürgen. 2015. "Deep Learning in Neural Networks: An Overview." *Neural Networks* 61 (January): 85–117. https://doi.org/10.1016/j.neunet.2014.09.003.

Schulman, J. H. 2008. "The Feasible FES System: Battery Powered BION Stimulator." *Proceedings of the IEEE* 96 (7): 1226–39. https://doi.org/10.1109/JPROC.2008.922588.

Schwan, H. P., and C. F. Kay. 1957. "The Conductivity of Living Tissues." *Annals of the New York Academy of Sciences* 65 (6): 1007–13. https://doi.org/10.1111/j.1749-6632.1957.tb36701.x.

Schwarz, David A., Mikhail A. Lebedev, Timothy L. Hanson, Dragan F. Dimitrov, Gary Lehew, Jim Meloy, Sankaranarayani Rajangam, Vivek Subramanian, Peter J. Ifft, and Zheng Li. 2014. "Chronic, Wireless Recordings of Large-Scale Brain Activity in Freely Moving Rhesus Monkeys." *Nature Methods* 11 (6): 670.

Schwerdt, H. N., F. A. Miranda, and J. Chae. 2012. "A Fully Passive Wireless Backscattering Neurorecording Microsystem Embedded in Dispersive Human-Head Phantom Medium." *IEEE Electron Device Letters* 33 (6): 908–10. https://doi.org/10.1109/LED.2012.2190967.

———. 2013. "Analysis of Electromagnetic Fields Induced in Operation of a Wireless Fully Passive Backscattering Neurorecording Microsystem in Emulated Human Head Tissue." *IEEE Transactions on Microwave Theory and Techniques* 61 (5): 2170–76. https://doi.org/10.1109/TMTT.2013.2252916.

———. 2015. "Wireless Fully Passive Multichannel Recording of Neuropotentials Using Photo-Activated RF Backscattering Methods." *IEEE Transactions on Microwave Theory and Techniques* 63 (9): 2965–70. https://doi.org/10.1109/TMTT.2015.2460746.

Schwerdt, Helen N., Wencheng Xu, Sameer Shekhar, Abbas Abbaspour-Tamijani, Bruce C. Towe, Félix A. Miranda, and Junseok Chae. 2011. "A Fully Passive Wireless Microsystem for Recording of Neuropotentials Using RF Backscattering Methods." *Journal of Microelectromechanical Systems* 20 (5): 1119–30.

Seo, Dongjin, Ryan M. Neely, Konlin Shen, Utkarsh Singhal, Elad Alon, Jan M. Rabaey, Jose M. Carmena, and Michel M. Maharbiz. 2016. "Wireless Recording in the Peripheral Nervous System with Ultrasonic Neural Dust." *Neuron* 91 (3): 529–39.

Serena, Elena, Elisa Figallo, Nina Tandon, Christopher Cannizzaro, Sharon Gerecht, Nicola Elvassore, and Gordana Vunjak-Novakovic. 2009. "Electrical Stimulation of Human Embryonic Stem Cells: Cardiac Differentiation and the Generation of Reactive Oxygen Species." *Experimental Cell Research* 315 (20): 3611–19. https://doi.org/10.1016/j.yexcr.2009.08.015.

Severs, Nicholas J. 2000. "The Cardiac Muscle Cell." *Bioessays* 22 (2): 188–99.

Shafi, Shahid, Ramon Diaz-Arrastia, Christopher Madden, and Larry Gentilello. 2008. "Intracranial Pressure Monitoring in Brain-Injured Patients Is Associated with Worsening of Survival." *Journal of Trauma and Acute Care Surgery* 64 (2): 335–40.

Sheffler, Lynne R., and John Chae. 2007. "Neuromuscular Electrical Stimulation in Neurorehabilitation." *Muscle & Nerve: Official Journal of the American Association of Electrodiagnostic Medicine* 35 (5): 562–90.

Shimada, Yoichi, Kozo Sato, Hitoshi Kagaya, Natsuo Konishi, Seiya Miyamoto, and Toshiki Matsunaga. 1996. "Clinical Use of Percutaneous Intramuscular Electrodes for Functional Electrical Stimulation." *Archives of Physical Medicine and Rehabilitation* 77 (10): 1014–18. https://doi.org/10.1016/S0003-9993(96)90061-1.

Singh, Arun, Klaus Mewes, Robert E. Gross, Mahlon R. DeLong, José A. Obeso, and Stella M. Papa. 2016. "Human Striatal Recordings Reveal Abnormal Discharge of Projection Neurons in Parkinson's Disease." *Proceedings of the National Academy of Sciences* 113 (34): 9629–34.

Singh, Hari, and Jaswinder Singh. 2012. "A Review on Electrooculography." *International Journal of Advanced Engineering Technology* 3 (4): 115–22.

Smith, S. J. M. 2005. "EEG in the Diagnosis, Classification, and Management of Patients with Epilepsy." *Journal of Neurology, Neurosurgery & Psychiatry* 76 (suppl 2): ii2–7.

Sodagar, Amir M., Gayatri E. Perlin, Ying Yao, Khalil Najafi, and Kensall D. Wise. 2009. "An Implantable 64-Channel Wireless Microsystem for Single-Unit Neural Recording." *IEEE Journal of Solid-State Circuits* 44 (9): 2591–2604.

Song, Yinchen, Basavaraju G. Sanganahalli, Fahmeed Hyder, Wei-Chiang Lin, and Jorge J. Riera. 2015. "Distributions of Irritative Zones Are Related to Individual Alterations of Resting-State Networks in Focal Epilepsy." *PLOS ONE* 10 (7): e0134352. https://doi.org/10.1371/journal.pone.0134352.

Stuart, Douglas G., and Robert M. Brownstone. 2011. "The Beginning of Intracellular Recording in Spinal Neurons: Facts, Reflections, and Speculations." *Brain Research* 1409: 62–92.

Takahashi, A., P. Camacho, J. D. Lechleiter, and B. Herman. 1999. "Measurement of Intracellular Calcium." *Physiological Reviews* 79 (4): 1089–1125.

Takeda, Kotaro, Genichi Tanino, and Hiroyuki Miyasaka. 2017. "Review of Devices Used in Neuromuscular Electrical Stimulation for Stroke Rehabilitation." *Medical Devices (Auckland, NZ)* 10: 207.

Tandon, Nina, Christopher Cannizzaro, Pen-Hsiu Grace Chao, Robert Maidhof, Anna Marsano, Hoi Ting Heidi Au, Milica Radisic, and Gordana Vunjak-Novakovic. 2009. "Electrical Stimulation Systems for Cardiac Tissue Engineering." *Nature Protocols* 4 (2): 155–73. https://doi.org/10.1038/nprot.2008.183.

Tandon, Nina, Anna Marsano, Robert Maidhof, Leo Wan, Hyoungshin Park, and Gordana Vunjak-Novakovic. 2011. "Optimization of Electrical Stimulation Parameters for Cardiac Tissue Engineering." *Journal of Tissue Engineering and Regenerative Medicine* 5 (6): e115–25. https://doi.org/10.1002/term.377.

Tankisi, Hatice, David Burke, Liying Cui, Mamede de Carvalho, Satoshi Kuwabara, Sanjeev D. Nandedkar, Seward Rutkove, Erik Stålberg, Michel JAM van Putten, and Anders Fuglsang-Frederiksen. 2020. "Standards of Instrumentation of EMG." *Clinical Neurophysiology* 131 (1): 243–58.

Tekriwal, Anand, Neema Moin Afshar, Juan Santiago-Moreno, Fiene Marie Kuijper, Drew S. Kern, Casey H. Halpern, Gidon Felsen, and John A. Thompson. 2019. "Neural Circuit and Clinical Insights from Intraoperative Recordings During Deep Brain Stimulation Surgery." *Brain Sciences* 9 (7): 173.

Thakor, Nitish V. 2013. "Translating the Brain-Machine Interface." *Science Translational Medicine* 5 (210): 210ps17-210ps17.

———. 2015. "Biopotentials and Electrophysiology Measurements." In *Telehealth and Mobile Health*, 595–614. CRC press.

Thomas, Stewart J., Reid R. Harrison, Anthony Leonardo, and Matthew S. Reynolds. 2012. "A Battery-Free Multichannel Digital Neural/EMG Telemetry System for Flying Insects." *IEEE Transactions on Biomedical Circuits and Systems* 6 (5): 424–36.

Thomsen, Poul Erik Bloch, Christian Jons, M. J. Pekka Raatikainen, Rikke Moerch Joergensen, Juha Hartikainen, Vesa Virtanen, J. Boland, et al. 2010. "Long-Term Recording of Cardiac Arrhythmias With an Implantable Cardiac Monitor in Patients With Reduced Ejection Fraction After Acute Myocardial InfarctionClinical Perspective: The Cardiac Arrhythmias and Risk Stratification After Acute Myocardial Infarction (CARISMA) Study." *Circulation* 122 (13): 1258–64. https://doi.org/10.1161/CIRCULATIONAHA.109.902148.

Tolstosheeva, E., J. Hoeffmann, J. Pistor, D. Rotermund, T. Schellenberg, D. Boll, T. Hertzberg, V. Gordillo-Gonzalez, S. Mandon, and D. Peters-Drolshagen. 2013. "Towards a Wireless and Fully-Implantable ECoG System." In *2013 Transducers & Eurosensors XXVII: The 17th International Conference on Solid-State Sensors, Actuators and Microsystems (TRANSDUCERS & EUROSENSORS XXVII)*, 384–87. IEEE.

Valdés-Hernández, Pedro A., Jihye Bae, Yinchen Song, Akira Sumiyoshi, Eduardo Aubert-Vázquez, and Jorge J. Riera. 2019. "Validating Non-Invasive EEG Source Imaging Using Optimal Electrode Configurations on a Representative Rat Head Model." *Brain Topography* 32 (4): 599–624.

Van Gompel, Jamie J., Gregory A. Worrell, Michael L. Bell, Todd A. Patrick, Gregory D. Cascino, Corey Raffel, W. Richard Marsh, and Fredric B. Meyer. 2008. "Intracranial Electroencephalography with Subdural Grid Electrodes: Techniques, Complications, and Outcomes." *Neurosurgery* 63 (3): 498–506.

Vansteensel, Mariska J., Elmar GM Pels, Martin G. Bleichner, Mariana P. Branco, Timothy Denison, Zachary V. Freudenburg, Peter Gosselaar, Sacha Leinders, Thomas H. Ottens, and Max A. Van Den Boom. 2016. "Fully Implanted Brain–Computer Interface in a Locked-in Patient with ALS." *New England Journal of Medicine* 375 (21): 2060–66.

Walter, Peter, Zoltán F. Kisvárday, Michael Görtz, Nils Alteheld, Gernot Rossler, Thomas Stieglitz, and Ulf T. Eysel. 2005. "Cortical Activation via an Implanted Wireless Retinal Prosthesis." *Investigative Ophthalmology & Visual Science* 46 (5): 1780–85. https://doi.org/10.1167/iovs.04-0924.

Wang, Ran, Arad Lajevardi-Khosh, Seokheun Choi, and Junseok Chae. 2011. "Regenerative Surface Plasmon Resonance (SPR) Biosensor: Real-Time Measurement of Fibrinogen in Undiluted Human Serum Using the Competitive Adsorption of Proteins." *Biosensors and Bioelectronics* 28 (1): 304–7.

Wang, Ran, Wei Wang, Hao Ren, and Junseok Chae. 2014. "Detection of Copper Ions in Drinking Water Using the Competitive Adsorption of Proteins." *Biosensors and Bioelectronics* 57: 179–85.

Wang, Wei, Alan D. Degenhart, Jennifer L. Collinger, Ramana Vinjamuri, Gustavo P. Sudre, P. David Adelson, Deborah L. Holder, Eric C. Leuthardt, Daniel W. Moran, and Michael L. Boninger. 2009. "Human Motor Cortical Activity Recorded with Micro-ECoG Electrodes, during Individual Finger Movements." In *2009 Annual International Conference of the IEEE Engineering in Medicine and Biology Society*, 586–89. IEEE.

Welle, Cristin G., and Victor Krauthamer. 2012. "FDA Regulation of Invasive Neural Recording Electrodes: A Daunting Task for Medical Innovators." *IEEE Pulse* 3 (2): 37–41. https://doi.org/10.1109/MPUL.2011.2181022.

Wise, Kensall D., David J. Anderson, Jamille F. Hetke, Daryl R. Kipke, and Khalil Najafi. 2004. "Wireless Implantable Microsystems: High-Density Electronic Interfaces to the Nervous System." *Proceedings of the IEEE* 92 (1): 76–97.

Wolf, Patrick D. 2008. "Thermal Considerations for the Design of an Implanted Cortical Brain–Machine Interface (BMI)." In *Indwelling Neural Implants: Strategies for Contending with the In Vivo Environment*, edited by William M. Reichert. Boca Raton (FL): CRC Press/Taylor & Francis. http://www.ncbi.nlm.nih.gov/books/NBK3932/.

Wu, Yunfen, María Ángeles Martínez Martínez, and Pedro Orizaola Balaguer. 2013. "Overview of the Application of EMG Recording in the Diagnosis and Approach of Neurological Disorders." In *Electrodiagnosis in New Frontiers of Clinical Research*, 1–24. IntechOpen.

Xu, Sheng, Yihui Zhang, Lin Jia, Kyle E. Mathewson, Kyung-In Jang, Jeonghyun Kim, Haoran Fu, et al. 2014. "Soft Microfluidic Assemblies of Sensors, Circuits, and Radios for the Skin." *Science* 344 (6179): 70–74. https://doi.org/10.1126/science.1250169.

Yamamoto, Junichi, Akio Ikeda, Takeshi Satow, Kazuhide Takeshita, Motohiro Takayama, Masao Matsuhashi, Riki Matsumoto, et al. 2002. "Low-Frequency Electric Cortical Stimulation Has an Inhibitory Effect on Epileptic Focus in Mesial Temporal Lobe Epilepsy." *Epilepsia* 43 (5): 491–95. https://doi.org/10.1046/j.1528-1157.2002.29001.x.

Yang, Xiang-Lin, Guo-Zhen Liu, Yun-Hai Tong, Hong Yan, Zhi Xu, Qi Chen, Xiang Liu, Hong-Hao Zhang, Hong-Bo Wang, and Shao-Hua Tan. 2015. "The History, Hotspots, and Trends of Electrocardiogram." *Journal of Geriatric Cardiology: JGC* 12 (4): 448.

Yap, Yee Guan, and A. John Camm. 2003. "Drug Induced QT Prolongation and Torsades de Pointes." *Heart* 89 (11): 1363–72. https://doi.org/10.1136/heart.89.11.1363.

Zardoshti-Kermani, M., B. C. Wheeler, K. Badie, and R. M. Hashemi. 1995. “EMG Feature Evaluation for Movement Control of Upper Extremity Prostheses.” *IEEE Transactions on Rehabilitation Engineering* 3 (4): 324–33. https://doi.org/10.1109/86.481972.

Zarnik, Marina Santo, and Darko Belavic. 2012. “An Experimental and Numerical Study of the Humidity Effect on the Stability of a Capacitive Ceramic Pressure Sensor.” *Radioengineering* 21 (1).

Zhang, X., and J. Chae. 2011. “Working Distance Comparison of Inductive and Electromagnetic Couplings for Wireless and Passive Underwater Monitoring System of Rinsing Process in Semiconductor Facilities.” *IEEE Sensors Journal* 11 (11): 2932–39. https://doi.org/10.1109/JSEN.2011.2151185.

Ziaie, B., M. D. Nardin, A. R. Coghlan, and K. Najafi. 1997. “A Single-Channel Implantable Microstimulator for Functional Neuromuscular Stimulation.” *IEEE Transactions on Biomedical Engineering* 44 (10): 909–20. https://doi.org/10.1109/10.634643.

Zou, Ling, Qin Wang, Mengmeng Tong, Hongbo Li, Jun Wang, Ning Hu, and Ping Wang. 2016. “Detection of Diarrhetic Shellfish Poisoning Toxins Using High-Sensitivity Human Cancer Cell-Based Impedance Biosensor.” *Sensors and Actuators B: Chemical* 222: 205–12.

Zrenner, Eberhart. 2008. “The Role of Electrophysiology and Psychophysics in Ocular Toxicology.” In *Clinical Ocular Toxicology*, 21–38. Elsevier.

APPENDIX A

COPYRIGHT

Chapter 4 is reproduced with permission from Liu, Shiyi, Carolina Moncion, Jianwei Zhang, Lakshmini Balachandar, Dzifa Kwaku, Jorge J. Riera, John L. Volakis, and Junseok Chae. 2019. Fully Passive Flexible Wireless Neural Recorder for the Acquisition of Neuropotentials from a Rat Model. ACS Sensor*s* 4 (12): 3175–8

Chapter 6 is reproduced with permission from Liu, Shiyi, Xueling Meng, Jianwei Zhang, and Junseok Chae. 2019. A Wireless Fully-Passive Acquisition of Biopotentials. Biosensors and Bioelectronics, 111336.

Chapter 8 is reproduced with permission from Liu, Shiyi, Ali Navaei, Xueling Meng, Mehdi Nikkhah, and Junseok Chae. 2017. Wireless Passive Stimulation of Engineered Cardiac Tissues. ACS Sensors 2 (7): 1006–12.

Figure 1.1a is reprinted with permission from Springer: Nature, Neuronal ensemble control of prosthetic devices by a human with tetraplegia, Hochberg, L. R. et al. 2006.

Figure 1.1b is reproduced with permission from Vansteensel et al. Fully Implanted Brain–Computer Interface in a Locked-in Patient with ALS. New England Journal of Medicine 375 (21): 2060–66, Copyright Massachusetts Medical Society.

Figure 1.5 is reprinted with permission from springer: Nature Protocols, Electrical Stimulation Systems for Cardiac Tissue Engineering. Tandon, N. et al., 2009.

Figure 2.1a is reprinted with permission from Chestek et al. 2009, HermesC: Low-Power Wireless Neural Recording System for Freely Moving Primates, IEEE Transactions on Neural Systems and Rehabilitation Engineering 17 (4): 330–38. Copyright: © [2009] IEEE.

Figure 2.1b is reprinted with permission from IOP Publishing, Borton et al. 2013, An Implantable Wireless Neural Interface for Recording Cortical Circuit Dynamics in Moving Primates, Journal of Neural Engineering 10 (2).

Figure 2.1c is reprinted with permission from Springer: Nat. Methods. Chronic, Wireless Recordings of Large-scale Brain Activity in Freely Moving Rhesus Monkeys. Schwarz, D. A. et al, 2014.

Figure 2.1d is reprinted with permission from Cheng et al. 2012, 100-Channel Wireless Neural Recording System with 54-Mb/s Data Link and 40%-Efficiency Power Link. In 2012 IEEE Asian Solid State Circuits Conference (A-SSCC), 185–88. Copyright: © [2012] IEEE.

Figure 2.1e is reprinted with permission from Sodagar et al. 2009, An Implantable 64-Channel Wireless Microsystem for Single-Unit Neural Recording. IEEE Journal of Solid-State Circuits 44 (9): 2591–2604. Copyright: © [2009] IEEE.

Figure 2.2a is reprinted with permission from Mestais et al. 2015, WIMAGINE: Wireless 64-Channel ECoG Recording Implant for Long Term Clinical Applications, IEEE Transactions on Neural Systems and Rehabilitation Engineering: A Publication of the IEEE Engineering in Medicine and Biology Society 23 (1): 10–21. Copyright: © [2015] IEEE.

Figure 2.2b is reprinted with permission from Muller et al. 2014, A Minimally Invasive 64-Channel Wireless MECoG Implant, IEEE Journal of Solid-State Circuits 50 (1): 344–59. Copyright: © [2014] IEEE

Figure 2.2c is reprinted from Neuron, 91, Seo et al. Wireless Recording in the Peripheral Nervous System with Ultrasonic Neural Dust, 529–539, 2016, with permission from Elsevier.

Figure 2.3a is reprinted with permission from Besnoff et al. 2013, Battery-Free Multichannel Digital ECG Biotelemetry Using UHF RFID Techniques, In 2013 IEEE International Conference on RFID (RFID), 16–22. Copyright: © [2013] IEEE.

Figure 2.3b is reprinted by permission from Dementyev et al. 2013, A Wearable UHF RFID-Based EEG System, In 2013 IEEE International Conference on RFID (RFID), 1–7. Copyright: © [2013] IEEE.

Figure 2.3c is reprinted from Sensor and Actuators A: Physical, 130, Coosemans, J., Hermans, B. & Puers, R, Integrating wireless ECG monitoring in textiles, 48–53, 2006, with permission from Elsevier.

Figure 2.3d is reprinted with permission from Thomas et al. 2012, A Battery-Free Multichannel Digital Neural/EMG Telemetry System for Flying Insects, IEEE Transactions on Biomedical Circuits and Systems 6 (5): 424–36. Copyright: © [2012] IEEE.

Figure 2.4a is from Science, 344, Xu et al. Soft Microfluidic Assemblies of Sensors, Circuits, and Radios for the Skin. 70–74, 2014. Reprinted with permission from AAAS.

Figure 2.5a is reprinted from World Neurosurgery, 91, Antes, S., Tschan, C. A., Heckelmann, M., Breuskin, D. & Oertel, J., Telemetric Intracranial Pressure Monitoring with the Raumedic Neurovent P-tel, 133–148, 2006, with permission from Elsevier.

Figure 2.5b is reprinted with permission from Jiang et al, 2018. Implantable Wireless Intracranial Pressure Monitoring Based on Air Pressure Sensing, IEEE Transactions on Biomedical Circuits and Systems 12 (5): 1076–87. Copyright: © [2018] IEEE.

Figure 2.5c is reprinted with permission from Meng et al, 2012. Dynamic Evaluation of a Digital Wireless Intracranial Pressure Sensor for the Assessment of Traumatic Brain Injury in a Swine Model. IEEE Transactions on Microwave Theory and Techniques 61 (1): 316–25. Copyright: © [2012] IEEE.

Figure 2.6a is reprinted with permission from Chen et al. 2010. Wireless Intraocular Pressure Sensing Using Microfabricated Minimally Invasive Flexible-Coiled LC Sensor Implant. Journal of Microelectromechanical Systems 19 (4): 721–34. Copyright: © [2010] IEEE.

Figure 2.6b is reprinted with permission from Behfar et al. 2016. Inductive Passive Sensor for Intraparenchymal and Intraventricular Monitoring of Intracranial Pressure. In 2016 38th Annual International Conference of the IEEE Engineering in Medicine and Biology Society (EMBC), 1950–54. Copyright: © [2016] IEEE.

Figure 2.6c is reprinted with permission from Springer: Nature Communications, Continuous Wireless Pressure Monitoring and Mapping with Ultra-small Passive Sensors for Health Monitoring and Critical Care, Chen et al., 2014.

Figure 2.7a is reprinted with permission from Schulman, J. H. 2008. The Feasible FES System: Battery Powered BION Stimulator. Proceedings of the IEEE 96 (7): 1226–39. Copyright: © [2008] IEEE.

Figure 2.7b is reprinted with permission from Ziaie et al. 1997. A Single-Channel Implantable Microstimulator for Functional Neuromuscular Stimulation. IEEE Transactions on Biomedical Engineering 44 (10): 909–20. Copyright: © [1997] IEEE.

Figure 2.7c is reprinted with permission from Cho et al. 2010. A MEMS-Based Fully-Integrated Wireless Neurostimulator. In 2010 IEEE 23rd International Conference on Micro Electro Mechanical Systems (MEMS), 300–303. Copyright: © [2010] IEEE.

Figure 2.7d is reprinted with permission from Lee et al. 2009. A Biomedical Implantable FES Battery-Powered Micro-Stimulator. IEEE Transactions on Circuits and Systems I: Regular Papers 56 (12): 2583–96. Copyright: © [2009] IEEE.

Figure 2.8a is reprinted with permission from Schwerdt et al. 2011. A Fully Passive Wireless Microsystem for Recording of Neuropotentials Using RF Backscattering Methods. Journal of Microelectromechanical Systems 20 (5): 1119–30, and Schwerdt et al 2012. A Fully Passive Wireless Backscattering Neurorecording Microsystem Embedded in Dispersive Human-Head Phantom Medium. IEEE Electron Device Letters 33 (6): 908–10. Copyright: © [2011] IEEE. © [2012] IEEE.

Figure 2.8b is reprinted with permission from Schwerdt et al. 2013. Analysis of Electromagnetic Fields Induced in Operation of a Wireless Fully Passive Backscattering Neurorecording Microsystem in Emulated Human Head Tissue. IEEE Transactions on Microwave Theory and Techniques 61 (5): 2170–76. Copyright: © [2013] IEEE.

Figure 2.9 is reprinted with permission from Kiourt et al. 2016. A Wireless Fully Passive Neural Recording Device for Unobtrusive Neuropotential Monitoring. IEEE Trans. Biomed. Engineering 63 (1): 131–37. Copyright: © [2016] IEEE.289